Title
Mechanisms of Dynein Motility: Insights from Single-Molecule Studies

Author
Niekamp, Stefan

Publication Date
2020

Peer reviewed|Thesis/dissertation

Mechanisms of Dynein Motility: Insights from Single-Molecule Studies

by
Stefan Niekamp

DISSERTATION
Submitted in partial satisfaction of the requirements for degree of
DOCTOR OF PHILOSOPHY

in

Biophysics

in the

GRADUATE DIVISION
of the
UNIVERSITY OF CALIFORNIA, SAN FRANCISCO

Approved:

DocuSigned by:
Ronald D. Vale
A5A0784E09DA477...

Ronald D. Vale
Chair

DocuSigned by:
Sophie Dumont

Sophie Dumont

DocuSigned by:
Wallace Marshall
43941FCFA7C0447...

Wallace Marshall

Committee Members

DEDICATION

To my parents and grandparents, who supported me with all their love.

ACKNOWLEDGEMENT

I am extremely grateful for all the support and mentorship I received during the last 6 years. I would like to thank:

My mentor and advisor, Ron Vale, for giving me the tremendous freedom to pursue the questions that I found most interesting while at the same time being a source of unwavering support and wisdom. Thank you for all your guidance, advice, and inspiration. You are a role model to me and many others. Your way to ask and address questions, your curiosity, your generosity, your contribution to the community (open publishing, teaching, education, communication), and your passion for science amazed and inspired me every single day during my time in the lab and will always inspire me. Ron, thank you for all your help and for being a wonderful mentor.

Everyone in the Vale lab, past and present, for making the lab feel like home. I am thankful for every advice and laughter you shared over the last years. Without this wonderful lab environment that Ron created and each amazing lab member fills with life, every experiment would only have been half the fun. In particular, I would like to thank the “Dynein, Cilia, and Friends” team for their support, motivation, and inspiration - you are awesome. I would especially like to thank Gira Bhabha for all her invaluable advice and endless support in science and otherwise. Without Gira, the dyneins that I prepped would probably never have learnt to walk and I would still be using paper notepads as a calendar. Moreover, I am grateful for the mentorship and inspiration I received from Nico Stuurman. Nico’s microscopy support makes me see the world through a different lens. I would also like to thank Nan Zhang and Phoebe Grigg for all their support and for keeping the lab running.

My early teachers and mentors from high school and undergraduate who fostered my love for science - Hans Peter Schulz, Wolfgang Fricke, Toni Helm, Mark Kartsovnik, and Jonas Funke. In particular, I am thankful for the support and mentorship of Hendrik Dietz (TU Munich), who gave me the opportunity to experience research in a lab for the first time. I also would like to thank Shawn Douglas (UCSF) for his support, insights, mentorship, and joy for science. Without Shawn's support and encouragement to apply to graduate school, I would not have started my PhD at UCSF.

My thesis committee members, Sophie Dumont and Wallace Marshall, who provided advice, motivation, and inspiration for my research projects and much more. Thank you for all your wonderful support.

My classmates, the entire UCSF community and beyond for all your support and inspiration - Yifan Cheng, Jean-Paul Armache, Bob Stroud, David Agard, Jeremy Reiter, Dyche Mullins, Orion Weiner, Michael Grabe, Tanja Kortemme, James Fraser, Nicole Flowers, Rebecca Dawson, Christina Hueschen, Seth Axen, Erin Thompson, Paul Thomas, Miguel Betegon, Andrew York, Manu Prakash, the entire Morgan, Mullins, Vale, and Walter lab neighborhood and so many more.

My friends and roommates - I am grateful to my incredible friends for all their support, for sharing laughters and wonderful food. Thank you for filling graduate school with so many wonderful memories: Karina, Fernando, Nairi, Chris, Marco, Ishraq, Kimiko, Frances, Alex, Anne, Susan, and Jess. I am thankful to my "735" roommates, friends, and fellow classmates Eugene Palovcak, Evan Green, and Lillian Kenner, with whom I shared many wonderful moments both scientifically and outside of science.

My friends in Germany - Niklas, Mario, Peter, Simon, and Andreas, who were there for me through the entire journey and who I could count on every single day.

My family - for all their love and support through this journey, which has led me so far from home. Thank you, Mama (Brigitte) and Papa (Albert), for your unconditional love, for your support, and encouragement with whatever I do. You taught me how to walk, speak, listen, think, grow, and love. I would also like to thank my grandparents, Oma and Opa, who are always there with open arms, advice, and endless love. I would like to thank Arne, my brother, from whom I learn every day. You are an inspiration. Thank you for your advice, open ears, and for bringing Irma into our family. Throughout graduate school I gained a new family, my now in-laws. Thank you for welcoming me with open arms, lots of amazing food, and for making me feel at home.

My wife, Han, for her endless love and support though everything, who is filling my life with joy and gives me purpose. Thank you for showing me what matters and what life is all about.

STATEMENT REGARDING AUTHOR CONTRIBUTIONS

Chapter 2 of this dissertation contains partial reprints of previously published material:

Niekamp, S., Coudray, N., Zhang, N., Vale, R. D. & Bhabha, G. Coupling of ATPase activity, microtubule binding, and mechanics in the dynein motor domain. *EMBO J*. **38**, e101414 (2019)

Chapter 3 of this dissertation contains partial reprints of previously published material:

Niekamp, S., Sung, J., Huynh, W., Bhabha, G., Vale, R. D., & Stuurman, N. Nanometer-accuracy distance measurements between fluorophores at the single-molecule level. *Proc. Natl. Acad. Sci.* **116**, 4275–4284 (2019)

Chapter 4 of this dissertation contains partial reprints of previously published material:

Niekamp, S., Stuurman, N. & Vale, R. D. A 6-nm ultra-photostable DNA FluoroCube for fluorescence imaging. *Nat. Methods* **17**, 437–441 (2020)

Chapter 5 of this dissertation contains ongoing work and unpublished material:

Niekamp, S., Stuurman, N., Zhang, N., & Vale, R. D.

With the tentative title: Three-color single-molecule imaging reveals conformational dynamics and minimal requirements for directed motility of dynein

ABSTRACT

Mechanisms of Dynein Motility: Insights from Single-Molecule Studies

Stefan Niekamp

Transport of cargos not only plays a critical role on the meter scale in our daily life when we travel from A to B but also plays an essential role for cellular processes on the nanometer scale without which we would not exist. This cellular transport is carried out by motor proteins which walk on cellular highways and are responsible for almost all directed transport in cells. Moreover, these motor proteins play key roles in other cellular processes including mitosis and cilia motility. One of these motor proteins is the microtubule-based motor dynein. Dynein is a complex, flexible, and large machine that has to coordinate it's two engines and feet in order to achieve directed and continuous motility. Recent structural and biochemical studies uncovered key molecular mechanisms contributing to dynein motility. However, a comprehensive understanding of how dynein steps along its microtubule track, and how its different domains are coordinated to achieve this movement were lacking in the field.

Therefore, I first set out to determine how dynein's ATPase activity and mechanics are coupled among the motor domain of dynein and showed that the ~15 nm long coiled-coil linking the catalytic AAA ring and its microtubule-binding domain is indispensable in regulating motor activity. Moreover, I found that the length rather than the sequence of this coiled-coil is remarkably well conserved and that the length conservation is paramount for directional motility. Integrating these observations allowed us to generate an updated model for the internal regulation of dynein.

Our understanding of how the different domains of dynein move relative to each other has been limited by insufficient high spatiotemporal resolution. To overcome this, I first created a method that enables three-color image registration and distance measurements with one nanometer accuracy and second, I developed DNA FluoroCubes that enabled me to track the

position of multiple domains of dynein for a prolonged time with nanometer precision. Combining both of these methods enabled me to gain insights into the conformational changes of dynein's domains while moving along microtubules. I found that the motor domain of dynein is very flexible and that this flexibility is important for dynein motility and enables dynein to adopt a large variety of conformations. Together, these findings revealed a new model for dynein stepping that defines the minimal requirements to facilitate directed and continuous motility.

TABLE OF CONTENTS

LIST OF FIGURES

CHAPTER 2

CHAPTER 3

CHAPTER 5

LIST OF TABLES

CHAPTER 2

CHAPTER 3

CHAPTER 4

CHAPTER 1

Introduction and Summary

A city without cars, trucks, and trains is a cell without motor proteins. Eukaryotic cells depend on motor proteins to achieve almost all directional transport within cells, to divide, and to move themselves. Similar to roads and tracks in cities, these molecular motors move along cellular “highways”. The largest of these motor proteins is dynein, which walks with two “feet” each powered by a separate engine. The motor protein dynein plays key roles in many cellular processes including cargo transport, mitosis, and cilia motility[1–4]. Moreover, dynein is a complex, flexible, and large machine that has to coordinate conformational heterogeneity among its many domains to achieve directed and continuous motility. Mutations or defects in dyneins are associated with several pathologies including cancers and neurological diseases[5,6].

Dynein was first discovered by Ian Gibbons[7], who showed that dynein is required to power the beating of cilia in Tetrahymena. Later it was shown that dynein exists as axonemal as well as cytoplasmic dynein. While there are multiple isoforms of axonemal dyneins, there are only two isoforms of cytoplasmic dynein of which one is responsible for intraflagellar transport (cytoplasmic dynein 2) and the other (cytoplasmic dynein 1) performs all other cytoplasmic tasks ranging from cargo transport such as membranes, RNAs, proteins and viruses to force generating processes such as mitosis[6,7]. For my thesis work I only focused on cytoplasmic dynein 1 to which I will refer as dynein from now on.

The cellular highway dynein is walking on is called microtubule. These microtubules are micrometer long filaments which can stretch through an entire cell and therewith connect different parts of the cell with each other[8–10]. Moreover, microtubules are known to have a polarity (plus and minus ends) and some motor proteins favor walking in one direction, while others have the tendency to walk in the other direction. While dynein has been shown to

exclusively move towards the minus end[11], kinesin[12], another microtubule based motor protein, typically walks towards the plus end. Since both motor proteins are often attached to the same cargo, dynein and kinesin undergo a so-called “tug-of-war”[13,14], in which the winner determines where the cargo goes. During my thesis work, I asked questions regarding dynein’s ability to walk, which I will introduce below.

Compared to the much smaller and more compact cytoskeletal motors, kinesin[15,16] and myosin[17,18], dynein is the largest and most complex cytoskeletal motor protein with a complex size of ~1.4 MDa. In order to move and generate force, mammalian dynein requires activators and other regulatory complexes. For instance, it was discovered that dynactin as well as other coiled-coil proteins, called cargo-adaptors, are required for processive movement of mammalian dynein[2,19,20]. These cargo-adaptors such as BICD and HOOK3[20,21] are not only essential to activate dynein motility but also link dynein and dynactin to their cargo. Moreover, it has recently been shown that cargo-adaptors such as BICDR1 and HOOK3 can recruit two dynein homodimers to the same complex enabling faster motility[22,23]. In addition to dynactin and cargo-adaptors, regulatory proteins such as Lis1 can bind to dynein and enable the assembly of an activated complex[24–26].

The cytoplasmic dynein holoenzyme is composed of two, more than 4000 amino acid long, identical heavy chains and multiple associated polypeptide chains, which bind to the N-terminal part of the heavy chain, the dynein tail. The dynein tail also connects the dynein homodimer to dynactin and cargo-adaptors. However, the core element for dynein motility lies in the C-terminal motor domain of the dynein heavy chain, which can be divided into the linker domain, AAA+ ring (ATPases Associated with diverse cellular Activities), stalk, buttress, and microtubule-binding domain (MTBD). Of the six different AAA domains that are linked together as an asymmetric hexameric ring (AAA1–AAA6) only AAA1-4 can bind or hydrolyze ATP[27–33]. While ATP hydrolysis in AAA1 is required for dynein to take a step, AAA3 has a regulatory function and acts as a switch, which only enables robust motility when ADP is bound to its

pocket[34–36]. On top of the AAA ring lies the N-terminal linker which not only serves as the mechanical element but also links the C-terminal motor domain to dynein's tail. Upon ATP binding to AAA1 dynein releases from microtubules and the linker bends[27,30,37,38]. After ATP hydrolysis, dynein rebinds to microtubules while the linker undergoes the force-generating power stroke by straightening back to its initial conformation[29,34–36,39]. Unlike for the compact motor proteins, kinesin and myosin the large catalytic AAA ring of dynein is separated from the small microtubule-binding domain (MTBD) by a ~15 nm long, coiled-coil extending from AAA4 called the stalk[40–42]. Thus, in dynein the main ATP hydrolysis site AAA1 is separated by ~240 Å from the track-binding MTBD and information between both has to be transmitted through the entire motor domain.

To enable the two-way communication between the track-binding MTBD and the catalytic AAA ring, it has been suggested that the stalk undergoes conformational changes[29,40,42–46]. However, how the allosteric communication between the AAA ring and the MTBD occurs was poorly understood. Moreover, even though tremendous insights into dynein stepping have been achieved by labeling the two AAA rings of the dynein motor domain with fluorescent probes showing that dynein moves in an uncoordinated manner[47,48], a comprehensive understanding of how the distant MTBDs step along the microtubule track was lacking in the field. This was particularly interesting as the AAA ring and the MTBD have been observed to move relative to each other when bound to microtubules, indicating flexible elements within the dynein motor domain[11,49,50]. Furthermore, it was unclear how this large and complex motor protein dynein coordinates its different and separated domains (AAA ring and MTBD) to achieve directed motility when moving along microtubules. In my thesis work, I have addressed these questions mainly by developing new methods for single-molecule microscopy and will discuss the development of these methods as well as our biological findings which led to a new model for dynein motility.

I first set out to understand how dyneins ATPase activity and mechanics are coupled among the motor domain of dynein and teamed up with Gira Bhabha, a former postdoctoral fellow in the Vale lab. By combining bioinformatics analysis, cryo-electron microscopy, enzymatic assays, and single-molecule imaging we showed that the coiled-coil linking the main hydrolysis site and the microtubule-binding domain is indispensable in regulating motor activity (Chapter 2). Moreover, we uncovered that the length rather than the sequence of this coiled-coil is remarkably well conserved and that the length conservation is paramount for directional motility of dynein. For instance, when we altered the length of the stalk by one amino acid, dynein lost its ability to move in a directed and processive fashion. Integrating our findings with previously published work enabled us to develop a new model that explains how dynein's microtubule-binding domain communicates with the ~24 nm distant ATP hydrolysis sites.

Our understanding of how the different domains of dynein move relative to each other has been limited by insufficient high spatiotemporal resolution. Therefore, I set out to develop a single-molecule imaging approach that allows me to precisely track the position of multiple domains of a walking dynein at the same time. The first step towards achieving this goal was to set up a microscopy-pipeline that permits multicolor imaging with nanometer resolution. To this end, I worked together with Nico Stuurman, a senior scientist and microscopy expert in the Vale lab, and established image registration and distance measurement routines that enable fluorescent imaging with subnanometer accuracy (Chapter 3). Another obstacle was that existing fluorescent probes for labeling the domains either perturb function or do not provide enough signal. To overcome this, I utilized DNA nanotechnology and developed small and ultra-photostable fluorescent probes (DNA FluoroCubes) that are up to 50-fold more photo stable than organic dyes (Chapter 4).

Combining both methods and applying them to a three-colored dynein allowed me to track the movement of one AAA ring and two MTBDs of a dynein homodimer simultaneously. Analyzing the stepping traces of all three domains I found that the motor domain of dynein is

very flexible and that this flexibility is important for dynein motility and enables dynein to adopt a large variety of conformations. Together, these findings provide an updated model for dynein stepping that defines the minimal requirements to facilitate directed and continuous motility (Chapter 5). I note that this is ongoing work and therefore has not been peer reviewed.

In addition to the biologically findings, I am anticipating that our new fluorescent microscopy methods will open the door to study conformational dynamics and mechanisms of many other molecular machines.

CHAPTER 2

Coupling of ATPase activity, microtubule binding and mechanics in the dynein motor domain

Abstract

The movement of a molecular motor protein along a cytoskeletal track requires communication between enzymatic, polymer-binding, and mechanical elements. Such communication is particularly complex and not well understood in the dynein motor, an ATPase that is comprised of a ring of six AAA domains, a large mechanical element (linker) spanning over the ring, and a microtubule-binding domain (MTBD) that is separated from the AAA ring by a ~135 Å coiled-coil stalk. We identified mutations in the stalk that disrupt directional motion, have microtubule-independent hyperactive ATPase activity, and nucleotide-independent low affinity for microtubules. Cryo-electron microscopy structures of a mutant that uncouples ATPase activity from directional movement reveal that nucleotide-dependent conformational changes occur normally in one half of the AAA ring, but are disrupted in the other half. The large-scale linker conformational change observed in the wild-type protein is also inhibited, revealing that this conformational change is not required for ATP hydrolysis. These results demonstrate an essential role of the stalk in regulating motor activity and coupling conformational changes across the two halves of the AAA ring.

Introduction

Dyneins are minus-end directed, microtubule-based molecular motors that belong to the AAA+ (ATPases associated with diverse cellular activities) superfamily of proteins. Cytoplasmic dynein is responsible for the transport of numerous cargoes along microtubules (MTs), such as organelles, vesicles, viruses, and mRNAs[51,52]. In addition, cytoplasmic dynein plays key roles in facilitating basic cell biological processes such as spindle positioning during mitosis[1]. Mutations and defects in cytoplasmic dyneins are associated with many diseases such as neurodegene[53,54] rative diseases and cancers[5].

The cytoplasmic dynein holoenzyme is composed of two identical ~500 kDa heavy chains and multiple associated polypeptide chains that primarily bind to the N-terminal [53,54]tail of dynein[55]. Regulatory proteins such as Lis1 and NudE bind to some dyneins and can modify its motility properties[53,54]. To initiate processive motility for cargo transport, human cytoplasmic dynein also requires dynactin as well as cargo-adaptor proteins such as BicD and Hook3[20,21]. However, the core element for motility of all dyneins lies in the conserved motor domain of the heavy chain, which consists of six different AAA domains that are linked together as an asymmetric hexameric ring (AAA1-AAA6). Only AAA1-AAA4 can bind nucleotides[27–33] (**Fig. 2.1**); ATP hydrolysis in AAA1 is required for dynein stepping and AAA3 acts as a switch that facilitates robust motility when ADP is bound[34–36]. The catalytic domains in the AAA ring are spatially distant from the microtubule binding domain (MTBD); the two are connected via the coiled-coil “stalk” that emerges from AAA4. Another coiled-coil element, called the buttress, protrudes from AAA5 and interacts with the stalk close to the ring (**Fig. 2.1**). The buttress also has been shown to be important for the allosteric communication between ring and MTBD[30]. The N-terminal linker, which lies on top of the ring, is believed to serve as a mechanical element that drives motility[27] and Can et al.[11] have recently shown that the direction in which the linker swings is critical to define the directionality of dynein. Over the last few years, several structural studies have illuminated a series of conformational changes in the dynein AAA ring during the

ATPase cycle[28–30,35]. The key conformational changes include domain rotations within the AAA ring and rearrangements of the linker domain.

To coordinate motility, motor proteins must communicate between the ATPase and polymer binding site. ATP binding to AAA1 results in a weakened affinity (K_d >10 μM) of dynein for microtubules (MTs). After ATP hydrolysis and phosphate release, the motor binds MTs with stronger affinity (K_d <1 μM)[40]. In this manner, the AAA ring controls the affinity of the MTBD for MTs. Conversely, interaction of the MTBD with MTs regulates the ATPase activity in the AAA ring[40]. How this allosteric communication occurs is still poorly understood. In the case of kinesin and myosin, the ATPase and track binding sites are located relatively close (within ~25 Å) to each other in the same domain[56]. In dynein, however, the very small ~10 kDa microtubule-binding domain is spatially separated from the AAA ring by the ~135 Å long coiled-coil stalk[40,42,57–59]. Furthermore, the stalk is positioned between AAA4 and AAA5, which is on the opposite side of the ring from AAA1, resulting in a ~240 Å separation between the main catalytic site and the MTBD.

To enable two-way communication between the MTBD and AAA ring, it has been suggested that the stalk undergoes conformational changes[40,43,44]. One hypothesis is that sliding between the two antiparallel helices of the stalk coiled-coil leads to changes in their register with respect to each other, with each registry corresponding to different microtubule affinities; the stalk in the β+ registry results in a low MT affinity state and the α registry results in high MT affinity[40,42]. This is further supported by structural work which has shown that when ADP-vanadate (ADP-vi) is bound to AAA1, the coiled-coil 2 (CC2) of the stalk is kinked and slides together with the buttress relative to coiled-coil 1 (CC1)[29]. Another study speculates that local melting of the coiled-coil between different states of the hydrolysis cycle plays a major role in the communication[45,46]. However, how relative length changes of the stalk either via sliding or local melting drive the communication between the ring to the MTBD is not well understood.

To gain better insights into the allosteric communication between the AAA ring and the MTBD, we have identified mutants in the dynein stalk that block communication between the ATPase and microtubule binding sites. These mutants show diffusive movement along MTs and also hydrolyze ATP at maximal rates in a microtubule-independent manner. Structural characterization by cryo-electron microscopy (cryo-EM) of one of these mutants reveals a stabilization of a previously uncharacterized open conformation of the AAA ring in the presence of the non-hydrolysable ATP analogue AMPPNP. In the presence of ADP-vanadate (ADP-vi), mimicking the post-hydrolysis state of dynein, we observed that this mutant is primed for hydrolysis, but with the linker in an extended conformation, which differs from the bent conformation of the linker in wild-type dynein[29,35]. This result reveals that linker bending is not essential for ATP hydrolysis. Moreover, we gained new insights into domain movements in the AAA ring. The cryo-EM structure of the mutant in AMPPNP and ADP-vi states show that one half of the AAA ring undergoes a conformational change similar to the wild-type enzyme, while the AAA domain movements in the other half of the ring, from which the stalk extends, are disrupted. This result reveals that the stalk likely plays a key role in coupling conformational changes throughout the AAA ring. Our results provide insight into how the movements of different domains within the motor domain of dynein are coordinated to allow microtubule regulation of ATPase activity and motility.

Results

Stalk mutants show nucleotide-independent diffusion

Given the spatial separation between dynein's catalytic AAA ring and the MTBD, it is apparent that allosteric communication must be mediated in some way via the stalk (**Fig. 2.1**). To understand what regions of the stalk may play a role in allosteric communication, we aligned and analyzed 534 sequences of dynein's motor domain. We found that the length of the stalk is very well conserved (99% of the sequences have the exact same stalk length) among species and types of dynein, such as cytoplasmic, axonemal and IFT dynein, but the sequence is not (**Fig. S2.1**). Based on the conserved length of the stalk and our sequence analyses, we decided to investigate how insertions and deletions in the stalk affect dynein's motility. We designed a panel of 18 insertion and deletion mutants in the yeast cytoplasmic dynein background, based on our sequence analysis (**Fig. 2.1, Fig. S2.2, Fig. S2.3, Table S2.1**). We expressed and purified GST-dimerized versions of each mutant (**Fig. S2.4**) with an N-terminal GFP[60,61], assessed the quality of the protein using negative stain electron microscopy to ensure structural integrity, and used single-molecule total internal reflection fluorescence (TIRF) microscopy assays[60,62] for initial characterization of single-molecule motility.

Our panel of mutants displayed a wide variety of phenotypes (**Fig. 2.1**). Of the eighteen mutants, seven mutants (mutants 1, 3, 4, 6, 7, 11, and 12) showed single-molecule movement with velocities and processivity that were between ~50-100% of the wild-type protein (**Fig. S2.4**). Remarkably, some of these mutants had relatively large insertions of 6 (mutant 4) or 9 (mutant 11) residues or a deletion of 5 residues (mutant 12), but still moved in a similar way as the wild-type motor. Of these seven mutants that showed wild-type phenotypes, six are in CC1 (mutants 1, 3, 4, 7, 11, and 12), suggesting that this helix is more tolerant of changes in length than CC2 (mutant 6) (**Fig. S2.1 - S2.3, Fig. S2.5**). One region that is particularly sensitive to mutation is at the interface of the stalk and buttress (**Fig. S2.1**). Most of the mutations that resulted in a dead (mutants 8, 9, 10, 17, and 18) or unstable (mutants 15 and 16) motor are

clustered in the proximal region of the stalk, close to the AAA ring (**Fig. S2.1**), and are in regions that are important for the stalk and buttress interaction (**Fig. S2.1, Fig. S2.3**). This stalk and buttress interface has been shown previously to play a role in nucleotide-dependent conformational change[29] and thus our observations suggest that mutations in the stalk and buttress interface can severely compromise dynein motility, consistent with the model that the stalk and buttress interface is critical for dynein motility. Interestingly, we observed one mutant (mutant 14) that contains two distinct populations of molecules: the major population (96%, population 1) transiently binds to and releases from microtubules and the minor population (4%, population 2) appears to move in a similar way as the wild-type motor (**Fig. S2.6**). Surprisingly, the site of mutation for mutant 14 overlaps with that of mutant 18, yet single-molecule properties observed for mutant 18 show a dead motor (**Fig. S2.2 - S2.4**). Lastly, three mutants from our panel (2, 5, and 13) presented a diffusive-like behavior, with single molecules randomly moving back-and-forth along the microtubule (**Fig. 2.1, C, Fig. S2.7**). This observation suggests that these diffusive-like motors are weakly bound to microtubules but unable to undergo effective unidirectional motion. We further analyzed the movement of mutant 5 along microtubules by measuring the displacement distance and directionality per one second interval. The histogram of the displacements (**Fig. S2.8**) reveals a uniform Gaussian distribution centered close to zero with an average displacement of -3.3 nm. This analysis supported the notion that the back-and-forth motion of mutant 5 reflects random thermal-driven motion along the microtubule.

We decided to further characterize the three interesting mutants (mutants 2, 5, and 13) that showed similar one-dimensional diffusion along the microtubule and the one mutant (mutant 14) that showed weak binding and occasional directional motion. To assess the nucleotide-dependence of the diffusive phenotypes, we carried out single-molecule experiments in the absence of ATP. As expected, the wild-type control showed no movement, and was rigor bound to microtubules (**Fig. S2.7**). Surprisingly, in the absence of ATP, all three mutants (mutants 2, 5, and 13) displayed diffusive behavior very similar to that observed in the presence

of ATP (**Fig. 2.1, Fig. S2.7**). Diffusion, that we observed even in the absence of nucleotide, suggests that mutant 2, mutant 5, and mutant 13 have a weakened interaction with microtubules (**Fig. 2.1, Fig. S2.7**). Mutant 14 also seems to have weak affinity for microtubules in the apo state because we observed transient binding events in the absence of ATP (**Fig. S2.6**).

We also assessed the nucleotide-dependent binding affinity of dynein for microtubules using a cosedimentation assay. In wild-type dynein, the motor binds tightly to microtubules in the absence of ATP, but weakly in the presence of ATP (**Fig. 2.2**). In contrast to the nucleotide-dependent microtubule-affinity of wild-type enzyme, the microtubule affinity of the diffusive mutants (mutants 2, 5, and 13) and the transient binding mutant (mutant 14) was low in the absence of nucleotide and in the presence of ATP or AMPPNP (**Fig. 2.2, Fig. S2.6, Table S2.2**), which is consistent with the single-molecule motility results. These results confirm that the diffusive mutants and mutant 14 have a weakened microtubule affinity which remained unchanged in different nucleotide states.

Since we did not observe any directional movement of these three mutants in single-molecule assays, we asked whether there is any net directionality in a microtubule gliding assay when there are many motors interacting with a microtubule. In this microtubule gliding assay, dimeric dyneins (wild-type or mutants) were attached to a glass coverslip (**Fig. S2.9**). Results from this assay show that the three mutants generated microtubule gliding across the glass surface, although their velocities were ~10-fold lower than wild-type dynein (**Fig. S2.9**). This phenotype is reminiscent of human cytoplasmic dynein (dynein 1) purified from rat brains (McKenney et al, 2014), which also shows diffusive motility in single-molecule assays, but shows robust directional movement in gliding assays. We also determined whether the microtubules were moving in the same direction as for wild-type dynein and assessed the direction of motion with single molecules of a human homodimeric kinesin-1 (K490)[63], which move processively towards the microtubule plus end (**Fig. S2.9**). By observing the direction of kinesin movement along the gliding microtubules, we could assess their polarity. Our results

showed that the direction of mutant 2, 5, and 13 in microtubule gliding assays was the same as for wild-type dynein. In conclusion, mutants 2, 5, and 13 show nucleotide-independent diffusive movement as single molecules, while ensembles of these motors can produce extremely slow directional movement towards the MT minus end.

Diffusive mutants show microtubule-independent hyperactive ATP hydrolysis

Since single-molecule analysis of mutants 2, 5, and 13 showed diffusive movement uncoupled from the nucleotide state, we asked whether these mutants were capable of hydrolyzing ATP. One possible hypothesis was that the mutants could no longer bind or hydrolyze ATP, while another possibility is that ATP hydrolysis was uncoupled from directional movement. We measured the ATPase activity of mutant 2, mutant 5, and mutant 13 at varying concentrations of microtubules. In wild-type dynein, ATPase activity is stimulated in the presence of microtubules, resulting in a characteristic increase in ATPase activity as microtubule concentration increased, until maximal ATPase activity is reached. For wild-type dynein, we measured a basal ATPase turnover of 0.75 ± 0.34 ATP/motor/sec, which increased with increasing concentrations of microtubules to a k_{cat} of 15.18 ± 1.18 ATP/motor/sec and K_m of 0.50 ± 0.17 μM for tubulin dimer (**Fig. 2.2**). These ATPase values are similar to those previously reported[32,59,64] (**Table S2.3**). Surprisingly, and in contrast to wild-type dynein, the three diffusive mutants (mutants 2, 5 and 13) showed high basal ATPase activity that did not significantly increase upon the addition of microtubules. Interestingly, the basal ATPase activities of mutants 5 and 13 were very similar to the maximal microtubule-stimulated ATPase activity of the wild-type protein (**Fig. 2.2, F, Table S2.4**). In addition to the diffusive mutants (mutants 2, 5, and 13), mutant 14 also showed high basal ATPase activity that is independent of microtubule concentration (**Fig. S2.6**). Together, these results indicate that the four weak binding mutants (mutants 2, 5, 13, and 14) all showed high ATPase activity and loss of microtubule regulation of the ATPase activity.

Structural basis for hyperactivity of mutant 5

Our functional and biochemical assays showed that insertions and deletions in mutants 2, 5, and 13 result in: 1) diffusive movement of single dynein molecules on microtubules, 2) constitutively hyperactive ATPase, and 3) constitutively weak microtubule binding that is not modulated by nucleotide. Taken together, these results suggest that these mutations disrupt the two-way communication between the MTBD and AAA ring in the dynein motor domain. Next, we sought to understand the structural basis underlying the uncoupling between the microtubule and ATPase sites in the diffusive mutants. Because of its high basal ATPase activity, we decided to focus on mutant 5.

We first collected a cryo-electron microscopy dataset of mutant 5 in the presence of 2 mM AMPPNP to mimic one of the post-force-generating states at AAA1 and AAA3. After 3D classification and refinement, we identified two distinct classes, with reconstructions at ~7.5-8 Å resolution (**Fig. S2.10, Fig. S2.11)**. This resolution allowed us to establish conformational changes at the subdomain level and model helices in some parts of the structure (**Fig. S2.10, Fig. S2.11**). Each AAA domain consists of a large subdomain (AAAL) and a small subdomain (AAAs), which can be considered as rigid bodies in the context of our resolution. Each AAAL and AAAs subdomain is fit independently as rigid bodies into each density map to generate a model corresponding to each map.

The most evident change in the motor domain of the majority (~71% of all particles - class 1, 7.7 Å resolution) of mutant 5 particles was an substantial opening between the small and large domains of AAA5 (**Fig. 2.3**), which was previously only observed as a minor conformation for the wild-type motor (**Fig. S2.12**). In addition, density for most of the distal stalk as well as the buttress is missing, suggesting that these regions are flexible. For the minor conformation (~29% of all particles - class 2, 7.6 Å resolution), the cryo-EM map shows a closed ring with no gap between the small and large domain of AAA5 and the helices of the initial part of the stalk and for the buttress are well defined (**Fig. 2.3**, **Fig. S2.10**). In this class, we can

identify a conformation that has previously been referred to as the high microtubule affinity state in which the coiled-coil 2 of the stalk is not kinked (**Fig. S2.10**) [29]. An additional and more subtle difference between the class 1 and 2 density is found in the N-terminal GFP tag at the end of the linker. In contrast to class 2, for class 1 (major class with “open” ring), the density for the N-terminal GFP tag is not well defined (**Fig. S2.10**), which may indicate that the N-terminus of the linker is more flexible and potentially undocked from the ring at AAA5. Looking at domain movements in both class 1 and class 2 (**Fig. 2.3**), we also found that AAA2L is positioned away from the active site of AAA1 (**Fig. S2.10**). Since the gap between AAA1 and AAA2 must close for productive ATP hydrolysis, we concluded that the ring of mutant 5 in the AMPPNP state is not primed for hydrolysis, as is true for wild-type dynein.

We next examined mutant 5 in the ADP-vanadate (ADP-vi) state, which mimics the post-hydrolysis state of dynein[29]. In this state, the AAA domains in wild-type dynein adopt a more compact conformation in which the gap between AAA1 and AAA2 closes, which primes AAA1 for nucleotide hydrolysis (**Fig. S2.10**). In addition, in the wild-type protein, the linker changes from a “straight” conformation (extended linker spanning from AAA1 to AAA5) to a “bent” conformation (the N-terminus of the linker making contacts with AAA 3/2). Our cryo-EM data for mutant 5 in the presence of 2 mM ATP and 2 mM vanadate resulted in a ~9 Å reconstruction, for which subdomain movements could be mapped with confidence (**Fig. 2.4, Fig. S2.13**). Based on fitting AAAs and AAAL domains into our density as described above, our data show that the gap between AAA1L and AAA2L for mutant 5 closes when transitioning from the AMPPNP to the ADP-vi state (**Fig. 2.4**), similar to what was observed for wild-type dynein. The AAA2L domain of mutant 5 undergoes a rotation between the AMPPNP and ADP-vi state of ~21° which is similar to the ~20° domain rotation in wild-type dynein (**Fig. S2.13**). The approximate distance between the Arginine finger and Walker-A motif of mutant 5 and wild-type decrease from ~22 Å and ~20 Å in the AMPPNP state, respectively to ~17 Å and ~14 Å in the

ADP-vi state, respectively (**Fig. S2.13**), highlighting that the gap between AAA1L and AAA2L for mutant 5 and wild-type dynein indeed close in a similar manner.

Unlike the bent linker observed for wild-type dynein in the presence of ADP-vi[29], the mutant 5 linker is not bent at the hinge-point (**Fig. 2.4**). However, the N-terminal region of the linker is undefined, suggesting increased flexibility at its N-terminal region (**Fig. 2.4, Fig. S2.13**). We confirmed the binding of vanadate to the AAA1 nucleotide binding pocket of mutant 5 by demonstrating vanadate-mediated UV photo-cleavage and vanadate inhibition of the ATPase activity (**Fig. S2.13**). Thus, our structural data for mutant 5 in the presence of ATP and vanadate indicate that the motor is primed for hydrolysis, but does not undergo the large conformational change in the linker that is believed to be essential for motility[27,34].

To better understand how mutant 5 can be primed for hydrolysis while the linker remains in a straight conformation, we analyzed the AAA domain movements as dynein transitions from the AMPPNP to the ADP-vi state. When both states are aligned on AAA1L, we observe similar domain movements in approximately one-half of the ring surrounding AAA1 (from AAA5s to AAA2L) (**Fig. 2.5,**), while the domain movements in the other half of the ring, AAA2s to AAA5L, are quite different (**Fig. 2.5, Fig. S2.13**). In contrast to the pronounced nucleotide-dependent motions in the AAA2s-AAA5L half of the ring for wild-type dynein, very little motion is observed for these domains in mutant 5 and the mode of movement is different (**Fig. 2.5**). Thus, between the AMPPNP and ADP-vi states, mutant 5 exhibits normal AAA domain movements in one half of the ring (AAA5s-AAA2L), but shows a considerable lack of motion in the other half (AAA2s-AAA5L) (**Fig. 2.5**). This result reveals that this stalk mutation uncouples nucleotide-dependent conformational changes in the two halves of the ring. Moreover, these results provide new insight into domain movements of the AAA ring and could explain why mutant 5 shows high ATPase activity but little motility, as will be described in the discussion.

Discussion

We have identified mutations in the dynein stalk that show nucleotide-independent weak binding to microtubules and diffusional motion along the microtubule surface. A microtubule-stimulated ATPase assay revealed that these mutants hydrolyze ATP independently of microtubule concentration; two of these mutants (mutant 5 and 13) are hyperactive and have a basal ATPase activity that is as high as the maximal microtubule-stimulated turnover rate in the wild-type protein. Performing structural analysis on one of these mutants (mutant 5) using cryo-electron microscopy, we found that nucleotide-dependent “straight-to-bent” conformational change in the linker domain is inhibited. Moreover, we observed that AAA domain movements in one part of the ring are altered, while the other part of the ring becomes primed for hydrolysis very similarly as in wild-type dynein. These data provide new information on how the microtubule-binding domain (MTBD), stalk, linker, and AAA ring communicate with one another during the ATPase cycle, as discussed below.

Domain movements in the AAA ring

Dynein is a large and complex allosteric protein that must coordinate the conformations of four independent domains: 1) the AAA ring (consisting of 6 AAA domains), 2) the largely helical linker (which spans over the ring and serves as a mechanical element), 3) the small, globular microtubule-binding domain, and 4) the stalk-buttress apparatus (a pair of antiparallel coiled-coils that extend from the AAA ring and connect via the stalk to the microtubule binding domain). Current structural data suggests that ATP binding to AAA1, with ADP bound at AAA3, drives full AAA ring closure[29,30,35], which is associated with a large-scale conformational change in the linker and a shift in registry of the two antiparallel coiled coils that affects the affinity of the distal microtubule binding domain. However, the manner in which these different domains communicate with one another is incompletely understood.

Previous models for conformational changes in the AAA ring upon ATP binding suggest a rigid body movement of AAA2-AAA4, which propagates as a rotational motion to AAA5s and AAA6L which in turn pull the buttress relative to the stalk[29,35]. ATP hydrolysis and/or product release then straightens the linker (thought to be the “power-stroke”), and relaxes the ring back to its original conformation. Another model by Kon et al.[65] suggests an important role of the C-terminal domain (C-sequence), located on the surface of the ring opposite to the linker, in connecting AAA1L and AAA5s and triggering a movement of the buttress and, in turn, conformational changes of the stalk and MTBD. Even though the full C-terminal domain is not found in every dynein[29], the H1 alpha helix of the C-sequence that staples the AAA1L/AAA6s and AAA6L/AAA5s blocks together[65] appears to be present in virtually all dyneins.

Comparing the conformational states sampled by mutant 5 with the conformational states previously reported for the wild-type protein, we can understand how the stalk mutation in mutant 5 perturbs normal conformational changes in the dynein motor protein, thus provide insight into stalk-mediated conformational changes of the AAA ring.

Our cryo-EM data of mutant 5 revealed wild-type like nucleotide-dependent AAA domain conformational rearrangements in one part of the ring (AAA5s-AAA6-AAA1-AAA2L), but absence /alteration of these conformational changes in the other part of the ring (AAA2s-AAA3-AAA4-AAA5L) (**Fig. 2.5**). Specifically, movements in AAA5L and AAA4s are much smaller in magnitude, and different in their vector of movement (**Fig. 2.5**). This result indicates that the domain movements in the AAA5s-AAA2L block are insulated, at least to some extent, from the rest of the ring and from disruptive mutations in the stalk (**Fig. 2.5**). Thus, we hypothesize that the two halves of the ring can undergo two independent modes of conformational change, which require the stalk-buttress apparatus to be properly coupled.

Based on the conformational changes seen in the cryo-EM data for mutant 5, we speculate that ATP binding does not primarily propagate in a clockwise (viewed from the linker side), domino-like manner from AAA1 to AAA6[29,35,66]. Instead, the data for mutant 5 shows

bidirectional domain movement around the ATP-bound pocket of AAA1, with a block of AAA5s-AAA6Ls-AAA1L moving towards the AAA1s-AAA2L block upon ATP binding to AAA1. The C-terminal domain might provide the underlying bridging support between AAA5s/AAA6L and AAA6s/AAA1L that allows this block of AAA domains to move in a unified manner, consistent with the proposal of Kon et al.[65].

The structural data also emphasize the important role that the stalk-buttress play in coupling the conformational changes in the two halves of the ring. Although we cannot see the precise lesion in the stalk caused by mutant 5 due to flexibility in this region, the downstream effect is an enlarged gap between AAA5s and AAA5L, which we speculate is the underlying cause in the disruption in the allosteric communication within the ring (**Fig. 2.5**). Specifically, our data for mutant 5 in the presence of ADP-vanadate suggests that movement of AAA5s/AAA6L towards the nucleotide binding pocket of AAA1 is unable to pull AAA5L/AAA4s with it (and the other half of the ring) (**Fig. 2.5**). The interaction between the buttress (emerging from AAA5s) and stalk (emerging from AAA4s) is likely needed for this coordination between the two halves of the ring. Interestingly, the failure to connect AAA5L/AAA4s to the movement of the AAA5s-AAA6Ls-AAA1Ls-AAA2L block severely impacts the nucleotide-dependent movements of the half of the ring from AAA2s-AAA5L. This result suggests that domain movements in this part of the ring are dependent upon the integrity of the stalk-buttress apparatus and its connection to the autonomous nucleotide-driven motions of the continuous AAA5s-AAA6Ls-AAA1Ls-AAA2L block.

This new model suggests why the stalk mutants hydrolyze ATP independently of microtubule concentration. Specifically, the disruption of the stalk-buttress interface allows the buttress and AAA5s/AAA6/AAA1L to undergo open-closed transitions accompanying ATP binding, hydrolysis and product release, without any regulation by microtubules through the stalk-buttress apparatus (**Fig. 2.5**). Interestingly, buttress mutations that presumably disrupt the stalk-buttress interaction[30] also show high ATPase activity independent of microtubules, similar

to our mutants 5 and 13. Thus, we suggest that the stalk-buttress interaction is a key regulator for dynein's ATPase activity by controlling the coupling between AAA4s/AAA5L and AAA5s/AAA6L and thus the coordination of domain movements in the two halves of the ring.

Uncoupling of linker bending from robust ATP hydrolysis

Our structural analysis revealed that mutant 5 has uncoupled nucleotide-dependent changes in one half of the AAA ring and ATP hydrolysis from the large conformational change of the linker domain. Previous findings[35,36] suggested that in order for ATP hydrolysis to proceed, the linker must be undocked from the ring, to allow full closure of AAA2L. Thus far, structures in which the AAA ring is primed for hydrolysis (i.e. the gap between AAA2 and AAA1L is closed) have been accompanied by linker bending and docking onto AAA3/2[29,35]. However, our cryo-EM reconstruction of mutant 5 in the presence of ADP-vanadate shows a motor that is primed for hydrolysis with an unbent linker (**Fig. 2.4**). Weak/missing density for the N-terminus of the linker suggests that it is flexible and might be undocked; however, it is clearly not in a bent conformation (**Fig. S2.13**). These data therefore suggest that linker bending is not a prerequisite to prime the motor for hydrolysis. However, the linker bending is not only necessary for efficient directional motion[35,67] (since single mutant 5 motors show random bidirectional motion) but also important to set the directionality of the motor [11]. Together, these data further support our model that the hydrolysis cycle arises from autonomous conformational changes within the AAA5s-AAA6Ls-AAA1Ls-AAA2L block and neither require linker bending nor an intact stalk-buttress interface.

Our structural data also allow us to speculate on how linker bending is initiated and why it fails to occur in the mutant 5. In the nucleotide-free and ADP state, the linker forms contacts with AAA5L. Movement of AAA5L upon ATP binding in AAA1 may induce a steric clash with the linker (perhaps with contributions from AAA4L[29]), and linker bending may ensue to minimize such clashes. In mutant 5 however, AAA5L movement is minimal and thus may be unable to

induce the linker steric clash (**Fig. S2.13**), which is highlighted in the “gap” between AAA5L and AAA5s. We therefore speculate that the interface between AAA5s and AAA5L (AAA5s connecting to the AAA1 ATPase site via the AAA5s-AAA6Ls-AAA1Ls-AAA2L block and AAA5L interacting with the linker and AAA4s/stalk/MTBD) may be a critical region for coordinating ATPase activity (AAA1), microtubule binding (stalk and MTBD), and mechanics (linker) in the dynein motor domain.

Figures and figure legends

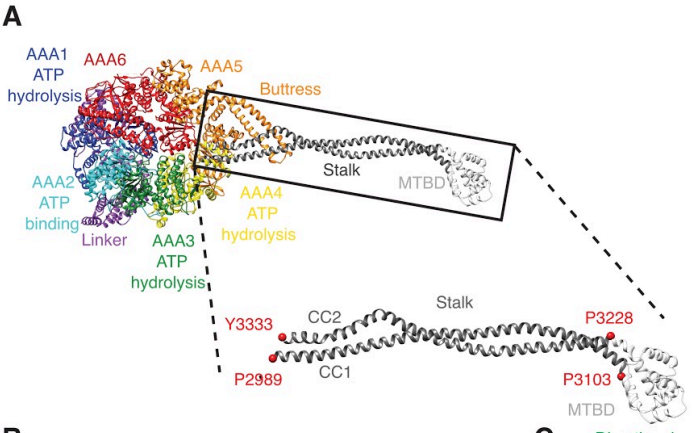

B

Mutant	Coiled-Coil	Number of Residues	Type of movement
Mutant 1	CC1	Insertion of 1	Directional - WT like
Mutant 2	CC2	Insertion of 1	Diffusive like
Mutant 3	CC1	Insertion of 3	Directional - WT like
Mutant 4	CC1	Insertion of 6	Directional - WT like
Mutant 5	CC1	Deletion of 10	Diffusive like
Mutant 6	CC2	Deletion of 3	Directional - WT like
Mutant 7	CC1	Deletion of 1	Directional - WT like
Mutant 8	CC2	Deletion of 1	No movement
Mutant 9	CC2	Insertion of 2	No movement
Mutant 10	CC1	Insertion of 2	No movement
Mutant 11	CC1	Insertion of 9	Directional - WT like
Mutant 12	CC1	Deletion of 5	Directional - WT like
Mutant 13	CC2	Insertion of 1	Diffusive like
Mutant 14	CC1	Insertion of 3	Transient binding
Mutant 15	CC2	Insertion of 1	No expression
Mutant 16	CC1	Insertion of 2	No expression
Mutant 17	CC2	Deletion of 22	No movement
Mutant 18	CC1	Insertion of 1	No movement

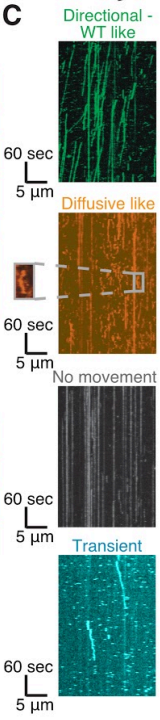

D

Motor / Nucleotide	WT	Mutant 2	Mutant 5	Mutant 13
ATP	Directional - minus end	Diffusive	Diffusive	Diffusive
no ATP	No movement	Diffusive	Diffusive	Diffusive

Figure 2.1 | Single-molecule motility properties of dynein stalk mutants reveal mutants with nucleotide-independent diffusive motility. (A) Structure and domain organization of the motor domain of cytoplasmic dynein (PDB 4RH7[29]). Inset shows zoom of MTBD (white) and coiled-coil stalk (grey), which consist of two helices, CC1 and CC2. Well conserved residues, that were used as anchor points to define CC1 and CC2 in this study are depicted as red spheres. Numbering is based on yeast cytoplasmic dynein. (B) Table showing location, number of inserted or deleted residues and motility phenotype of all 18 stalk mutants. Examples of single-molecule assay results are shown in **Figure S2.4** and **Figure S2.5**. Sequence information and exact position of individual mutants are shown in **Figure S2.2, Figure S2.3**. Quantification and classification is based on three technical repetitions. (C) Example

kymographs for ‘Directional - WT like’, ‘Diffusive like’ ,‘No movement’, and ‘Transient binding’. Magnified area for ‘Diffusive like’ motion shows run of a single molecule. Kymographs for each mutant are shown in **Figure S2.4**. (D) Table showing the type of movement found for wild-type, mutant 2, mutant 5, and mutant 13 in a modified single-molecule assay with and without ATP. Classification of type of movement is based on two repetitions of different dynein preparations. Kymographs for each mutant are shown in **Figure S2.7**.

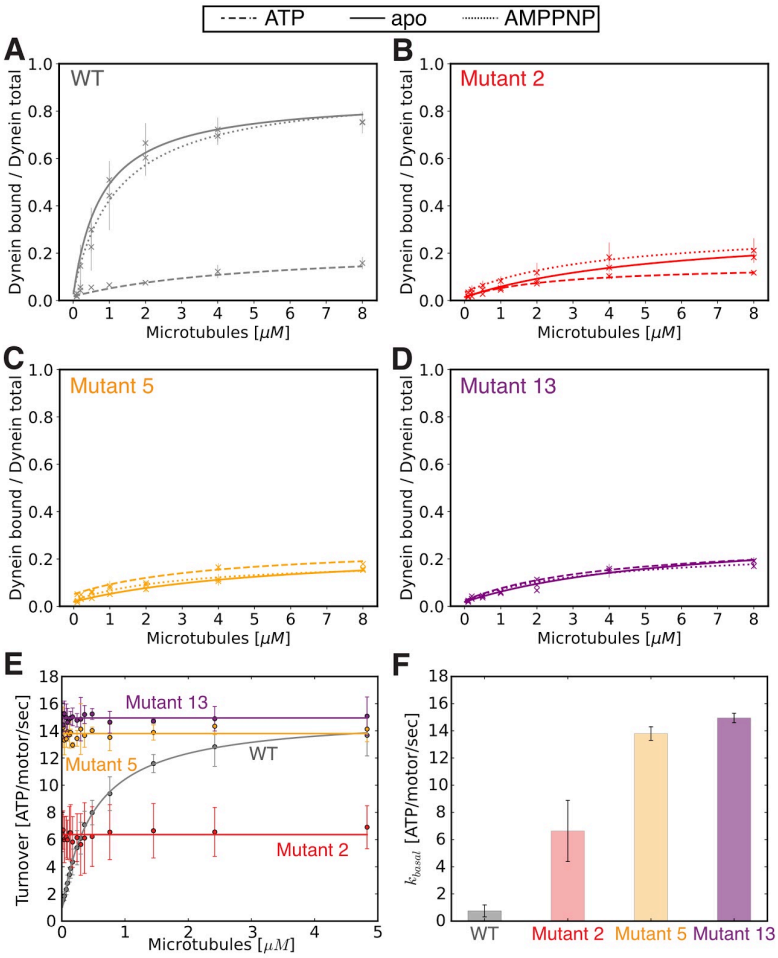

Figure 2.2 | Diffusive mutants show microtubule-independent, high basal ATPase activity and low affinity for microtubules. (A-D) Microtubule affinity measured by a cosedimentation assay in the apo state (full line) and in the presence of ATP (dashed line), and AMPPNP (dotted line) for wild-type (A), mutant 2 (B), mutant 5 (C), and mutant 13 (D). Error bars show standard deviation of three repetitions of different dynein preparations. **Table S2.2** shows fit equation and rate quantification for microtubule affinity data. (E) Microtubule stimulated ATPase activity of wild-type (grey), mutant 2 (red), mutant 5 (orange), and mutant 13 (purple). Error bars show standard deviation of three repetitions of different dynein preparations. **Table S2.4** shows fit equation and rate quantification for ATPase data. (F) Bar plot of basal ATPase activity of wild-type (grey), mutant 2 (red), mutant 5 (orange), and mutant 13 (purple). Error bars show standard deviation of three repetitions of different dynein preparations.

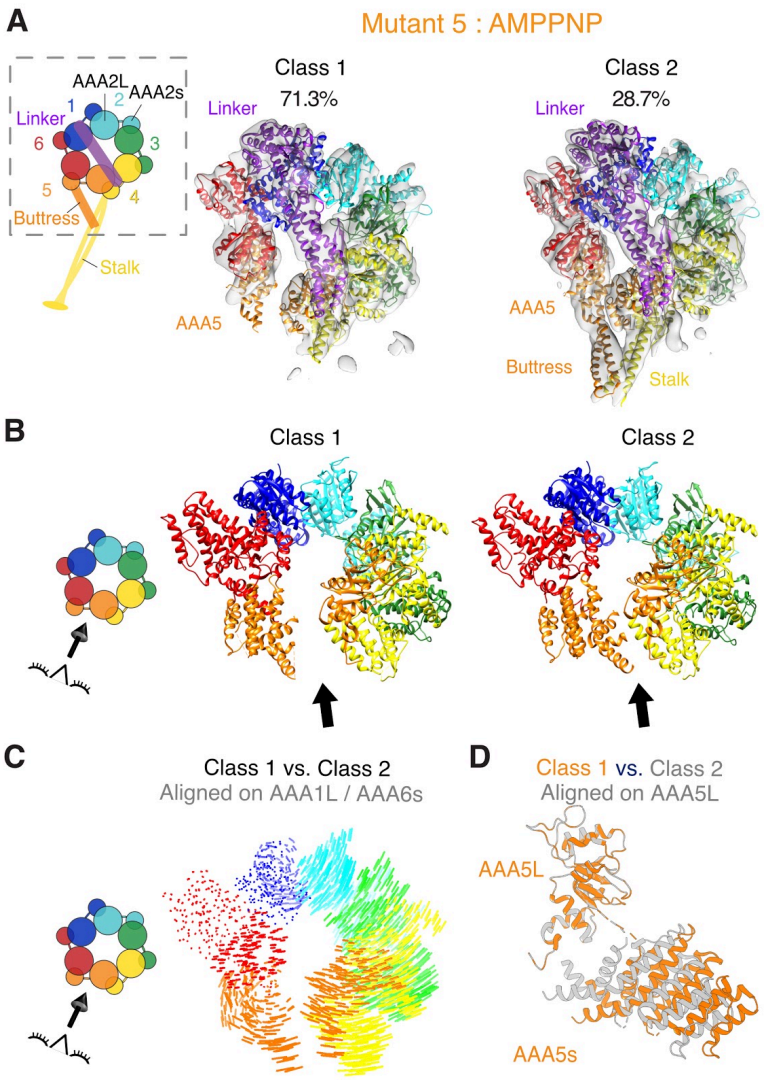

Figure 2.3 | Cryo-EM structure of mutant 5 in the presence of AMPPNP shows a gap in the AAA ring. (A) Cryo-EM reconstructions and fitted models for class 1 and class 2 resulting from 3D classification of the data. Class 1 is composed of 71.3% of all particles (left) and class 2 of 28.7% of all particles (right). The cryo-EM density map for both classes is shown as a semi-transparent surface with a fitted model (fit as described in **Materials and Methods**) as cartoon. Color coding of domains is the same as for **Figure 2.1**. Left: schematic of monomeric dynein construct, box indicates region that was resolved in the cryo-EM maps. (B) Cartoon representation of models for both classes. Black arrow indicates the position of the gap between AAA5L and AAA5s in class 1. Left: schematic indicates the point-of-view. (C) Visualization of inter alpha carbon distances between class 1 and class 2 as shown in B after alignment on AAA1L and AAA6s. We removed the linker for clarity. Left: schematic indicates the point-of-view. (D) Movements between the large and small domains of AAA5 between class 1 (orange) and class 2 (grey). The large domain of AAA5 is aligned.

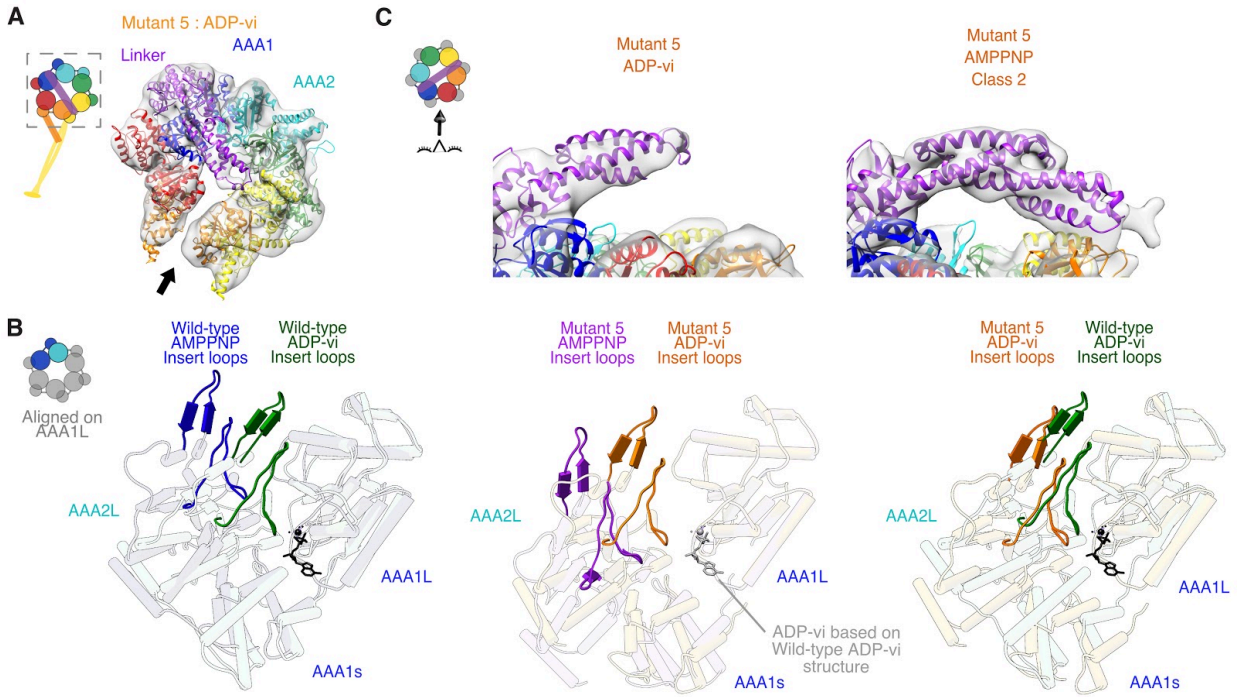

Figure 2.4 | Cryo-EM structure of mutant 5 in the presence of ADP-vanadate shows priming for hydrolysis with unbent linker. (A) Cryo-EM reconstructions and fitted models from 3D classification of the data. The cryo-EM density map is shown as a semi-transparent surface with a fitted model (fit as described in **Materials and Methods**) as cartoon. The black arrow indicates the position of the gap between AAA5L and AAA5s of mutant 5 in the presence of ADP-vi. This gap is smaller than for mutant 5 in the presence of AMPPNP but larger than in wild-type ADP-vi (**Fig. S2.13**). Color coding of domains is the same as for **Figure 2.1**. Left: schematic of monomeric dynein construct. The box indicates the region that was resolved in the cryo-electron microscopy map. (B) View of the AAA1 and AAA 2 interface. The AAA2L inserts (the 'H2 insert' and the 'pre-sensor-I' (PS-I) insert) are shown in non opaque colors. The structures of human cytoplasmic dynein 2 in the ADP-vi state (green - PDB: 4RH7[29]), yeast cytoplasmic dynein in the AMPPNP state (blue - PDB: 4W8F[35]), yeast cytoplasmic dynein mutant 5 in ADP-vi state (orange - this study), and yeast cytoplasmic dynein mutant 5 in AMPPNP - class 1 state (purple - this study) were aligned on AAA1L. ADP and vanadate are depicted in black or grey and modeled in based on the human cytoplasmic dynein 2 structure. Left: The schematic indicates the region of the nucleotide pocket. We also calculated the degree of rotation of AAA2L for the transition from the AMPPNP to the ADP-vi state of wild-type and mutant 5 and found rotations of 20° and 21°, respectively (**Fig. S2.13**). (C) Close-up view of linker of cryo-EM reconstructions and fitted models for mutant 5 in ADP-vi (middle) and in AMPPNP class 2 (right). For the ADP-vi state only the part of the linker with sufficient density was fitted. Left: The schematic shows the point-of-view.

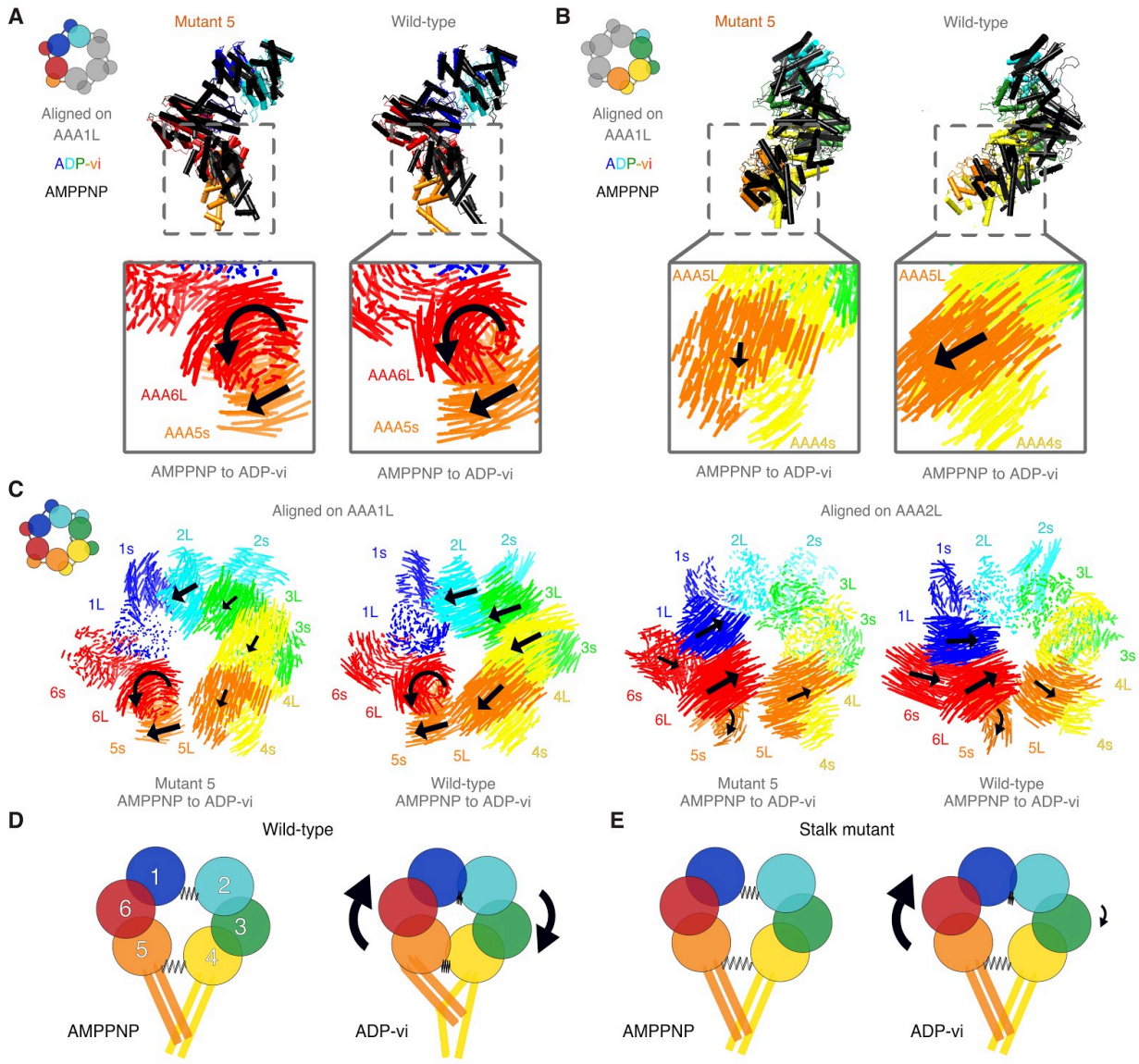

Figure 2.5 | Domain movements in the AAA ring of dynein. (A) Domains AAA5s to AAA2L of wild-type and mutant 5 are shown for the ADP-vi state (color) and the AMPPNP state (black). Box: Visualization of inter alpha carbon distances between AMPPNP and ADP-vi state of mutant 5 and wild-type dynein. Black arrows indicate direction of movement when transitioning from the AMPPNP to the ADP-vi state while the size of the arrow indicates the magnitude of movement. All structures are aligned on AAA1L. For wild-type, the structures of human cytoplasmic dynein 2 (ADP-vi state - PDB: 4RH7[29]), and the yeast cytoplasmic dynein (AMPPNP state - PDB: 4W8F[35]) were used. For mutant 5 AMPPNP, we used the class 1 structure. (B) Same as in A but for domains AAA2s to AAA5L. (C) Visualization of inter alpha carbon distances between the AAA domains in the AMPPNP and the ADP-vi state of mutant 5 and wild-type dynein for alignments on AAA1L (left) and AAA2L (right). Black arrows indicate direction of movement when transitioning from the AMPPNP to the ADP-vi state while the size of the arrow indicates the magnitude of movement. We removed the linker for clarity. For wild-type, the structures of human cytoplasmic dynein 2 (ADP-vi state - PDB: 4RH7[29]), and the yeast cytoplasmic dynein (AMPPNP state - PDB: 4W8F[35]) were used. For mutant 5 AMPPNP, we used the class 1 structure. (D) Model for domain movements in the AAA ring of dynein

during ATP hydrolysis at AAA1. The AAA ring can be divided into two halves that are connected by two springs. Upon ATP binding / hydrolysis, the gap between AAA1/ AAA2 closes and moves AAA6 / AAA5 which in turn pulls on AAA4 so that the gap between AAA4 / AAA5 closes as well. In addition, this conformational change will pull the buttress and therewith change the stalk registry. (E) In the stalk mutant, the spring between AAA4 / AAA5 does not close upon ATP binding / hydrolysis presumably due to a disruption of the stalk / buttress interface. Moreover, the gap at the AAA4 / AAA5 interface is larger for the stalk mutant in both states, AMPPNP and ADP-vi, than for wild-type in the AMPPNP state. This “loose spring” at AAA4 / AAA5 uncouples these domains from the closure of the AAA1 / AAA2 interface, and this accounts for microtubule independent ATP hydrolysis.

Supplemental figures and tables with legends

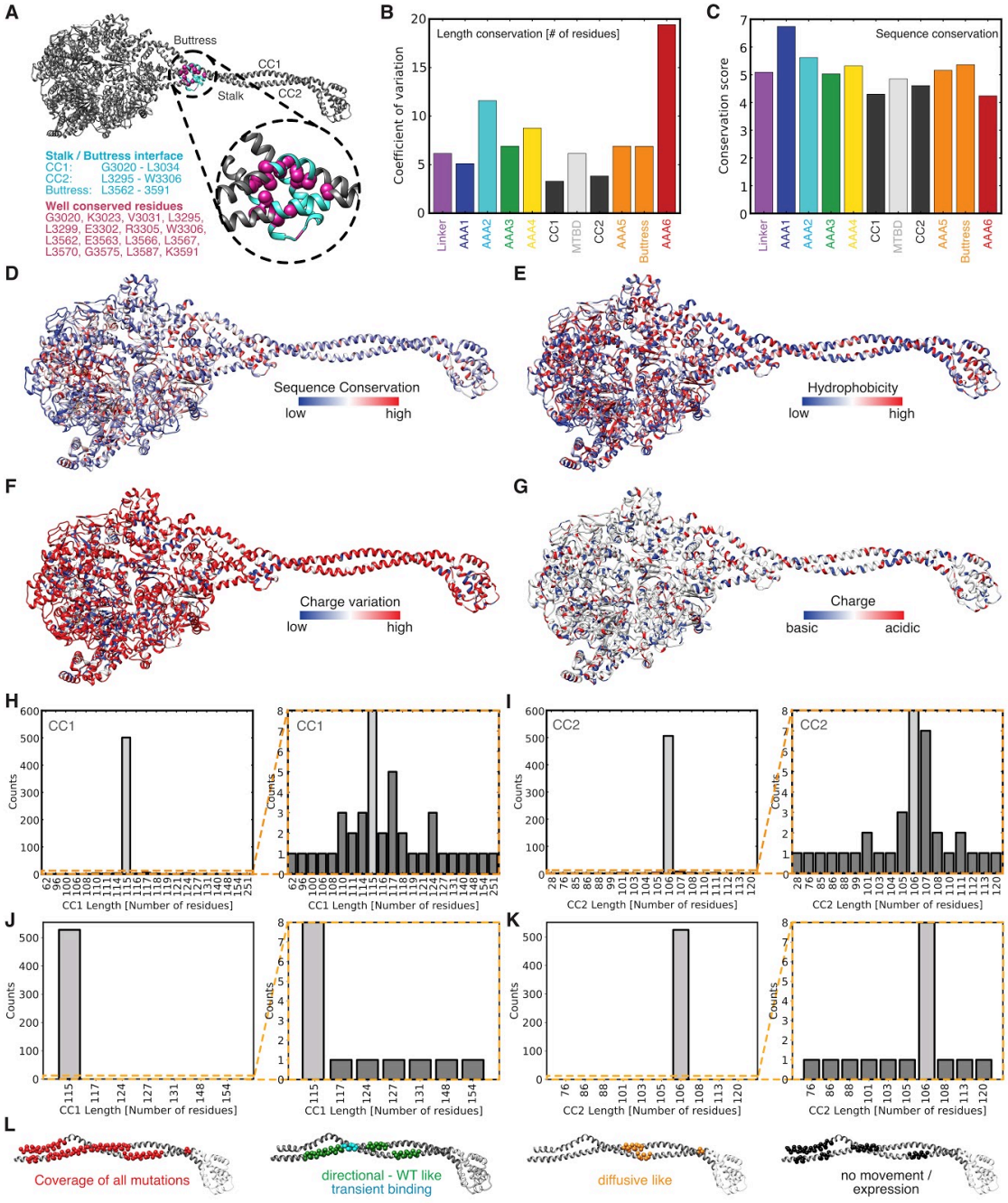

Figure S2.1 | Sequence analysis and conservation in the dynein motor domain. (A) Conserved residues in the stalk / buttress interface of dynein mapped onto the structure of the human cytoplasmic dynein 2 (PDB: 4RH7 [29]). Note, the amino acids listed are based on numbering from yeast cytoplasmic dynein 1. (B, C) The length (number of residues) conservation (B) and the sequence conservation (C) of domains of the dynein motor domain are shown. The conservation score is derived from Jalview [68,69] and is shown for each domain. The conservations are based on 534 different sequences that were curated. (D-G) Sequence conservation (D), Conservation of hydrophobic residues (E), Charge variation (F) (how many

residues at the same position among different sequences switch between D/E and H/K/R), and Conservation of charge (G) where basic residues (D/E) are in blue and acidic residues (H/K/R) are in red. The conservations shown are based on 534 different sequences that were curated**.** (H, I) Histogram showing the length distribution of CC1 (H) and CC2 (I) of the dynein stalk among 534 sequences with initial sequence data (used to derive mutants). Orange box indicates the area that is magnified on the right. (J, K) Histogram showing the length distribution of CC1 (J) and CC2 (K) of the dynein stalk among 534 sequences that were updated based on most recent sequencing reads in various databases. Orange box indicates an area that is magnified on the right, showing a handful of outlier sequences with different stalk lengths. (L) Coverage of all mutations (red) generated in the yeast dynein background based on our sequence analysis (most left) mapped onto the structure of human cytoplasmic dynein 2 stalk (PDB: 4RH7[29]). Regions of individual mutants are shown in **Figure S2.3**. Positions of insertions/deletions that showed 'Diffusive like' (orange) movement, 'No movement / No expression' (black), 'Directional - WT like' (green), and 'transient binding' (blue) mapped onto the stalk (classification as shown in **Figure 2.1**).

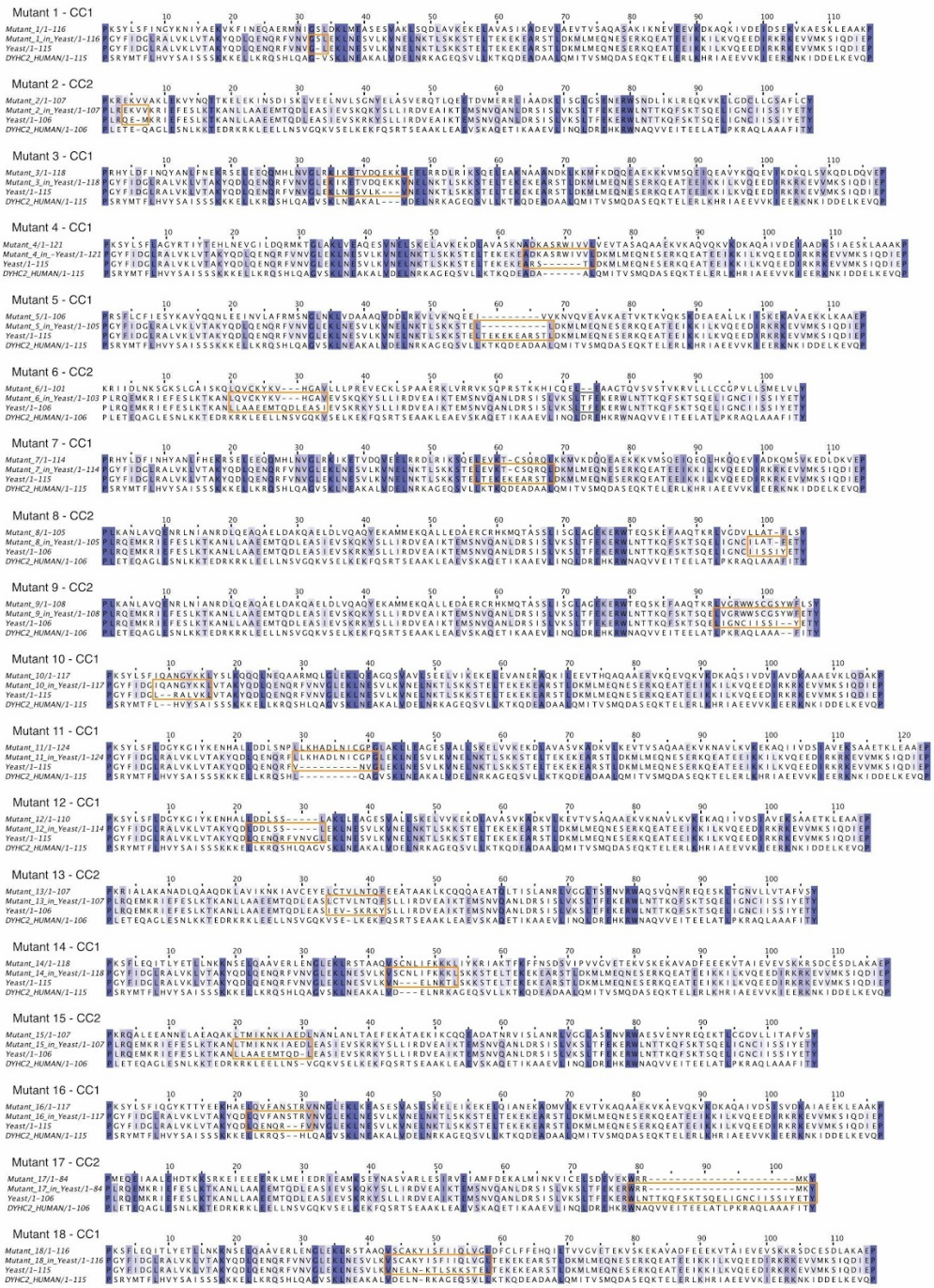

Figure S2.2 | Sequence alignments of the panel of stalk mutants. For each of the 18 mutants we compare the sequence of the species with insertion or deletion (top sequence), mutant created in yeast dynein background (second from the top), yeast dynein wild-type (second from bottom), and human cytoplasmic dynein 2 (bottom). Orange boxes highlight areas of mutation. Note: Grey box in sequence alignment for mutant 6 shows second position of mutation for mutant 6 which was not created. Sequence conservation is indicated from white (not well conserved) to blue (highly conserved).

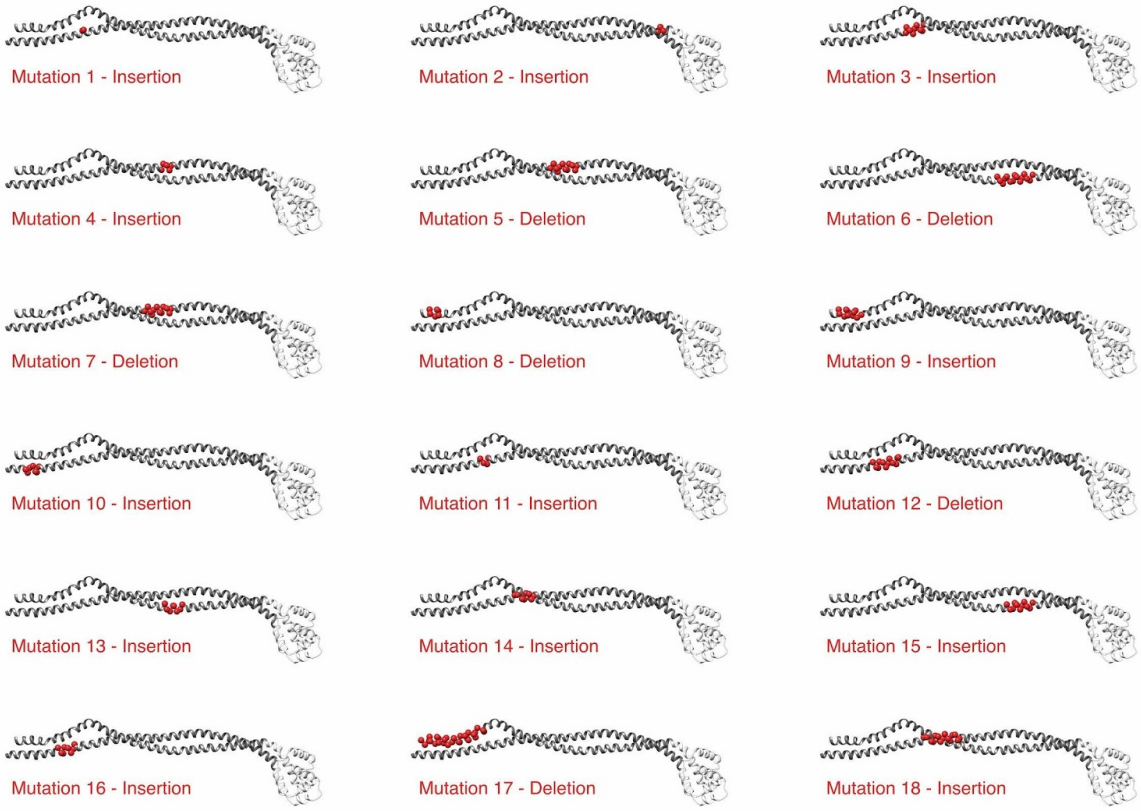

Figure S2.3 | Position of all 18 insertion or deletion mutants mapped onto the structure of human cytoplasmic dynein 2 stalk (PDB: 4RH7[29]). Red spheres show residues that were altered in the stalk to either create an insertion or deletion.

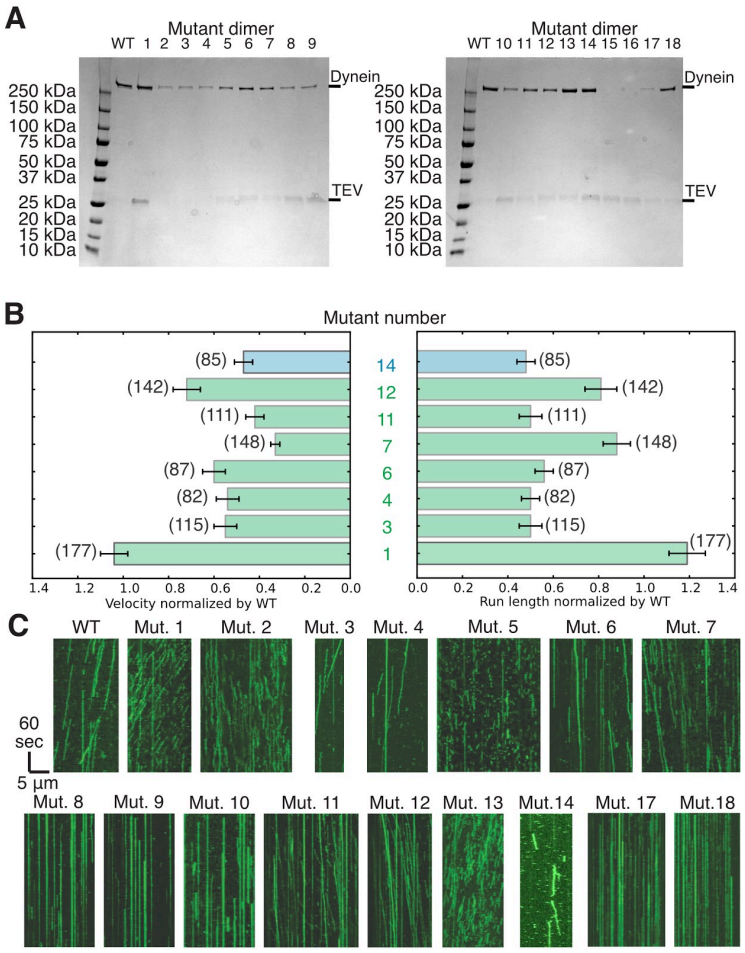

Figure S2.4 | Example kymographs and single-molecule motility properties of stalk mutants. (A) Purified dynein, wild-type and mutants, after affinity purification shown by PAGE. No dynein band is visible for mutants 15 and 16 indicating that they did not express. For some constructs residual TEV, which was used to cleave the dynein of beads during the affinity purification (see **Materials and Methods**), is visible. All constructs that were used for assays other than the single-molecule motility assay were further purified by size exclusion chromatography, which removed the residual TEV entirely (see **Materials and Methods**). (B) Velocity and run length of 'Directional - WT like' motors (green - mutants 1, 3, 4, 6, 7, 11, and 12) and the 'transient binding' motor (blue - mutant 14) normalized by wild-type dynein. Error bars show standard deviation and number in brackets indicates the number of motors quantified. Data used for quantification is shown in **Figure S2.5**. (C) Example kymographs showing different types of movement as classified in **Figure 2.1**. Kymographs for mutants 15 and 16 are not shown since they did not express.

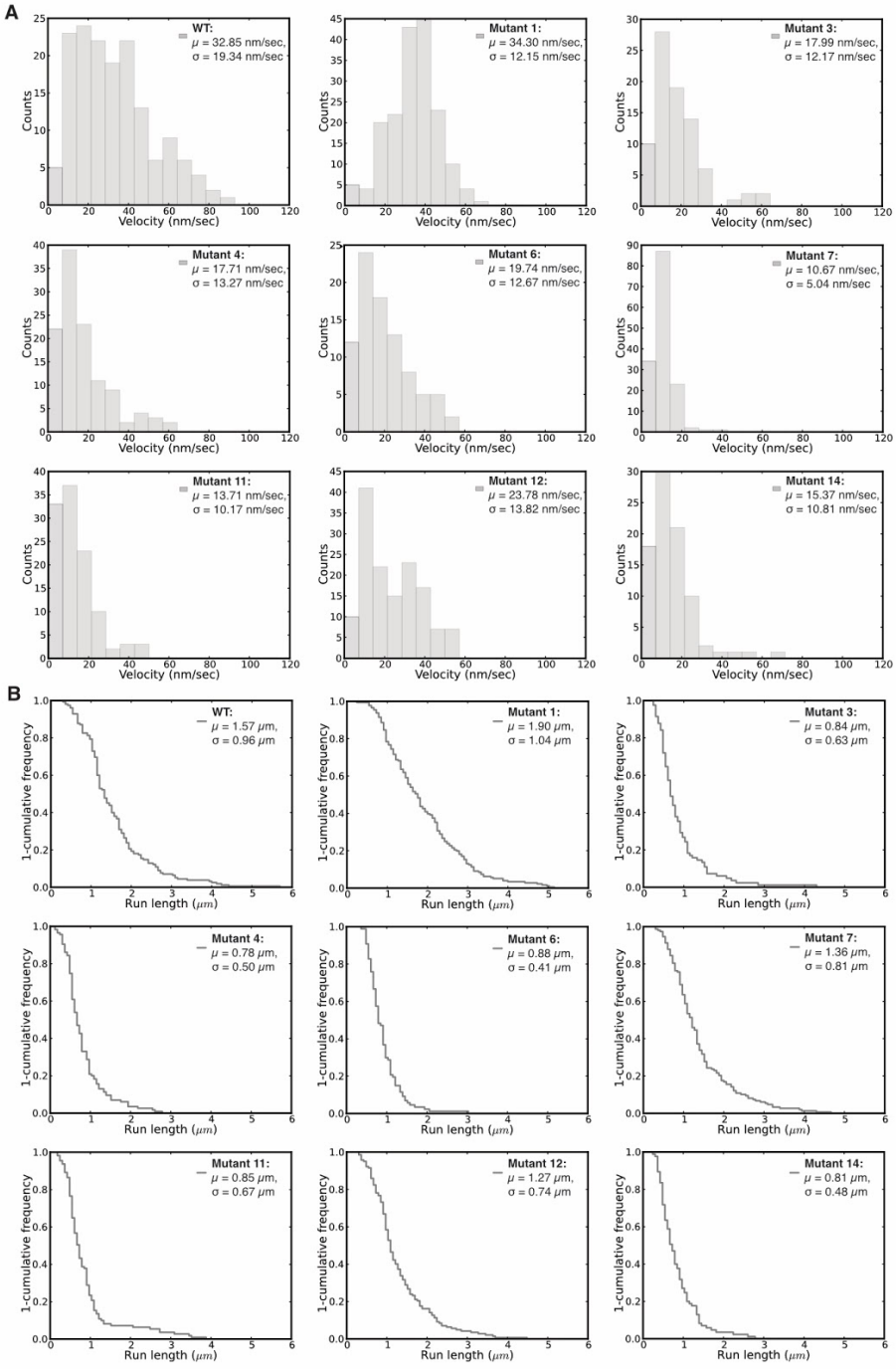

Figure S2.5 | Appendix Figure S3. Single-molecule motility properties of wild-type like and transient binding stalk mutants. (A) Velocity histogram with average velocity (μ) and its standard deviation (σ) for wild-type, 'Transient binding', and 'Directional - WT like' mutants. Note: For mutant 14 only directional molecules were quantified and not the transient binding ones. (B) A '1-cumulative frequency distribution plot' of run length with average length (μ) and its standard deviation (σ) for wild-type, 'Transient binding', and 'Directional - WT like' mutants. Note: For mutant 14 only directional molecules were quantified and not the transient binding ones.

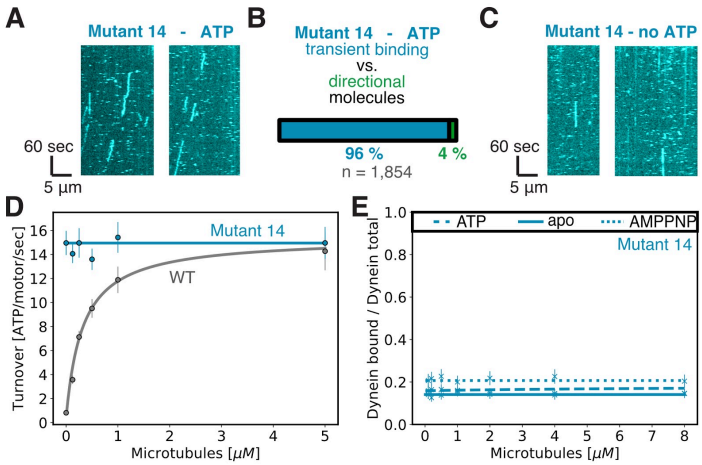

Figure S2.6 | Biochemical properties of mutant 14. (A) Kymographs of mutant 14 from single-molecule assay with 1 mM ATP. (B) Quantification of percentage of transient binding or directionally moving motors of mutant 14 in the presence of ATP. (C) Kymographs of mutant 14 from single-molecule assay without ATP. (D) Microtubule stimulated ATPase activity of mutant 14 (cyan) and wild-type (grey) dynein. Error bars show standard deviation of three repetitions of different dynein preparations. Caption for **Table S2.4** shows a fit equation for ATPase data. The basal ATPase rate k_{basal} for mutant 14 is 14.51 ± 0.27 s^{-1} while k_{cat} and [MT] K_M were not measurable. For wild-type dynein we measured a k_{cat} of 15.41 ± 1.31 s^{-1}, [MT] K_M of 0.42 ± 0.10 μM and k_{basal} of 0.42 ± 0.33 s^{-1} which is in good agreement with the measurements shown in **Figure 2.2** and **Table S2.4**. (E) Microtubule affinity measured by a cosedimentation assay in the apo state (full line) and in the presence of ATP (dashed line), and AMPPNP (dotted line) for mutant 14. Error bars show standard deviation of three repetitions of different dynein preparations. Caption for **Table S2.2** shows fit equation for microtubule affinity data. The maximum binding (B_M) and the dissociation constant K_d were not measurable for mutant 14 in all three nucleotides states.

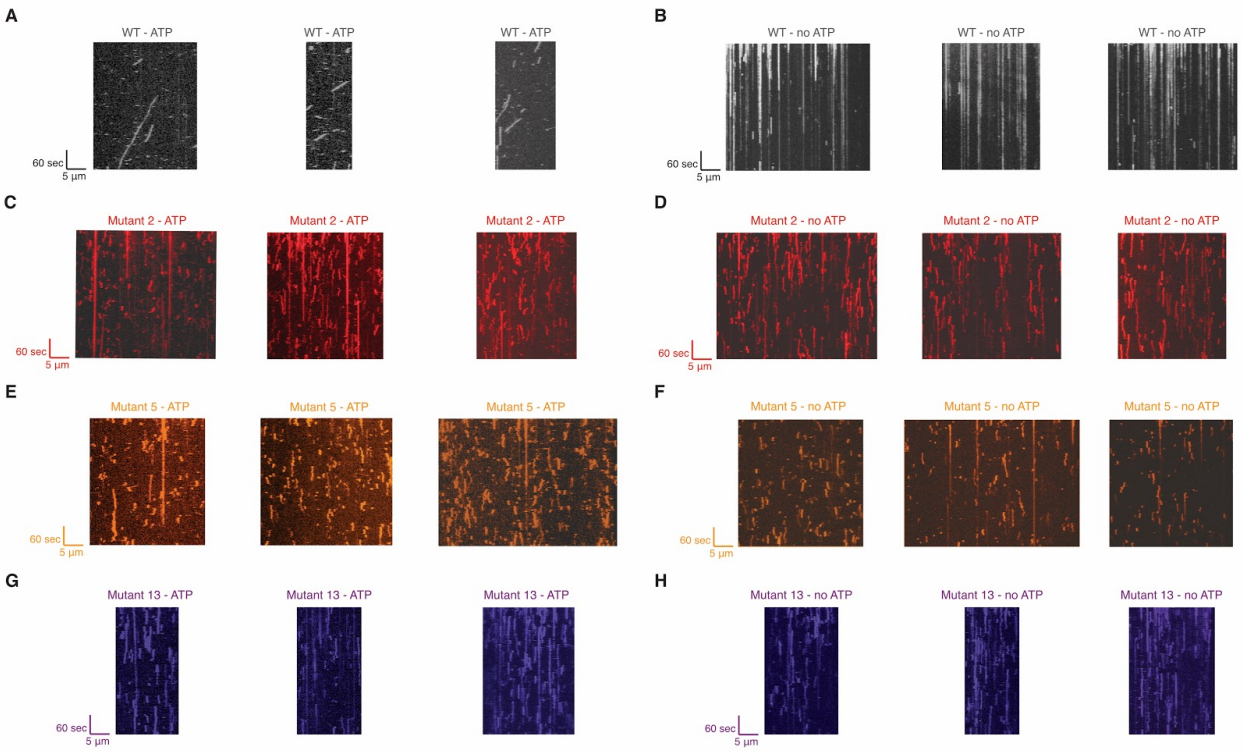

Figure S2.7 | Kymographs of wild-type and diffusive mutants with and without ATP. (A, C, E, G) Kymographs of wild-type (grey), mutant 2 (red), mutant 5 (orange), and mutant 13 (purple) with 1 mM ATP. (B, D, F, H) Kymographs of wild-type (grey), mutant 2 (red), mutant 5 (orange), and mutant 13 (purple) without ATP.

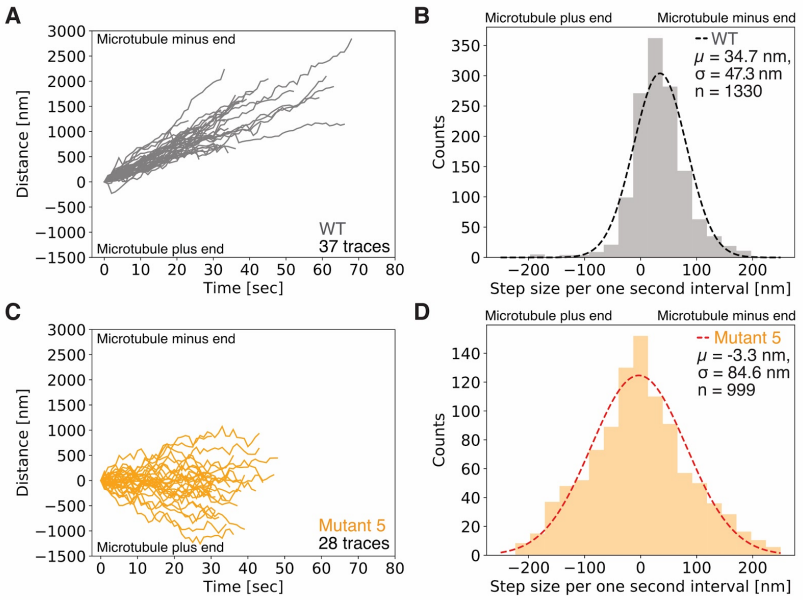

Figure S2.8 | Quantification of movements of single molecules of wild-type and mutant 5 dynein. (A) Individual traces of wild-type dynein that were tracked using the 'localization microscopy' plug-in from μManager[70] (see **Materials and Methods**). Each trace is a single molecule that moved along a microtubule in the presence of 1 mM ATP. The traces in the panel were aligned so that all start at 0 nm and 0 sec. The polarity of microtubules was determined with human homodimeric kinesin-1 (K490)[63], which moves processively towards the plus end of microtubules. (B) Histogram of displacements of wild-type dynein per one second interval from all traces shown in A. Here, the movement towards the [70]microtubule minus end is a positive distance value while the movement towards the microtubule plus end results in a negative distance value. Black dashed line is a Gaussian fit over the entire data. (C) Individual traces of mutant 5 that were tracked using the 'localization microscopy' plug-in from μManager[70] (see **Materials and Methods**). Each trace is a single molecule that moved along a microtubule in the presence of 1 mM ATP. The traces in the panel were aligned so that all start at 0 nm and 0 sec. The polarity of microtubules was determined with human homodimeric kinesin-1 (K490)[63], which moves processively towards the plus end of microtubules.(D) Histogram of displacements of mutant 5 per one second interval from all traces shown in C. Here, the movement towards the microtubule minus end is a positive distance value while the movement towards the microtubule plus end results in a negative distance value. The red dashed line is a Gaussian fit over the entire data. (B, D) The number of samples (n), the average step size per one second interval (μ) and its corresponding standard deviation (σ) are given.

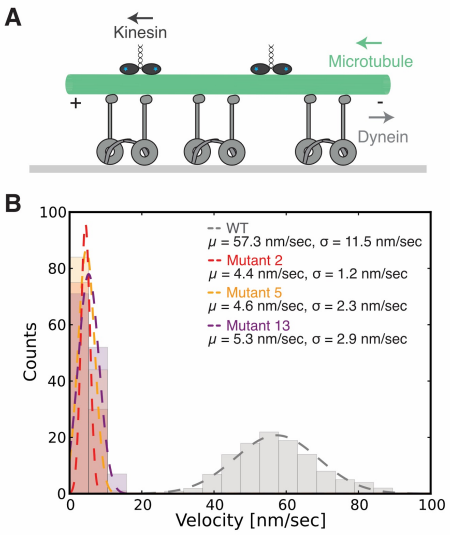

Figure S2.9 | Gliding assay shows slow directional movement for mutants 2, 5, and 13. (A) Schematic of modified gliding assay. Dyneins (dimeric - dark grey) are immobilized on microscope slides (light grey) and can translocate microtubules (green). Plus end directed kinesins (dark blue) move on top of microtubules to mark directionality. (B) Histogram of gliding velocities of wild-type (grey, n=116), mutant 2 (red, n=105), mutant 5 (orange, n=129), and mutant 13 (purple, n=130) with average velocity (μ) and its standard deviation (σ). Data of one dynein preparation is shown but a total of three repetitions of different dynein preparations resulted in very similar velocities.

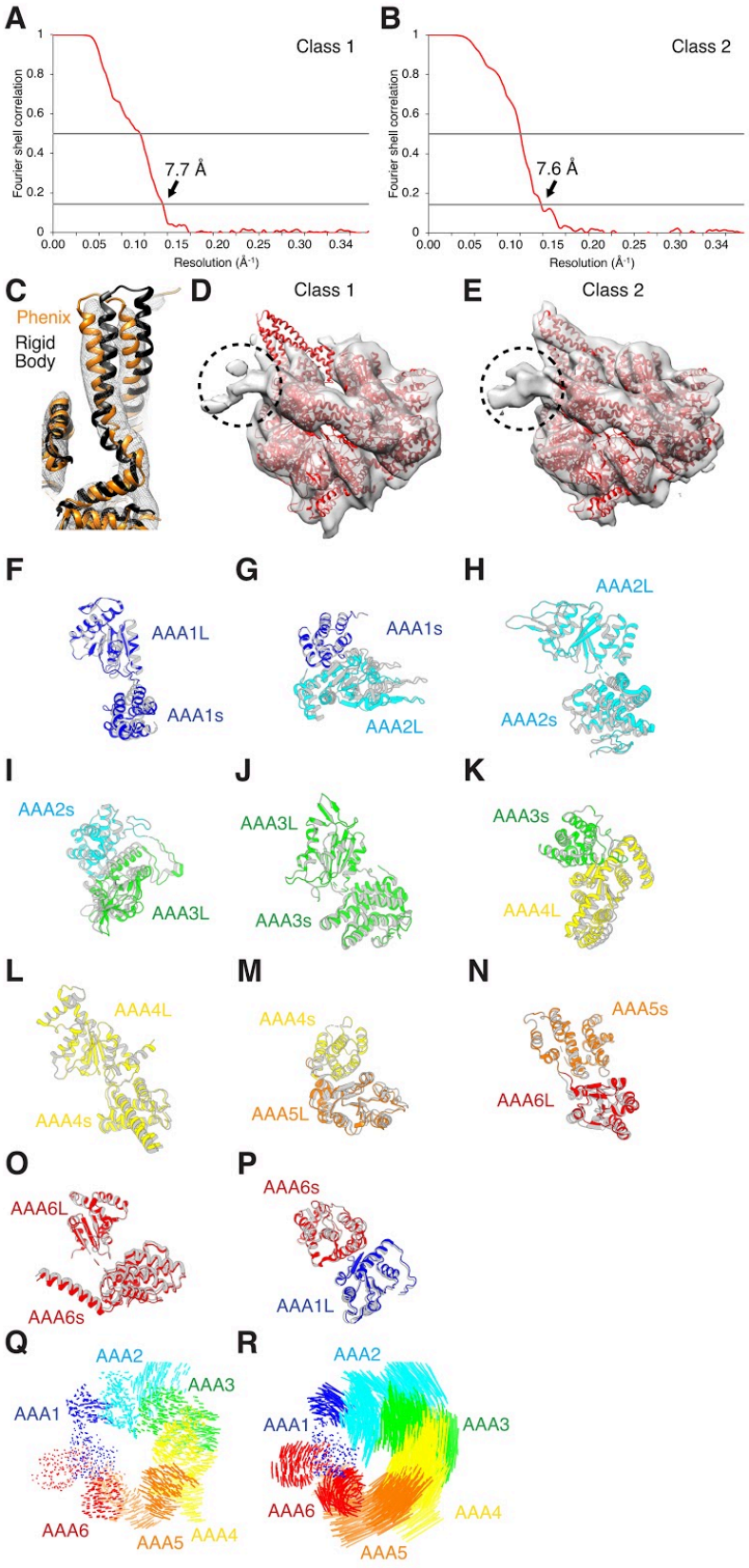
A
Class 1
Fourier shell correlation
7.7 Å
Resolution (Å⁻¹)
B
Class 2
7.6 Å
C
Phenix
Rigid Body
D
Class 1
E
Class 2
F
AAA1L
AAA1s
G
AAA1s
AAA2L
H
AAA2L
AAA2s
I
AAA2s
AAA3L
J
AAA3L
AAA3s
K
AAA3s
AAA4L
L
AAA4L
AAA4s
M
AAA4s
AAA5L
N
AAA5s
AAA6L
O
AAA6L
AAA6s
P
AAA6s
AAA1L
Q
AAA2
AAA3
AAA1
AAA6
AAA5
AAA4
R
AAA2
AAA3
AAA1
AAA6
AAA4
AAA5

Figure S2.10 | Cryo-EM analysis for class 1 and class 2 of mutant 5 in the presence of AMPPNP. (A, B) Plot of Fourier Shell Correlation (FSC) for class 1 (A) and class 2 (B). Local resolution estimation of the mutant 5 density maps in AMPPNP are shown in **Figure S2.11.** (C) Cryo-EM density for the buttress region of class 2 with rigid body and flexibly fit models. The rigid body fit (black) of AAA5L into the density clearly showed that some rearrangement of the buttress had occurred. Flexible fitting in Phenix (orange) resulted in a model that fit the density in the buttress region significantly better. (D, E) Cryo-EM reconstruction of class 1 (D) and class 2 (E) showing unfiltered maps with AMPPNP-bound crystal structure (PDB: 4W8F, red) shown for reference. Black dotted-circle indicates position of a GFP tag at the N-terminus of the linker, which is better defined in class 2. (F-P) Domain movements between class 1 and class 2 of mutant 5 in AMPPNP cryo-EM data. In every panel the top domain is aligned, showing movement between that domain and the next. Class 1 is colored and class 2 is grey. Movement between AAA1L and AAA1s (F). Movement between AAA1s and AAA2L (G). Movement between AAA2L and AAA2s (H). Movement between AAA2s and AAA3L (I). Movement between AAA3L and AAA3s (J). Movement between AAA3s and AAA4L (K). Movement between AAA4L and AAA4s (L). Movement between AAA4s and AAA5L (M). Movement between AAA5s and AAA6L (N). Movement between AAA6L and AAA6s (O). Movement between AAA6s and AAA1L (P). (Q) Visualization of inter-alpha carbon distances between class 1 and class 2 of mutant 5 in the AMPPNP state after alignment on AAA1L as seen from the top. We removed the linker for clarity. (R) Visualization of inter alpha carbon distances between class 1 of mutant 5 in the AMPPNP state and the cryo-EM model of yeast dynein in the presence of ADP-vi [35]. We removed the linker for clarity.

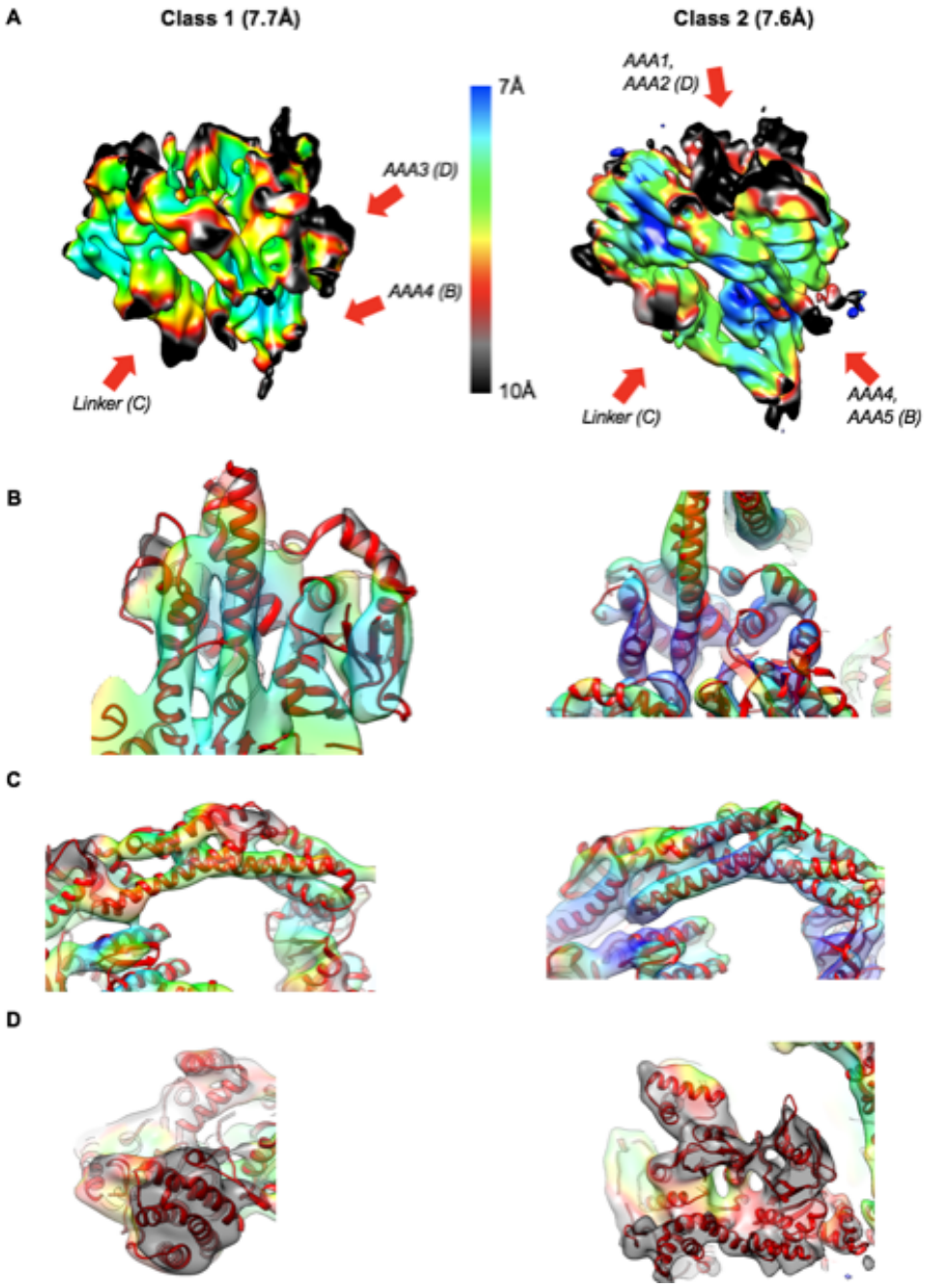

Figure S2.11 | Local resolution of mutant 5 density map in AMPPNP. (A) The local resolution of mutant 5 in the presence of AMPPNP of class 1 (left) and 2 (right) is shown. The local resolution was estimated with CryoSparc v2.5.0. The red arrows indicate domains that are shown in a close-up view in B-D. (B-D) Close-up view of different regions as indicated in A of well (B), medium (C) and poorly (D) defined parts of the density map with the PDB map docked-in.

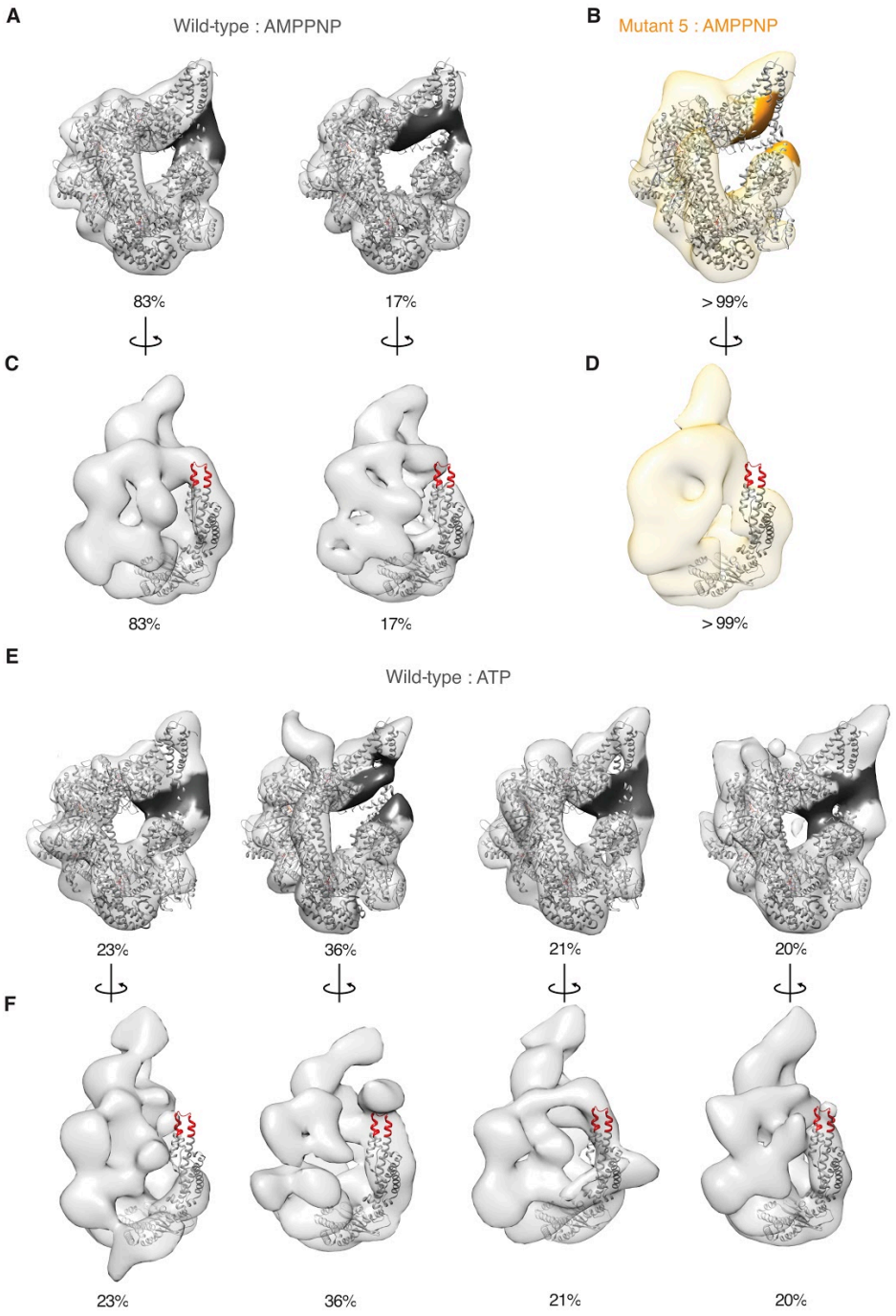

Figure S2.12 | Negative stain reconstructions of mutant 5 and WT dynein. (A, C) Negative stain EM reconstruction of wild-type dynein (grey) in the presence of AMPPNP (EMDB: 6064 and EMDB: 6063) with the AMPPNP crystal structure (PDB: 4W8F [35]) docked-in. Major (left, EMDB: 6064) and minor (right, EMDB: 6063) conformations are shown. This data was collected in a previous study [35]. (B, D) Negative stain EM density of mutant 5 (orange) in the presence of AMPPNP with the AMPPNP crystal structure (PDB: 4W8F[35]) docked-in. (A, B) Areas of weak density in the AAA5 region of minor wild-type conformation (dark grey) and for mutant 5 (bright orange) are highlighted. (C, D) N-terminus of linker in crystal structure is highlighted in red and

only linker and AAA1 of crystal structure are shown. (E, F) Negative stain EM density data from a previous study[35] analyzed in the light of our new findings with the AMPPNP crystal structure docked-in (PDB: 4W8F)[35]. E. Area of gap in density in the AAA5 region is highlighted in dark grey (EMDB: 6065-6068; from left to right, respectively). F. N-terminus of linker in crystal structure is highlighted in red and only linker and AAA1 of crystal structure are shown (EMDB: 6065-6068; from left to right, respectively).

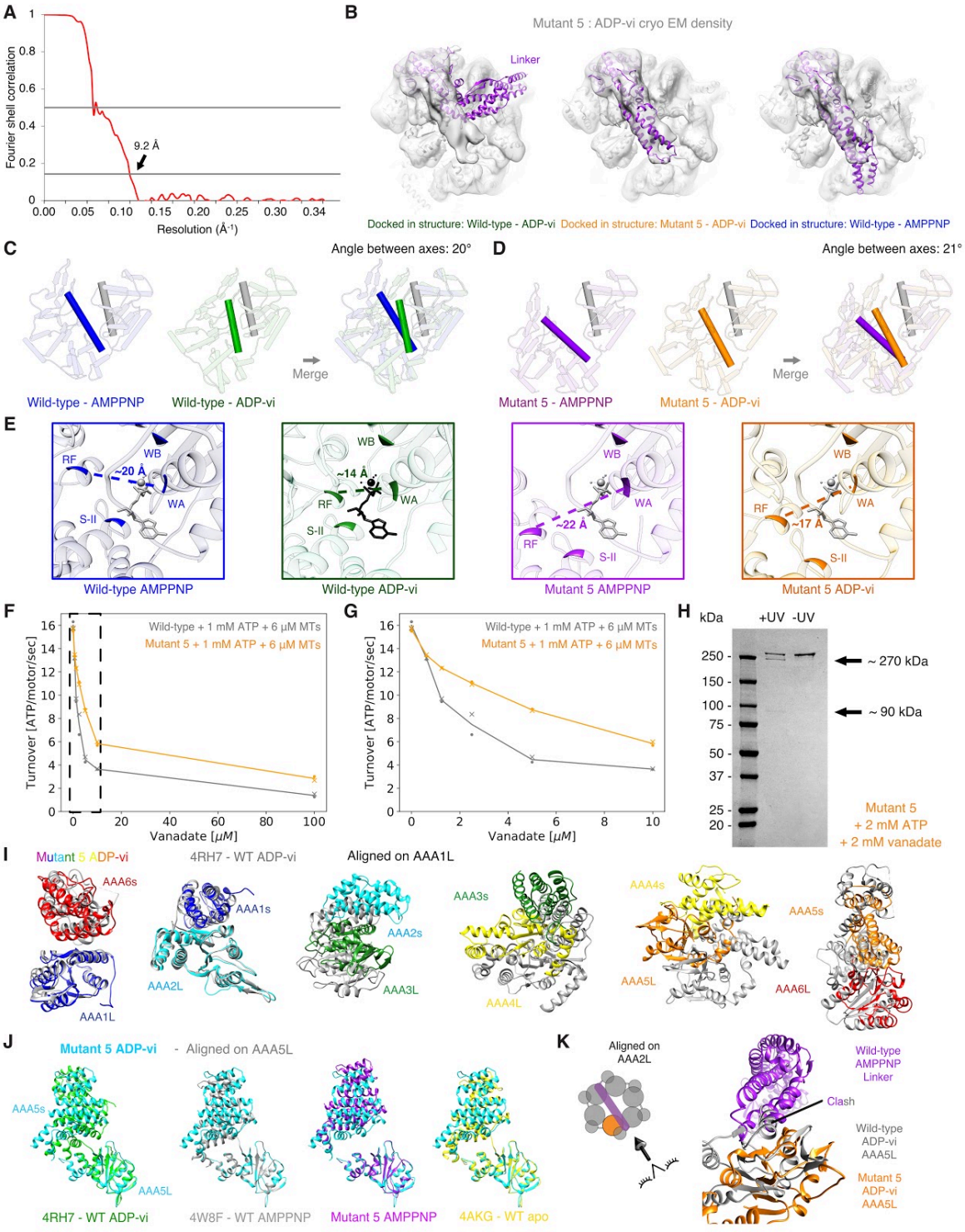

Figure S2.13 | Cryo-EM analysis of mutant 5 in the presence of ADP-vanadate.(A) Plot of Fourier Shell Correlation (FSC) for mutant 5 in the presence of ADP-vanadate. (B) Cryo-EM reconstruction of mutant 5 with ADP-vanadate (grey) fitted with models of human cytoplasmic dynein 2 in the ADP-vi state (left - PDB: 4RH7 [29]), yeast cytoplasmic dynein mutant 5 in ADP-vi state (middle - this study), and yeast cytoplasmic dynein in the AMPPNP state (right - PDB: 4W8F [35]). For the mutant 5 ADP-vi state only the part of the linker with sufficient density was

fitted. (C) Closure of AAA1L and AAA2L domains in wild-type dynein. Same view of the AAA1 and AAA 2 interface as shown in **Figure 2.4**. Left: Structures of of the human cytoplasmic dynein 2 in the ADP-vi state (green - PDB: 4RH7[29]) and the yeast cytoplasmic dynein in the AMPPNP state (blue - PDB: 4W8F[35]) with axes that were fit through the following residues: The grey AAA1L axis is defined with residues taken from the yeast structure using Walker-A (K1802), Walker-B (D1848), and Q1829. The green wild-type ADP-vi AAA2L axis is defined by the arginine finger (R2109), the Sensor-II (R1867), and a residue from the insert loop (G2020). The blue wild-type AMPPNP AAA2L axis is defined by the arginine finger (R2209), the Sensor-II (R1971), and a residue from the insert loop (G2116). Right: Merge between the two representations on the left. The angle between the green and blue axes were calculated using Chimera[71]. The structures were aligned on AAA1L. (D) Closure of AAA1L and AAA2L domains in mutant 5 dynein. Same view of the AAA1 and AAA2 interface as shown in **Figure 2.4**. Left: Structures of of the yeast cytoplasmic dynein mutant 5 in ADP-vi state (orange - this study) and the yeast cytoplasmic dynein mutant 5 in AMPPNP - class 1 state (purple - this study) with axes that were fit through the following residues: The grey AAA1L axis is defined with residues taken from the yeast structure using Walker-A (K1802), Walker-B (D1848), and Q1829. The orange mutant 5 ADP-vi AAA2L axis is defined by the arginine finger (R2209), the Sensor-II (R1971), and a residue from the insert loop (G2116). The purple mutant 5 AMPPNP AAA2L axis is defined by the arginine finger (R2209), the Sensor-II (R1971), and a residue from the insert loop (G2116). Right: Merge between the two representations on the left. The angle between the orange and purple axes were calculated using Chimera[71]. The structures were aligned on AAA1L. (E) Approximate distances between key regions of the ATP-binding sites in wild-type and mutant 5 dynein structures. Close-up view of ADP-vi binding pocket in AAA1. The structures of (from left to right) yeast cytoplasmic dynein in the AMPPNP state (blue - PDB: 4W8F [35]), human cytoplasmic dynein 2 in the ADP-vi state (green - PDB: 4RH7[29]), yeast cytoplasmic dynein mutant 5 in AMPPNP - class 1 state (purple - this study), and yeast cytoplasmic dynein mutant 5 in ADP-vi state (orange - this study) were aligned on AAA1L. ADP and vanadate are depicted in black or grey and taken from the human cytoplasmic dynein 2 structure. The positions of the arginine finger (RF - human structure: R2109; yeast structures: R2209), the Walker-A (WA - human structure: K1695; yeast structures: K1802), the Walker-B (WB - human structure: D1741; yeast structures: D1848) and the Sensor-II (S-II - human structure: R1867; yeast structures: R1971) are shown in non opaque colors for the respective structures. For each structure we calculated the approximate distance between the alpha carbon of the arginine finger (RF) and the Walker-A (WA) motif using Chimera [71] as an approximation for the closure of the nucleotide binding pocket. (F) ATPase activity of wild-type and mutant 5 at different concentrations of vanadate (0-100 µM). The turnover rate of both, wild-type (grey) and mutant 5 (orange) are reduced as the concentration of vanadate increases indicating that vanadate binds to the AAA1 nucleotide binding pocket of wild-type as well as mutant 5. The x and the dot are measurements of two technical repeats. The solid line connects the average values of the two technical repeats. Dashed box shows the area that is shown in **G**. All measurements were performed in the presence of 1 mM Mg-ATP and 6 µM microtubules (MTs). (G) Same as in C but for vanadate concentrations from 0-10 µM. (H) Vanadate mediated UV-photo cleavage of mutant 5 in the presence of 2 mM Mg-ATP and 2 mM vanadate. The arrows show two bands of ~270 and ~90 kDa after exposure to ultraviolet light (+UV) which suggests that vanadate binds to the AAA1 nucleotide binding pocket of mutant 5. (I) Domain movements between mutant 5 and wild-type (PDB: 4RH7[29]) in the presence of ADP-vi. The two structures were aligned on AAA1L (matchMaker in Chimera[71]). (J) Domain movements between mutant 5 in the presence of ADP-vi and - from left ro right - wild-type in the ADP-vi state (PDB: 4RH7[29]), wild-type in the AMPPNP state (PDB: 4W8F[35]), class 1 of mutant 5 with AMPPNP, and wild-type in the apo state (PDB: 4AKG[31]). For every structure the domains are aligned on AAA5L (matchMaker in Chimera[71]). (K) Linker of wild-type motor in the presence of AMPPNP

(PDB: 4W8F[35]) is shown in purple with AAA5L domain in the ADP-vi state of wild-type (grey - PDB: 4RH7[29]) and mutant 5 (orange). All structures were aligned on AAA2L. While there is a visible clash between the AMPPNP linker and the AAA5L domain of wild-type in the presence of ADP-vi, there is no clash of the linker with the AAA5L of mutant 5 in ADP-vi. This observation might explain why the linker in wild-type dynein bends in the presence of ADP-vanadate and why it remains straight for mutant 5.

Table S2.1 | Annotation of all dynein stalk mutant strains used in this study. The VY208 genotype is: MATa; his3-11,15; ura3-1; leu2-3,112; ade2-1; trp1-1; PEP4::HIS5; PRB1D pDyn-pGAL-ZZ-TEV-GFP-3XHA-GST-D6-DYN1-gsDHA:Kan) and the VY137 genotype is: PGal:ZZ:Tev:GFP:HA:D6 MATa; his3-11,15; ura3-1; leu2-3,112; ade2-1; trp1-1; PEP4::HIS5; PRB1D. All sequences that say "UPDATED" do not have any insertions or deletions anymore (based on NCBI (December 22nd, 2017)).

"-" indicates that the sequence was not found (sequence identity less than 60%).

Mutation Number / dimeric or monomeric	**Strain name**	**Organism**	**NCBI - proteinBLAST**	**EBI - European Bioinformatics Institute**	**Uniprot - HMMER search**
WT / dimer	VY208	Saccharomyces cerevisiae	https://www.ncbi.nlm.nih.gov/protein/767040268?report=genbank&log$=protalign&blast_rank=2&RID=XUTTCCYZ014	-	http://www.uniprot.org/uniprot/P36022
1 / dimer	VY1044	Gorilla gorilla gorilla	UPDATED: https://www.ncbi.nlm.nih.gov/protein/XP_004044002	https://www.ebi.ac.uk/ebisearch/search.ebi?db=allebi&query=ENSGGOP00000020228	http://www.uniprot.org/uniprot/G3RWP4
2 / dimer	VY1045	Helobdella robusta	UPDATED: https://www.ncbi.nlm.nih.gov/protein/675890198?report=genbank&log$=protalign&blast_rank=1&RID=XUU15W9Y014	-	http://www.uniprot.org/uniprot/T1G9C1
3 / dimer	VY1046	Takifugu rubripes	UPDATED: https://www.ncbi.nlm.nih.gov/protein/XP_011616710?report=genbank&log$=protalign&blast_rank=1&RID=41WVKX4Y014	https://www.ebi.ac.uk/ebisearch/search.ebi?db=allebi&query=ENSTRUP00000031696	http://www.uniprot.org/uniprot/H2U434
4 / dimer	VY1047	Branchiostoma floridae	UPDATED (Branchiostoma belcheri): https://www.ncbi.nlm.nih.gov/protein/XP_019639192?report=genbank&log$=protalign&blast_rank=1&RID=41WVXYCX014	-	-
5 / dimer	VY1048	Nasonia vitripennis	UPDATED: https://www.ncbi.nlm.nih.gov/protein/XP_008209982?report=genbank&log$=protalign&blast_rank=1&RID=41WWA4A8014	-	http://www.uniprot.org/uniprot/K7J523

Mutation Number / dimeric or monomeric	Strain name	Organism	NCBI - proteinBLAST	EBI - European Bioinformatics Institute	Uniprot - HMMER search
6 / dimer	VY1049	Takifugu rubripes	-	https://www.ebi.ac.uk/ebisearch/search.ebi?db=allebi&query=ENSTRUP00000000144	http://www.uniprot.org/uniprot/H2RJ31
7 / dimer	VY1050	Cavia porcellus	UPDATED: https://www.ncbi.nlm.nih.gov/protein/XP_003463142?report=genbank&log$=protalign&blast_rank=2&RID=41Y4RCPD015	https://www.ebi.ac.uk/ebisearch/search.ebi?db=allebi&query=ENSCPOP00000003676	http://www.uniprot.org/uniprot/H0V2C0
8 / dimer	VY1051	Takifugu rubripes	UPDATED: https://www.ncbi.nlm.nih.gov/protein/XP_003966059?report=genbank&log$=protalign&blast_rank=1&RID=41WXNEUS015	https://www.ebi.ac.uk/ebisearch/search.ebi?db=allebi&query=ENSTRUP00000008414	http://www.uniprot.org/uniprot/H2S7P2
9 / dimer	VY1052	Takifugu rubripes	UPDATED: https://www.ncbi.nlm.nih.gov/protein/XP_003966059?report=genbank&log$=protalign&blast_rank=1&RID=41WY1J2K014	https://www.ebi.ac.uk/ebisearch/search.ebi?db=allebi&query=ENSTRUP00000008415	http://www.uniprot.org/uniprot/H2S7P3
10 / dimer	VY1053	Ciona intestinalis	UPDATED: https://www.ncbi.nlm.nih.gov/protein/XP_018671050?report=genbank&log$=protalign&blast_rank=1&RID=41WYCT79014	https://www.ebi.ac.uk/ebisearch/search.ebi?db=allebi&query=ENSCINP00000008812	-
11 / dimer	VY1054	Ciona savignyi	UPDATED (Ciona intestinalis): https://www.ncbi.nlm.nih.gov/protein/XP_009858173?report=genbank&log$=protalign&blast_rank=1&RID=41WYPZH4015	https://www.ebi.ac.uk/ebisearch/search.ebi?db=allebi&query=ENSCSAVP00000008997	http://www.uniprot.org/uniprot/H2YUI7
12 / dimer	VY1062	Ciona savignyi	UPDATED (Ciona intestinalis): https://www.ncbi.nlm.nih.gov/protein/XP_009858173?report=genbank&log$=protalign&blast_rank=1&RID=41WZ437X015	https://www.ebi.ac.uk/ebisearch/search.ebi?db=allebi&query=ENSCSAVP00000009000	http://www.uniprot.org/uniprot/H2YUJ0

Mutation Number / dimeric or monomeric	Strain name	Organism	NCBI - proteinBLAST	EBI - European Bioinformatics Institute	Uniprot - HMMER search
13 / dimer	VY1056	Ciona savignyi	UPDATED (Ciona intestinalis): https://www.ncbi.nlm.nih.gov/protein/XP_018669141?report=genbank&log$=protalign&blast_rank=1&RID=41WZF9S8014	https://www.ebi.ac.uk/ebisearch/search.ebi?db=allebi&query=ENSCSAVP00000010325	http://www.uniprot.org/uniprot/H2YYB4
14 / dimer	VY1057	Ciona intestinalis	-	https://www.ebi.ac.uk/ebisearch/search.ebi?db=allebi&query=ENSCINP00000011393	-
15 / dimer	VY1058	Anolis carolinensis	UPDATED: https://www.ncbi.nlm.nih.gov/protein/XP_003217173?report=genbank&log$=protalign&blast_rank=1&RID=41X056ZX015	https://www.ebi.ac.uk/ebisearch/search.ebi?db=allebi&query=ENSACAP00000016375	http://www.uniprot.org/uniprot/G1KSW2
16 / dimer	VY1059	Gallus gallus	UPDATED: https://www.ncbi.nlm.nih.gov/protein/XP_015137732.1?report=genbank&log$=prottop&blast_rank=8&RID=41X0FWDX015	-	-
17 / dimer	VY1060	E. cuniculi	https://www.ncbi.nlm.nih.gov/protein/19074673?report=genbank&log$=protalign&blast_rank=1&RID=XWEHW0TG015	-	http://www.uniprot.org/uniprot/Q8SR52
18 / dimer	VY1061	Ciona intestinalis	-	https://www.ebi.ac.uk/ebisearch/search.ebi?db=allebi&query=ENSCINP00000011395	-
WT / monomer	VY137	See WT / dimer			
2 / monomer	VY1063	See 2 / dimer			
5 / monomer	VY1065	See 5 / dimer			
13 / monomer	VY1085	See 13 / dimer			

Table S2.2. Microtubule affinity measurements. The data were fit to the following equation $k_{obs} = (B_M - k_{basal}) \frac{[MT]}{K_d+[MT]} + k_{basal}$ in which B_M is the maximum binding, K_d is the dissociation constant, k_{basal} is the basal "binding" fraction and accounts for the pelleting of dynein without microtubules present, and k_{obs} is the observed fraction of dynein bound (pelleted) over the total amount of dynein. We could have also used the simplified equation $k_{obs} = (B_M) \frac{[MT]}{K_d+[MT]}$ (B_M maximum binding, K_d dissociation constant) but we wanted to account for potential pelleting of dynein without microtubules (k_{basal}). However, since k_{basal} is very low, using the simplified equation gives almost identical results for B_M and K_d. Values are shown as averages of triplicates ± standard deviation. n/m is not measurable.

Construct	**Nucleotide**	**K_d [MT]**	**B_M**	**k_{basal}**
Wild-type	ATP	5.22 ± 0.92 μM	n/m	0.02 ± 0.01
Wild-type	apo	0.78 ± 0.27 μM	0.86 ± 0.02	0.02 ± 0.01
Wild-type	AMPPNP	1.22 ± 0.72 μM	0.90 ± 0.04	0.03 ± 0.01
Mutant 2	ATP	2.62 ± 0.89 μM	n/m	0.01 ± 0.01
Mutant 2	apo	5.83 ± 0.04 μM	n/m	0.01 ± 0.00
Mutant 2	AMPPNP	3.93 ± 1.59 μM	n/m	0.03 ± 0.01
Mutant 5	ATP	4.10 ± 1.28 μM	n/m	0.05 ± 0.00
Mutant 5	apo	5.89 ± 1.38 μM	n/m	0.02 ± 0.01
Mutant 5	AMPPNP	3.08 ± 2.06 μM	n/m	0.02 ± 0.01
Mutant 13	ATP	4.00 ± 0.79 μM	n/m	0.02 ± 0.00
Mutant 13	apo	6.19 ± 0.99 μM	n/m	0.02 ± 0.00
Mutant 13	AMPPNP	3.66 ± 0.08 μM	n/m	0.02 ± 0.00

Table S2.3 | ATPase rates for dynein mutations in the literature.

Mutation	Organism	K_M [MT]	k_{cat}	k_{basal}	Reference
Wild-type	Yeast	0.59 ± 0.28 μM	14.1 ± 0.36 s^{-1}	3.74 ± 0.35 s^{-1}	Cho et al. JCB 2008 [32]
AAA3 (E2488Q)	Yeast	0.03 ± 0.01 μM	1.38 ± 0.14 s^{-1}	0.30 ± 0.05 s^{-1}	Cho et al. JCB 2008
AAA4 (E2819Q)	Yeast	0.09 ± 0.03 μM	10.6 ± 0.72 s^{-1}	3.36 ± 0.59 s^{-1}	Cho et al. JCB 2008
Wild-type	Yeast	-	20 ± 4 s^{-1}	6 ± 2 s^{-1}	Carter et al. Science 2008 [28]
Removal of 7 heptads in stalk	Yeast	-	21 ± 2 s^{-1}	13 ± 2 s^{-1}	Carter et al. Science 2008
Insertion of 7 heptads in stalk	Yeast	-	21 ± 5 s^{-1}	6 ± 2 s^{-1}	Carter et al. Science 2008
Wild-type	Yeast	1.06 ± 0.16 μM	16.75 ± 0.49 s^{-1}	3.51 ± 0.31 s^{-1}	Toropova et al. eLife 2014 [64]
AAA1	Yeast	-	-	~ 1 s^{-1}	Toropova et al. eLife 2014
AAA5 - linker docking (F3446D, R3445E, K3438E)	Yeast	-	-	~ 2 s^{-1}	Toropova et al. eLife 2014
Wild-type	D.discoideum	33.3 ± 2.6 μM	105.2 ± 4.2 s^{-1}	8.7 ± 0.8 s^{-1}	Kon et al. NSMB 2009 [40]
Fixed α registry (oxidized)	D.discoideum	5.0 ± 1.0 μM	158.0 ± 1.7 s^{-1}	128.4 ± 6.6 s^{-1}	Kon et al. NSMB 2009
Fixed β + registry (oxidized)	D.discoideum	19.2 ± 1.7 μM	17.0 ± 0.6 s^{-1}	3.3 ± 0.1 s^{-1}	Kon et al. NSMB 2009

Mutation	Organism	K_M [MT]	k_{cat}	k_{basal}	Reference
Fixed β - registry (oxidized)	D.discoideum	20.4 ± 4.6 μM	112.9 ± 4.1 s^{-1}	74.0 ± 2.1 s^{-1}	Kon et al. NSMB 2009
Delta buttress (Q3824-E3864)	D.discoideum	-	-	~ 90 s^{-1}	Kon et al. Nature 2012 [30]
Delta c-terminus (S4416-I4730)	D.discoideum	-	-	~ 10 s^{-1}	Kon et al. Nature 2012
Wild-type	Yeast	-	~ 17 s^{-1}	~ 3 s^{-1}	Bhabha et al. Cell 2014 [35]
AAA2 - linker docking (A2121G, T2122G, L2123G)	Yeast	-	~ 7 s^{-1}	~ 3 s^{-1}	Bhabha et al. Cell 2014
AAA2 - linker docking (R2183A)	Yeast	-	~ 5 s^{-1}	~ 2 s^{-1}	Bhabha et al. Cell 2014
GST-Dynein (1219-4093)	Yeast	0.39 ± 0.06 μM	16.1 ± 0.3 s^{-1}	-	Reck-Peterson et al. Cell 2006 [60]
Dynein-GST (1219-4093)	Yeast	-	4.3 ± 0.3 s^{-1}	-	Reck-Peterson et al. Cell 2006
GST-Dynein (1390-4093)	Yeast	-	-	~ 1 s^{-1}	Reck-Peterson et al. Cell 2006

Table S2.4 | ATPase assay rate measurements. The data were fit to the following equation $k_{obs} = (k_{cat} - k_{basal}) \frac{[MT]}{K_M + [MT]} + k_{basal}$. Values are shown as averages of triplicates ± standard deviation. n/m is not measurable.

Construct	**K_M [MT]**	**k_{cat}**	**k_{basal}**
Wild-type	0.50 ± 0.17 μM	15.18 ± 1.18 s^{-1}	0.75 ± 0.34 s^{-1}
Mutant 2	n/m	n/m	6.23 ± 2.25 s^{-1}
Mutant 5	n/m	n/m	13.80 ± 0.50 s^{-1}
Mutant 13	n/m	n/m	14.95 ± 0.35 s^{-1}

Table S2.5 | Statistics on cryo-EM data collection and processing.

Data Collection (Cryo-EM)	**Mutant 5 + AMPPNP**		**Mutant 5 + ATP-vi**	
Microscope	Titan Krios		Arctica	
Camera	K2		K2	
Magnification	22,500		36,000	
Voltage (kV)	300		200	
Electron dose (e-/pixel/second)	10		8	
Focus range (μm)	1.5-3.0		1.5-3.0	
Pixel size (Å)	1.31		1.156	
Number of images/movies	1200		664	
Reconstruction				
Particles selected after 2D classification (no.)	310,085		35,565	
CTF correction tool	GCTF 1.0.6		ctffind 4.1.10	
Particle picking method	Gaussian blobs		Gaussian blobs	
Ab-initio models generated (no.)	4		5	
Last round of 3D heterogeneous refinement (no.)	4		5	
Class name	**Class 1**	**Class 2**	**Class 1**	**Class 2 (not shown)**
Point group symmetry	C1	C1	C1	C1
Final particles (no.)	97,008	39,048	8,653	6,629
Resolution (Å)	7.7	7.6	9.2	16.6
B-factor (Å^2)	-400	-400	-400	-400
Modelling from 4W8F domains	rigid-body (Chimera)	rigid-body (Chimera) + refinement (PHENIX)	rigid-body (Chimera)	None

Materials and Methods

Bioinformatic analysis of dynein sequences

Briefly, we used 677 unique axonemal and cytoplasmic dynein heavy chain sequences from 229 fully sequenced eukaryotic genomes, which we received from Christian Zmasek, Godzik lab, Burnham. This data set was pruned based on well defined criteria and analyzed using Jalview[69]. Remaining sequences were aligned using MAFFT[72] in the Bioinformatic Toolkit[73] and mutations in the stalk were manually identified by comparing sequences in Jalview.

Yeast strains used in this study

Recombinant *S.cerevisiae* cytoplasmic dynein (Dyn1) truncated at the N-terminus (1219-4093 aa) was used in this study. All constructs used in this study are listed in **Table S2.1**. Dimeric constructs are based on VY208 and were created by artificially dimerization through an N-terminal GST-tag[60] and tagged with a HaloTag (Promega) at the C-terminus as well as a GFP at the very N-terminus. Monomeric constructs (VY137) are GFP tagged at the N-terminus. Stalk mutations were inserted by homologous recombination as previously described[60].

Protein expression and purification

Dynein was expressed and purified as previously described [60]. Monomeric and dimeric constructs were further purified by gel filtration on a GE Healthcare Superdex 200 10/300GL and a GE Healthcare Superose 6 10/300GL column, respectively in dynein gel filtration buffer (50 mM K-Ac, 20 mM Tris, pH 8.0, 2 mM $Mg(Ac)_2$, 1 mM EGTA, 1 mM TCEP, and 10% glycerol) and flash frozen afterwards. The 'cysteine-light' human ubiquitous kinesin-1 dimer E215C K490 construct was cloned and purified as previously described[63,74]. Following dialysis the E215C K490 construct reacted for 4 h at 4°C with Cy3-maleimide (GE Healthcare, PA13131) at a motor/Cy3 dye ratio of 1:10 as previously described[63]. The unreacted maleimide dyes were then quenched with 1 mM dithiothreitol (DTT). Afterwards the kinesin was purified by gel filtration

over a S200 10/300GL column (GE Healthcare) in kinesin gel filtration buffer (25 mM Pipes (pH 6.8), 2 mM $MgCl_2$, 200 mM NaCl, 1 mM EGTA, 1 mM DTT, and 10% sucrose) and flash frozen.

Preparation of microtubules

Tubulin was purified and polymerized as previously described[20]. For single-molecule motility assays unlabeled tubulin, biotinylated tubulin, and fluorescent tubulin were mixed at an approximate ratio of 20:2:1 in BRB80 (80 mM Pipes (pH 6.8), 1 mM EGTA, and 1 mM $MgCl_2$). For the gliding assay unlabeled tubulin and fluorescent tubulin were mixed at an approximate ratio of 20:1 in BRB80. For tubulin that was used in the ATPase assay as well as the microtubule affinity assay only unlabeled tubulin was used. We added 1 mM GTP to all polymerization reactions. Then the mixtures were incubated for 15 min in a 37°C water bath. 20 µM of Taxol (Sigma, T1912) was added afterwards and the mixture was incubated for 2 more hours at 37°C. Before usage, microtubules were spun over a 25% sucrose cushion in BRB80 at ~160,000 g for 10 min in a tabletop centrifuge.

Gliding and single-molecule motility assay

We made custom flow chambers using laser-cut double-sided adhesive sheets (Soles2dance, 9474-08x12 - 3M 9474LE 300LSE). We used glass slides (Thermo Fisher Scientific, 12-550-123) and coverslips (Zeiss, 474030-9000-000). We cleaned the coverslips in a 5% v/v solution of Hellmanex III (Sigma, Z805939-1EA) at 50°C overnight and then washed them extensively with Milli-Q water. The flow-cells were assembled in a way that each chamber holds approximately 10 µl.

Every data collection was carried out at room temperature (~23 °C) using a total internal reflection fluorescence (TIRF) inverted microscope (Nikon Eclipse Ti microscope) equipped with a 100× (1.45 NA) oil objective (Nikon, Plan Apo ƛ). We used an Andor iXon 512x512 pixel EM camera, DU-897E and a pixel size of 159 nm. Dynein (always as dimer and either labeled with

GFP only or with GFP and a Halo488 dye (Promega, G1001)) was excited with a 488 nm laser (Coherent Sapphire 488 LP, 150 mW), kinesin with a 561 nm laser (Coherent Sapphire 561 LP, 150 mW), and microtubules with a 640 nm laser (Coherent CUBE 640-100C, 100 mW). For the gliding assay, images were recorded with 100 ms exposure time and a 2 sec frame rate for MTs and a 100 msec frame rate for kinesin. For the single-molecule assay of dynein, we used 100 msec exposures and a 2 sec frame rate and a 100 msec frame rate for kinesin. The acquisition software was μManager[70] 2.0 and data was analyzed in ImageJ[75].

For the gliding assay, we first added 10 μl of GFP antibody (Abcam, ab1218) and incubated for 5 min. Then we washed with 20 μl of DAB with 2 mg/ml β-casein and 0.4 mg/ml κ-casein. We then added 10 μl of dimeric dynein and incubated for another 5 min which was followed by an additional wash with 20 μl of DAB with 2 mg/ml β-casein and 0.4 mg/ml κ-casein. Next, we added 10 μl of polymerized microtubules and incubated for 5 min. Then we washed with 30 μl of DAB with 2 mg/ml β-casein and 0.4 mg/ml κ-casein. Finally, 10 μl of DAB with kinesin, 0.4 mg/ml κ-casein, 10 μM Taxol, 1 mM Mg-ATP, and the PCA/PCD/Trolox oxygen scavenging system[76] was added.

Prior to the single-molecule motility assays, dynein was labeled with Halo488 dye (Promega, G1001) as previously described[35]. Briefly, dynein constructs were mixed with 20 μM Halo Alexa488 dye and incubated on ice for 10 min and a PD MiniTrap G-25 column (GE Healthcare) equilibrated with dynein gel filtration buffer was used to remove excess dye.

The flow chambers for the single-molecule motility assay were prepared as previously described [62]. Briefly, we first added 10 μl of 5 mg/ml Biotin-BSA in BRB80 and incubated for 2 min. Then we washed with 20 μl of BRB80 with 2 mg/ml β-casein (Sigma, C6905), 0.4 mg/ml κ-casein (Sigma, C0406). Afterwards we added 10 μl of 0.5 mg/ml Streptavidin in PBS for a 2 min incubation. Next, we again washed with 20 μl of BRB80 with 2 mg/ml β-casein, and 0.4 mg/ml κ-casein. This was followed by the addition of 10 μl of polymerized microtubules and a 5 min incubation. Then we washed with 30 μl of DAB (50 mM K-Ac, 30 mM HEPES, pH 7.4, 2 mM

$Mg(Ac)_2$, 1 mM EGTA) with 2 mg/ml β-casein, 0.4 mg/ml κ-casein, and 10 μM Taxol. Finally we added 10 μl of dynein and kinesin in DAB with 0.4 mg/ml κ-casein, 10 μM Taxol, 1 mM Mg-ATP, and the PCA/PCD/Trolox oxygen scavenging system[76]. In the single-molecule assay where ATP was omitted, the final solution contained 10 μl of dynein in DAB with 0.4 mg/ml κ-casein, 10 μM Taxol, and the PCA/PCD/Trolox oxygen scavenging system[76]. The acquisition software for all microscopy data was μManager [70] 2.0.

Diffusion analysis of single-molecule movements

The imaging was performed as described for the single-molecule motility assay. Subsequently, tracks of wild-type dynein and mutant 5 along microtubules in the presence of 1 mM ATP were obtained. We tracked single molecules using the 'localization microscopy' plug-in from μManager 2.0[70] by fitting emitters with a Gaussian based maximum-likelihood estimation[77] as previously described[78] and extracted tracks based on a nearest neighbor search. We then straightened these single-molecule traces along the main axis of motion along the microtubule using a principal component analysis implemented in the 'localization microscopy' plug-in from μManager 2.0[70]. Following this, the displacement of wild-type dynein and mutant 5 were binned into 1 sec intervals and the polarity of microtubules was determined by analyzing the directionality of human homodimeric kinesin-1 (K490)[63], which moves processively towards the plus end of microtubules.

The ATPase assay

The ATPase assays were carried out in DAB (50 mM K-Ac, 30 mM HEPES, pH 7.4, 2 mM $Mg(Ac)_2$, 1 mM EGTA) as follows. We mixed dynein (monomeric for all constructs) to a final concentration of 10-20 nM with 2 mM Mg-ATP (Sigma), 0.2 mM NADH (Sigma), 1 mM phosphoenolpyruvate (Sigma), 0.01 U pyruvate kinase (Sigma), 0.03 U lactate dehydrogenase (Sigma), 10 μM Taxol, 1 mM DTT, and 0-5 μM microtubules in DAB. Absorbance at 340 nm was

continuously measured in an Eppendorf Spectrophotometer (UV-Vis BioSpectrometer) and the data was fit to the following equation[35] using an excel curve fitting routine: $k_{obs} = (k_{cat} - k_{basal}) \frac{[MT]}{K_M + [MT]} + k_{basal}$.

The vanadate inhibition of dynein ATPase activity was performed as previously described [79]. Briefly, we mixed dynein (monomeric of wild-type and mutant 5 (from the same batch that was used to solve the structure of mutant 5 in the presence of ADP-vi)) to a final concentration of 20 nM with 1 mM Mg-ATP (Sigma), 0.2 mM NADH (Sigma), 1 mM phosphoenolpyruvate (Sigma), 0.01 U pyruvate kinase (Sigma), 0.03 U lactate dehydrogenase (Sigma), 10 μM Taxol, 1 mM DTT, 6 μM microtubules and 0-100 μM vanadate (Sigma) in DAB. The vanadate was boiled for 10 min before usage. Absorbance at 340 nm was continuously measured in an Eppendorf Spectrophotometer (UV-Vis BioSpectrometer) and the turnover rate was calculated as described above.

Vanadate-mediated UV-photo cleavage

Protein from the same batch that was used to solve the structure of mutant 5 in the presence of ADP-Vi was used in the vanadate-mediated UV-photo cleavage. The assay was performed in a similar way as previously described[29]. Briefly, mutant 5 monomer was mixed with 2 mM Mg-ATP (Sigma) and 2 mM vanadate (Sigma) and either exposed to UV-light (365 nm) or kept in the dark for 90 min. The vanadate was boiled for 10 min before usage. Afterwards the samples were analysed by SDS-PAGE.

Microtubule affinity assay

The microtubule affinity assays were carried out in DAB (50 mM K-Ac, 30 mM HEPES, pH 7.4, 2 mM $Mg(Ac)_2$, 1 mM EGTA) as follows. We mixed dynein (monomeric for all constructs) to a final concentration of approx. 50 nM with 10 μM Taxol, 1 mM DTT, and 0-8 μM microtubules

in DAB. For the measurements with ATP we added 5 mM Mg-ATP (Sigma) and for the experiment with AMPPNP we added 5 mM Mg-AMPPNP (Sigma). After a 3 min incubation at room temperature the samples were spun over a 25% sucrose cushion in DAB at ~160,000 *g* for 10 min in a tabletop centrifuge. The concentration of dynein in the supernatant (unbound) and in the pellet (bound) was determined by measuring the intensity of the N-terminal GFP on a Typhoon laser scanner (GE Healthcare). The data was fit to the following equation using an excel curve fitting routine $k_{obs} = (B_M - k_{basal}) \frac{[MT]}{K_d + [MT]} + k_{basal}$ in which B_M is the maximum binding, K_d is the dissociation constant, k_{basal} is the basal "binding" fraction and accounts for the pelleting of dynein without microtubules present, and k_{obs} is the observed fraction of dynein bound (pelleted) over the total amount of dynein. We could have also used the simplified equation $k_{obs} = (B_M) \frac{[MT]}{K_d + [MT]}$ (B_M maximum binding, K_d dissociation constant) but we wanted to account for potential pelleting of dynein without microtubules (k_{basal}). However, since k_{basal} is very low, using the simplified equation gives almost identical results for B_M and K_d.

Electron microscopy data collection

For negative stain, data for mutants 5 (monomer) was collected on a Tecnai F20 microscope with a Tietz F416 CMOS detector at the New York Structural Biology Center (NYSBC). Leginon software[80] was used for the semi-automated collection of 825 images at a magnification of x62,000 and a pixel size of 3 Å per pixel. For cryo-EM data collection, 1200 movies of mutant 5 (monomer) mixed with 2 mM AMPPNP were recorded with SerialEM[81] at 300 kV on a Titan Krios (FEI) equipped with a K2 summit camera (Gatan) at 0.655 Å per pixel in super-resolution mode at Janelia Research Campus. Another 664 movies of the same mutant (mutant 5 - monomer) mixed with 2 mM ATP and 2 mM vanadate were recorded with SerialEM at 200 kV on a Arctica (FEI) equipped with a K2 summit camera (Gatan) at 0.578 Å per pixel in super-resolution mode at New York University.

Electron microscopy data processing and analysis

For the images of the negatively stained sample, particles were selected using DoG picker[82] in APPION[83], then extracted in Relion 2.1.0[84] into boxes of 180x180 pixels, leading to 156,199 boxes for mutant 5. A round of 2D classification was performed to remove junk and noisy particles, leading to 54,913 particles selected. Subsequent image processing steps were carried out using CryoSPARC[85]. After having generated an ab-initio model, those particles were used to generate eight 3D classes. Because of the similarity between all those classes, a final round of 3D refinement was completed using all of the particles.

For the cryo-EM images (see also **Table S2.5**), the movies of mutant 5 with 2 mM AMPPNP were first aligned and binned to 1.31 Å per pixel with MotionCor2 v1.0.5[86], and then the contrast transfer function parameters were estimated with GTCF 1.06 [87]. The particles were picked automatically in Relion 2.1.0[84] using a Gaussian blob as a reference and further processing was done in CryoSPARC[85]. Out of the 310,085 regions automatically picked, 136,056 were kept after evaluation of 2D classes. Two ab-initio models were first generated in CryoSPARC, and the best one was used in a 4-class 3D heterogeneous refinement. Then, two 3D homogeneous refinements were completed: one with class 3 (here refered to as class 2 - with 29% of remaining particles and with a resolution of 7.6 Å), and another one (here refered to as class 1 - with 71% of remaining particles and with a resolution of 7.7 Å) with the three other classes which looked very similar and were therefore combined before refinement. Note that the overall and local resolutions we report are the average resolution after refinement in CryoSparc v2.5.0 (**Fig. S2.10 and Fig. S2.11**). The final maps were then filtered for display using a B-factor of -400. For modelling, we used PDB 4W8F as a reference. The PDB file was split into 13 domains (small and large subdomains for each AAA domain, and the linker) and, for each of those domains, we simultaneously fit all 13 subdomains into the map using UCSF Chimera[71]. We noticed that the rigid body of the buttress region in class 2 map did not perfectly fit the

densities (**Fig. S2.10**). This model was therefore subjected to the real_space_refine algorithm in PHENIX[88] using 2 cycles and 100 iterations to optimize the fit. Figures and movies of structures and density maps were generated with the UCSF Chimera package or the Pymol Molecular Graphics System (version 2.0, Schröodinger, LLC).

For the images of mutant 5 with 2 mM ATP and 2 mM vanadate acquired on the Arctica, a similar process was followed. First aligned and binned to 1.31 Å per pixel with MotionCor2 v1.0.5[86], and the contrast transfer function parameters estimated with GCTF 1.06[87]. A first round of auto-picking was conducted in Relion 2.1.0[84] using a Gaussian blob as a reference. Two of the resulting classes were then used as a template for a round of reference-based auto-picking. Further processing was also conducted in CryoSPARC[85]. Out of 35,565 picked particles, 32,442 particles were kept for the generation of ab-initio models and a 4 and a 5-class heterogeneous refinement were tried. One class with 8,653 particles lead to a clear dynein 3D model that we refined to 9.2 Å (**Fig. S2.13**) and finally filtered for display using a B-factor of -400. Another class at 17 Å seemed to show only the AAA domains while the linker could not be seen. The model for the 9.2 Å map was constructed as for mutant 5 in the AMPPNP-state, using rigid body docking of domains from PDB 4W8F. However, the model was not further refined in PHENIX due to its lower resolution.

Figure and graph preparation

Figures and graphs were created using Pymol (version 2.0 Schröodinger, LLC) and Chimera[71] (structure representation), ImageJ[75] (light microscopy data), Jalview[69] (sequence analysis and representation), Affinity designer (version 1.6.1, Serif (Europe) Ltd) and Python (version 2.7, Python Software Foundation).

Statistics and error calculation

For each result obtained, the inherent uncertainty due to random or systematic errors and their validation are discussed in the relevant sections of the manuscript. Details about the sample size, number of independent calculations, and the determination of error bars in plots are included in the figures and figure captions.

Acknowledgements

We are grateful to J. Sheu-Gruttadauria, Iris Grossman-Haham, and Zhen Chen for critical discussions of the manuscript. We would like to thank Christian Zmasek at the Burnham Institute for the initial sequence alignment file. We thank Nico Stuurman and Walter Huynh for their assistance and advice in light microscopy. Some of this work was performed at the Simons Electron Microscopy Center and National Resource for Automated Molecular Microscopy located at the New York Structural Biology Center, supported by grants from the Simons Foundation (349247), NYSTAR, and the NIH National Institute of General Medical Sciences (GM103310). We thank Kelsey Jordan at the New York Structural Biology Center for assistance with data collection of negatively stained samples. Cryo EM data were collected on the Titan Krios ("Krios 2") at Janelia Research Campus and the Talos Arctica at the NYU Langone Health's Cryo–Electron Microscopy Laboratory. We thank Hui-Ting Chou and Zhiheng Yu at HHMI Janelia Research Campus, and Zheng Liu at NYU for assistance in microscope operation and data collection. For EM data processing, this work has utilized computing resources at the High-Performance Computing Facility at NYU Langone Medical Center. We thank Martin Ossowski and his HPC team as well as Joe Katsnelson for EM data processing support. The authors gratefully acknowledge funding support from the NIH National Institute of General Medical Sciences: R00GM112982 (G.B.), R01GM097312 (R.D.V.), Damon Runyon Cancer Research Foundation DFS-20-16 (G.B.), Howard Hughes Medical Institute (R.D.V.) and the UCSF Discovery Fellowship (S.N.).

CHAPTER 3

Nanometer-accuracy distance measurements between fluorophores at the single-molecule level

Abstract

Light microscopy is a powerful tool for probing the conformations of molecular machines at the single-molecule level. Single-molecule Förster resonance energy transfer can measure intra-molecular distance changes of single molecules in the range of 2-8 nm. On the other hand, current super-resolution measurements become error prone below 25 nm. Thus, new single-molecule methods are needed for measuring distances in the 8-25 nm range. Here, we describe methods that utilize information about localization and imaging errors to measure distances between two different color fluorophores with ~1 nm accuracy at distances >2 nm. These techniques can be implemented in high-throughput using a standard TIRF microscope and open-source software. We applied our two-color localization method to uncover an unexpected ~4 nm nucleotide-dependent conformational change in the coiled-coil “stalk” of the motor protein dynein. We anticipate that these new methods will be useful for high-accuracy distance measurements of single molecules over a wide range of length scales.

Introduction

Understanding the spatial arrangement of biological macromolecules is crucial for elucidating molecular mechanisms. While three-dimensional structures provide insight into the mechanism of a protein, the static state alone is often insufficient to understand how macromolecular machines perform action. By labeling single molecules or complexes at defined sites with fluorescent dyes, it is possible to obtain static or dynamic distance measurements that provide information about conformational changes or molecular interactions.

A widely used method for obtaining such distance information is single-molecule Förster resonance energy transfer (smFRET)[89] between two different colored fluorophores. However, smFRET is limited to a short distance range, typically 2-8 nm. Calculation of absolute distances is influenced by orientation and chemical environment of fluorophores[90], which are difficult to measure, and hence smFRET is most widely used to detect relative distance changes. Direct fluorescent-based measurements of longer distances can be achieved by single-molecule colocalization microscopy[91–93] but distances below ~25 nm have proven to be very difficult to measure correctly. Thus, there is a gap in resolution (**Fig. S3.1**) that is important to fill since it corresponds to the size distribution of various proteins as well as many protein complexes.

Previously studies have made considerable progress in tackling distance measurements between 8-25 nm. Single-molecule high resolution colocalization (SHREC)[91,94] resolves nanometer distances by accounting for localization errors when measuring the separation between two different color fluorophores. Pertsinidis et al.[95] developed a feedback-controlled system that enabled distance measurements with subnanometer precision, and Mortensen et al.[96] reported ~1 nm resolution by imaging the same single molecules multiple times. However, distance measurements with nanometer accuracy and precision have not been more broadly adopted, either because these available methods suffer from inaccuracy and/or low throughput or involve highly specialized optical setups[95].

Here, we report new methods capable of reliably measuring two-color fluorophore distances at ~1 nm accuracy over a wide range of distances (from ~2 nm to hundreds of nanometers) using readily available microscope hardware. To achieve this level of accuracy, we first correct for chromatic aberrations and distortions using a piecewise affine transformation[97], yielding registration errors (image alignment of different fluorophores) of less than 1 nm over the entire field of view of a standard total internal reflection fluorescence (TIRF) microscope. We show that existing distance analysis methods, like those of Churchman et al.[94], become error prone when the true distance and localization errors of the individual probes are similar, which is common for distances of ~2-30 nm. To overcome these limitations, we developed two related methods: Sigma-P2D, which incorporates information about localization and imaging errors, and Vector-P2D, which makes use of averaging multiple observations of the same molecule. We applied our new methods to investigate nucleotide-dependent conformational changes of the molecular motor dynein[1,51,52] and found that the stalk of dynein likely undergoes a large conformational change during its hydrolysis cycle[40]. These results could not have been obtained by smFRET or other direct two-color imaging methods, since the distances measured changed from ~16 nm to ~20 nm in different nucleotide states. Thus, the two methods presented here, together with our improved image registration procedure, should have broad applications for inter- and intramolecular distance measurements, particularly in the range of 8-25 nm where current techniques for two-color imaging are suboptimal. Our methods are also easily implemented using commercially available microscopes and open-source μManager[70] software.

Results

Registration error in subnanometer range

To achieve highly accurate distance measurements between two fluorophores that emit at different wavelengths, multiple obstacles have to be overcome. First, the sample of interest needs to be fluorescently labeled at specific sites and immobilized to the coverslip surface at a defined orientation (**Fig. 3.1**). Then, one needs to image two channels, localize the individual probes, align the two channels (image registration), and calculate the distance between centroids from multiple observations of the same or multiple particles (**Fig. 3.1**). While localization of individual fluorophores by fitting a point spread function (PSF) or 2D Gaussian to the fluorophore's intensity distribution has been well established and delivers precision close to the theoretical limit[77], current image registration methods correct poorly for commonly observed chromatic aberrations over the entire field of view at the nanometer scale[95] or have problems in throughput since they are limited to imaging one pixel at time[96]. Thus, in order to enable high-throughput and accurate two-color distance measurements, we first set out to improve two channel image registration over the entire field of view.

As multicolor fiducial markers, we imaged TetraSpeck™ beads and used a registration function to correct for the offset between color positions (**Fig. 3.2**). While previously described registration methods either use a second-degree polynomial fit[98] or linear mapping functions[95] to calculate a registration map, we used a two-step affine based registration procedure[97] commonly employed in other fields[97], but to our knowledge, not previously used to align multi-color single-molecule images. To this end, we first performed a global affine transformation to bring single spots (imaged on two different cameras) in proximity for automated pair assignment (**Fig. 3.2**). Next, we applied a piecewise affine transformation, correcting spot positions locally (as detailed below) only using nearby fiducial points (**Fig. 3.2, Fig. S3.1**). In practice, we always acquired three datasets - the first was TetraSpeck beads, the second was the sample of interest, and the third was another acquisition of the TetraSpeck beads (**Fig.**

S3.1). With the corrected second fiducial marker dataset, we then calculated the target registration error (TRE), determining the deviation between the markers' x and y positions in the two channels after alignment (**Fig. 3.2, Materials and Methods**). Their mean μ_x and μ_y are the registration error along the x-axis and y-axis, respectively. The registration error σ_{reg} is given by

$$\sigma_{reg} = \sqrt{\mu_x^2 + \mu_y^2}. \quad (1)$$

Only those samples for which σ_{reg} was < 1 nm were analyzed.

To find the optimal parameter space for image registration, we varied settings for the local piecewise affine transformation as described in more detail in the Materials and Methods section. A minimum of 10 and maximum of 100 fiducial points and a maximum distance of 2 μm resulted in optimal channel registration (**Fig. S3.3, S3.4**) when a sufficient number of fiducial markers was acquired. This is approximately 10,000 fiducial markers for an 80 μm x 80 μm image (**Fig. S3.1**), and requires the collection of ~400 images with ~25 beads per field of view.

Using this approach, we routinely (76%) achieved registration accuracy σ_{reg} of < 1 nm (**Fig. 3.2**). When registration failed (24% of the time), the cause was almost always a slight change in focus during acquisition of the datasets of fiducial markers. Thus, successful execution requires stable optical alignment of the two channels for the duration of the experiment (i.e. < 1 nm change in approximately 5-20 min), a high quality autofocus system, a motorized xy-stage, minimal sample movement during image exposure (i.e. < 1 nm sample movement for approximately 1 sec), and imaging of fiducial markers for image registration and sample of interest on the same slide (**Fig. S3.1**). To minimize drift effects we waited 3 sec after every stage movement before acquiring data at a new position. We noticed that the precision (σ_x, σ_y) for registering TetraSpeck™ beads is lower than expected based on their localization errors. We found this to be caused by displacement of the color centers of TetraSpeck™ beads by a few nanometers, as reported by others[96] (**Fig. S3.5-S3.7**). Together, piecewise affine alignment enables image registration at subnanometer accuracy over the entire field of view.

Measuring distances of uniform samples

Next, we set out to optimize the accuracy and throughput of direct distance determination. Previously, Churchman et al.[91,94] showed that distances on the scale of the localization error are non-Gaussian distributed (**Fig. 3.3, Fig. S3.8**) and described by the following two-dimensional probability distribution (P2D)[94]

$$p_{2D}(r|\mu,\ \sigma_d) = \left(\frac{r}{\sigma_d^2}\right) exp\left(-\frac{\mu^2+r^2}{2\sigma_d^2}\right) I_0\left(\frac{r\mu}{\sigma_d^2}\right) \quad (2)$$

in which r is the measured Euclidean distance of individual particles, μ the estimated average distance, σ_d the distance uncertainty, and I_0 the modified Bessel function of integer order zero. We refer to the true sample distance as "d". Churchman et al.[91,94] fit this distribution (P2D - Eq. 2) to Euclidean distance data by means of a maximum likelihood estimation (MLE) with two parameters (μ and σ_d). We refer to this method simply as two-dimensional probability distribution "P2D". However, using both experimental data and Monte Carlo simulations, we found that in case of small changes in distance uncertainty σ_d, P2D yields large changes in the estimated distance μ (**Fig. S3.8**). An approximation for $\sigma_d \geq \mu$ shows that the probability distribution (P2D - Eq. 2) becomes independent of distance μ, resulting in a fit that is driven by the distance uncertainty σ_d. Thus, distance estimations of P2D are error prone for cases where the distance is smaller or of similar size as the distance uncertainty, which is very common for distance measurements in the range of 2-30 nm.

To overcome this inaccuracy of the P2D method, we decided to fit the distance distribution with only one parameter, the distance μ, and to determine the distance uncertainty σ_d experimentally ($p_{2D}(r,\ \sigma_d|\mu)$). This is possible, because all parameters of the distance uncertainty σ_d can be measured as it is given by

$$\sigma_d = \sqrt{\sigma_{reg}{}^2 + \sigma_{loc_1}{}^2 + \sigma_{loc_2}{}^2} \quad (3)$$

in which σ_{loc_1} and σ_{loc_2} are the localization errors of single particles of fluorophore 1 and 2, respectively, and σ_{reg} the registration error. Thus, by using additional information from the

images, we can fit the data only with the important parameter, the distance μ and avoid overfitting. We named this new method “Sigma-P2D” (**Materials and Methods**). Applying Sigma-P2D to Monte Carlo simulated data, for which P2D predicted an incorrect distance, we now recovered the true distance with subnanometer accuracy (**Fig. 3.3**).

Given that our new method can refine measurements made over all distances for which a distance uncertainty can be determined (e.g. ~2 to hundreds of nanometers), we compared Sigma-P2D and P2D first using Monte Carlo simulations. We generated model datasets for different ratios of distance uncertainty to distance (σ_d / d) and evaluated the performance of Sigma-P2D and P2D by calculating the difference between true and estimated distance, normalized by the true distance (distance discrepancy) (**Fig. 3.3, Materials and Methods**). We found that Sigma-P2D outperforms P2D, especially if $\sigma_d \geq \mu$, and that even if only 100 particles were used, Sigma-P2D estimates the true distance with an offset of less than 20% for almost all ratios of distance uncertainty to distance (**Fig. 3.3**). We note that even though the average distance discrepancy might appear small (as for the case with 100 particles) the performance on a single dataset can be poor because large error bars indicate bimodal cases for which we measured both distances that are much larger and distances that are much smaller than the expected distance. However, the accuracy and reproducibility of Sigma-P2D can further be improved by quantifying more particles (**Fig. 3.3**) to accuracies of better than 1% of the true distance, while P2D reproducibly (small error bars) underestimates the distance for most conditions by almost 100%. This is an example of a precise and reproducible yet highly inaccurate measurement. Taken together, by incorporating available knowledge of localization and registration errors we greatly improved the fitting routine and can determine distances with subnanometer accuracy and precision.

To evaluate Sigma-P2D experimentally (**Fig. S3.9-S3.11**), we imaged a kinesin-1 homodimer for which both heads were rigor-bound with the non-hydrolyzable nucleotide analogue AMPPNP to adjacent tubulin dimers along a microtubule protofilament[74] (**Fig. 3.3**).

Based on electron microscopy data[99], the distance between the two motor domains is 8.2 nm (the tubulin dimer spacing). A kinesin motor domain construct[63,74] with a single cysteine residue (E215C) was reacted with an equimolar mixture of maleimide-Cy3 and maleimide-Cy5. Motors that contained both Cy3 and Cy5 and that bound to a biotin-streptavidin immobilized and Alexa-488 labeled microtubule were selected for two-color distance measurements.

When fitting the data for the apparent head-to-head distance of the rigor-bound kinesins with Sigma-P2D, we measured 8.5 ± 0.3 nm (**Fig. 3.3**), which is very close to the expected distance of 8.2 nm. Fitting the same data with the P2D method shows that P2D dramatically underestimated the distance and finds 0.3 ± 1.0 nm (**Fig. 3.3**). Unbound kinesins had variable distances causing the probability distribution fits to yield incorrect results (**Fig. 3.3**) since Sigma-P2D does not consider conformational heterogeneity. Hence, Sigma-P2D can only fit samples that are uniform in distance unless prior knowledge about the conformational heterogeneity σ_{con} is available. Nevertheless, utilizing Sigma-P2D we measured the head-to-head distance of a kinesin dimer with subnanometer accuracy and precision.

Measuring average distances of heterogeneous samples

Since distance measurements for heterogeneous samples with Sigma-P2D are inadequate and many proteins and protein complexes are heterogeneous in distance, we needed an additional method. To obtain meaningful population statistics for samples which are heterogeneous in distance, it is important to improve the precision with which the two-color distances of individual molecules can be measured. To do so, we collected multiple observations (frames) of the same molecule, by time-lapse imaging (**Fig. 3.4**). Rather than directly averaging the distance in each frame, observations of the same fluorescent pair in multiple frames are combined by first averaging distances in x and y separately, and then using these to calculate the Euclidean distance of individual particles (vector distance average). As previously shown [96], this leads to more accurate distance predictions than direct frame-by-frame

Euclidean distance averaging (**Fig. 3.4, Fig. S3.12**), because vector averaging helps to reduce the width of the distance distribution significantly. If for example 10,000 particles are imaged and 5 observations per particle are recorded, either all 50,000 distance measurements (frame-by-frame Euclidean distance) or all 10,000 vector averaged distances can be combined. For the vector averaged distances, the distribution is narrower (**Fig. 3.4**) but still not perfectly Gaussian distributed. Instead of fitting with a Gaussian probability distribution as done in a previously developed method[96] (here named "Vector"), we noticed that the fit can further be improved using the two-dimensional probability distribution (P2D - Eq. 2) and two parameters (μ and σ_d). Moreover, we noticed that maximum likelihood estimation (MLE) fitting often resulted in inaccurate distance determination for experimental data since it is fairly sensitive to outliers (background noise). Therefore, we fit the P2D function by means of non-linear least squares (NLLSQ), which is more robust to background noise than MLE (see **Materials and Methods**). We called this method "Vector-P2D" and found that Vector-P2D outperforms Vector for all conditions tested using Monte Carlo simulations which was evaluated as described for the comparison of Sigma-P2D and P2D (**Materials and Methods**). Using Vector-P2D, 100 particles with 20 observations each are enough to resolve distances within 20% of the true distance (**Fig. 3.4**) for ratios of distance uncertainty to distance (σ_d / d) of less than 3.5. Increasing the number of particles to 1,000 with 20 observations results in fitted distances that diverge less than 5% from the true distance for ratios of distance uncertainty to distance (σ_d / d) of less than 5 (**Fig. S3.12**). Since we only used a true distance of 10 nm in our simulations, we further tested if Vector-P2D can also resolve distances between 2 and 500 nm and found an almost perfect agreement between the true and measured distance (**Fig. S3.12**). To test whether Vector-P2D can determine the average distance of samples that are variable in distance, we ran Monte Carlo simulations at varying degrees of sample heterogeneity σ_{con} (standard deviation of true distances in the population). If, for instance, 20 frames per particle are recorded, we still recovered the correct population average even for cases where σ_{con} is twice as large as the true

distance d, (**Fig. S3.13**). However, the more heterogeneous the sample, the more frames have to be recorded to achieve accurate results (accuracy being defined as a 20% difference between the measured and predicted distance).

To test the performance of Vector-P2D experimentally, we used DNA-origami based nanorulers[100,101]. The average 'center-of-mass' distance between Cy3 and Alexa647 fluorophore binding sites on these nanorulers is either 10 nm, 20 nm, or 40 nm. Each color has up to 10 binding sites with an expected labeling efficiency of 50-80% (**Fig. 3.4**). Together with bleaching effects, this results in variable distances of the color centers of the individual rulers (**Fig. 3.4, Fig. S3.14**). However, when we analyzed these rulers using Vector-P2D, we found average distances that were within a nanometer of the expected values (**Fig. 3.4**) whereas the Vector method predicted distances up to 100% larger (**Fig. 3.4, Fig. S3.14**). Plotting the Vector-P2D measured population distances for all three nanorulers of three repeats over the expected distances and calculating the slope, we found a slope of 0.97, very close to the ideal value of 1.0 (**Fig. 3.4, Fig. S3.14**). Summarizing, using multiple observations of the same molecule and by performing a vector distance average, we can recover distances of variable samples with nanometer precision and accuracy.

Measurements of the dynein stalk length in multiple nucleotide states

We next applied our two-color colocalization methods to measure conformational changes in the minus-end-directed, microtubule-based motor dynein[1,51,52]. An intriguing problem for the function of this molecular motor is the two-way communication between the catalytically active AAA ring and the microtubule binding domain through conformational changes in an intervening ~13 nm antiparallel coiled-coil stalk[40,42–44] (**Fig. 3.5**). Earlier studies have suggested that local melting of the coiled-coil stalk in different states of the nucleotide hydrolysis cycle plays a major role in this communication[45,46,102], while others have shown that a 4 amino acid sliding between different registries is critical[40,46]. However, no direct measurements of the

distances between the AAA ring and microtubule binding domain have been reported, which could help to distinguish between these models.

To tackle this problem, we prepared a yeast cytoplasmic dynein monomer with a C-terminal Halo-tag[103] and a YBBR-tag[104] that was inserted into the microtubule binding domain (**Fig. 3.5**). Based on crystallographic data, the predicted distance between Halo- and YBBR-tag is ~20 nm[29] (**Fig. 3.5**). To simultaneously immobilize and fluorescently label dynein, both tags were labeled with a 16 bp long double stranded DNA that was biotinylated at one end and dye-labeled at the other. We then imaged dynein in the apo and ATP-vanadate (ATP-vi) state and measured the distance between the fluorescent labels using Vector-P2D, since we expected a heterogeneous distance distribution. Using three technical repeats, we measured a distance of 19.6 ± 0.9 nm for the ATP-vanadate state (**Fig. 3.5**). This is consistent with the X-ray crystallographic studies[29]. However, in the apo state (no ATP), we measured a distance of 15.8 ± 0.6 nm between the Halo-tag on the ring and the YBBR-tag in the microtubule binding domain. This shorter distance cannot be explained by the “simple helical sliding” model[40,46], which predicts essentially no distance change.

To further understand the structural basis of our two-color fluorescence measurement, we turned to negative stain electron microscopy. Two-dimensional class averages for the ATP-vanadate bound state show a clear density for the stalk and microtubule binding domain in most classes (“full stalk”). In contrast, the stalk density in the apo state was rarely observed (“no stalk”) (**Fig. 3.5**). This suggests two possibilities: 1) The angle of the stalk differs significantly in the individual molecules in the apo state, leading to these angles being averaged out in 2D classes, or, 2) The coiled-coil stalk of individual particles in the apo state cannot be identified in the micrographs, suggesting a large-scale conformational change in the stalk. To address these two possibilities, we analyzed the negative stain data on a single particle level. Individual particles for multiple nucleotide states were manually scored as belonging to one of three categories: no stalk, partial stalk, and full stalk. Consistent with the results of the class

averages, we saw full stalk density for 79% of all particles in the presence of ATP-vanadate and only for 4% in the apo state (**Fig. 3.5, Fig. S3.15, Table S3.1**). Moreover, almost all particles (90%) in the apo state do not have any visible density of the stalk, whereas the number of particles for the ATP-vanadate state is a little more distributed among all three categories. This agrees well with our two-color fluorescent distance measurements as the distance distribution in the apo state is narrower than in the ATP-vanadate state. The negative stain electron microscopy data also suggest local melting or conformational changes of the stalk in the apo state. This result is consistent with our two-color fluorescent distance measurements, since disorder (apo state) is expected to reduce the stalk length in comparison to the ordered state (ATP-vanadate state). Together, these single-molecule distance measurements and electron microscopy findings suggest that a disorder-to-order transition occurs in the stalk during dynein's mechanochemical cycle.

Discussion

Here, we described single-molecule two-color fluorescent microscopy methods that provide nanometer accuracy distance measurements on the length scale of most macromolecules (2-30 nm). Using Monte Carlo simulations and experiments, we show that our techniques enable distance measurements from ~2 nm to hundreds of nanometers (**Fig. S3.12**) and can operate with heterogeneous samples. Thus, our methods fill a resolution gap from 8 nm (upper distance of smFRET) to 25 nm (lower bound of current single-molecule colocalization methods). Applying our methods to the molecular motor dynein, we found that the dynein stalk likely undergoes large conformational changes in different nucleotide states.

Distance calculations with nanometer accuracy

While smFRET can accurately determine distances in a high-throughput fashion, it is limited to distances that are <8 nm[89,90]. Furthermore, absolute distance measurements are difficult because smFRET is sensitive to fluorophore orientation, which is often assumed to be randomly oriented but non-trivial to measure. There are some existing single-molecule colocalization methods that can be used at the 8-25 nm range but all of these methods face certain limitations. For instance, single-molecule high resolution colocalization (SHREC)[91,94] inaccurately determines distances for cases where distance uncertainty and distance are of similar size. We overcame this limitation by using additional experimental information from the images (Sigma-P2D). A method developed by Pertsinidis et al.[95] also achieves nanometer resolution but is limited to single pixel measurements and requires highly specialized optical setups, whereas our new methods work on the entire field of view of a standard TIRF microscope. Lastly, a method by Mortensen et al.[96] resolves nanometer distances with lower resolution (Vector method) and only measures tens of molecules, whereas our methods can measure up to 10,000 molecules in a single experiment.

In general, we significantly improved and extended existing methods by using additional experimental information (Sigma-P2D) and by improving analysis techniques of multiple observations of the same particle[96] (Vector-P2D). Whether Sigma-P2D or Vector-P2D performs better depends on the experimental conditions, such as distance uniformity of the molecules, whether or not multiple frames can be acquired, and whether distances of an individual single molecule or populations of single molecules are desired. Our Sigma-P2D approach only recovers the distance from a collection of uniform particles and is useful to determine whether or not a sample is uniform in distance (**Fig. S3.16**). The Vector-P2D method can measure the average distance of both samples that are uniform and variable in distance. However, Sigma-P2D works better for samples that are uniform in distance because it can recover distances even for extremely high ratios of distance uncertainty to distance (σ_d / d). In addition, Vector-P2D requires more than one frame per particle to determine the vector average distance while Sigma-P2D also works for single frame data. In **Figure S3.16**, we provide detailed guidelines to help choose between Sigma-P2D and Vector-P2D.

If only a single molecule and not a population is of interest, applicable methods are Sigma-P2D and Vector (Vector and Vector-P2D are equivalent under this condition since only one data point can be fitted with the P2D function after vector averaging). Comparing both using Monte Carlo simulated data, we found that Sigma-P2D performs better than Vector for almost all conditions when distance distributions of single particles are analyzed (**Fig. S3.17**). Thus, for distance analysis of an individual single molecule, Sigma-P2D is the method of choice.

Like other existing colocalization-based two-color distance measurement methods[40,46,95,96], our methods require surface immobilization of the sample and are limited to projections in two-dimensions. Nevertheless, using versatile labeling techniques (such as the DNA-based surface coupling combined with labeling as we used for the dynein experiment), we believe that there are many ways to obtain useful information - difficult or impossible to acquire otherwise - while being aware of this limitation. A high quality autofocus system is essential for

these two-color distance measurements, since the image registration changes with focus. Thus, imaging of fiducial markers for image registration and sample of interest on the same slide (**Fig. S3.1**) is necessary. Restricted dye mobility causes changes in the point spread function leading to systematic localization errors[95,105] and incorrect distance measurements. We observed a "normal" point spread function shape in all our samples, and also used intensity comparisons between linearly and circularly polarized light to ascertain full dye mobility. In summary, our new methods, Sigma-P2D and Vector-P2D, together with the piecewise image registration and the μManager plugin[70] allow distance measurements in less than two hours on a standard TIRF microscope, enabling high-throughput distance measurements with nanometer accuracy.

Stalk of dynein likely undergoes large conformational changes

In order for dynein to step along microtubules, the hydrolysis state of the nucleotide binding AAA ring is coupled to microtubule affinity of the microtubule binding domain through the stalk[40,42–44]. Several studies suggest that local melting of the coiled-coil in different states of the nucleotide hydrolysis cycle plays a major role in this communication[45,46,102], while others have shown that sliding between different registries is essential[40,46]. However, no direct measurements of the distances between the AAA ring and microtubule binding domain have been reported. Using the Vector-P2D method, we measured this distance directly in different nucleotide states and found evidence for a large conformational change in the dynein stalk. These measurements would not have been possible with other methods such as smFRET, since we could not have placed any fluorescent labels in the working range of smFRET (2-8 nm) as the stalk of dynein is 13 nm long. Moreover, the negative stain electron microscopy approach also did not allow direct distance measurements, since one of the conformational states was not visible presumably due to disorder.

Our observations do not rule out registry sliding of the stalk[40,46], however, the changes in distance cannot be explained by simple sliding and small conformational rearrangements alone. Rather, our evidence is consistent with a local “melting” of the stalk[45,46,102]. Based on the distance measured in the apo state, we speculate that some part of the stalk between the microtubule binding domain and the buttress / stalk interaction is involved in these conformational changes. This is in good agreement with the model in which a highly conserved tryptophan in the stalk, located close to the buttress contact, melts coiled-coil 1[66]. Such melting could underlie the reduction in the distance between the ring and microtubule binding domain.

Concluding remarks

In summary, we have developed nanometer-accuracy distance measurements for two different color fluorophores bound to static proteins. In the future, it will be worthwhile to extend our techniques to perform dynamic measurements of individual molecules. If, for instance, one wants to map the stepping of an individual molecular motor onto the lattice of its track, Sigma-P2D will be particularly useful. We are planning to test such methods in the near future.

The theoretical concepts and their application to nanometer distance measurements presented in this work are not limited to two-color fluorescent single-molecule colocalization microscopy but can be applied to all distance measurements where the distance is similar to the imaging error and thus also to other super-resolution imaging techniques[106]. As these methods venture into the regime of nanometer resolution[107], we anticipate that our methodology and open-source software will be useful for a broad range of super-resolution fluorescence microscopy technologies.

Figures and figure legends

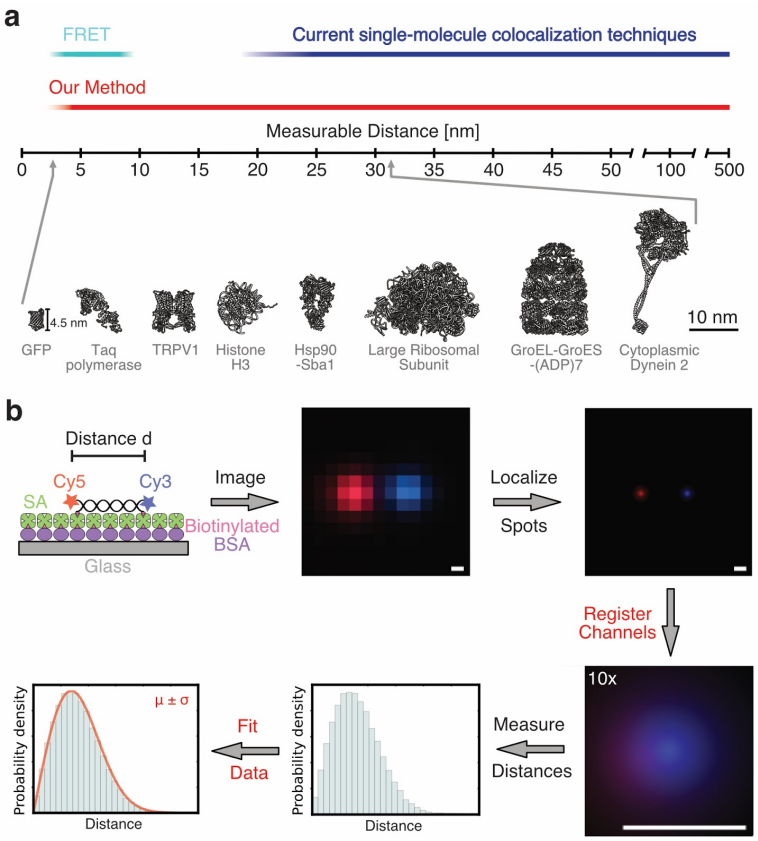

Figure 3.1 | Relevance and workflow of fluorescent single-molecule distance measurements. (a) Comparison of resolution of various methods for fluorescent single-molecule distance measurements (top). Size distribution of protein structures (bottom - PDB codes from left to right: 1gfl[108], 1taq[109], 5irz[110], 1aoi[111], 2cg9[112], 1jj2[113], 1aon[114], 4rh7[29]). (b) Workflow for two-color distance measurements. First, the sample of interest is labeled at specific sites with two fluorescent dyes, immobilized via biotin-streptavidin (SA) onto a glass coverslip and imaged with a TIRF microscope. Then, the exact positions of the fluorophores are determined and the positions of both dyes are registered (aligned) utilizing a registration map that was previously determined. Subsequently, distances of all spot pairs are measured and the average distance between fluorophores is determined using a fit of a probability distribution function to the data.

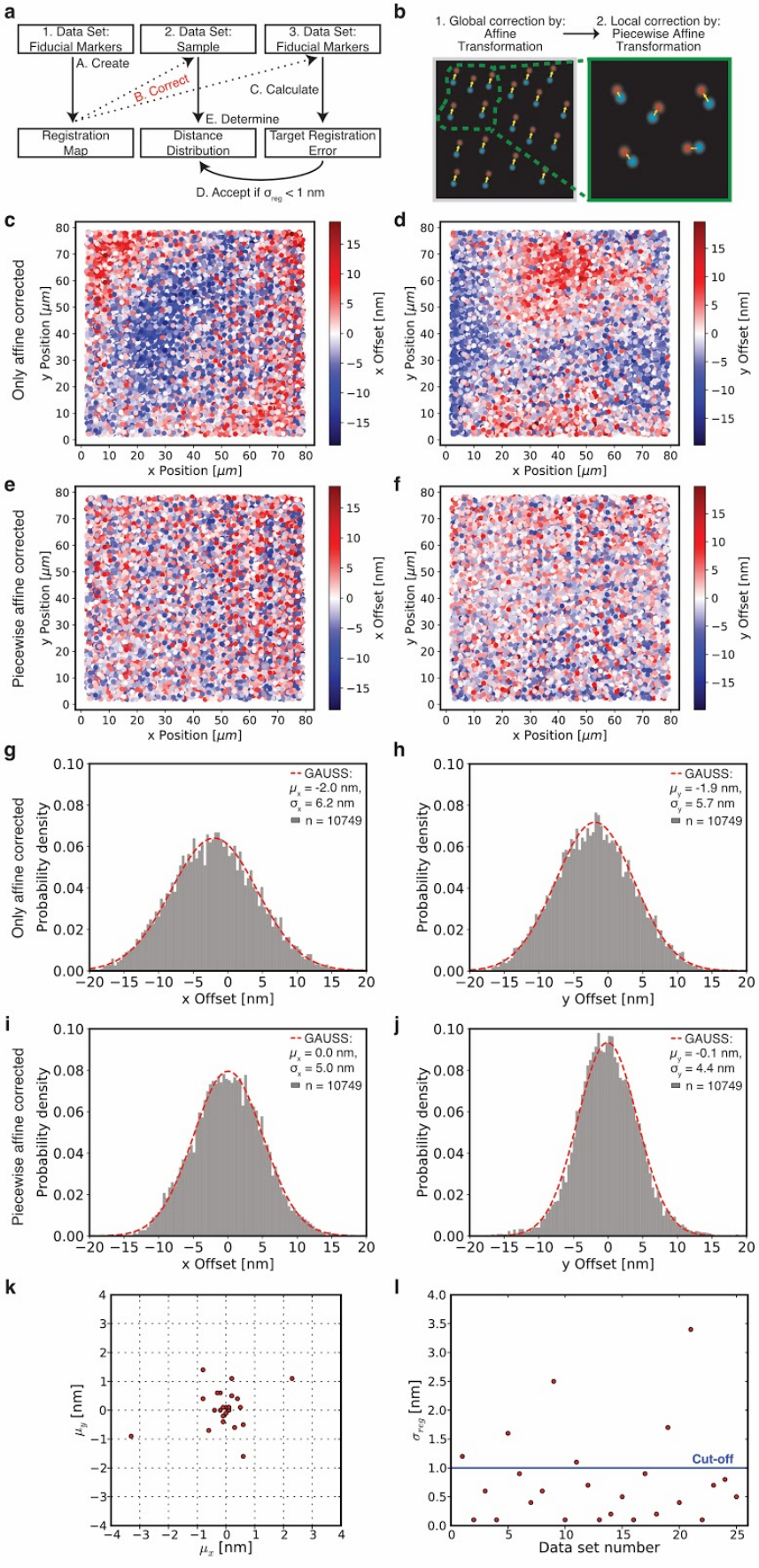
a
1. Data Set: Fiducial Markers
2. Data Set: Sample
3. Data Set: Fiducial Markers
A. Create
B. Correct
C. Calculate
E. Determine
Registration Map
Distance Distribution
Target Registration Error
D. Accept if σreg < 1 nm
b
1. Global correction by: Affine Transformation
2. Local correction by: Piecewise Affine Transformation
c
Only affine corrected
y Position [μm]
x Position [μm]
x Offset [nm]
d
y Position [μm]
x Position [μm]
y Offset [nm]
e
Piecewise affine corrected
y Position [μm]
x Position [μm]
x Offset [nm]
f
y Position [μm]
x Position [μm]
y Offset [nm]
g
Only affine corrected
Probability density
GAUSS:
μx = -2.0 nm,
σx = 6.2 nm
n = 10749
x Offset [nm]
h
Probability density
GAUSS:
μy = -1.9 nm,
σy = 5.7 nm
n = 10749
y Offset [nm]
i
Piecewise affine corrected
Probability density
GAUSS:
μx = 0.0 nm,
σx = 5.0 nm
n = 10749
x Offset [nm]
j
Probability density
GAUSS:
μy = -0.1 nm,
σy = 4.4 nm
n = 10749
y Offset [nm]
k
μy [nm]
μx [nm]
l
σreg [nm]
Cut-off
Data set number

Figure 3.2 | Image registration workflow, accuracy, and reproducibility. (a) Workflow of image acquisition and registration process. (b) Procedure for image registration with affine (global) and piecewise affine (local) correction. Comparing results for the affine correction (c, d, g, and h) and for the affine correction followed by piecewise affine correction (e, f, i, and j) shows that an additional piecewise affine correction reduces local distortions and results in better image registration overall. (c) Target registration error after affine correction along the x-axis. Each dot shows a single fiducial marker for which the distance offset between the two colors of the same fiducial marker is color-coded. Negative values (blue dots) mean that channel 1 has a smaller number for its x position whereas positive values (red dots) represent fiducials where channel 2 has a smaller number for its x position. (d) Same dataset as in c but the offset is along the y-axis. (e) Target registration error after piecewise affine correction along the x-axis for the same beads as in c. (f) Same dataset as in e but the offset is along the y-axis. (g) Histogram of x-axis offset (after affine correction) with Gaussian fit (dashed red line) of data shown in c. (h) Histogram of y-axis offset (after affine correction) with Gaussian fit (dashed red line) of data shown in d. (i) Histogram of x-axis offset (after piecewise affine correction) with Gaussian fit (dashed red line) of data shown in e. (j) Histogram of y-axis offset (after piecewise affine correction) with Gaussian fit (dashed red line) of data shown in f. (g-j) Comparison of the width and the mean of the offset distributions along the x- and y-axis for affine and piecewise affine corrected data shows that the additional piecewise correction reduces the width and more importantly results in a mean close to 0.0 nm and thus a very accurate registration. (k) X-axis μ_x and y-axis μ_y component of registration error for 25 independent image registrations. (l) Same data as in i, but registration accuracy σ_{reg} (TRE) is shown for each of the 25 datasets. We accepted datasets for distance determination if $\sigma_{reg} < 1$nm (blue line cutoff). One frame per TetraSpeck™ bead was acquired. Details of fitting parameters are provided in **Table S3.4**.

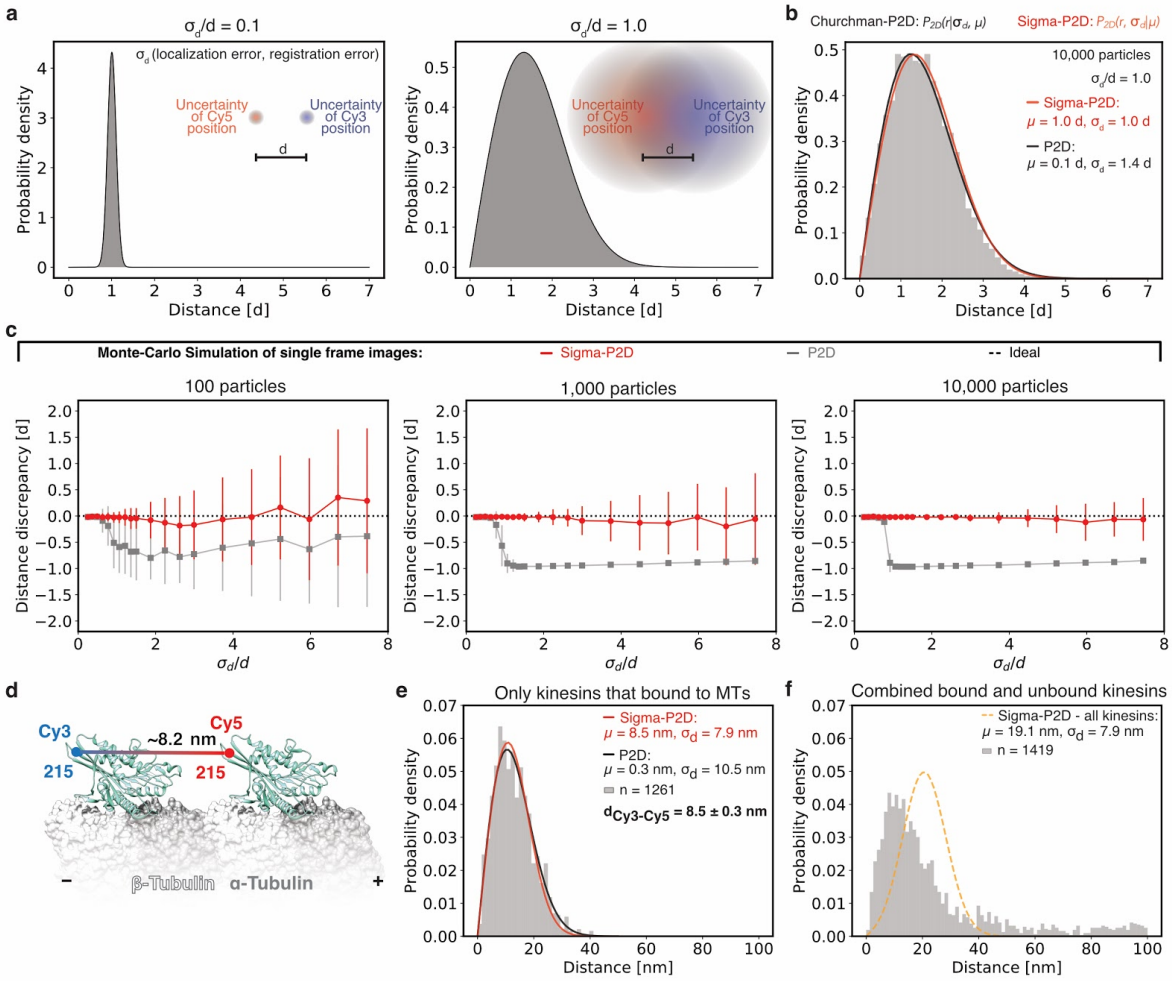

Figure 3.3 | Sigma-P2D - measuring distances of uniform samples with nanometer accuracy. (a) Probability distributions of measured distances between two differently colored fluorophores separated by a true distance d for different ratios of uncertainty σ_d over distance d. For example, a distance uncertainty of 1 nm and a true distance of 10 nm would generate data as shown on the left while a distance uncertainty of 10 nm and a true distance of 10 nm would generate data as shown on the right. (b) Histogram of Monte Carlo simulated data with a true distance d of 1 and distance uncertainty σ_d of 1 fitted with Sigma-P2D (red) and P2D (black). (c) Performance of distance prediction by Sigma-P2D (red) and P2D (grey) evaluated using the distance discrepancy (calculated by subtracting the expected distance from the measured distance and normalizing with the expected distance) of Monte Carlo simulated data. Here, the average distance discrepancy from the true distance was calculated using 100 simulations for different ratios of uncertainty σ_d over distance d for 100, 1,000, and 10,000 particles. Error bars show the standard deviation of 100 independent simulations. Distance discrepancies around -1.0 represent cases where the measured distance was 0 nm and the small error bars show that this was very reproducible. This is an example of a precise yet highly inaccurate measurement. Large error bars typically indicate bimodal cases for which we measured both distances that are much larger and distances that are much smaller than the expected distance. (d) Diagram of two-head-bound kinesin on a microtubule based on crystal structure (PDB: 4LNU)[115] created with UCSF Chimera[71]. The positions of Cy3 and Cy5 dye are shown as blue and red dots, respectively. (e) Histogram of head-to-head distance measurements of rigor-bound kinesin fitted

with Sigma-P2D (red) and P2D (black). The standard deviation of the head-to-head distance with Sigma-P2D fit (bold font - $d_{Cy3\text{-}Cy5}$) was calculated by evaluating the Fisher Information matrix. (f) Histogram of head-to-head distance measurements of all kinesins (microtubule bound and unbound) fitted with Sigma-P2D (orange dashed line). Details about the fitting parameters are listed in **Table S3.4**.

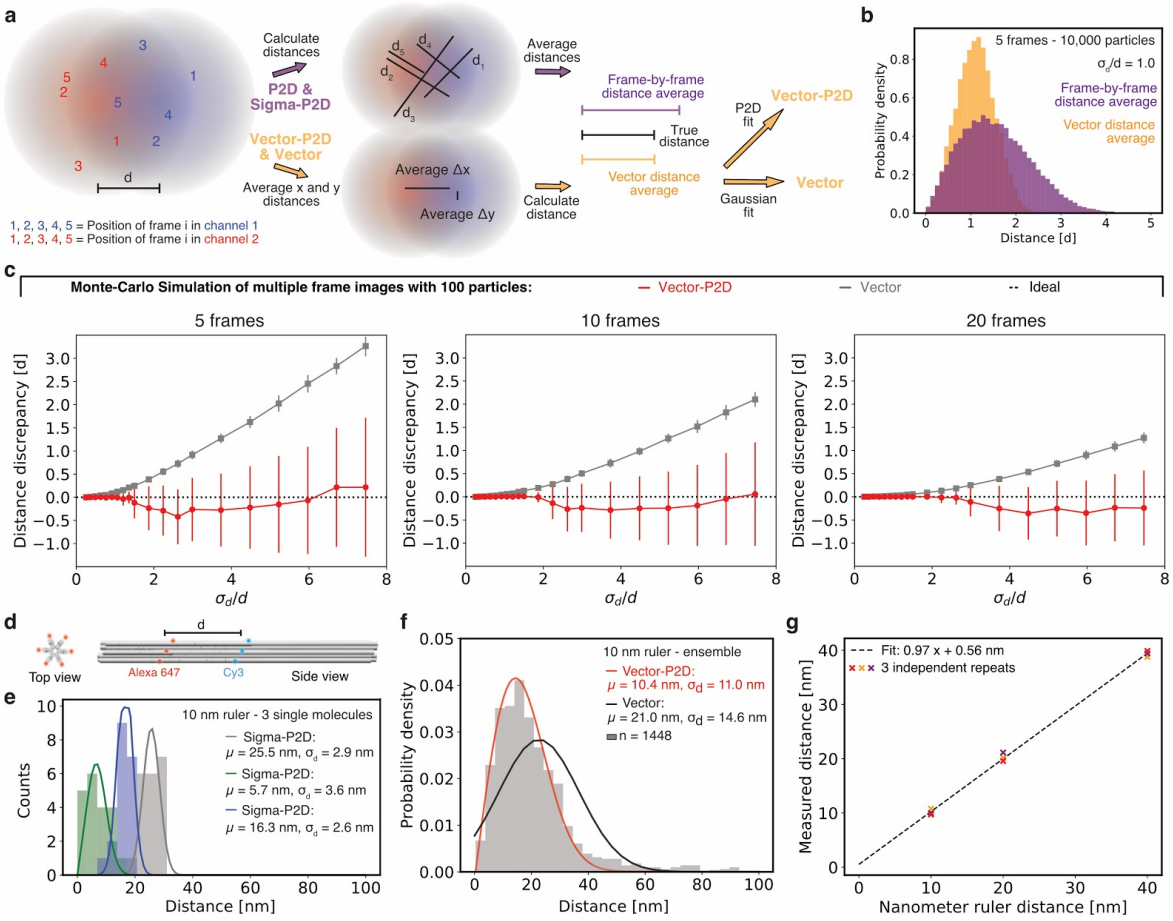

Figure 3.4 | Vector-P2D - measuring distances of variable samples with nanometer accuracy. (a) Determining vector averaged distances from data with multiple observations per particle. Intensity distributions for two fluorescent molecules in a red and a blue channel at a true distance d of 1. Five independent observations of both molecules were obtained by Monte Carlo simulations (red and blue colored numbers 1 to 5). Now either the individual distances of spot pairs can be calculated first and then averaged (frame-by-frame distance average) or average distances along the x-axis and y-axis can be determined first and then used to calculate the absolute distance (vector averaged distances). The vector averaged distance distribution can then be fit with a Gaussian distribution or the two dimensional probability distribution "P2D" as shown in equation 2, which use the calculated distance μ and the distance uncertainty σ_d as parameters, to yield Vector or Vector-P2D, respectively. (b) Histograms for distances generated by means of Monte Carlo simulation with 5 frames (observations) per particle. Purple histogram shows the distance distribution for a frame-by-frame distance average and orange histogram shows distribution for vector averaged distances. (c) Performance of distance prediction by Vector-P2D (red) and Vector (grey) evaluated using the distance discrepancy (calculated by subtracting the expected distance from the measured distance and normalizing with the expected distance) of Monte Carlo simulated data. Here, the average discrepancy from the true distance was calculated using 100 simulations for different ratios of uncertainty σ_d over distance d for 5, 10, and 20 frames. Error bars show standard deviations of 100 independent simulations. Large error bars typically indicate bimodal cases for which we measured both distances that are similar to the expected distance and distances that are much smaller than the expected distance. Hence, the increasing size of error bars with increasing σ_d/d ratios shows that the

fitting outcome is becoming more bimodal until it collapses to one side (measuring distances of around 0 nm). Additional data in **Fig. S3.12**. (d) Design of DNA-origami based nanorulers for which the 'center-of-mass' between 6-10 dyes for each of the two colors determines the distance. (e) Histogram of distance distribution of three different single molecules of the 10 nm DNA-origami nanoruler (green, blue, and gray). Solid line is a Sigma-P2D fit. (f) Histogram of vector averaged distance measurements of multiple 10 nm DNA-origami nanorulers analyzed with Vector-P2D (red) and Vector (black). (g) Correlation between measured and expected average distance for 10, 20, and 40 nm ruler from three technical repeats. Example fits for 20 and 40 nm rulers are shown in **Fig. S3.14**. Fitting parameter details are given in **Table S3.4**.

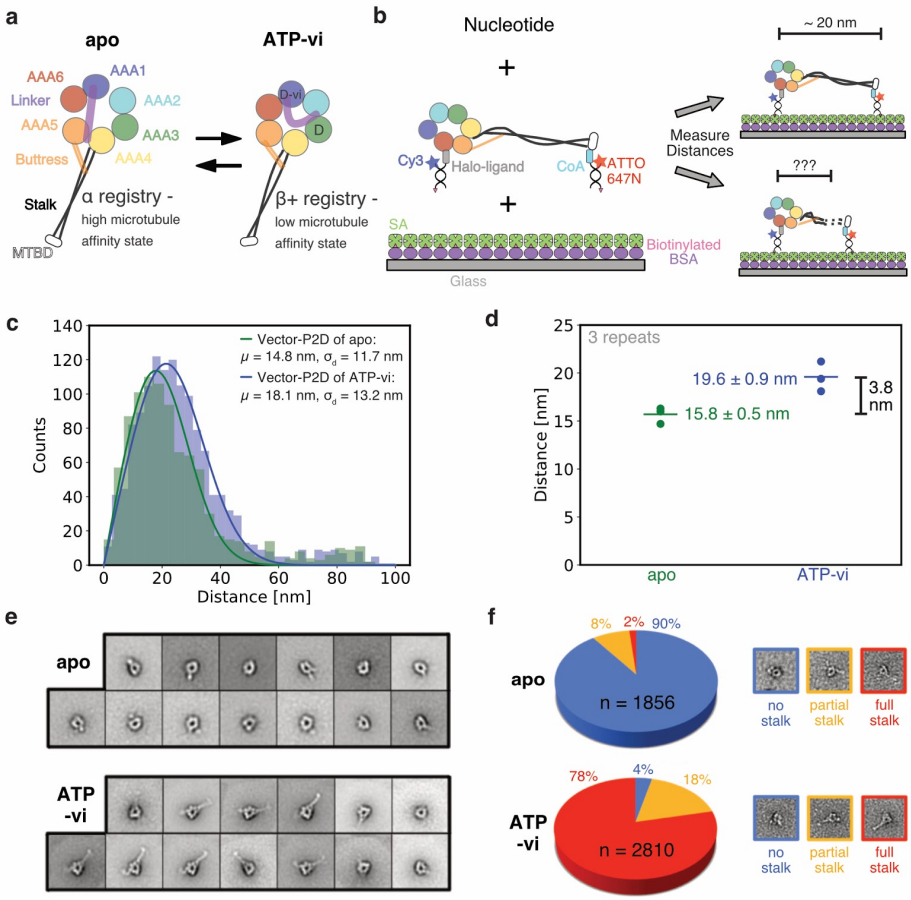

Figure 3.5 | Dynein stalk conformation in two different nucleotide-bound states measured by Vector-P2D and negative stain electron microscopy. (a) Schematic of the monomeric dynein motor domain without nucleotide (apo / left) and bound to ATP-vanadate (ATP-vi / right) resulting in a high and low microtubule affinity state, respectively. Transition between both microtubule affinity states happens twice during the hydrolysis cycle: first detachment from microtubule by ATP binding and transition to a low affinity state and then rebinding to microtubule after ATP hydrolysis and change to a high affinity state. MTBD is the microtubule binding domain. D indicates ADP in the AAA binding pocket whereas D-vi indicates ADP-vanadate. (b) Design for two-color fluorescent distance measurement between AAA ring and microtubule binding domain of a dynein monomer. Fluorescent dye, Halo-tag[103] or YBBR-tag[104] ligands and biotin for surface immobilization are attached to a double stranded DNA oligomer of 16 bp where Cy3 labels the Halo-tag on the C-terminus of the AAA ring and ATTO647N is attached to the YBBR tagged microtubule binding domain via the small molecule CoA. The biotin of the double stranded DNA binds to streptavidin (SA) which is bound to biotinylated BSA (bovine serum albumin). If the stalk is fully extended we expect a distance of about 20 nm[29] between the two colors. (c) Histogram of vector averaged distance measurements of dynein monomer as shown in b with apo in green and ATP-vi in blue fitted with Vector-P2D. Only molecules that had both a Cy3 and ATTO647N label were selected for analysis to ensure measurement of the distance between ring and microtubule binding domain. (d) Results of distance measurements of three technical repeats of dynein monomer as shown in b with apo in green and ATP-vi in blue. Fitting was done as shown in c. (e) Negative stain electron microscopy class averages of a dynein monomer in the apo (top) and ATP-vanadate (bottom) state. (f) Count and classification of individual particles from negative stain electron

microscopy micrographs (as shown in **Fig. S3.15, Table S3.1**) into three categories (no, partial, and full stalk) for the apo state and the ATP-vi state. Single-molecule distances in c and d were obtained by selecting time-lapse series of individual molecules (see Table S6). Error in d is the standard error of the mean of 3 technical repeats. Details about the fitting parameters are provided in **Table S3.4**.

Supplemental figures and tables with legends

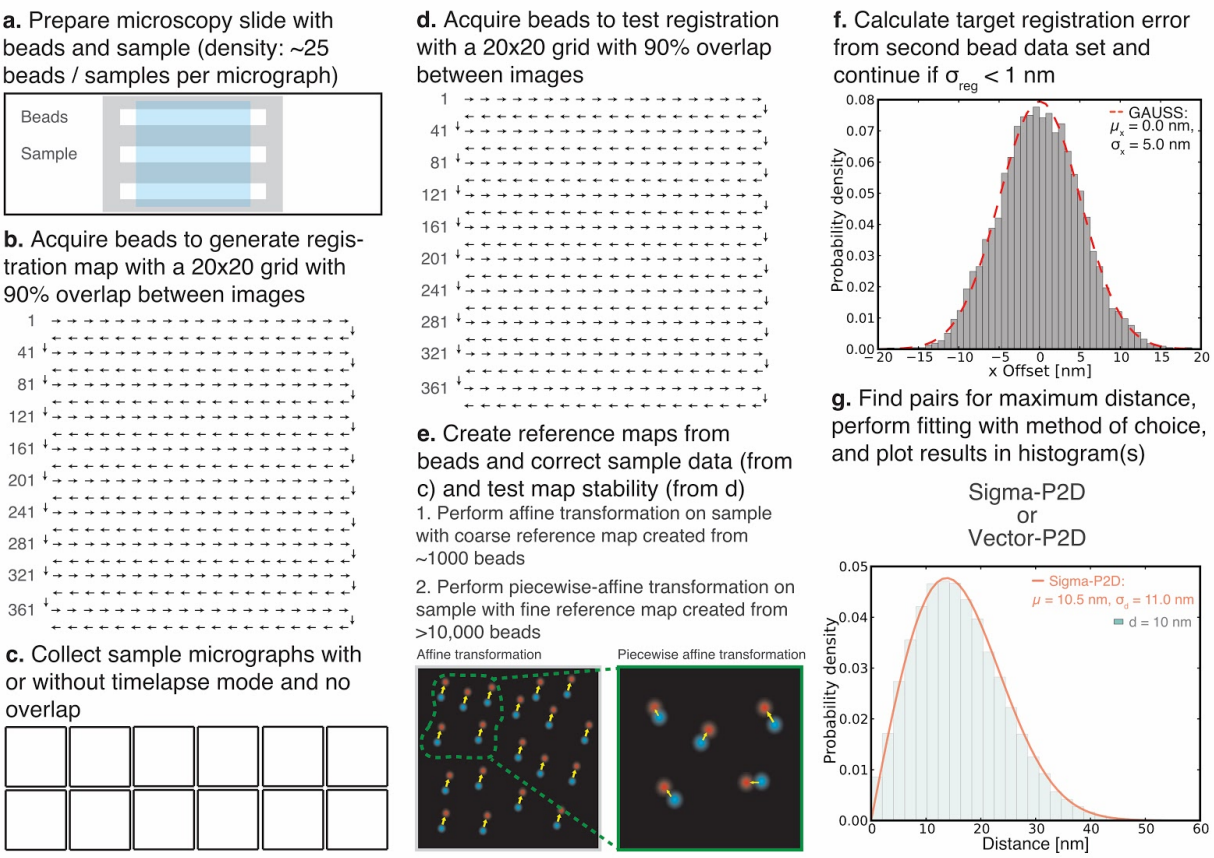

Figure S3.1 | Workflow for image registration and distance measurements. (a) Set-up of microscope slide with fiducial markers in one and sample of interest in the other chamber. (b) Image acquisition pattern for fiducial markers to create registration maps. (c) Image acquisition pattern for sample of interest. (d) Same as in b but this time to test the registration map after sample data collection. (e) μManager[70] analysis procedure to create affine and piecewise affine registration maps. (f) Calculation of image registration accuracy. (g) μManager[70] analysis procedure to determine distance distribution with Sigma-P2D (sample uniform in distance) or Vector-2D (sample heterogeneous / variable in distance).

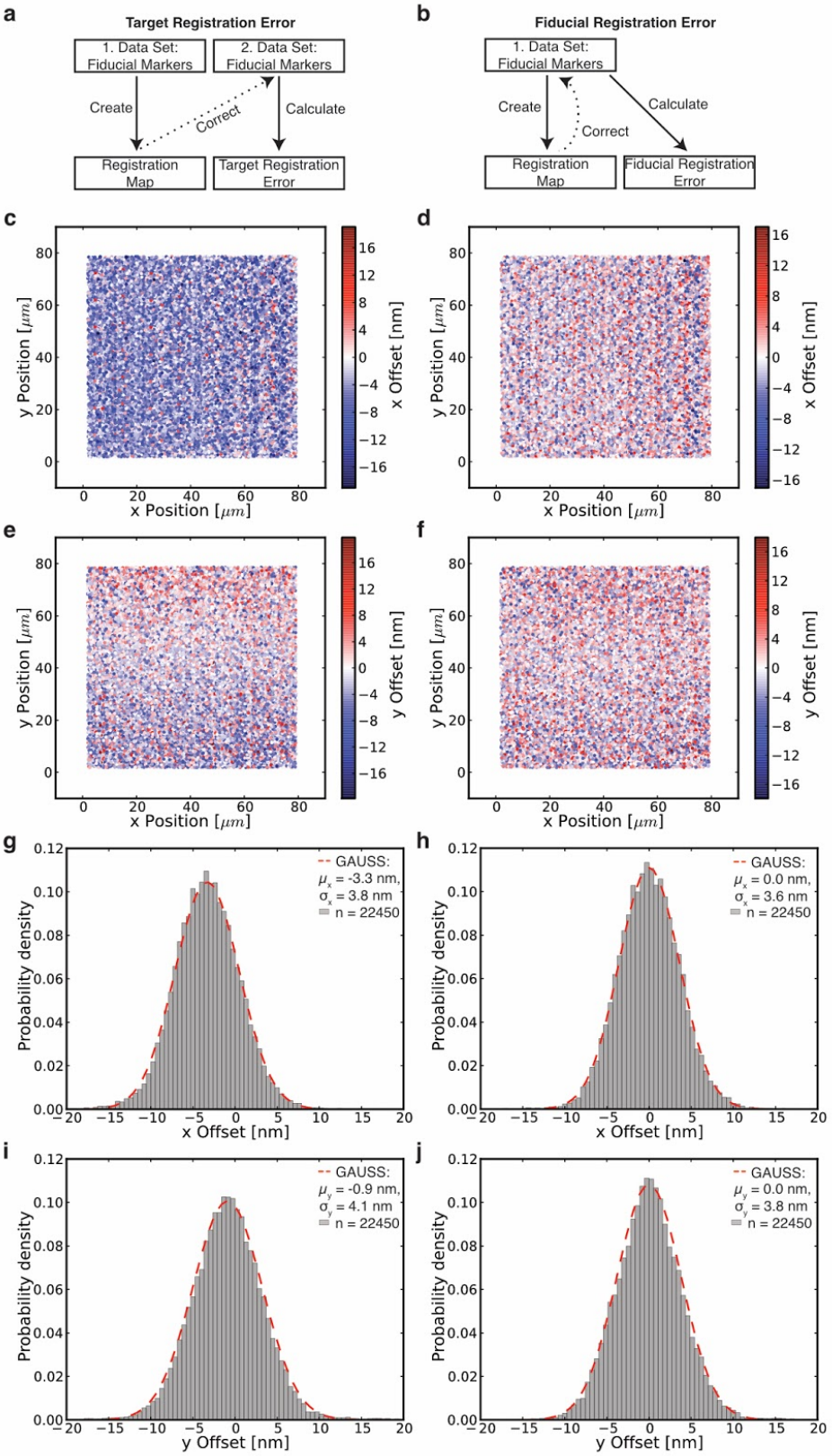
a
Target Registration Error
1. Data Set: Fiducial Markers
2. Data Set: Fiducial Markers
Create
Correct
Calculate
Registration Map
Target Registration Error
b
Fiducial Registration Error
1. Data Set: Fiducial Markers
Create
Correct
Calculate
Registration Map
Fiducial Registration Error
c
d
e
f
y Position [μm]
x Position [μm]
x Offset [nm]
y Offset [nm]
g
h
i
j
Probability density
x Offset [nm]
y Offset [nm]
GAUSS:
μ_x = -3.3 nm,
σ_x = 3.8 nm
n = 22450
μ_x = 0.0 nm,
σ_x = 3.6 nm
n = 22450
μ_y = -0.9 nm,
σ_y = 4.1 nm
n = 22450
μ_y = 0.0 nm,
σ_y = 3.8 nm
n = 22450

Figure S3.2 | Comparison of target registration error (TRE) and fiducial registration error (FRE) shows that FRE is unreliable and that TRE should always be reported as registration error. The target registration error (TRE) reports the distance (ideally 0) for fiducials other than the points used to create the registration map[116] and is more critical than the fiducial registration error (FRE) which uses the same fiducials to create and test the map. The TRE reports inaccurate image registrations while FRE does not always do so (as shown in this figure). Failure of image registration (as detected by the TRE calculation) is usually caused by a slight change in focus between or during the acquisition of the first and second fiducial marker dataset. Thus, TRE should always be used to evaluate the performance of an image registration process. (a) Workflow for target registration error (TRE) calculation. (b) Workflow for fiducial registration error (FRE) calculation. (c-j) The same registration map is used for both, TRE and FRE, but different datasets are used to test the map. For TRE we use an additional fiducial marker dataset to evaluate the map while for FRE we use the same dataset (fiducial markers) to create and test the registration map. (c) Distance offset along the x-axis for TRE. Each dot shows a single fiducial marker for which the distance offset between the two colors of the same fiducial marker is color-coded. Negative values (blue dots) mean that channel 1 has a smaller number for its position whereas positive values (red dots) represent fiducials where channel 2 has a smaller number for its position. (d) Same as in c but for FRE. (e) Distance offset between the two colors of the same fiducial marker along the y-axis for TRE. (f) Same as in e but for FRE. (g) Histogram of x-axis offsets with Gaussian fit (dashed red line) for TRE. (h) Same as in g but for FRE. (i) Histogram of y-axis offset with Gaussian fit (dashed red line) for TRE. (j) Same as in i but for FRE. One frame per TetraSpeck™ bead was acquired. Details about the fitting parameters are in **Table S3.4**.

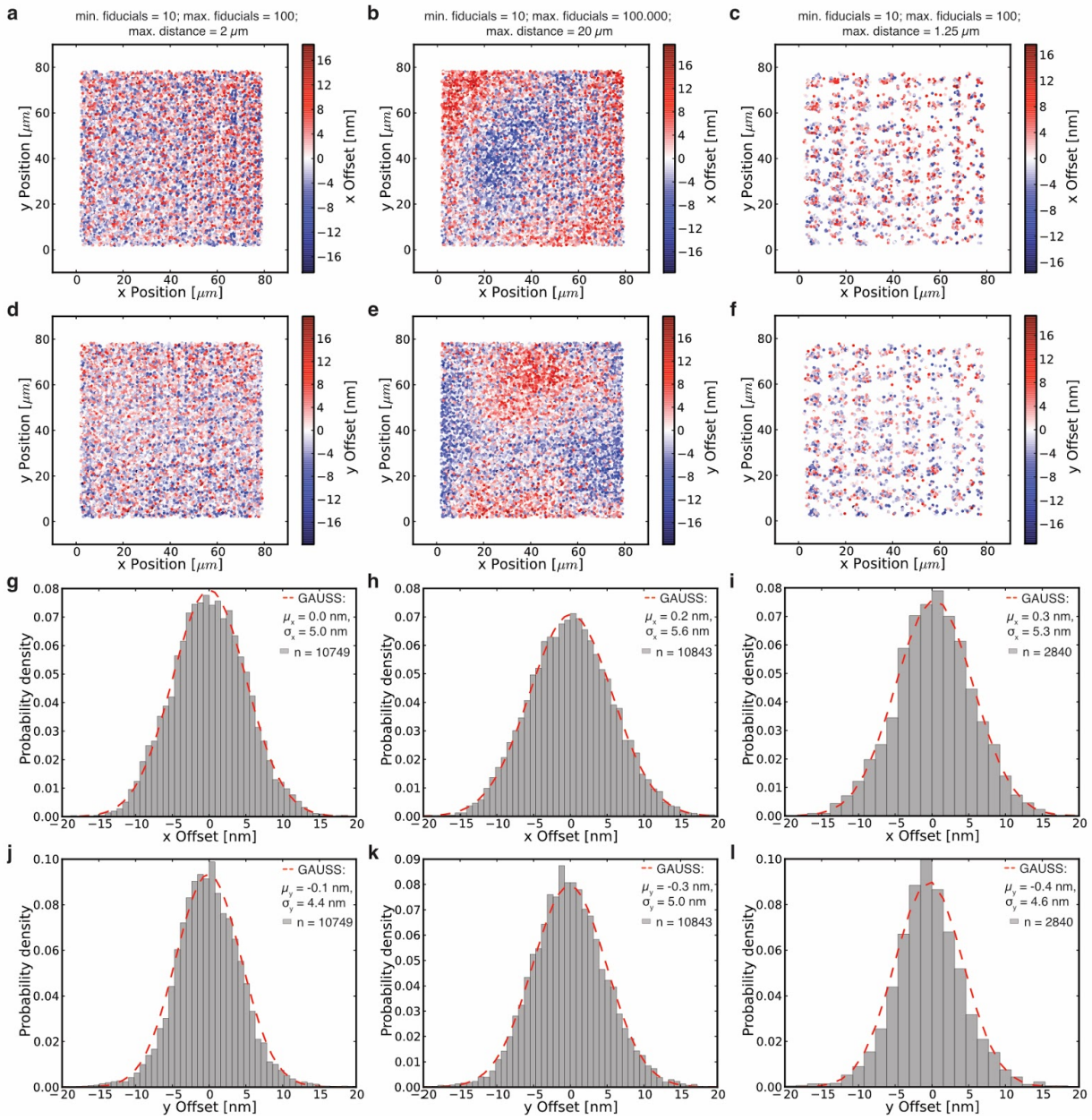

Figure S3.3 | Comparison of different parameters for piecewise affine image registration. TetraSpeck™ beads were imaged, localized and registered using a previously determined registration map with different parameter settings for the piecewise affine transformation. Since piecewise affine alignment is based on a nearest neighbor search[97], three parameters can influence registration outcome: minimum and maximum number of fiducial points and the maximum distance to the control point. Higher maximum distance and higher maximum number of points cause distortions indicating that the registration was not executed properly because local effects are not being corrected (as shown in this figure - panels in the middle column). Thus, setting a maximum distance is important to ensure correction of local distortions. On the other hand, when the maximum distance is too small, an area in the micrograph may not contain the minimum number of fiducials, and thus will not be corrected (as shown in this figure - panels in the right column). This could be overcome by acquiring more fiducials but that is not necessary as we show in this figure and **Fig. S3.4**.

The first parameter setting has a minimum of 10, a maximum of 100 fiducial points and a maximum distance of 2 μm. The second parameter setting has a minimum of 10, maximum of 100,000 fiducial points and maximum distance of 20 μm. The third parameter setting uses a minimum of 10, maximum of 100 fiducial points and maximum distance of 1.25 μm. The data presented in this figure clearly shows that there are significant differences between settings for the piecewise affine correction and that a more detailed analysis is needed (see **Fig. S3.4**). (a) Distance offset along the x-axis for the first setting. Each dot shows a single fiducial marker for which the distance offset between the two colors of the same fiducial marker is color-coded. Negative values (blue dots) mean that channel 1 has a smaller number for its x position whereas positive values (red dots) represent fiducials where channel 2 has a smaller number for its x position. (b) Same as in a but for the second setting. (c) Same as in a but for the third setting. Registration of many beads fails (hence the sparse number of points) because often less than 10 fiducial points are present within 1.25 μm. (d) Distance offset along the y-axis for first setting. Negative values (blue dots) mean that channel 1 has a smaller number for its y position whereas positive values (red dots) represent fiducials where channel 2 has a smaller number for its y position. (e) Same as in d but for the second setting. (f) Same as in d but for the third setting. (g) Histogram of x-axis offset with Gaussian fit (dashed red line) of data in a. (h) Same as in g but for the second setting and of data in b. (i) Same as in g but for third setting and of data in c. (j) Histogram of y-axis offset with Gaussian fit (dashed red line) of data in d. (k) Same as in j but for second setting and of data in e. (l) Same as in j but for third setting and of data in f. Details about fitting parameters are in **Table S3.4**.

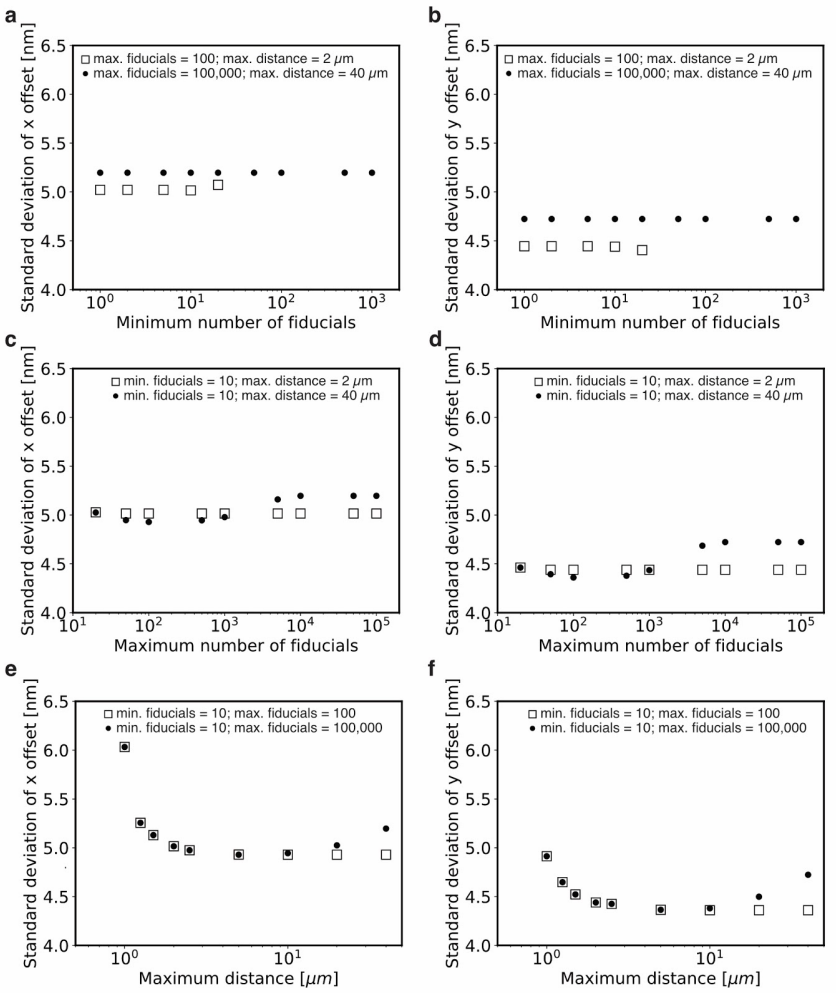

Figure S3.4 | Optimization of parameters for piecewise affine image registration. As shown in **Fig. S3.3**, different parameter settings for the piecewise affine transformation have a significant effect on the goodness of the registration. Thus, we performed an in-depth analysis of the influence of the following parameter on image registration: minimum and maximum number of fiducial points and maximum distance between points (for a more detailed description of what these parameters mean in the context of image registration see **Fig. S3.3**). We are using the standard deviation of registration errors as a measure of goodness of registration over the entire field of view. Hence, the lower the standard deviation of the offset, the better the parameter setting for image registration. (a) Standard deviation of average offset along x-axis as a function of minimum number of fiducials. Results are shown for two different settings of maximum number of fiducials and maximum distance (filled circle and empty square). (b) Same as in a but along y-axis. (c) Standard deviation from average offset along x-axis as a function of maximum number of fiducials. Results are shown for two different settings of minimum number of fiducials and maximum distance (filled circle and empty square). (d) Same as in c but along the y-axis. (e) Standard deviation from average offset along x-axis as a function of maximum distance. Results are shown for two different settings of minimum and maximum number of fiducials (filled circle and empty square). (f) Same as in e but along the y-axis. Details about fitting parameters are in **Table S3.4**. Overall, the optimal parameter settings for piecewise affine maps are a minimum of 10 and a maximum of 100 fiducial points at a maximum distance of 2 µm.

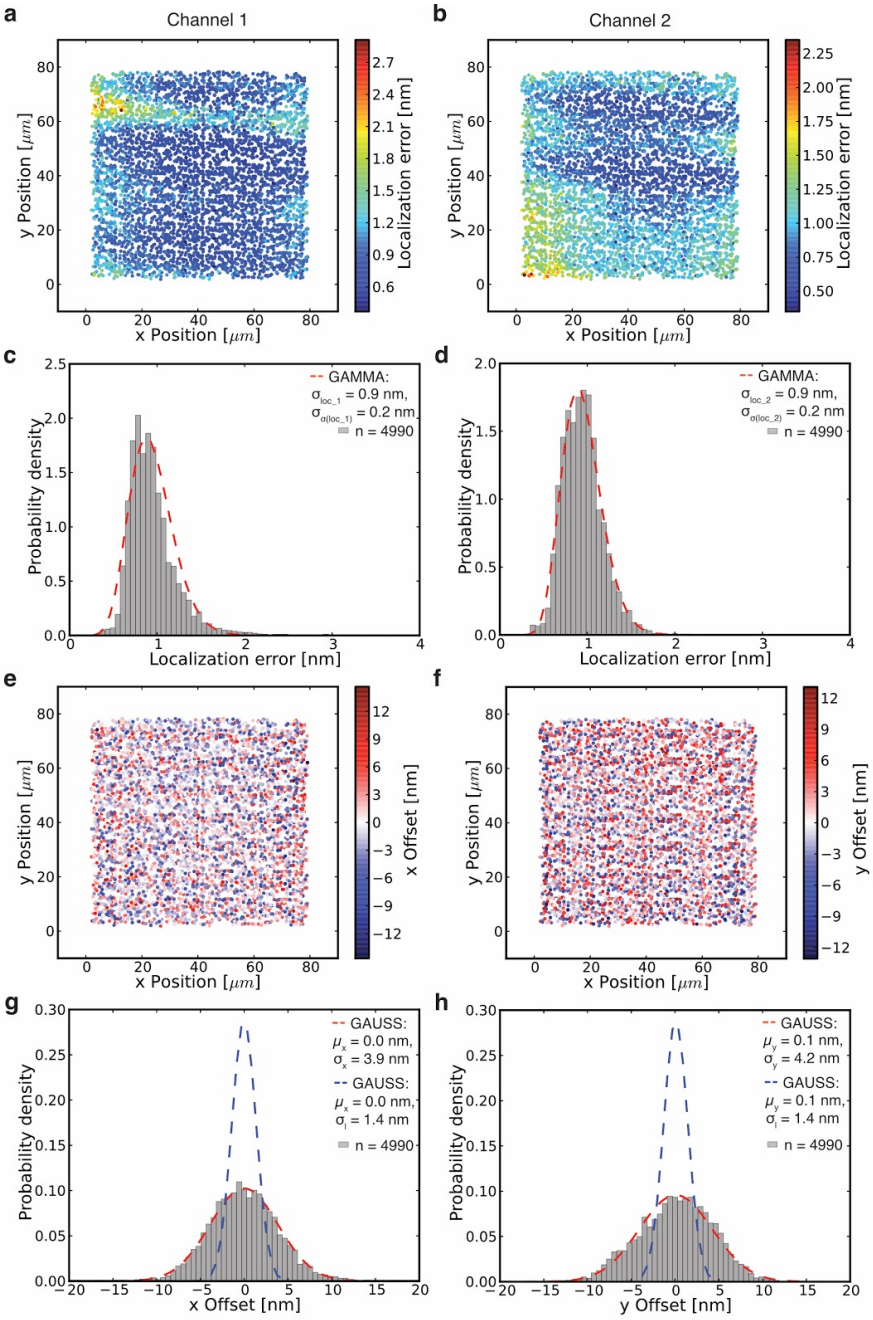

Figure S3.5 | Registration precision of TetraSpeck™ beads can not solely be explained by localization errors. If the localization error is the only contributor to the registration imprecision, the uncertainty of localization and registration should be the same. As we see with data, this is not the case for TetraSpeck™ beads because they have non-overlapping color centers (**Fig. S3.6**). (a) Localization errors in channel 1 of individual TetraSpeck™ beads (each dot represents a single bead) over the entire field of view calculated with the maximum likelihood with Gaussian (MLEwG) equation from Mortensen et al.[77]. Red dots indicate large and blue dots small localization errors. (b) Same as in a but for channel 2. (c) Histogram of localization errors in channel 1 with fit of gamma distribution (dashed red line) of data shown in a. This clearly shows that the localization errors are different among different beads and that they follow a

probability distribution (**Fig. S3.9**). (d) Same as in c but for channel 2 and of data in b. (e) Distance offset along the x-axis for the same data as shown in a. Negative values (blue dots) mean that channel 1 has a smaller number for its x position whereas positive values (red dots) represent fiducials where channel 2 has a smaller number for its x position. (f) Same as in e but for distance offset along the y-axis. (g) Histogram of x-axis offset with Gaussian fit (dashed red line) of data in e. Blue dashed line shows fit if σ_x was only comprised of the localization error σ_l. (h) Same as in g but for offset along y-axis and of data in f. One frame per TetraSpeck™ bead was acquired. Details about fitting parameters are in **Table S3.4**.

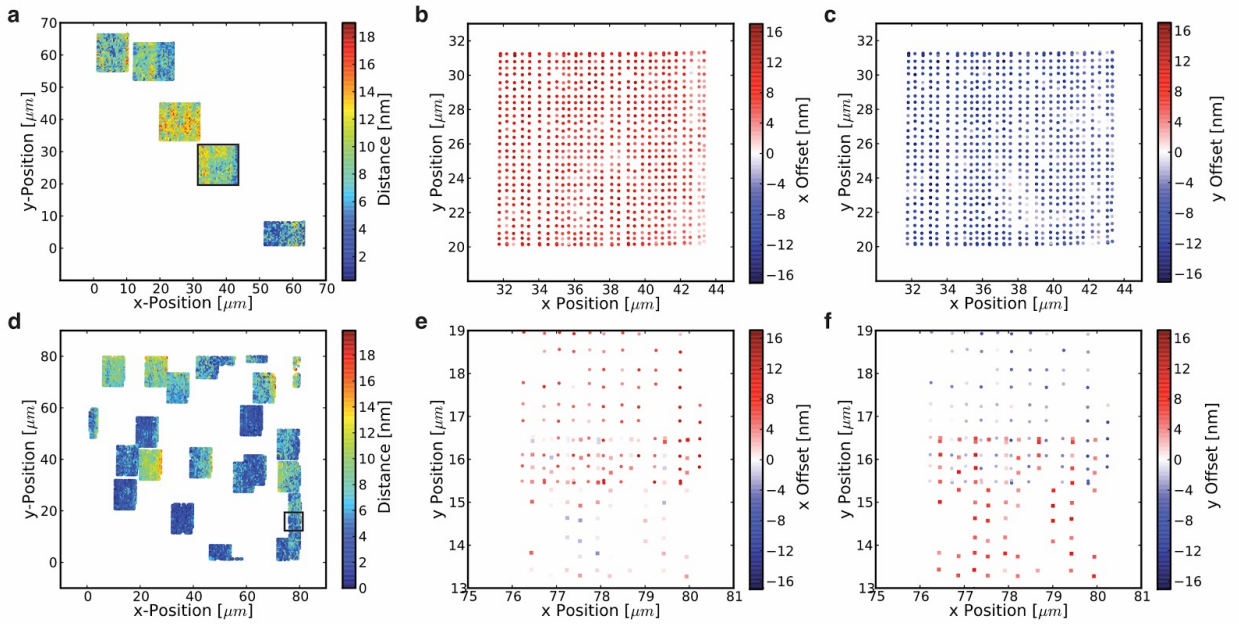

Figure S3.6 | Color centers of TetraSpeck™ beads do not overlap perfectly. To investigate whether the distance discrepancies we found with TetraSpeck™ beads (**Fig. S3.5**) were due to problems with our registration procedure, or an intrinsic property of the beads, we acquired a registration map, and used it to register many images of the same set of beads, slightly displaced from each other. Two different datasets of fiducial markers (a-c and d-f) show that the distance of individual beads is very stable over time and position (a-c), but that the color centers of these fiducial markers do not overlap (i.e. the distance between the red and far-red channel is not zero nanometer (d-f)). (a) Euclidean distance of image registered, 30x30 grid translated, TetraSpeck™ beads. Each grid shows data for one and the same bead. Distances are color-coded as indicated (blue represents short distances, red large distances). Black box highlights the area shown at higher magnification in b and c. (b) Distance offset along the x-axis of the magnified part of the micrograph in a. (c) Same as in b but distance offset along the y-axis. (d) Euclidean distance of image registered, 20x30 grid translated TetraSpeck™ beads. Each grid shows data for one and the same bead. Red dots indicate large and blue dots short distances. Black box highlights the area shown at higher magnification in e and f. (e) Distance offset along the x-axis of the magnified part of the micrograph in d. Here grids of two beads that have overlapping positions are shown where the positions of one bead are shown as circles and the positions of the other bead are shown as squares. (f) Same as in e but distance offset along the y-axis. Details about fitting parameters are in **Table S3.4**.

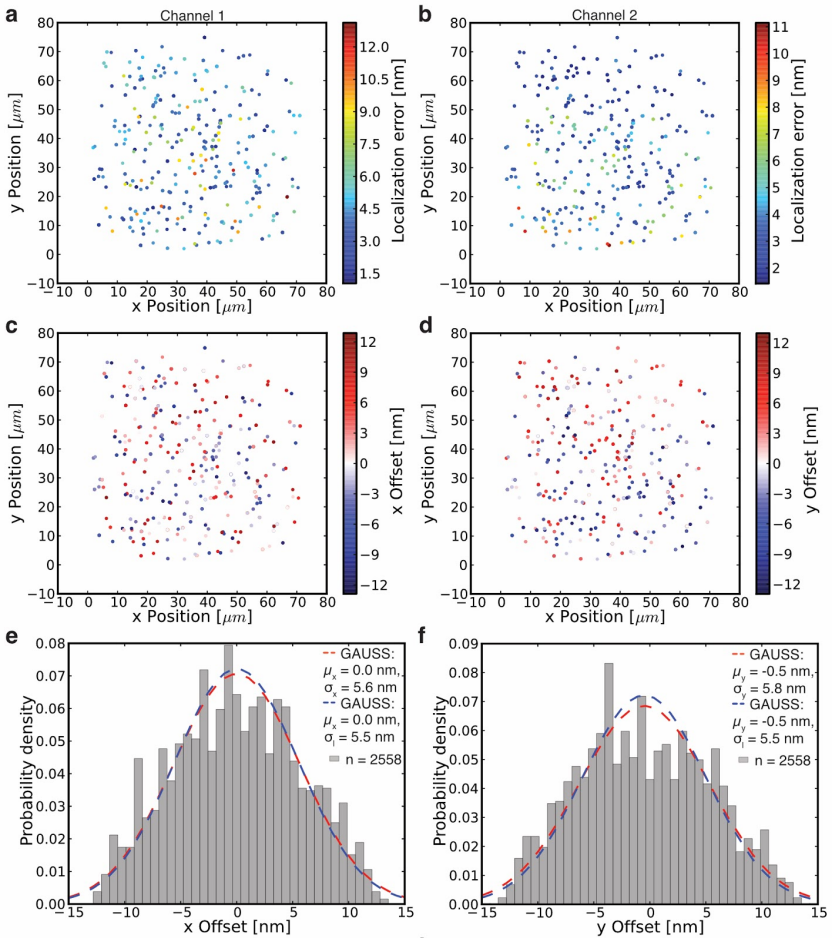

Figure S3.7 | Errors in distance measurements are caused by localization errors for a single biotinylated Cy3/Cy5 double stranded DNA (dsDNA) construct. Since the registration imprecision for TetraSpeck™ beads could not fully be explained by localization errors (**Fig. S3.6**) but the wider distribution was caused by sample imperfections (non-overlapping color centers), we used a control with perfectly overlapping color centers[95]. A 30 bp long dsDNA construct was biotinylated and Cy3 labeled on one end, and Cy5 labeled on the other end[95]. While attached to the surface at one end through biotin, the other end is free to rotate. Since the tumbling time is much faster than the acquisition time, we expect an average distance between the color centers of zero nanometers. If the localization error is the only contributor to the registration imprecision, the uncertainty of localization and registration should be the same. As we see in these data, this is indeed the case for this Cy3/Cy5 dsDNA construct. (a) Localization errors in channel 1 of Cy3/Cy5 dsDNA construct over the entire field of view calculated with MLEwG equation from Mortensen et al.[77]. Red dots indicate large and blue dots small localization errors. (b) Same as in a but for channel 2. (c) Distance offset along the x-axis for the same data as shown in a. Negative values (blue dots) mean that channel 1 has a smaller number for its x position whereas positive values (red dots) represent fiducials where channel 2 has a smaller number for its x position. (d) Same as in c but for distance offset along the y-axis. (e) Histogram of x-axis offset with Gaussian fit (dashed red line) of data in c. Blue dashed line shows fit if σ_x was only comprised of the localization error σ_l. (f) Same as in e but for offset along y-axis and of data in d. 20 frames of each molecule were collected. Single-molecule distances were obtained by selecting time-lapse series of individual molecules (see **Table S3.6**). Details about fitting parameters are in **Table S3.4**.

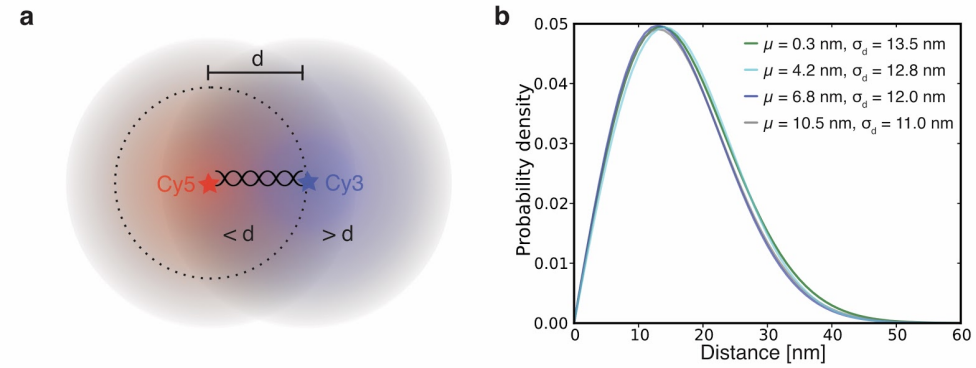

Figure S3.8 | Determination of nanometer distances from skewed distributions. (a) This is a graphical explanation of why the distance distribution on the nanometer scale appears non-Gaussian: Top view of two fluorescence intensity distributions that are separated by distance d. Circle with a dotted line has a radius d around the position of the Cy5 molecule. Assuming the true position of Cy5 is known, each measurement that finds Cy3 inside the circle will be less than d and measurements finding Cy3 outside the circle are larger than d. Integrating the intensities of the blue molecule inside and outside the circle shows that the total intensity outside the circle is higher than inside. Consequently, the probability for measuring distances larger than d is higher than measuring distances lower than d. Halos represent position / distance uncertainty. (b) Probability distribution (Eq. 2) plotted for various parameter combinations of calculated distance μ and distance uncertainty σ_d shows that small variations in σ_d lead to large changes in estimation of μ.

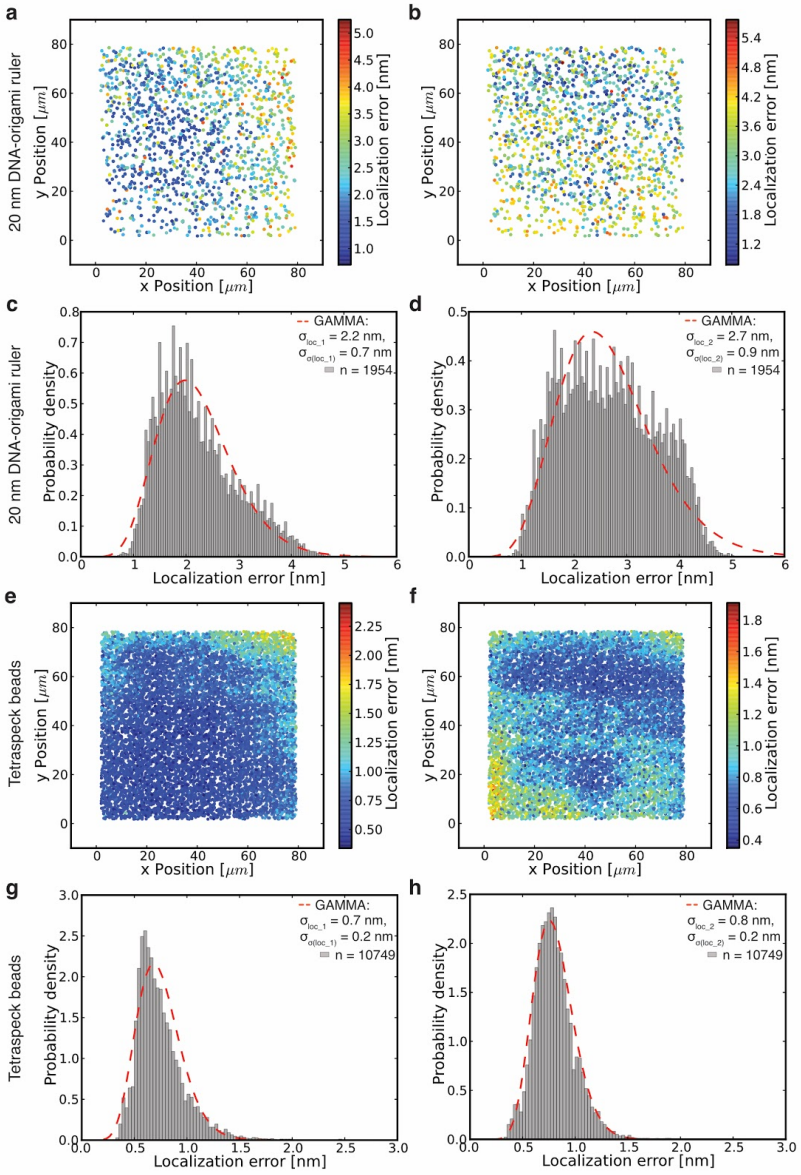

Figure S3.9 | Localization errors of many particles have an underlying distribution. Here, we show localization errors over the entire field of view for two different probes in two channels. Quantification of 20 nm DNA-origami nanorulers with 5-10 dyes of Cy3 and 5-10 dyes of Alexa 647 whose center of mass is 20 nm apart (a-d), and of TetraSpeck™ beads (e-h). The variation in localization error among different particles is likely caused by the emission of different number of photons, which itself follows a distribution. (a) Localization errors calculated with MLEwG equation from Mortensen et al.[77] in channel 1 (Cy3 or Cy3 like dye(s)) for 20 nm DNA-origami nanoruler. Red dots indicate large and blue dots small localization errors. (b) Same as in a but for channel 2 (Cy5 or Cy5 like dye(s)). (c) Histogram of localization error in channel 1 for 20 nm DNA-origami nanoruler with fit of gamma distribution (dashed red line) of data shown in a. (d) Same as in c but for channel 2. (e-h) Same as in a-d but for TetraSpeck™ beads. For 20 nm DNA-origami nanoruler 20 frames per molecule were recorded. For TetraSpeck™ beads one frame per molecule was acquired. Details about fitting parameters are in **Table S3.4**.

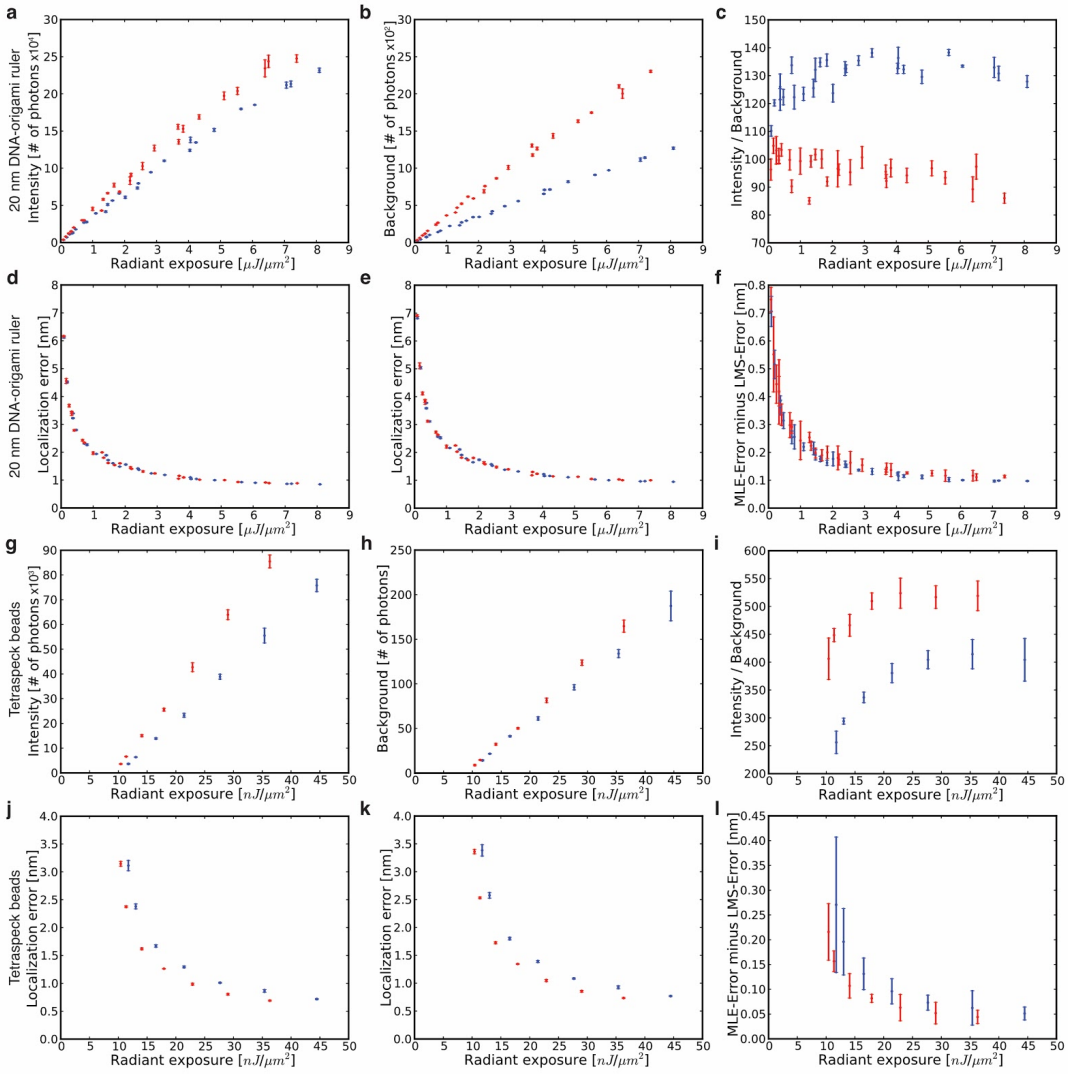

Figure S3.10 | Evaluation of photophysical properties of two different probes in two channels. Quantification of 20 nm DNA-origami nanorulers with 5-10 dyes of Cy3 and 5-10 dyes of Alexa 647 whose center of mass is 20 nm apart (a-f), and of TetraSpeck™ beads (g-l). For the intensity as well as the background we expect a linear increase for increasing radiant exposure. Only if for instance photobleaching occurs faster than the acquisition time or if a pixel gets saturated, we expect divergence from the linear behavior. Blue dots show values for channel 1 (Cy3 or Cy3 like dye(s)) and red dots for channel 2 (Cy5 or Cy5 like dye(s)). (a, g) Intensity in number of photons as a function of radiant exposure (**Table S3.2**). (b, h) Background in number of photons as a function of radiant exposure. (c, i) Intensity over background ratio as a function of radiant exposure. (d, j) Localization error calculated with the equation from Thompson et al. [117] (Least Mean Squared (LMS)-Error) as a function of radiant exposure. (e, k) Localization error calculated with the MLEwG equation from Mortensen et al.[77] (MLE-error) as a function of radiant exposure. (f, l) Difference between LMS- and MLE-error as a function of radiant exposure. Error bars in a, b, d, e, g, h, j, and k show standard deviation of five repeats (new microscopy slides with fresh sample). Each repeat consists of at least 100 molecules and one frame was taken per molecule. For c, f, i, and l the error bar is calculated based on error propagation (linear addition). Details about fitting parameters are in **Table S3.4**.

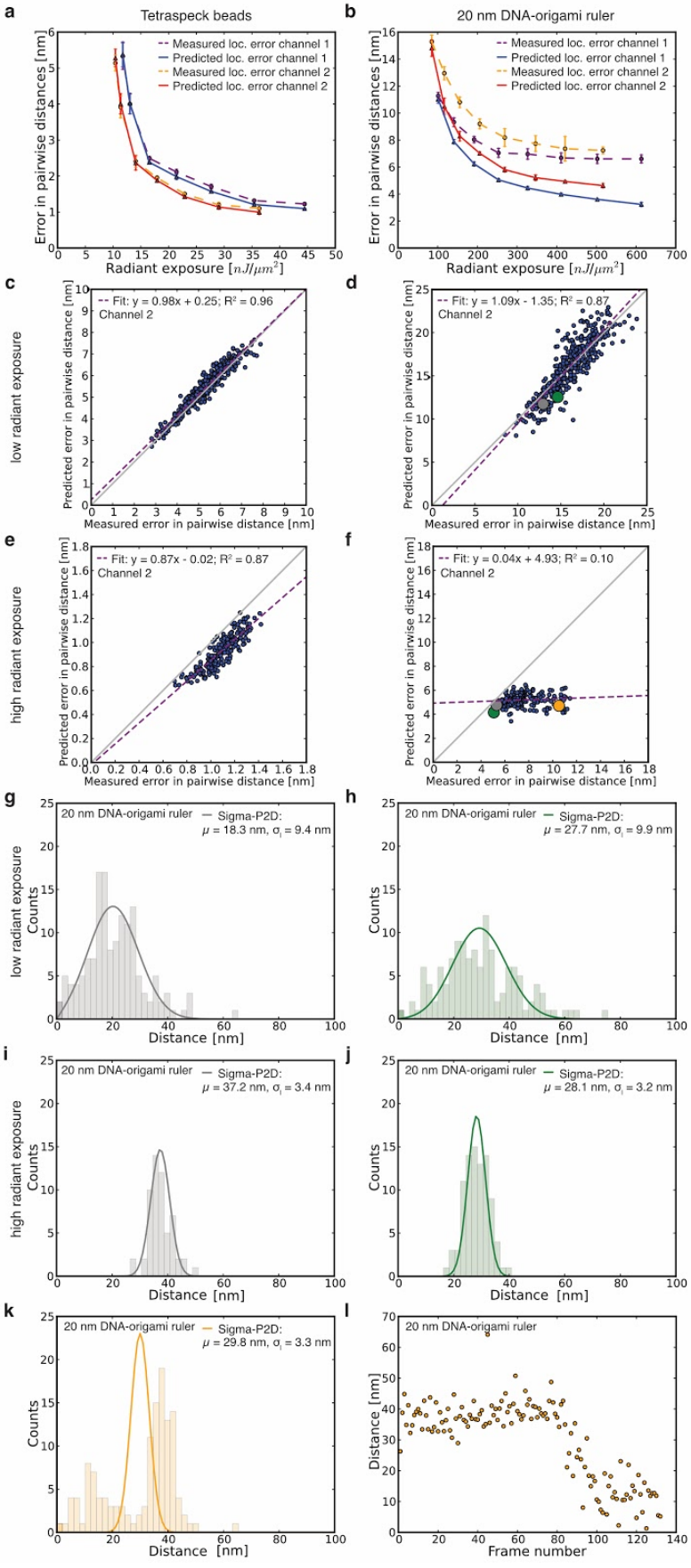
a
Tetraspeck beads
Measured loc. error channel 1
Predicted loc. error channel 1
Measured loc. error channel 2
Predicted loc. error channel 2
Error in pairwise distances [nm]
Radiant exposure [$nJ/\mu m^2$]
b
20 nm DNA-origami ruler
Measured loc. error channel 1
Predicted loc. error channel 1
Measured loc. error channel 2
Predicted loc. error channel 2
Error in pairwise distances [nm]
Radiant exposure [$nJ/\mu m^2$]
c
low radiant exposure
Fit: y = 0.98x + 0.25; R² = 0.96
Channel 2
Predicted error in pairwise distance [nm]
Measured error in pairwise distance [nm]
d
Fit: y = 1.09x - 1.35; R² = 0.87
Channel 2
Predicted error in pairwise distance [nm]
Measured error in pairwise distance [nm]
e
high radiant exposure
Fit: y = 0.87x - 0.02; R² = 0.87
Channel 2
Predicted error in pairwise distance [nm]
Measured error in pairwise distance [nm]
f
Fit: y = 0.04x + 4.93; R² = 0.10
Channel 2
Predicted error in pairwise distance [nm]
Measured error in pairwise distance [nm]
g
low radiant exposure
20 nm DNA-origami ruler
Sigma-P2D:
μ = 18.3 nm, σ_i = 9.4 nm
Counts
Distance [nm]
h
20 nm DNA-origami ruler
Sigma-P2D:
μ = 27.7 nm, σ_i = 9.9 nm
Counts
Distance [nm]
i
high radiant exposure
20 nm DNA-origami ruler
Sigma-P2D:
μ = 37.2 nm, σ_i = 3.4 nm
Counts
Distance [nm]
j
20 nm DNA-origami ruler
Sigma-P2D:
μ = 28.1 nm, σ_i = 3.2 nm
Counts
Distance [nm]
k
20 nm DNA-origami ruler
Sigma-P2D:
μ = 29.8 nm, σ_i = 3.3 nm
Counts
Distance [nm]
l
20 nm DNA-origami ruler
Distance [nm]
Frame number

Figure S3.11 | Comparison of measured and predicted localization errors for two different probes in two channels. We evaluated how well measured and predicted localization errors correlate. This is important because Sigma-P2D depends on accurate determination of localization errors and small discrepancies will lead to incorrect distance determination. Quantification of TetraSpeck™ beads (a, c, e), and of 20 nm DNA-origami nanorulers with 5-10 dyes of Cy3 and 5-10 dyes of Alexa 647 whose center of mass is 20 nm apart (b, d, f). (a, b) Predicted errors in pairwise distances calculated with MLEwG equation from Mortensen et al.[77] for channel 1 (Cy3 or Cy3 like dye(s)) in blue and channel 2 (Cy5 or Cy5 like dye(s)) in red as function of radiant exposure (**Table S3.3**). Measured error (standard deviation) in pairwise distances for channel 1 in purple and channel 2 in orange as function of radiant exposure (for more details see SI Note 3). (c, d) Scatter plot of predicted over measure error in pairwise distances of individual molecules (blue dots) for lowest radiant exposure in channel 2 from data in a, b. Dashed purple line shows fit of linear regression and gray solid line shows theoretical limit (Cramér–Rao lower bound[118]) for localization errors. (e, f) Same as in c and d but for highest radiant exposure setting. For higher radiant exposures, correlations between predicted and measured localization errors were suboptimal. To understand why, we looked at individual molecules for which predicted and measured localization errors correlated poorly, in this case for nanorulers which were imaged at high intensity. For these molecules, we noticed that the distance between colors and therewith either the position of channel 1 or channel 2 changed. Bleaching of individual dyes is likely an important contributor to this position change. The position change leads to an increase in measured localization error since we determined it via pairwise distances (fluctuation in pairwise distance → increase in measured localization error). (d) Larger, colored dots refer to histograms shown in g and h. (f) Larger, colored dots refer to histograms shown in i-k. (g, h) Histogram of distance distribution of a single molecule of a 20 nm DNA-origami nanoruler at low radiant exposure. Solid line is fit with Sigma-P2D. (i, j, k) Same as g and h but at high radiant exposure. (l) Distance as a function of time (frame number) of a single molecule of a 20 nm DNA-origami nanoruler (orange dots). Same data as shown in k. Error bars in a and b show standard deviation of three repeats (new microscopy slides with fresh sample). Each repeat consists of at least 120 pairwise distance measurements, the minimum number of frames per molecule was set to 60 and the maximum number of frames to 200. Single-molecule distances in g-l were obtained by selecting time-lapse series of individual molecules (see **Table S3.6**). Details about fitting parameters are in **Table S3.4**.

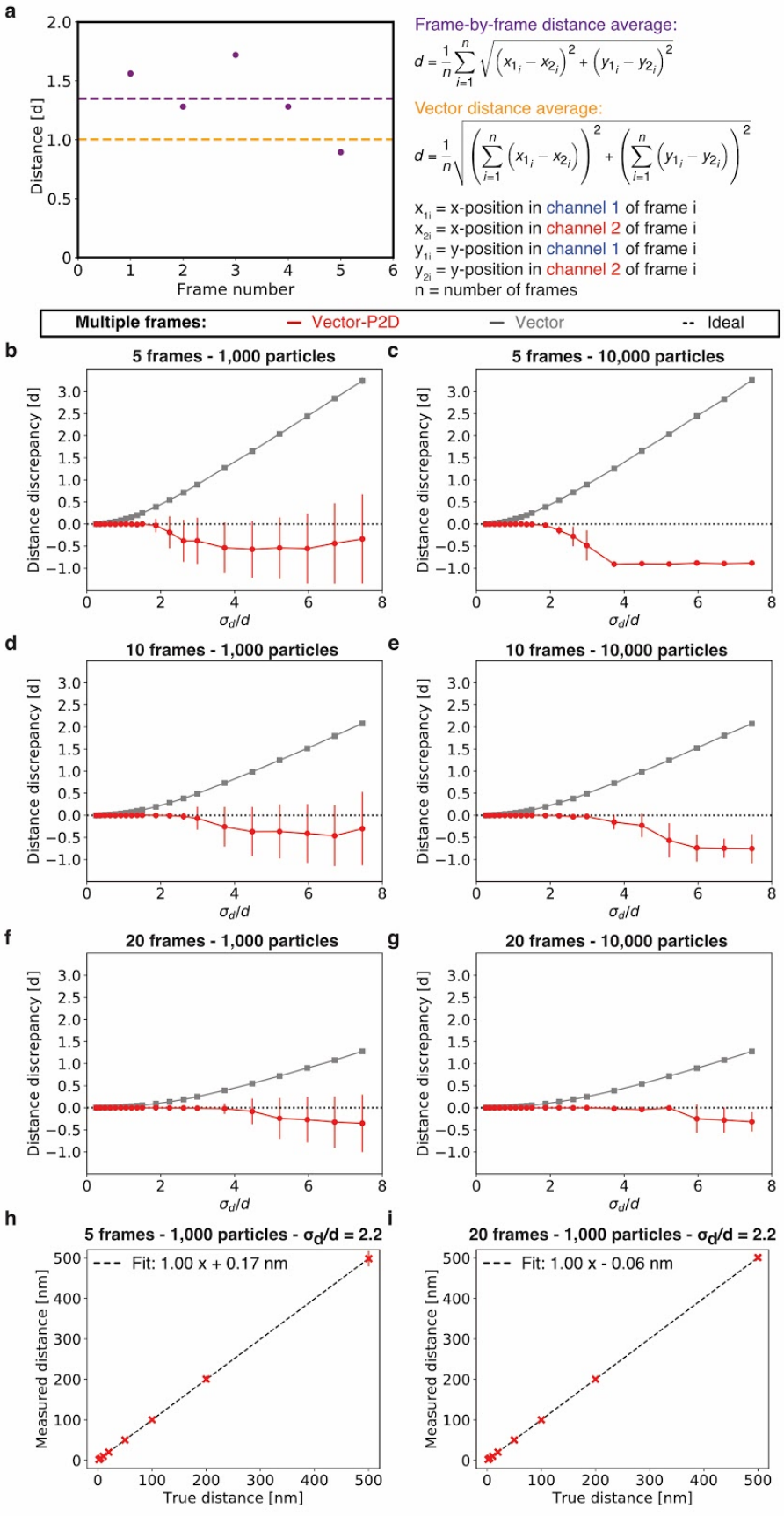
a
Distance [d]
Frame number
Frame-by-frame distance average:
$d = \frac{1}{n}\sum_{i=1}^{n}\sqrt{\left(x_{1_i} - x_{2_i}\right)^2 + \left(y_{1_i} - y_{2_i}\right)^2}$
Vector distance average:
$d = \frac{1}{n}\sqrt{\left(\sum_{i=1}^{n}\left(x_{1_i} - x_{2_i}\right)\right)^2 + \left(\sum_{i=1}^{n}\left(y_{1_i} - y_{2_i}\right)\right)^2}$
x_{1i} = x-position in channel 1 of frame i
x_{2i} = x-position in channel 2 of frame i
y_{1i} = y-position in channel 1 of frame i
y_{2i} = y-position in channel 2 of frame i
n = number of frames
Multiple frames: — Vector-P2D — Vector -- Ideal
b 5 frames - 1,000 particles
c 5 frames - 10,000 particles
d 10 frames - 1,000 particles
e 10 frames - 10,000 particles
f 20 frames - 1,000 particles
g 20 frames - 10,000 particles
Distance discrepancy [d]
σ_d/d
h 5 frames - 1,000 particles - σ_d/d = 2.2
Fit: 1.00 x + 0.17 nm
i 20 frames - 1,000 particles - σ_d/d = 2.2
Fit: 1.00 x - 0.06 nm
Measured distance [nm]
True distance [nm]

Figure S3.12 | Performance of distance prediction by Vector-P2D and Vector methods evaluated with Monte Carlo simulated data. (a) Addition to **Fig. 3.4**: Observed distances for each pair (purple dots) and their average (dashed purple line - d = 1.35) as obtained by a frame-by-frame distance average. To calculate the vector average distance (dashed orange line, resulting in d = 1.0), the average distances in x and y are calculated separately first, before combining them in the overall average distance. (b-g) Additional performance results to those shown in **Fig. 3.4**. Here, not 100 particles but 1,000 (b, d, f) and 10,000 (c, e, g) particles were used. We evaluated the performance of Vector-P2D (red) and Vector (grey) by calculating the distance discrepancy (calculated by subtracting the expected distance from the measured distance and normalizing with the expected distance) of Monte Carlo simulated data. Here, the average distance discrepancy for Vector-P2D and Vector from the true distance was calculated using 100 simulations for different ratios of uncertainty σ_d over distance d for 5, 10, and 20 frames. Error bars show standard deviation of 100 independent simulations. The values around -1.0 represent cases for which we measured 0 nm and for which we find very small error bars showing that this is very reproducible. This is an example of a precise yet highly inaccurate measurement. Large error bars typically indicate bimodal cases for which we measured both, distances that are similar to the expected distance and distances that are much smaller than the expected distance. Hence, the increasing size of error bars with increasing σ_d/d ratios shows that the fitting outcome is becoming more and more bimodal until it collapses to one side (measuring distances of around 0 nm). (h, i) Since we always used a true distance of 10 nm in all our simulations, we also tested if Vector-P2D can resolve distances of 2 nm, 10 nm, 20 nm, 50 nm, 100 nm, 200 nm, and 500 nm. We therefore used Monte Carlo simulated data with 1,000 particles, a ratio of distance uncertainty over distance of 2.2, either 5 (h) or 20 frames (i) and the different distances listed above. For each condition we created 100 datasets. We then used Vector-P2D to determine the distance for all datasets and calculated the average distance for each condition. We used this data to calculate the correlation between the true and measured distance by determining the slope and found a value of 1.00 for the 5 and 20 frame data which indicates a perfect agreement between the true and measured distance. (b-i) The error bars show the standard deviation.

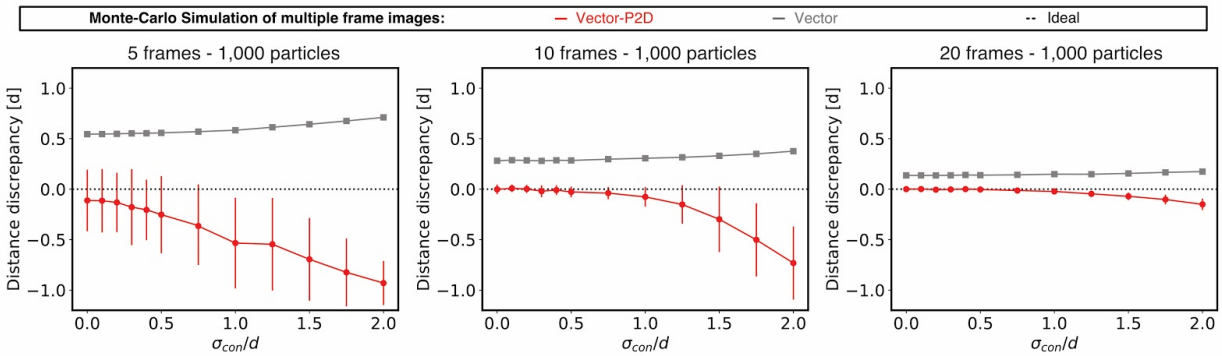

Figure S3.13 | Performance of distance prediction as a function of sample heterogeneity of Vector-P2D and Vector using Monte Carlo simulated data by calculating the distance discrepancy (calculated by subtracting the expected distance from the measured distance and normalizing with the expected distance). Here, the average discrepancy from the true distance d for Vector-P2D (red) and Vector (grey) was calculated using 100 simulations for different ratios of sample heterogeneity σ_{con} over distance d for 5, 10, and 20 frames. In all cases we used 1,000 particles and a ratio of distance uncertainty σ_d over distance d of 2.2. Error bars show standard deviation of 100 independent simulations. Large error bars typically indicate bimodal cases for which we measured both, distances that are similar to the expected distance and distances that are much smaller than the expected distance.

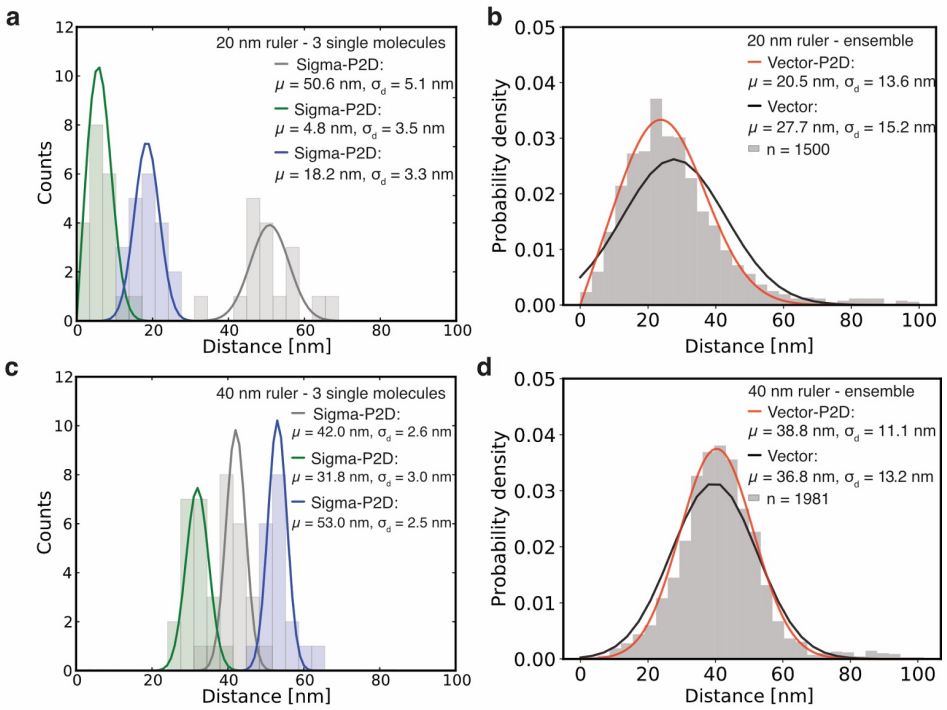

Figure S3.14 | Distance measurements for DNA-origami nanorulers. Detailed depiction of results shown in **Figure 3.4** with distance distributions for single and multiple 20 and 40 nm rulers. (a) Histogram of distance distribution of three different single-molecule 20 nm DNA-origami nanoruler (green, blue, and gray). Solid line is fit with Sigma-P2D. (b) Histogram of vector averaged distance measurements of multiple 20 nm DNA-origami nanorulers analyzed with Vector-P2D (red) and Vector (black). (c) Same as a but for 40 nm DNA-origami nanoruler. (d) Same as b but for 40 nm DNA-origami nanoruler. 20 frames for each molecule in a-d were collected. Details about fitting parameters are in **Table S3.4**.

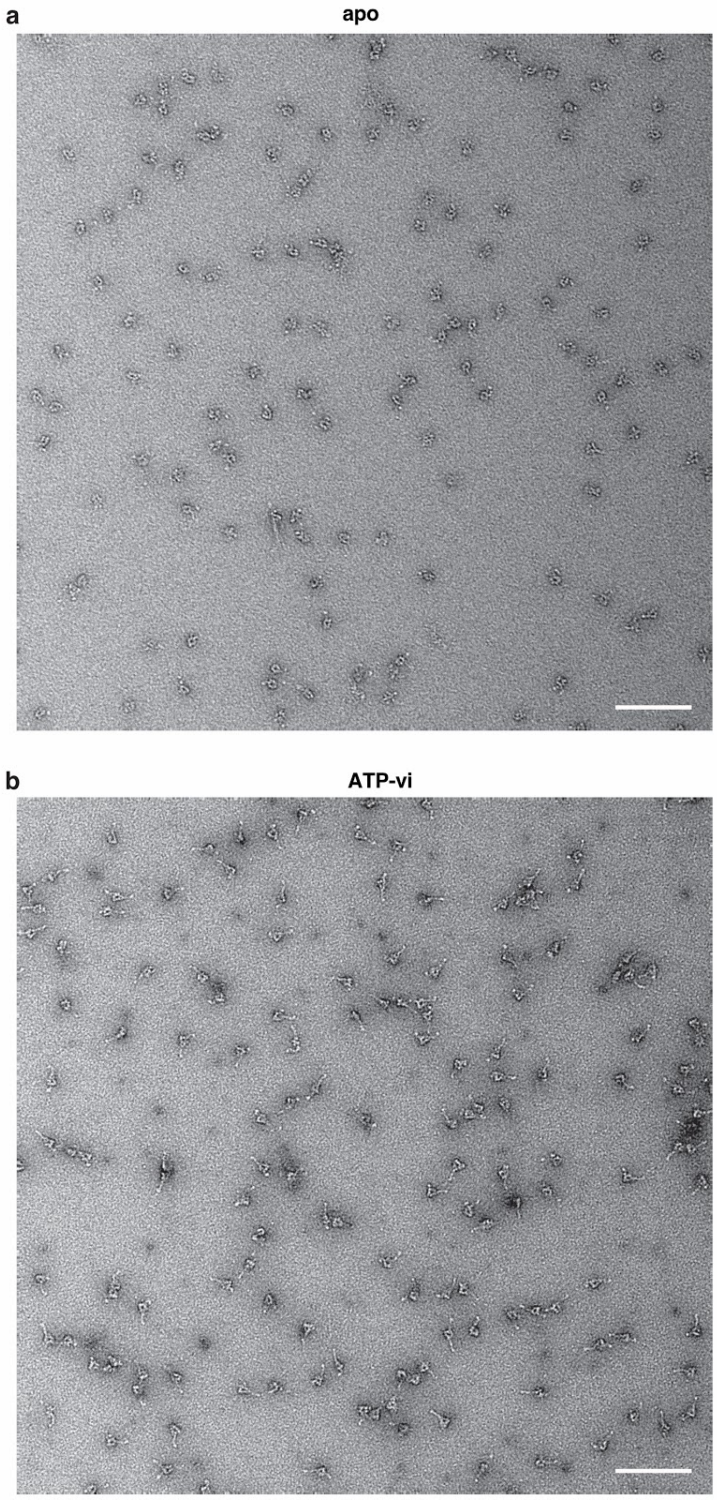

Figure S3.15 | Example negative stain electron microscopy micrographs for (a) apo and (b) ATP-vanadate (ATP-vi). For the ATP-vi image, density of the stalk can be seen for many molecules while there is little stalk density for the apo state. Scale bar: 100 nm.

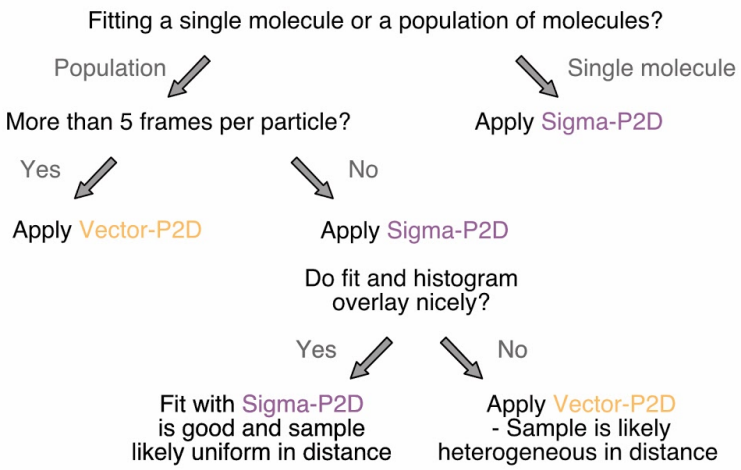

Population or single molecule	Method	Sample uniform or variable in distance	Number of frames	Number of particles	Distance uncertainty over distance cutoff
Population / ensemble	Sigma-P2D	Uniform	1	100	~ 2.0
				1,000	~ 3.5
				10,000	~ 6.0
	Vector-P2D	Uniform	5	100	~ 1.5
				1,000	~ 2.0
				10,000	~ 2.5
	Vector-P2D	Variable	5	100	~ 1.5
				1,000	~ 2.0
				10,000	~ 2.5
			10	100	~ 2.0
				1,000	~ 3.0
				10,000	~ 4.0
			20	100	~ 3.5
				1,000	~ 4.5
				10,000	~ 5.5
Single molecule / particle	Sigma-P2D	-	1	1	~ 0.2
			5		~ 0.5
			10		~ 0.8
			20		~ 1.0

Figure S3.16 | Top: Workflow to decide whether to use Sigma-P2D or Vector-P2D. This workflow is based on the strength and limitations of each of the two methods as discussed in the Discussion section of the manuscript. Bottom: Upper bounds for distance uncertainty over distance under given conditions (sample variable or uniform in distance, number of particles, number of frames) until Sigma-P2D or Vector-P2D still deliver reliable results (this is an average distance discrepancy of less than 20% from the true distance with a standard deviation of less than 30% of the true distance).

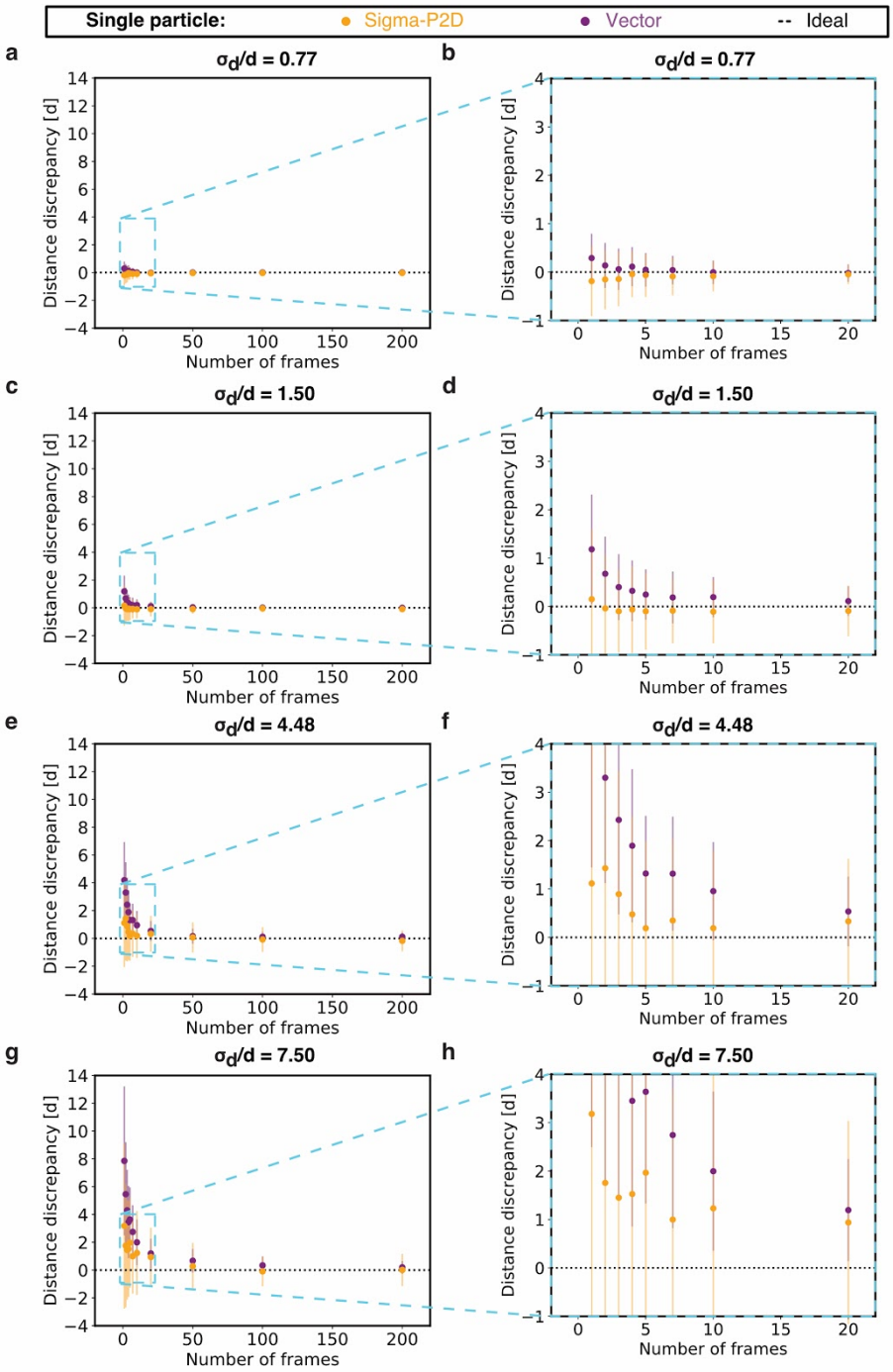

Figure S3.17 | Performance of distance prediction as a function of number of frames for Vector and Sigma-P2D on single particles using Monte Carlo simulated data. Since only single particles are analyzed, Vector and Vector-P2D are equivalent because there is only one data point that can be fitted with the P2D function after vector averaging. Thus, we only used the Vector method in this case. We evaluated the performance of Vector and Sigma-P2D by calculating the distance discrepancy. To do so, we subtracted the expected distance from the measured distance and normalized by the expected distance. Here, the average distance discrepancy for Vector (purple) and Sigma-P2D (orange) was calculated using 100 simulations

of single particles for various number of frames (observations). We used different ratios of distance uncertainty σ_d over distance d of 0.77 (a, b), 1.50 (c, d), 4.48 (e, f), and 7.50 (g, h). Blue box in a, c, e, and g is magnified in b, d, f, and h, respectively. Error bars show standard deviation of 100 independent simulations. Large error bars typically indicate bimodal cases for which we measured both, distances that are much larger and distances that are much smaller than the expected distance. As can be seen in this data, Sigma-P2D performs better than or at least equally well as Vector (smaller distance discrepancy) for all conditions when distance distributions of single particles and not ensembles are analyzed.

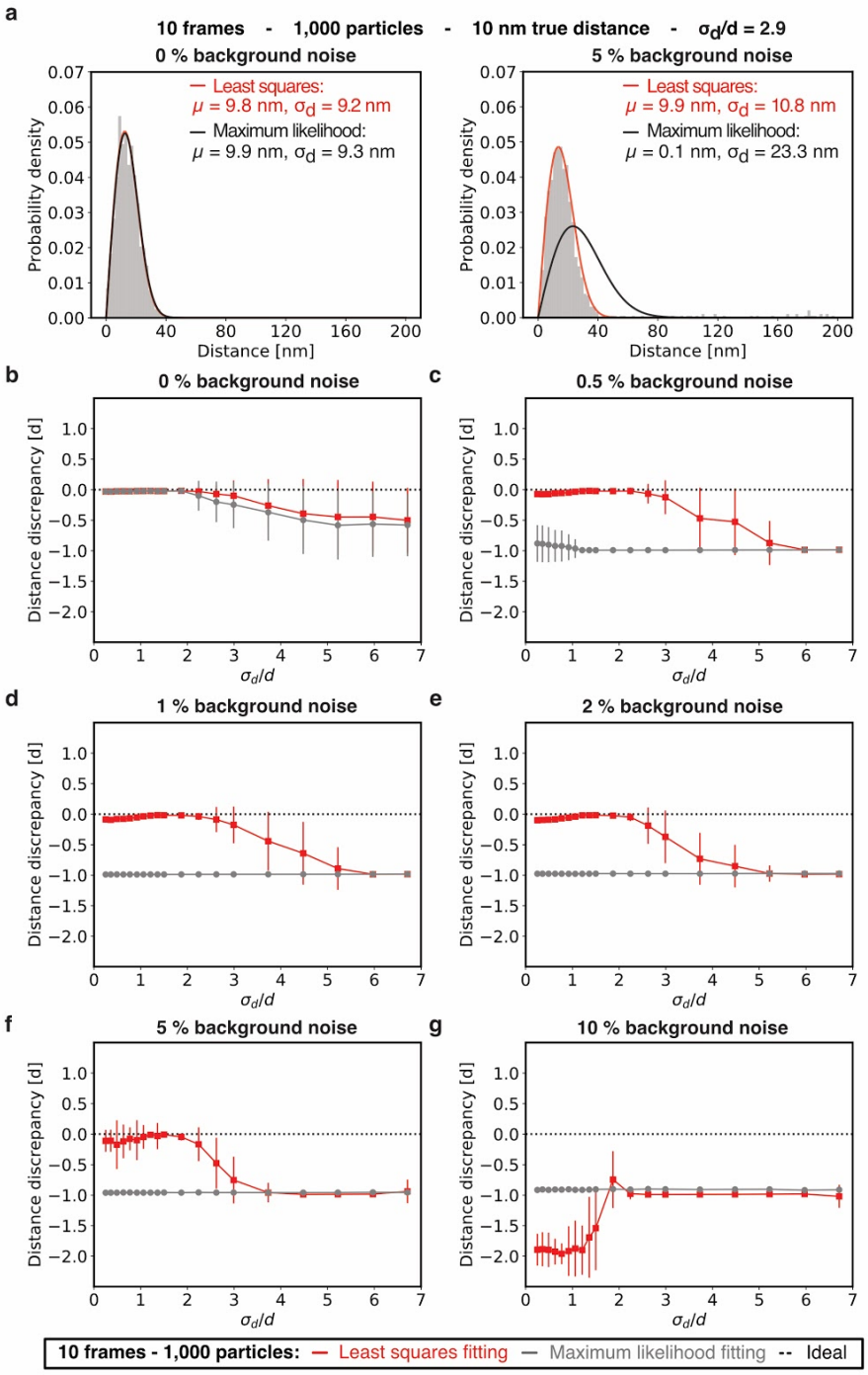

Figure S3.18 | Performance of distance prediction by Vector-P2D when fitted by means of maximum likelihood estimation (MLE) or non-linear least squares (NLLSQ) fitting evaluated with Monte Carlo simulated data. (a) Histogram of Monte Carlo simulated data with a true distance d of 10 nm and distance uncertainty σ_d of 29 nm fitted with Vector-P2D by means of MLE (black) and NLLSQ (red). Left: 0% of the data points are background noise. Right: 5 % of all data points are random background noise over a distance from 0 to 200 nm. (b-g) Average distance discrepancy for Vector-P2D fitted by means of maximum likelihood estimation (MLE) (grey) or non-linear least squares (NLLSQ) (red) based on 100 simulations with different amount of

background noise (outlier) and for different ratios of distance uncertainty to distance (σ_d/d). In all cases we used 1,000 particles and 10 frames. We evaluated the performance of MLE and NLLSQ by calculating the distance discrepancy (calculated by subtracting the expected distance from the measured distance and normalizing with the expected distance) of Monte Carlo simulated data. Error bars show standard deviation of 100 independent simulations. The values around -1.0 represent cases for which we measured 0 nm and for which we find very small error bars showing that this is very reproducible. This is an example of a precise yet highly inaccurate measurement. Large error bars typically indicate bimodal cases for which we measured both, distances that are similar to the expected distance and distances that are much smaller than the expected distance. Hence, the increasing size of error bars with increasing σ_d/d ratios shows that the fitting outcome is becoming more and more bimodal until it collapses to one side (measuring distances of around 0 nm). Overall this data shows that NLLSQ fitting is as good as MLE for data lacking background noise and that NLLSQ fitting is as good as or better than MLE fitting in all conditions where a random background noise up to 5% was added (for ratios of distance uncertainty to distance of up to 2). At higher levels of background noise, both methods fail to recover the true distance. Together, we observe that with increasing background noise the NLLSQ fitting becomes more sensitive to higher values of distance uncertainty σ_d.

Table S3.1 | Counts of stalk morphology of individual dynein particles in different nucleotide states from negative stain electron microscopy. Number of particles scored as shown in **Figure 3.5**. Some of the particles could not be assigned to any of the three categories (full stalk, no stalk, partial stalk) because of ambiguity. Thus, these were assigned to a 'not scored' category and are not taken into account for calculation of the percentages for **Figure 3.5**. Procedure of scoring is described in **Materials and Methods**.

Nucleotide state	**full stalk**	**no stalk**	**partial stalk**	**not scored**	**total**
apo	29	1670	157	606	2462
ATP vanadate	2206	104	500	478	3288

Table S2 | Calculation of radiant exposures as used in **Figure S3.10**. Laser power was measured after the objective. The field of illumination has a 2D Gaussian shape (reflecting the Gaussian shape of the laser beam), causing the radiant exposure to vary over the field of view. Here, we calculated an average radiant exposure by assuming a field of illumination of 60 µm by 60 µm. Noise tolerance refers to settings in µManager's[70] 'Localization Microscopy' plug-in. It was chosen so that approximately the same number molecules were fitted per micrograph and to avoid fitting background as true particles (especially for higher radiant exposures). More details about fitting parameters in **Table S3.4**.

Laser power Ch1 [mW]	**Laser power Ch2 [mW]**	**Exposure time [ms]**	**Radiant exposure Ch1 [nJ/um^2]**	**Radiant exposure Ch2 [nJ/um^2]**	**Noise tolerance - beads**	**Noise tolerance - 20 nm ruler**
0.42	0.38	100	11.75	10.42	100	-
0.47	0.41	100	13.03	11.36	200	-
0.60	0.51	100	16.53	14.08	300	-
0.77	0.65	100	21.42	17.92	400	-
1.00	0.82	100	27.67	22.89	800	-
1.27	1.05	100	35.39	29.03	1,500	-
1.60	1.31	100	44.47	36.31	2,500	-
0.84	0.74	400	93.33	82.22	-	220
0.84	0.74	800	186.67	164.44	-	400
0.84	0.74	1,200	280.00	246.67	-	650
0.84	0.74	1,600	373.33	328.89	-	800
0.84	0.74	2,000	466.67	411.11	-	1,100
3.3	3.0	400	366.7	333.3	-	750
3.3	3.0	800	733.3	666.7	-	1,600
3.3	3.0	1,200	1,100.0	1,000.0	-	2,250
3.3	3.0	1,600	1,466.7	1,333.3	-	2,850
3.3	3.0	2,000	1,833.3	1,666.7	-	3,750
7.3	6.6	400	811.1	733.3	-	1,650
7.3	6.6	800	1,622.2	1,466.7	-	3,300
7.3	6.6	1,200	2,433.3	2,200.0	-	4,500
7.3	6.6	1,600	3,244.4	2,933.3	-	6,000

Laser power Ch1 [mW]	Laser power Ch2 [mW]	Exposure time [ms]	Radiant exposure Ch1 [nJ/um^2]	Radiant exposure Ch2 [nJ/um^2]	Noise tolerance - beads	Noise tolerance - 20 nm ruler
7.3	6.6	2,000	4,055.6	3,666.7	-	8,000
12.7	11.5	400	1,411.1	1,277.8	-	2,100
12.7	11.5	800	2,822.2	2,555.6	-	5,500
12.7	11.5	1,200	4,233.3	3,833.3	-	8,000
12.7	11.5	1,600	5,644.4	5,111.1	-	10,000
12.7	11.5	2,000	7,055.6	6,388.9	-	12,000
18.2	16.6	400	2,022.2	1,844.4	-	3,500
18.2	16.6	800	4,044.4	3,688.9	-	7,000
18.2	16.6	1,200	6,066.7	5,533.3	-	11,000
18.2	16.6	1,600	8,088.9	7,377.8	-	13,000
18.2	16.6	2,000	10,111.1	9,222.2	-	-
21.6	19.5	400	2,400.0	2,166.7	-	4,300
21.6	19.5	800	4,800.0	4,333.3	-	8,800
21.6	19.5	1,200	7,200.0	6,500.0	-	12,500
21.6	19.5	1,600	9,600.0	8,666.7	-	-
21.6	19.5	2,000	12,000.0	10,833.3	-	-

Table S3.3 | Calculation of radiant exposures as used in **Fig. S3.11**. Laser power was measured at objective. The field of illumination has a 2D Gaussian shape (reflecting the Gaussian shape of the laser beam), causing the radiant exposure to vary over the field of view. Here, we calculated an average radiant exposure by assuming a field of illumination of 60 µm by 60 µm. Noise tolerance refers to settings in µManager's[70] 'Localization Microscopy' plug-in. It was chosen so that approximately the same number molecules were fitted per micrograph and to avoid fitting background as true particles (especially for higher radiant exposures). More details about fitting parameters in **Table S3.4**.

Laser power Ch1 [mW]	**Laser power Ch2 [mW]**	**Exposure time [ms]**	**Radiant exposure Ch1 [nJ/um^2]**	**Radiant exposure Ch2 [nJ/um^2]**	**Noise tolerance - beads**	**Noise tolerance - 20 nm ruler**
0.42	0.38	100	11.75	10.42	100	-
0.47	0.41	100	13.03	11.36	200	-
0.60	0.51	100	16.53	14.08	300	-
0.77	0.65	100	21.42	17.92	400	-
1.00	0.82	100	27.67	22.89	800	-
1.27	1.05	100	35.39	29.03	1,500	-
1.60	1.31	100	44.47	36.31	2,500	-
0.91	0.77	400	101.33	85.11	-	50
1.27	1.05	400	141.00	116.78	-	80
1.73	1.40	400	192.00	155.78	-	95
2.28	1.86	400	253.33	206.11	-	135
2.94	2.42	400	326.78	269.11	-	175
3.7	3.1	400	411.1	346.7	-	230
4.5	3.8	400	502.2	421.1	-	270
5.5	4.7	400	613.3	516.7	-	350

Table S3.4 | Fitting parameters used in μManager's[70] 'Localization Microscopy' plug-in.

Imaging Parameters	
Photon conversion factor	1.84
Linear (EM) gain	1.0
Pixel size [nm]	159.0
Time interval [ms]	0.0
Z-step [nm]	50.0
Camera offset [electron counts]	91.0
Read noise [electron counts]	9.84
Find Maxima	
Pre-Filter	None
Noise tolerance	See **Table S3.5**
Fit Parameters	
Dimensions	1
Filter	Simplex-MLE
Max Iterations	500
Box size [pixel]	12.0
Fix width	Not selected
Filter Data	Nothing selected
Positions	Always all, except for registration maps where data is split to create affine and piecewise affine maps so that ~1000 beads can be used for affine map. Remainder is used for piecewise affine map.
Skip Channels	Not selected

Table S3.5 | Radiant exposures used for the acquisition of different datasets if not specified elsewhere. Noise tolerance as used in the μManager's[70] 'Localization Microscopy' plug-in for different datasets if not specified elsewhere.

Dataset in Figure	**Radiant exposure used for sample of interest [nJ/um²]**		**Noise tolerance used for sample of interest**
	Channel 1	**Channel 2**	
Fiducials to create *all maps*	35.39	29.03	300
Figure 2	35.39	29.03	300
Figure 3	613.3	516.7	100
Figure 4	613.3	516.7	100
Figure 5	1,982.0	1,853.3	100
Supplementary Figure 2	35.39	29.03	300
Supplementary Figure 3	35.39	29.03	300
Supplementary Figure 4	35.39	29.03	300
Supplementary Figure 5	35.39	29.03	300
Supplementary Figure 6	35.39	29.03	300
Supplementary Figure 7	2,400.0	2,166.7	300
Supplementary Figure 9	20 nm ruler: 613.3 Beads: 35.39	20 nm ruler: 516.7 Beads: 29.03	All datasets: 300
Supplementary Figure 10	See **Table S3.2**		See **Table S3.2**
Supplementary Figure 11	See **Table S3.3**		See **Table S3.3**
Supplementary Figure 14	613.3	516.7	100

Table S3.6 | Settings for the 'Extract Tracks' function in the μManager's[70] 'Localization Microscopy' plug-in used to extract individual tracks of single molecules that were imaged for F number of frames. Here the maximum distance refers to the distance between the position of one molecule from channel n-1 to channel n. The minimum total distance indicates the distance of one molecules' position in frame 1 to its position in frame F. The maximum pair distance selects molecules in which the distance between the channel 1 and the channel 2 position is below a defined threshold.

Dataset in Figure	**Minimum # of Frames**	**Maximum # of missing Frames**	**Maximum Distance [nm]**	**Minimum total distance [nm]**	**Combine tracks from all channels**	**Maximum pair distance [nm]**
Figure 3	e, f: 5	e, f: 15	e, f: 15	e, f: 0	e, f: Checked	e, f: 30
Figure 5	c, d: 15	c, d: 5	c, d: 25	c, d: 0	c, d: Checked	c, d: 100
Supplementary Figure 7	3	17	20	0	Checked	20
Supplementary Figure 11	g-l: 60	g-l: 10	g-l: 90	g-l: 0	g-l: Unchecked	g-l: -

Materials and Methods

Flow-cell preparation

We custom made three-cell flow chambers using laser-cut double-sided adhesive sheets (Soles2dance, 9474-08x12 - 3M 9474LE 300LSE), glass slides (Thermo Fisher Scientific, 12-550-123), and 170 µm thick coverslips (Zeiss, 474030-9000-000). The coverslips were cleaned in a 5% v/v solution of Hellmanex III (Sigma, Z805939-1EA) at 50°C overnight and washed extensively with Milli-Q water afterwards. Flow-cells were assembled so that each chamber holds ~10 µl (**Fig. S3.1**).

Fluorescent beads for image registration

We used TetraSpeck™ beads (Thermo Fisher Scientific, T7279) with a diameter of ~100 nm for image registration. To prepare the beads for imaging we added 10 µl of 1 mg/ml Poly-D-lysine (Sigma, P6407) in Milli-Q water to the flow-cell and incubated for 3 min, washed with 20 µl of BRB80 (80 mM Pipes (pH 6.8), 1 mM EGTA, and 1 mM $MgCl_2$) and then added 10 µl of 1:1000 diluted TetraSpeck™ beads in BRB80 and incubated for 5 min. Finally, we washed the flow-cell with 40 µl of BRB80.

Preparation of dsDNA samples

For the 30 bp single biotin dsDNA construct we used

strand A: /5Cy3/GGGTATGGAGATTTTTAGCGGAGTGACAGC/3Cy5Sp/

strand B: /5BiosG/AAAAAAAAAAAAGCTGTCACTCCGCTAAAAATCTCCATACCC

both purchased from Integrated DNA Technologies (Skokie, IL). The double stranded constructs were assembled by mixing 10 µM of strand A and B with Assembly Buffer (20 mM Tris (pH 8.0), 1 mM EDTA, and 2.5 mM $MgCl_2$) and heating the mixture to 95°C for 5 min, followed by cooling down to 20°C at a rate of 1°C per minute. For imaging, we diluted the constructs in Assembly Buffer to 3 pM. Samples for imaging are prepared by adding 10 µl of 5 mg/ml Biotin-BSA

(Thermo Fisher Scientific, 29130) in BRB80 to the flow-cell, incubation for 2 min., addition of 10 µl of 5 mg/ml Biotin-BSA in BRB80, incubation for 2 min, washing with 20 µl of BRB80, addition of 10 µl of 0.5 mg/ml Streptavidin (Thermo Fisher Scientific, S888) in PBS pH 7.4 and a 2 min incubation. We then washed with 20 µl of PBS (pH 7.4), added 10 µl of 3 pM dsDNA construct in PBS (pH 7.4) and incubated for 5 min. Next, we washed with 30 µl of PBS (pH 7.4) and finally added the PCA/PCD/Trolox oxygen scavenging system [76] in PBS (pH 7.4).

DNA-origami standards

Custom DNA origami nanorulers[101] were purchased from GATTAquant GmbH (Braunschweig, Germany). The nanoruler design is based on the 12HB and is externally labeled with fluorescent dye molecules (Cy3 and Alexa647). The 'center-of-mass' between the Cy3 binding sites and the Alexa647 binding sites is either 10 nm, 20 nm, or 40 nm. Each color has up to 10 binding sites with an expected labeling efficiency of 50-80%. In addition, each nanoruler has multiple biotins attached for immobilization on a coverslip. Samples for imaging are prepared by twice adding 10 µl of 5 mg/ml Biotin-BSA in BRB80 to the flow-cell and incubation for 2 min., washing with 20 µl of BRB80, addition of 10 µl of 0.5 mg/ml Streptavidin in PBS (pH 7.4) and a 2 min incubation. We then washed with 20 µl of PBS (pH 7.4) supplemented with 10 mM $MgCl_2$. In a next step 10 µl of DNA-origami ruler was added and incubated for 5 min. Next, we washed with 30 µl of PBS (pH 7.4) supplemented with 10 mM $MgCl_2$ and finally added the PCA/PCD/Trolox oxygen scavenging system[76] in PBS (pH 7.4) supplemented with 10 mM $MgCl_2$.

Kinesin cloning, purification and labeling

The kinesin construct was cloned and purified as previously described[63,74]. Briefly, cysteine residues were introduced into a 'cysteine-light' human kinesin-1 dimer that is 490 amino acids long (K490). The homodimeric E215C K490 contains a carboxy-terminal His_6 tag.

The plasmid was transfected and expressed in Agilent BL21(DE3). Cells were grown in LB at 37°C until they reached 0.6 OD_{280}, expression was induced by addition of 1 mM IPTG and cells were incubated overnight at 18 °C. The cells were pelleted and harvested in lysis buffer (25 mM Pipes (pH 6.8), 2 mM $MgCl_2$, 250 mM NaCl, 20 mM imidazole, 2 mM TCEP, 5% sucrose), and lysed in the EmulsiFlex homogenizer (Avestin) in the presence of protease inhibitors. After a spin in a Sorvall SS-34 rotor for 30 min at 30,000 x g, the supernatant was loaded onto a Ni-NTA resin (QIAGEN, 30210) and washed with additional lysis buffer. Then the protein was eluted by adding 300 mM of imidazole to the lysis buffer. The elutions were dialyzed overnight against a dialysis buffer (25 mM Pipes (pH 6.8), 2 mM $MgCl_2$, 200 mM NaCl, 1 mM EGTA, 2 mM TCEP, 10% sucrose).

Afterwards, the E215C K490 was reacted for 4 h at 4°C with Cy3-maleimide (GE Healthcare, PA13131) and Cy5-maleimide (GE Healthcare, PA15131) at a motor/Cy3 dye/Cy5 dye ratio of 1:10:10. Unreacted maleimide dyes were quenched by the addition of 1 mM dithiothreitol (DTT). Subsequently the sample was purified by gel filtration over a S200 10/300GL column from GE Healthcare. Gel filtration buffer was composed of 25 mM Pipes (pH 6.8), 2 mM $MgCl_2$, 200 mM NaCl, 1 mM EGTA, 1 mM DTT, and 10% sucrose. Finally the sample was flash frozen and stored at -80°C.

Dynein cloning, purification and labeling

Dynein was expressed and purified as previously described[60]. Monomeric constructs for negative stain imaging were further purified by gel filtration on a GE Healthcare Superdex 200 10/300GL in dynein gel filtration buffer (20 mM Tris (pH 8.0), 50 mM K-Ac, 2 mM $Mg(Ac)_2$, 1 mM EGTA, 1 mM TCEP, and 10% glycerol) and flash frozen afterwards. For the negative stain images we used the VY137 construct with the following genotype: PGal:ZZ:Tev:GFP:HA:D6 MATa; his3-11,15; ura3-1; leu2-3,112; ade2-1; trp1-1; PEP4::HIS5; PRB1D. For the in solution distance measurements we added a c-terminal Halo-tag[103] and inserted a YBBR-tag[104] into the

MTBD - VY1067. Before gel filtration, the monomer was labeled on ice overnight with two 16 bp long double stranded DNA constructs (D-E and F-G) that were dimerized a priori with Assembly Buffer (20 mM Tris (pH 8.0), 1 mM EDTA, and 2.5 mM $MgCl_2$) and heating the mixture to 95°C for 5 min, followed by a cooling of 1°C per minute down to 20°C. The YBBR-tag labeling was carried out as previously described[119]. Briefly, we mixed 10 mM $MgCl_2$, 2.5 μM Sfp phosphopantetheinyl transferase, 5 μM DNA–CoA and 50 nM ybbR-tagged dynein (all final concentrations). Afterwards we removed excess DNA strands by gel filtration on a GE Healthcare Superdex 200 10/300GL in dynein gel filtration buffer and then flash froze the sample. The oligos were ordered from Biomers GmbH (Ulm, Germany) and Integrated DNA Technologies - IDT - (Skokie, IL) with the following sequences and modifications:

Strand D: /CoA/AGGATGAGTGAGAGTG (Biomers)

Strand E: /5BiosG/CACTCTCACTCATCCTT/3Cy3Sp/ (IDT)

Strand F: /HALO/AGGATGAGTGAGAGTG (Biomers)

Strand G: /5BiosG/CACTCTCACTCATCCTT/3ATTO647NN/ (IDT)

Preparation of microtubules

Tubulin was purified and polymerized as previously described[20]. Unlabeled tubulin, biotinylated tubulin, and fluorescent tubulin were mixed at a ratio of 50:2:1 in BRB80 and 1 mM GTP was added. Then the mixture was incubated in a 37°C water bath for 15 min. Afterwards 20 μM of Taxol (Sigma, T1912) was added and the mixture was incubated for an additional 2 h at 37°C. Before usage, microtubules were spun over a 25% sucrose cushion at ~160,000 *g* for 10 min in a tabletop centrifuge.

Preparation of flow-cells with kinesin

Flow-cells with immobilized kinesin were prepared as previously described[74]. First, we added 10 μl of 5 mg/ml Biotin-BSA in BRB80 to the flow-cell and incubated for 2 min. Then, we

again added 10 µl of 5 mg/ml Biotin-BSA in BRB80 and incubated for 2 min. Afterwards we washed with 20 µl of BRB80 with 2 mg/ml β-casein (Sigma, C6905), 0.4 mg/ml κ-casein (Sigma, C0406). This was followed by the addition of 10 µl of 0.5 mg/ml Streptavidin in PBS (pH 7.4) and a 2 min incubation. We then washed with 20 µl of BRB80 with 2 mg/ml β-casein, and 0.4 mg/ml κ-casein. In a next step 10 µl of polymerized Alexa488 labeled microtubules were added and incubated for 5 min. Next, we washed with 30 µl of BRB80 with 2 mg/ml β-casein, 0.4 mg/ml κ-casein, and 10 µM Taxol. Then, we added 10 µl of K490 in BRB80 with 2 mg/ml β-casein, 0.4 mg/ml κ-casein, 10 µM Taxol, and 1 mM AMPPNP (Sigma, 10102547001) and incubated for 5 min. Afterwards we washed the flow-cell with 30 µl of BRB80 with 1 mg/ml β-casein, 0.2 mg/ml κ-casein, 10 µM Taxol, and 1 mM AMPPNP. Finally we added the PCA/PCD/Trolox oxygen scavenging system[76] in BRB80 together with 1 mg/ml β-casein, 0.2 mg/ml κ-casein, 10 µM of Taxol, and 1 mM AMPPNP.

Preparation of flow-cells with dynein

The flow cells for the distance measurements between the AAA ring and the microtubule binding domain of dynein were prepared as follows. First, we mixed DNA labeled, monomeric dynein in DAB (30 mM HEPES (pH 7.4), 50 mM K-Ac, 2 mM $Mg(Ac)_2$, 1 mM EGTA, 1mM TCEP) with 1 mM Mg-ATP and 1 mM vanadate (Sigma, 450243) and incubated at RT for 15 min. We also prepared a dynein dilution in DAB for the apo state and also incubated it at RT for 15 min. In the meantime we prepared two identical flow-cells for the apo and ATP vanadate state on the same microscopy slide. Therefore, we added 10 µl of 5 mg/ml Biotin-BSA in BRB80 twice and incubated for 2 min each time. Afterwards the flow-cell was washed with 20 µl of BRB80 with 2 mg/ml β-casein (Sigma, C6905), 0.4 mg/ml κ-casein (Sigma, C0406). We then added 10 µl of 0.5 mg/ml Streptavidin in PBS (pH 7.4) and incubated for another 2 min. This was followed by a wash with 20 µl DAB with 2 mg/ml β-casein (Sigma, C6905), 0.4 mg/ml κ-casein (Sigma, C0406). Next, we incubated with 10 µl of either dynein solution, apo and ATP vanadate, for 5

min. Afterwards we washed with 30 µl of DAB with 1 mg/ml β-casein, and 0.2 mg/ml κ-casein. For the ATP vanadate state we added 1 mM of Mg-ATP and 1 mM of vanadate. Finally, we added 10 µl of the PCA/PCD/Trolox oxygen scavenging system[76] in DAB with 1 mg/ml β-casein, and 0.2 mg/ml κ-casein. For the ATP vanadate state the buffer was supplemented with 1 mM Mg-ATP and 1 mM vanadate.

Microscope setup

Data collection was performed at room temperature (~23 °C) using a through-the-objective total internal reflection fluorescence (TIRF) inverted microscopy on a Nikon Eclipse Ti microscope equipped with a 100× (1.45 NA) oil objective (Nikon, Plan Apo ƛ). We used two stepping motor actuators (Sigma Koki, SGSP-25ACTR-B0) mounted on a KS stage (KS, Model KS-N) and a custom-built cover to reduce noise from air and temperature fluctuations. A reflection based autofocus unit (FocusStat4) was custom adapted to our microscope (Focal Point Inc.). We applied Nikon Type NF2 immersion oil (Nikon, MXA22126) to all slides. Three laser lines at 488 nm (Coherent Sapphire 488 LP, 150 mW), 561 nm (Coherent Sapphire 561 LP, 150 mW), and 640 nm (Coherent CUBE 640-100C, 100 mW) were guided through an AOTF (Neos, 48062-XX-.55), enlarged 6 fold, passed through a quarter wave plate (ThorLabs, AQWP05M-600) and focused using an achromatic doublet f=100 mm on a conjugate back focal plane of the objective outside of the microscope. The TIRF angle was adjusted by moving a mirror and focusing lens simultaneously. A TIRF cube containing excitation filter (Chroma, zet405/491/561/638x), dichroic mirror (zt405/488/561/638rpc), and emission filter (Chroma, zet405/491/561/647m) was mounted in the upper turret of the microscope. The lower turret contained a filter cube (Chroma, TE/Ti2000_Mounted, ET605/70m, T660lpxr, ET700/75m) that directs Cy3 emission towards the back camera and the Cy5 emission towards the left camera. We used two Andor iXon 512x512 EM cameras, DU-897E. The acquisition software was µManager[70] 2.0. All acquisitions were carried out with alternating excitation between the

561 and 640 laser lines (to avoid considerable background fluorescence in the Cy5 channel caused by 561 nm laser excitation). Image pixel size was 159 nm.

Single-molecule TIRF data collection

For TetraSpeck™ bead acquisitions an exposure time of 100 msec and for all other samples 400 msec was used, if not otherwise specified. After every stage movement for data acquisition at a new position we waited 3 sec before collecting data to minimize drift effects, because we noticed large stage drift right after every stage movement, which was significantly lower a couple of seconds after stage movement. We used the cameras in conventional CCD mode (i.e., no EM gain). All datasets were acquired with a '16 bit, conventional, 3 MHz' setting and a preamp gain of 5x. More details of image acquisition settings and laser powers settings for each individual dataset are shown in **Table S3.4, S3.5, and S3.6**.

Negative stain electron microscopy data collection and processing

Nucleotide-bound samples were prepared with 5 mM ATP + Sodium vanadate in addition to equimolar magnesium acetate. For negative-stain EM, samples were applied to freshly glow discharged carbon coated 400 mesh copper grids and blotted off. Immediately after blotting, a 0.75% uranyl formate solution was applied for staining and blotted off. The stain was applied five times per sample. Samples were allowed to air dry before imaging. Data were acquired at UCSF, on a Tecnai T12 microscope operating at 120 kV, using a 4k×4k CCD camera (UltraScan 4000, Gatan) and a pixel size of 2.1 Å/pixel. Particles were picked and boxed using scripts from SAMUEL and SamViewer (https://liao.hms.harvard.edu/samuel). 2D classification was used to clean our stack and obtain a set of good particles. Only top view (views in which the AAA ring could be clearly identified) were used. Particles were manually scored as having a "full" stalk (MTBD visible), "partial stalk" (stalk is visible but MTBD is not) or "no stalk" (stalk cannot be identified in the micrograph) (**Table S3.1**). For an unbiased sorting,

we randomly assigned unique identifiers (10 digit number) to each particle in the apo and ATP-vanadate state, pooled all particles from both nucleotide states, sorted them manually into the three different classes (stalk, partial stalk, no stalk) and then decoded particles based on the unique identifier to sort the particle back into the apo or ATP-vanadate states.

Single-molecule localization

All emitters were fitted and localized using μManager's[70] "Localization Microscopy' plug-in. For emitter fitting we implemented a Gaussian based maximum-likelihood estimation[77] in μManager[70] and used the following starting conditions. The x- and y-position were determined by centroid calculation, the width was set to 0.9 pixels, background was calculated by summing the intensities of all outermost pixels of an ROI, and intensity was determined by summing up all intensities within the ROI minus the background value. After fitting, intensities and backgrounds were converted to photon count by applying the photon conversion factor and correcting for camera offset and read noise. Width and x-, y-coordinates were then converted from pixel to nanometer space (1 pixel = 159 nm). When fitting emitters with μManager's[70] "Localization Microscopy' plug-in a noise tolerance and box size can be set. Parameters for analysis are shown in **Table S3.4**.

We then calculated the variance in fluorophore localization using the MLEwG method[77]. Note that we used intensity and background values determined by the aperture method[120] and not values determined by the MLE emitter fitting because the aperture method values agreed better with the experimentally measured variance (**Fig. S3.11**). A step-by-step protocol for single-molecule localization is given in SI Protocol.

Image registration

For image registration two datasets were always acquired: Fiducial markers (TetraSpeck™ beads) to determine the registration map before imaging the sample of interest

and a second set of beads to test the stability of the registration (target registration error - TRE) after the sample of interest. To ensure high quality of the registration map during the experiment, we determined the target registration error (TRE), which reports the distance (ideally 0.0 nm) for fiducials other than the points used to create the registration map[116] and which is more critical than the fiducial registration error (FRE) (**Fig. S3.2**). Registrations were carried out by first applying a global affine transformation (determined from the bead images) to bring the coordinates in the two channels in close enough proximity for automated pair assignment (**Fig. S3.1**). Final registration was accomplished by applying a second affine transform constructed from beads in the immediate vicinity of each pair (i.e., each pair has its own piecewise affine transform). This piecewise affine transformation[97] was also used to calculate the TRE from the second set of bead images by determining the difference in x and y position of each bead after registration (Eq. 1). Since piecewise affine alignment is based on a nearest neighbor search[97], three parameters can influence registration outcome: minimum and maximum number of fiducial points and the maximum distance to the control point. Higher maximum distance and higher maximum number of points caused distortions indicating that the registration was not executed properly (**Fig. S3.3**). On the other hand, when the maximum distance is too small, an area in the micrograph may not contain the minimum number of fiducials, and thus will not be corrected (white areas in **Fig. S3.3**). Based on the analysis of many different parameter combinations (**Fig. S3.4**), we used the following settings for piecewise affine maps: a minimum of 10 and a maximum of 100 fiducial points as well as a maximum distance of 2 μm (except for **Fig. S3.7** where a maximum distance of 3 μm was used, and **Figure S3.3** where values are provided in the figure caption).

Single-molecule data analysis and distance determination

All datasets were analyzed using μManager's[70] "Localization Microscopy" plug-in. The fitting method (P2D, Sigma-P2D, Vector-P2D, and Vector) to calculate the distance between two

fluorophores is either indicated in the figure and/or figure caption. To avoid erroneous results caused by floating point under- or overflows during the calculation of P2D[91], intermediate results were tested for such conditions and set to minimum or maximum floating-point number when appropriate. Furthermore, an approximation (Appendix B of Churchman et al., 2006[94]) of the P2D function was used $p_{2D} \approx \frac{1}{\sqrt{2\pi}\sigma_d}\sqrt{\frac{r}{\mu}}exp\left(-\frac{(r-\mu)^2}{2\sigma_d{}^2}\right)$ when the estimate of σ_d was smaller than half the estimate of the distance.

For P2D and Sigma-P2D the data was fit by means of maximum likelihood estimation (MLE) as described in the results section. For Vector and Vector-P2D we used a more outlier robust fitting method (non-linear least squares (NLLSQ) fitting) since experimental data usually contain some background noise causing incorrect fitting results when using maximum likelihood estimation for Vector-P2D. We could have also removed outliers from the data but it is not always possible to distinguish “real” data points from outliers and small changes in threshold value (cut-off for measured distances) dramatically influence the outcome of the maximum likelihood fit of distance μ. Setting the cut-off for the measured distances too low or too high can dramatically change the value of the estimated distance for MLE fitting. When fitting with NLLSQ, setting the distance cut-off too low might influence the outcome. However, since NLLSQ is less sensitive to outliers, the cut-off can always be set to high values (e.g. 4-5 times of the expected distances) and therewith erroneous fitting results are less likely.

To overcome problems with bin size settings for histograms when fitting with NLLSQ we converted the experimental data into an empirical cumulative distribution function and fit this with numeric integration of the P2D. We show by means of Monte-Carlo simulation that NLLSQ fitting is as good as MLE for data lacking background noise and that NLLSQ fitting is as good as or better than MLE fitting in all conditions where random background noise up to 5% was added (for ratios of distance uncertainty to distance of up to 2). At higher levels of background noise, both methods fail to recover the true distance (**Fig. S3.18**). Overall, we observe that with

increasing background noise the NLLSQ fitting becomes more sensitive to higher values of distance uncertainty σ_d (**Fig. S3.18**).

A standard error of the mean (S.E.M.) for distance calculations using Sigma-P2D and P2D (**Fig. 3.3**) was determined by means of Fisher Information Matrix whereas bootstrapping was used for Vector-P2D and Vector (**Fig. 3.4 and 3.5**). Parameters for analysis are shown in **Table S3.4 and S3.6**.

Monte Carlo simulations

In silico two-color distance measurements by means of Monte Carlo simulation were carried out with a custom Python script. In brief, the true distance μ, the two localization errors σ_{loc_1} and σ_{loc_2}, their underlying distributions ($\sigma_{\sigma(loc\_1)}$, $\sigma_{\sigma(loc\_2)}$), sample conformational heterogeneity σ_{con}, the number of pairs observed, and the number of frames (observations) per pair can be varied in parallel. The simulation for each parameter combination can be repeated multiple times if desired. For the variance in the fluorophores localization a Gaussian distribution is applied to true positions of channel 1 and 2 and a Gamma distribution is applied as the underlying distribution of the variance in the fluorophores localization for channel 1 and 2. We analyzed model datasets based on different ratios of distance uncertainty to distance (σ_d / μ). For each ratio we evaluated 100 datasets with Sigma-P2D and P2D or Vector and Vector-P2D and calculated the average distance discrepancy. Therefore, we subtracted the expected distance from the measured distance and normalized by the expected distance. Thus, values around -1.0 represent cases for which we measured 0 nm and for which we find very small error bars showing that this is very reproducible. This is an example of a precise yet highly inaccurate measurement. Large error bars typically indicate bimodal cases for which we measured both distances that are much larger or similar to the expected distances and distances that are much smaller than the expected distance. We defined measurements as reliable when they resulted in an average distance discrepancy of less than 20% from the true distance with a standard

deviation of less than 30% of the true distance. Based on common localization errors for single-molecule studies (**Fig. S3.10**) and distances on the nanometer scale (~2-30 nm), we expect ratios (σ_d / μ) of up to 4 to be of experimental relevance. However, we included even higher ratios to probe the upper limits of Sigma-P2D and Vector-P2D.

Statistics and error calculation

For each result the inherent uncertainty due to random or systematic errors and their validation are discussed in the relevant sections of the manuscript. Details about the sample size, number of independent calculations, and the determination of error bars in plots are included in the figures and figure captions.

Acknowledgements

We thank A. Jain, D. Larsen, and T. Skokan for critical discussions of the manuscript. We are grateful to E. Jonsson for the kinesin plasmids and discussions about the kinesin distance measurements. The authors acknowledge funding from the National Institutes of Health (R01EB007187, R.D.V. and 1F32GM113366-01, J.S., and R00GM112982, G.B.), the Damon Runyon Cancer Research Foundation DFS-20-16 (G.B.) and the Howard Hughes Medical Institute.

CHAPTER 4

A 6-nm ultra-photostable DNA FluoroCube for fluorescence imaging

Abstract

Photobleaching limits extended imaging of fluorescent biological samples. We developed DNA based “FluoroCubes” that are similar in size to the green fluorescent protein (GFP), have single-point attachment to proteins, have a ~54-fold higher photobleaching lifetime and emit ~43-fold more photons than single organic dyes. We demonstrate that DNA FluoroCubes provide outstanding tools for single-molecule imaging, allowing the tracking of single motor proteins for >800 steps with nanometer precision.

Introduction

Imaging proteins and macromolecular complexes at the single-molecule level is a powerful method to study distribution, stoichiometry, dynamics and precise motion of molecular machines[121]. To achieve high spatiotemporal resolution, proteins of interest are often labeled with fluorescent probes[121]. An ideal probe is photostable (long half-life), (continuously) bright, small, and can be monovalently attached to biological molecules. While organic dyes[122,123] and fluorescent proteins[124] fulfill the latter two criteria, they often suffer from photobleaching, which leads to a low signal. Alternative probes such as quantum dots[122,125] and other fluorescent nanoparticles[126] are very bright and extremely photostable, but frequently exhibit large fluctuations in intensity (blinking). Labeling with these probes is complicated by their relatively large size[122,123,125] (~15 nm) (**Fig. S4.1**), which can perturb protein function and by the often missing control over surface chemistry, which can lead to multiple proteins attaching to the same fluorescent probe[127].

Here, we developed small (~6 nm) DNA-based FluoroCubes that have single-point attachment, exhibit continuous emission, emit up to ~43-fold more photons than single organic dyes, and have an up to ~54-fold longer half-life than single organic dyes. We show that the photostability of the DNA FluoroCubes varies with the type of organic dye attached to the DNA. We also provide some preliminary insights into the mechanism(s) for the increased photostability of DNA FluoroCubes. Attaching these DNA FluoroCubes to the microtubule-based motor protein kinesin, we were able to track its movement for more than 800 steps with nanometer precision.

Results

Design and assembly of six dye DNA FluoroCubes

Previous work established that placing organic dyes within 2 nm results in quenching[127], while dye spacing of >5 nm results in a linear intensity increase with the number of dyes[128]. We were interested in the properties of probes separated by 2 to 5 nm.

To set the position of dyes with nanometer precision, we took advantage of tools from DNA nanotechnology[128–130]. Using the single-stranded tiles (SST) approach[131,132], we designed a DNA FluoroCube composed of four 16 base-pair (bp) long double-stranded DNA helices labeled with six of the same organic dyes such as ATTO 488, ATTO 565, ATTO 647N, Cy3N (sulfonated Cy3), Cy3, or Cy5 (**Fig. 4.1, Fig. S4.1**) separated by distances ranging from ~2 to ~6 nm. We reserved one position for the placement of a functional tag such as HALO-ligand, benzylguanine (for SNAP tag), thiol, biotin, or amine to label proteins at specific locations (**Fig. 4.1**).

Since small DNA nanostructures are difficult to assemble because of high electrostatic repulsion between the negatively-charged DNA strands[133], we optimized the folding yield and determined the structural integrity of the DNA FluoroCubes after thermal annealing. Using agarose gel electrophoresis, we measured a folding yield of over 60% (**Fig. 4.1, Fig. S4.1**) and found that only folding reactions that contained all four oligos assembled into FluroroCubes (**Fig. S4.1**). Negative stain transmission electron microscopy (TEM) showed that FluoroCubes assembled into the desired shape, with slight variations (**Fig. 4.1, Fig. S4.1, Fig. S4.2**). In summary, the protocol for the assembly of FluoroCubes is easy and optimized for high yield.

Photophysical properties of six dye DNA FluoroCubes

Next, we examined the fluorescent properties of DNA FluoroCubes prepared with the commonly used fluorescent probe Cy3. We compared the six Cy3 dye FluoroCube to a single Cy3 dye attached to double-stranded DNA (dsDNA). Surface-immobilized samples were imaged by total internal reflection fluorescence (TIRF) microscopy (**Fig. 4.1**). To quantify photostability,

we determined the time when 50% of all probes photobleached (half-life) as well as the total number of photons emitted. To quantify the brightness of the different fluorescent probes, the average number of photons per frame were measured.

A single Cy3 dye conjugated to dsDNA or protein (streptavidin) (**Fig. S4.3**) displayed a constant intensity followed by one-step photobleaching (**Fig. 4.1, Fig. S4.4**). However, the six Cy3 dye FluoroCube was significantly more photostable than a single Cy3 dye bound to dsDNA (up to ~54-fold increase in half-life) (**Fig. 4.1**), and sometimes even increased in brightness during the time of acquisition (**Fig. 4.1, Fig. S4.4**). For instance, after 99% of the single Cy3 dyes bleached, more than 80% of the six Cy3 dye FluoroCubes were still in the "on" state. The total number of photons per six Cy3 dye FluoroCube was ~43-fold higher than for a single Cy3 dye bound to dsDNA (**Fig. 4.1**; $1.29 \pm 0.06 \times 10^7$ photons for the six Cy3 dye FluoroCube versus $3.1 \pm 0.5 \times 10^5$ photons for a single Cy3 dye bound to dsDNA, the latter being consistent with previous reports[134]). The six Cy3 dye FluoroCubes also blinked less than the single Cy3 dyes bound to dsDNA (**Fig. S4.5**). However, even though there are 6-fold more dyes, the brightness of a six Cy3 dye FluoroCubes was similar to a single Cy3 dye bound to dsDNA (**Fig. 4.1**). With increasing light exposure, the photon output of six Cy3 dye FluoroCubes behaved nonlinearly, as they plateaued in brightness at higher excitation powers (**Fig. S4.6**). In summary, six Cy3 dye FluoroCubes emit an average of ~43-fold more photons than single Cy3 dyes attached to dsDNA but are similar in overall brightness.

We next tested the behavior of other dyes coupled to FluoroCubes and found variable photophysical properties (**Fig. 4.1, Fig. S4.5-S4.8, Table S4.1**). The six Cy5 dye, six ATTO 647N dye, and six Cy3N dye FluoroCube also demonstrated a significant increase in photostability (34-fold, 10-fold, and 9-fold respectively) (**Fig. 4.1, Fig. S4.7**) and total number of photons (15-fold, 4-fold, and 14-fold respectively) (**Fig. 4.1, Fig. S4.7**). The six ATTO 488 dye and six ATTO 565 dye FluoroCubes were less photostable in absolute terms, but still showed a 10-fold and 8-fold increase relative to single dyes attached to dsDNA (**Fig. 4.1, Fig. S4.7**).

Intermediate photostability was observed for the six dye Janelia Fluorophores JF549 and JF646[135] (**Fig. S4.8**). As with the six Cy3 dye FluoroCube, all of the FluoroCubes were similar in brightness to their respective single dyes (**Fig. 4.1**). The various six dye FluoroCubes performed better with oxygen scavengers[76] and triplet quenchers[136] (**Fig. S4.6**). However, even without these aids all six dye FluoroCubes outperformed single dyes on dsDNA with oxygen scavengers[76] and triplet quenchers[136]. Taken together, the performance of the six dye FluoroCubes is dye dependent, but all are significantly more photostable than commonly used single organic dyes (**Fig. 4.1**) and some emit up to ~43-fold more photons than a single dye.

To further characterize our new fluorescent probes, we examined additional properties of the DNA FluoroCubes. Comparing the absorbance, excitation, and emission spectra of various six dye FluoroCubes and their respective single dyes, we found a dye charge-dependent, large increase in absorbance in a “shoulder” blue shifted from the main peak (**Fig. S4.9**). This “shoulder” absorbance is often observed for face-to-face dimers of dyes[137] and may result from the flexibility of FluoroCubes in solution and the relatively long linker (up to 1.5 nm) between dye and oligo. An alternative explanation for the observed shoulder absorbance is that face-to-face dimers form between dyes on different FluoroCubes. To test whether our six dye FluoroCubes are truly monomeric, we performed dynamic light scattering and found that the measured diameters of FluoroCube and Compact Cube agree well with their predicted diameters (**Fig. S4.10**). Moreover, the diameter distributions of the FluoroCubes are symmetric (no shoulders visible) indicating that the FluoroCubes are monodisperse in size. Additional experiments such as the measurement of the number of photobleaching steps (**Fig. S4.11**) and our previous negative stain imaging (**Fig. S4.2, Table S4.1**) confirmed the DLS data. Thus, we concluded that six dye FluoroCubes are predominantly monomeric and that the shoulder absorbance is likely caused by dyes on the same FluoroCube. Interestingly, the shoulder absorbance for six dye FluoroCubes mainly represents non-fluorescent dyes (except for the six Cy3 dye FluoroCube) as shown by comparing excitation and absorption spectra (**Fig. S4.9, Fig. S4.12**).

Lastly, we measured fluorescence lifetime and fluorescence anisotropy (**Fig. S4.13**), but did not find any change that might be correlated with increased photostability. Taken together, six dye FluoroCubes are predominantly monomeric and present a dye charge-dependent “shoulder” in absorbance that is blue shifted from the main peak.

Comparison of six dye DNA FluoroCubes and quantum dots

Next, we compared the behavior of the six ATTO 647N dye FluoroCubes to quantum dots which are known for their photostability. Quantum dots (655 Qdot Nanocrystals) emitted about four-fold more photons than six ATTO 647N dye FluoroCubes, were about four-fold brighter than six ATTO 647N dye FluoroCubes, and have a similar half-life time as six ATTO 647N dye FluoroCubes. However, quantum dots blink significantly more than DNA FluoroCubes (**Fig. S4.14**). In addition, quantum dots tend to enter dark states in which they do not emit photons for a couple of seconds (**Fig. S4.14**), making it difficult to track quantum dots continuously. Moreover, quantum dots are significantly larger in size (10-20 nm) than the six dye FluoroCubes[122,123,125] (**Fig. S4.1**) and typically not monovalent. In conclusion, six dye FluoroCubes display much more stable and uniform fluorescence than quantum dots.

Insights into potential mechanism(s) of increased photostability of six dye DNA FluoroCubes

To begin to understand the mechanism(s) behind the increase in photostability of the six dye FluoroCubes, we investigated how the DNA scaffold might influence dye photophysics. A single dye on the same FluoroCube scaffold (Single Dye Cube) (**Fig. S4.15**) displayed a slight increase in photostability and emitted between ~2 and ~10-fold more photons than corresponding one dye dsDNA (**Fig. S4.15**). Permuting through all six positions on the cube with a single Cy3N dye (**Fig. S4.16**), we noticed a higher photostability (~3-fold longer half-life time) when the dye is attached to the 5’ end compared to the 3’ end of the same oligo (**Fig.**

S4.16). Together, these data show that the local environment of the DNA (Single Dye Cube vs. one dye dsDNA) and the dye position (attachment linkage) can influence photostability.

To further investigate the effect of the geometry of dye placement on photostability, we compared the photostability of the six Cy3 dye FluoroCubes to the same number of Cy3 dyes on an 8-fold (by volume) larger structure (the previously described Compact Cube[133]), which places the dyes between ~6 and ~10 nm from one another (**Fig. S4.17**). The Compact Cube with one Cy3 dye behaved very similar to a Single Cy3 Dye Cube (**Fig. S4.17**), while the Compact Cube with six Cy3 dyes had a slight increase in photostability but far less than the six Cy3 dye FluoroCube. Thus, increasing the distances between the dyes from ~2-6 nm (FluoroCube) to ~6-10 nm (Compact Cube) decreases photostability, indicating the importance of distance between dyes for the photostability effect. We speculate that both direct dye interactions as well as resonance energy transfer between individual dyes in a FluoroCube play roles in this phenomenon (**Fig. S4.18**), although additional work is required to fully understand the photophysical mechanisms underlying six dye DNA FluoroCube photostability.

Tracking steps of a single kinesin over more than 6 µm

We next tested whether FluoroCubes can be attached to proteins and used for prolonged readouts of activity. For this purpose, we labeled an ultra processive kinesin KIF1A[138] with a six ATTO 647N dye FluoroCube using a C-terminal HALO-tag (**Fig. 4.2**) and imaged it moving along axonemes. To ensure that a FluoroCube labeled kinesin behaves similar to a single dye labeled kinesin (single TMR HALO-dye), we compared velocity and processivity and found almost identical values indicating that FluoroCubes do not interfere with protein function in this assay (**Fig. S4.19**). Labeling kinesin with a single six dye FluoroCube enabled us to record more than 800 steps of an individual motor with nanometer precision (**Fig. S4.2**). The trace in Figure 2 revealed an on-axis step size of 7.8 nm with almost no off-axis stepping (**Fig. S4.2**) which is in good agreement with previous reports[138,139] (discussion in **Fig. S4.20**). Moreover,

using six ATTO 647N dye FluoroCubes allowed us to collect more than 6,000 data points of an individual motor compared to approximately 200 data points that can be collected at a similar resolution with a single organic dye[140,141]. By recording very long traces, we could detect occasional pausing and velocity fluctuations within the trace of an individual kinesin (**Fig. 4.2**). Previous work demonstrated that different kinesins can have different velocities[142], but our prolonged observations showed that even individual kinesins undergo considerable velocity fluctuations over time.

Discussion

We developed small (~6-nm), ultra-photostable fluorescent probes. We have shown that six dye DNA FluoroCubes can emit up to 43-fold more photons and have an up to ~54-fold longer half-life than single organic dyes, making them ideal for long-term imaging. Comparing six dye FluoroCubes to single organic dyes, we found that the increase in photostability is dye specific. Currently, the six ATTO 647N dye and six Cy3N dye FluoroCubes demonstrate the most desirable properties, since they have the longest half-life and emit the most photons per probe (**Fig. 4.1**). Even the poorest performing six dye FluoroCube (ATTO 488) has a 10-fold longer half-life and emits 6-fold more photons than a single organic dye. Quantum dots are fluorescence emitters with comparable long half-lives. However, quantum dots exhibit significantly more blinking than FluoroCubes, and their larger size and multivalent attachment[122,123,125] makes them more challenging to use as a non-invasive probe for protein activity. Applying the six ATTO 647N dye FluoroCube to single-molecule imaging, we were able to track the movement of the motor protein kinesin with nanometer precision over more than 800 steps (**Fig. 4.2**) without any evidence of perturbation by the probe.

We investigated potential mechanism(s) that contribute to increased photostability of the six dye DNA FluoroCubes and found that the local environment of the DNA and the dye position (attachment linkage) influence photostability. We also found that increased photostability disappears when the spacing between dyes increases from ~2-6 nm (FluoroCubes) to ~6-10 nm (Compact Cubes[133]) in a similar DNA-based scaffold. Based on these observations, we speculate that resonance energy transfer between individual dyes in a six dye DNA FluoroCube contributes to the increased photostability. However, a more detailed understanding of the mechanism(s) for the increased photostability awaits further studies. It is also likely that further optimizations could be made to improve photostability. Based on our current work, we suggest that improvements could be achieved by using other dyes such as self-healing fluorophores[134], by adding DNA intercalating dyes[143], by increasing the number of fluorophores on the

FluoroCube[128], by changing the spacing between dyes (either by changing the cube size[127,133] or by alternating the dye linker length), or by changing the sequence of the oligonucleotide close to the attachment of fluorophores[144].

DNA FluoroCubes are easily prepared from commercially available reagents and can be attached to all commonly used protein tags, making them simple to use for in vitro studies. We anticipate that DNA FluoroCubes will become the reagent of choice for in vitro and extracellular single-molecule imaging experiments. Beyond single-molecule studies, the long photobleaching-lifetime and high number of total photons of DNA FluoroCubes could prove useful in numerous other fluorescence imaging applications, including FISH[145], MERFISH[146], DNA-PAINT[147], or immunofluorescence for research and medical diagnosis.

Figures and figure legends

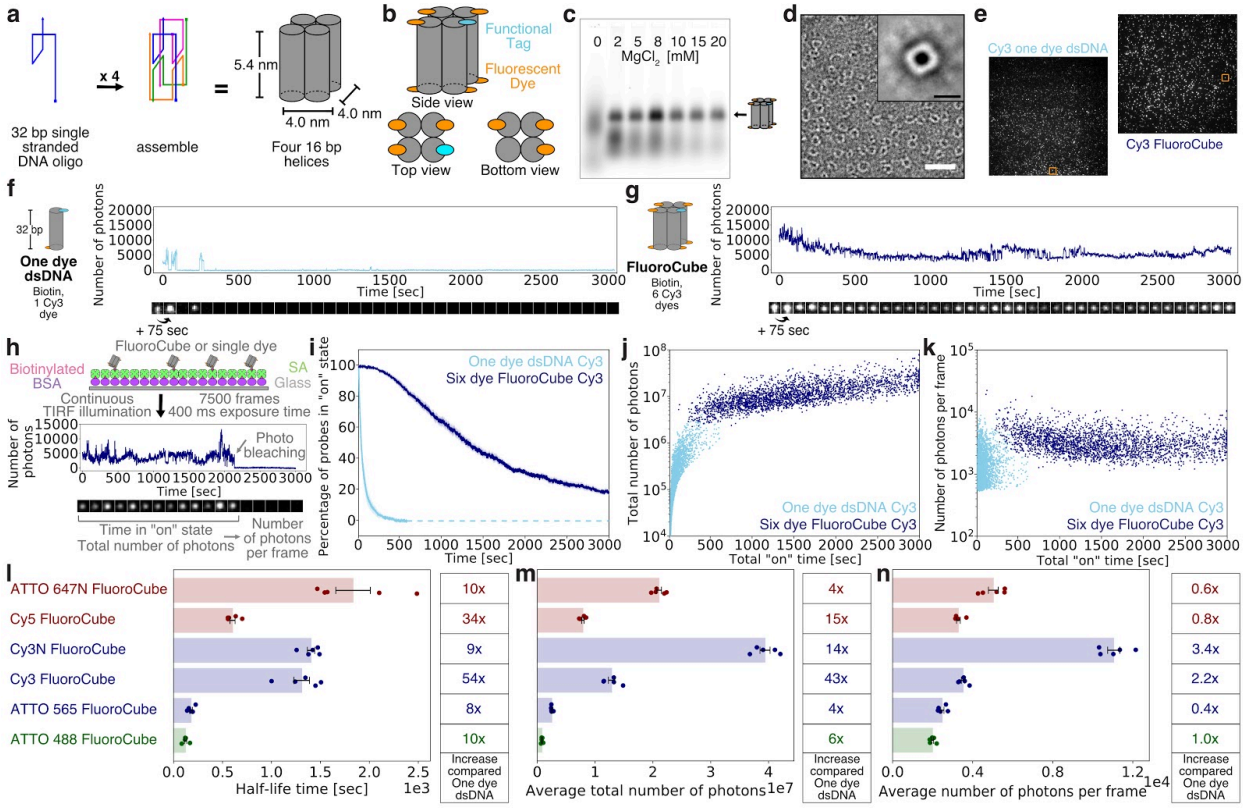

Figure 4.1 | Design, assembly, and photophysical properties of DNA FluoroCubes. (a) Design and shape of DNA FluoroCubes. (b) Cartoon depicting how each of the 5' and 3' ends of the DNA can be functionalized. For the DNA FluoroCube design we used six fluorophores and one functional tag such as HALO-ligand, benzylguanine for SNAP tag, thiol, biotin, or amine. (c) 3.0% agarose gel of DNA FluoroCubes after thermal annealing. The four ssDNA strands are annealed with different $MgCl_2$ concentrations. Quantification of assembly yield is shown in **Figure S4.1**. Here the ssDNAs were modified with six ATTO 647N dyes and one biotin. (d) Negative stain electron microscopy image of DNA FluoroCubes. Insert shows class average of 983 particles. Here the FluoroCube was labeled with six ATTO 647N dyes and one biotin. White scale bar: 30 nm. Black scale bar: 6 nm. Class averaging was performed once. (e) Example TIRF image of a biotin functionalized six Cy3 dye FluoroCube and a 32 bp long double-stranded DNA (dsDNA) with one Cy3 dye. Orange boxes show molecules whose intensity traces are shown in f (one dye dsDNA) and g (FluoroCube). (f, g) Example intensity trace of (f) Cy3 one dye dsDNA and (g) six Cy3 dye FluoroCube with one biotin. (h) Experimental setup for quantification of photophysical properties of six dye FluoroCubes and one dye dsDNA. Intensity traces of single-molecules are analyzed for time in "on" state (half-life), total number of photons, and number of photons per frame. (i) Photostability of six Cy3 dye FluoroCubes and Cy3 one dye dsDNA. The survival rate was quantified by counting the percentage of probes in the "on" state at any given time from 0 to 3,000 seconds. Opaque color is the standard error of the mean of five or four repeats (six dye FluoroCubes or one dye dsDNA, respectively) with more than 500 molecules each. Once all probes photobleached data analysis was terminated. This is indicated by the dashed line. (j) Total number of photons of six Cy3 dye FluoroCubes and Cy3 one dye dsDNA as a function of the total "on" time at the single-molecule level (pooled from all experiments). (k) Average number of photons per frame of six Cy3 dye FluoroCubes and Cy3

one dye dsDNA as a function of the total “on” time at the single-molecule level (pooled from all experiments). (l-n) Bar plot of the (l) half-life time, (m) average of the total number of photons, and (n) average number of photons per frame of six dye DNA FluoroCubes with different fluorophores. The error bars show the standard error of the mean of five repeats with more than 100 molecules each. Dots show the values of individual experiments. The tables on the right show fold increase of six dye DNA FluoroCubes compared to one dye dsDNA. (i-n) Each experiment was repeated five or four times with freshly assembled six dye FluoroCubes or one dye dsDNA, respectively. For every experiment we prepared new microscope slides. Exact numbers (also of the sample size) are given in **Table S4.1 and S4.2**. SA is Streptavidin. “Cy3” stands for the non-sulfonated version of Cy3 whereas “Cy3N” stands for the sulfonated version of Cy3. “n.m.” is not measured.

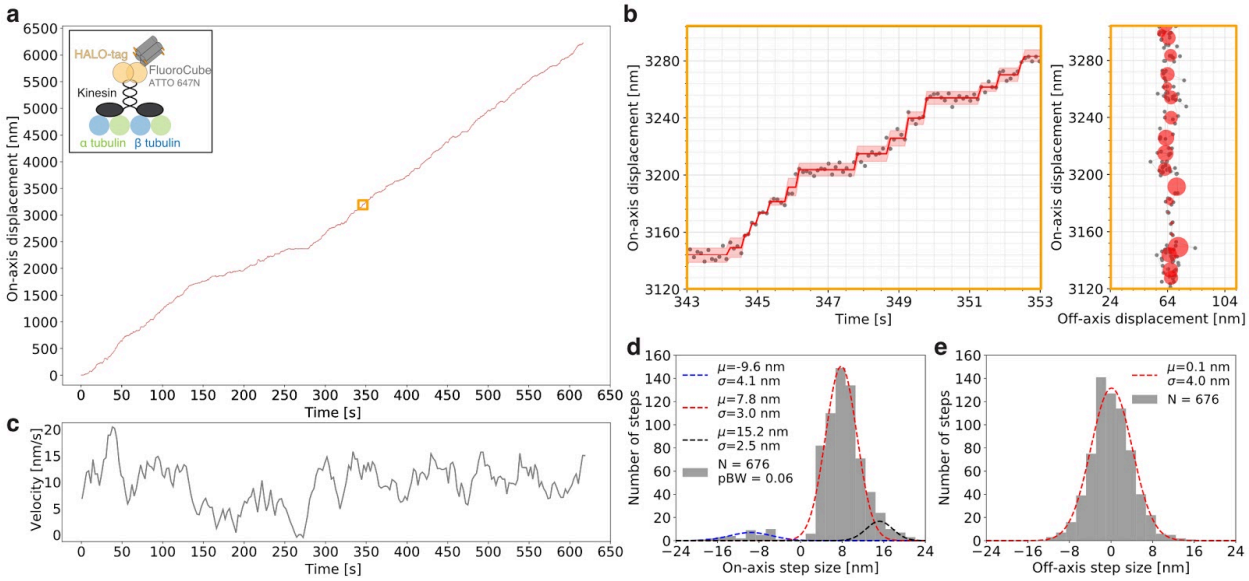

Figure 4.2 | Tracking steps of a single kinesin over more than 6 µm. (a) Raw stepping data with position versus time of one kinesin (grey dots) over 6 µm with detected steps (red line) along an axoneme. The opaque red line shows the standard deviation for each step. The insert shows the experimental setup for which a kinesin is labeled with one six dye ATTO 647N FluoroCube with a HALO-tag (for details see **Materials and Methods**). The orange box is enlarged in b. (b) Left: Zoom-in on the raw stepping data with position versus time of a single kinesin as shown in a. Right: Same trace as on the left but in XY space. The grey dots are raw data and the red circles show the fitted position for which the radius corresponds to the standard deviation. (c) Velocity over time for the stepping trace of a single kinesin as shown in a. The grey line shows a moving average of velocity binned into 15.6 sec (for details see **Materials and Methods**). (d) Histogram of the on-axis step size distribution of the data shown in a. The data was split into positive and negative steps and fit with Gaussians. For the negative steps, a single Gaussian was used (blue) whereas for the positive steps two Gaussians were used (red, black). pBW is the fraction of backward steps. (e) Histogram of the off-axis step size distribution of the data shown in a fitted with a single Gaussian. (d, e) We detected 821 steps but only used 676 steps for further quantification because we only counted steps for which the step itself, the previous and the following step had a standard deviation of less than 4 nm. (a-e) All data shown here is from a single kinesin stepping trace (sample size n =1). However, we analyzed and quantified additional stepping traces of more motors and found very similar results (**Fig. S4.20**).

Supplemental figures and tables with legends

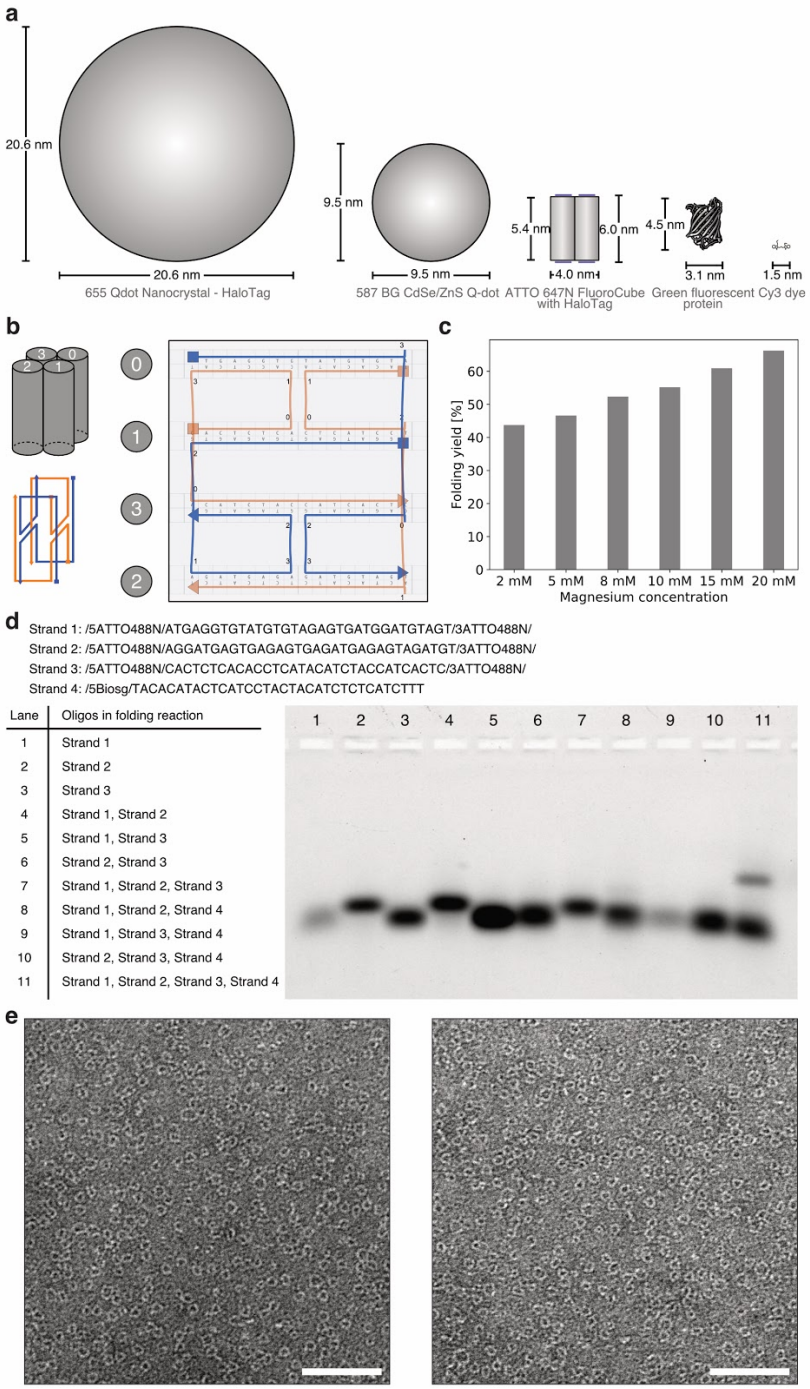

Figure S4.1 | Size, design, folding yield, and negative stain images of DNA FluoroCubes. (a) Size comparison of fluorescent probes. From left to right: HALO ligand modified 655 Qdot Nanocrystal[61], benzylguanine (BG) modified 587CdSe/ZnS Q-dot[125], ATTO 647N FluoroCube with one HALO ligand[103], green fluorescent protein[108], and Cy3 dye. (b) Routing of four 32 bp long single-stranded DNAs (ssDNA) that are connected using crossovers. Two strands are blue and two strands are orange. The sequence is depicted below the ssDNA. A detailed list of

sequences with exact modifications for all FluoroCubes used in this study is shown in **Table S4.3**. The DNA routing was designed using caDNAno[130]. (c) Folding yield of six ATTO 647N dye FluoroCubes at different $MgCl_2$ concentrations from the 3.0% agarose gel shown in **Figure S4.1**. The folding yield was quantified using ImageJ[75]. More details about the quantification are given in the **Materials and Methods**. (d) 3.0% agarose gel of folding reactions with different oligonucleotides (oligos). Every oligo in the folding reactions was used at 1 μM. The sequence of each oligo and the corresponding modification is listed above. The gel was scanned with a Typhoon scanner using an excitation wavelength of 488 nm. We purified the slower migrating band from lane 11 and confirmed that it assembled into a FluoroCube by negative stain electron microscopy. We repeated this experiment twice with new folding reactions and always saw a very similar migration pattern. Overall, this gel shows that the FluoroCubes run as a single, distinct band that is different from single oligos. Moreover, this gel shows that the FluoroCube only assembles if all four oligos are present in the folding reaction. (e) Two additional negative stain transmission electron microscopy (TEM) images of six dye ATTO 647N FluoroCube with one biotin. We repeated the electron microscopy imaging with six dye ATTO 647N FluoroCubes with one biotin two times with freshly assembled FluoroCubes and always saw similar results. Negative stain TEM images of six dye FluoroCubes with other dyes are shown in **Figure S4.2**. The scale bar is 60 nm.

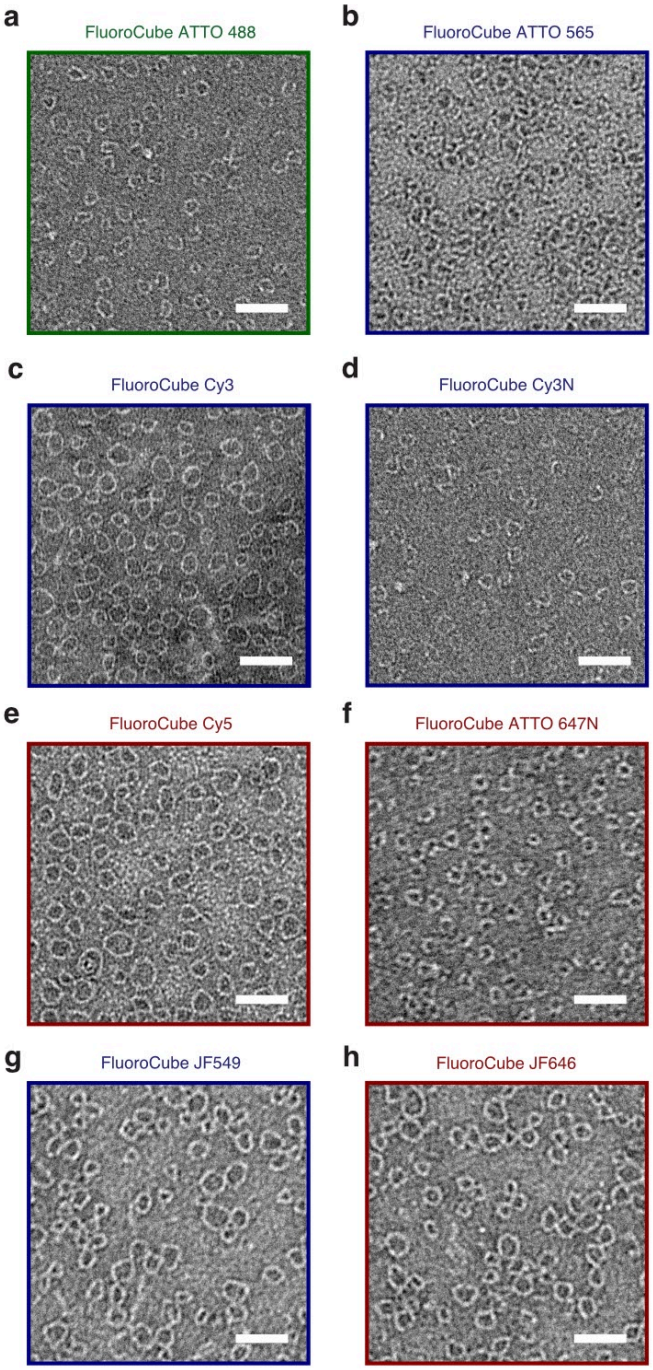

Figure S4.2 | Negative stain electron microscopy shows size variation of DNA FluoroCubes with different fluorophores. Section of micrographs from negative stain TEM for FluoroCubes with one biotin and six fluorophores of (a) ATTO 488, (b) ATTO 565, (c) Cy3, (d) Cy3N, (e) Cy5, (f) ATTO 647N, (g) JF549, and (h) JF646. (a-h) Scale bar is 30 nm. “Cy3” stands for the non-sulfonated version of Cy3 whereas “Cy3N” stands for the sulfonated version of Cy3. The average diameter of FluoroCubes is given in **Table S4.1 and S4.2**. This negative stain imaging was performed once with the exception of the six dye ATTO 647N FluoroCube with one biotin, which was performed three times (with freshly assembled FluoroCubes), the six dye ATTO 488 FluoroCube with one biotin, which was performed two times (with freshly assembled

FluoroCubes), the six dye Cy3 FluoroCube with one biotin, which was performed two times (with freshly assembled FluoroCubes), the six dye Cy3N FluoroCube with one biotin, which was performed two times (with freshly assembled FluoroCubes) and the six dye Cy5 FluoroCube with one biotin, which was performed two times (with freshly assembled FluoroCubes). We noticed a correlation between the dye-oligo linker length and shape; FluoroCubes with six ATTO dyes and with the sulfonated Cy3 (Cy3N) have a ~1.5 nm long linker and assembled into cubes with the predicted size, whereas FluoroCubes made with six non-sulfonated cyanine dyes have no linker and folded into slightly larger cubes with a hollow center.

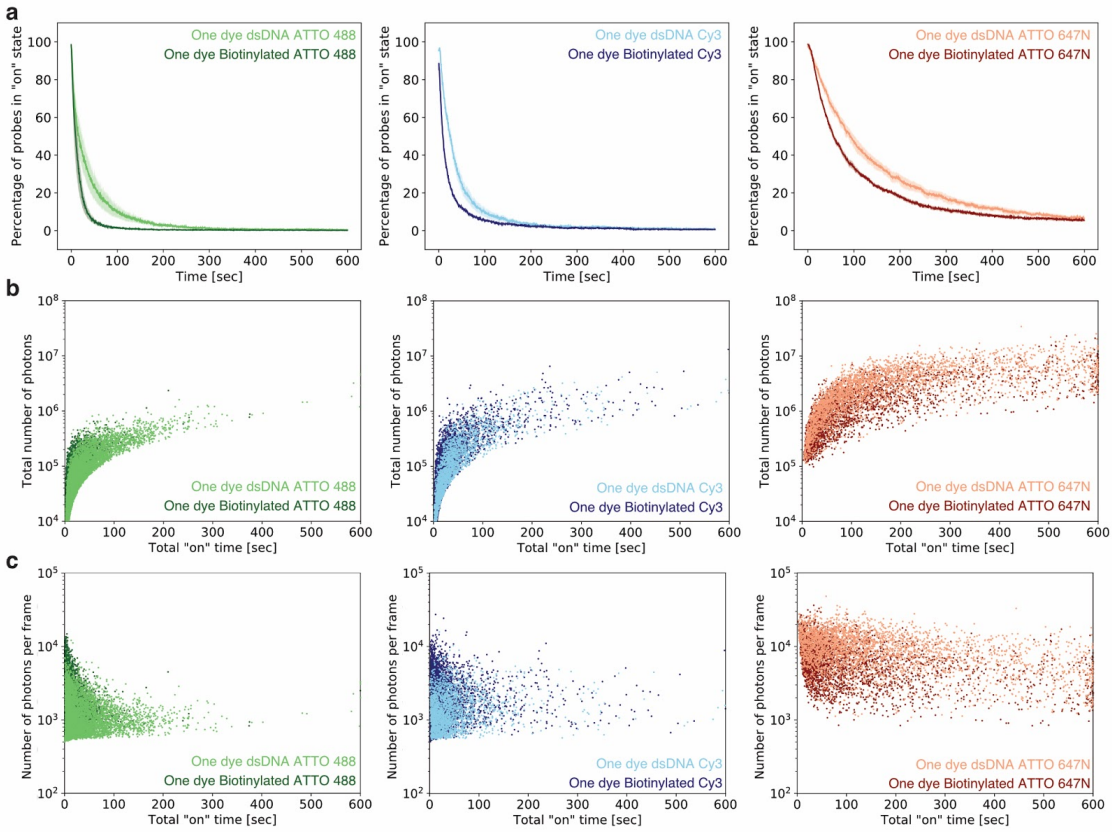

Figure S4.3 | Photophysical properties for single dyes bound to double-stranded DNA and biotinylated dyes bound to streptavidin are similar. (a) Photostability of biotinylated dyes bound to streptavidin (One dye Biotinylated) and dyes conjugated to double-stranded DNA (One dye dsDNA) with ATTO 488, Cy3, and ATTO 647N. Survival rate was quantified by counting the percentage of probes in the "on" state at any given time from 0 to 600 seconds. Opaque color is the standard error of the mean of four repeats with more than 180 molecules each. (b) Total number of photons of biotinylated dyes and one dye dsDNA as a function of the total "on" time at the single-molecule level (pooled from all four experiments). (c) Average number of photons per frame of biotinylated dyes and one dye dsDNA as a function of the total "on" time at the single-molecule level (pooled from all four experiments). (a-c) Each experiment was repeated four times with freshly assembled one dye double-stranded DNA and on new microscope slides. For the single, biotinylated dyes, we always used a new dye aliquot from the same stock that was previously aliquoted. Exact numbers (also of the sample size) are given in **Table S4.11**.

The photophysical properties of one dye dsDNA were similar to single, biotinylated dyes bound to streptavidin. Overall, the one dye dsDNA performed slightly (~1.5 fold) better than biotinylated dyes. Taken together, the one dye dsDNA serve as a good reference for the performance of single dyes.

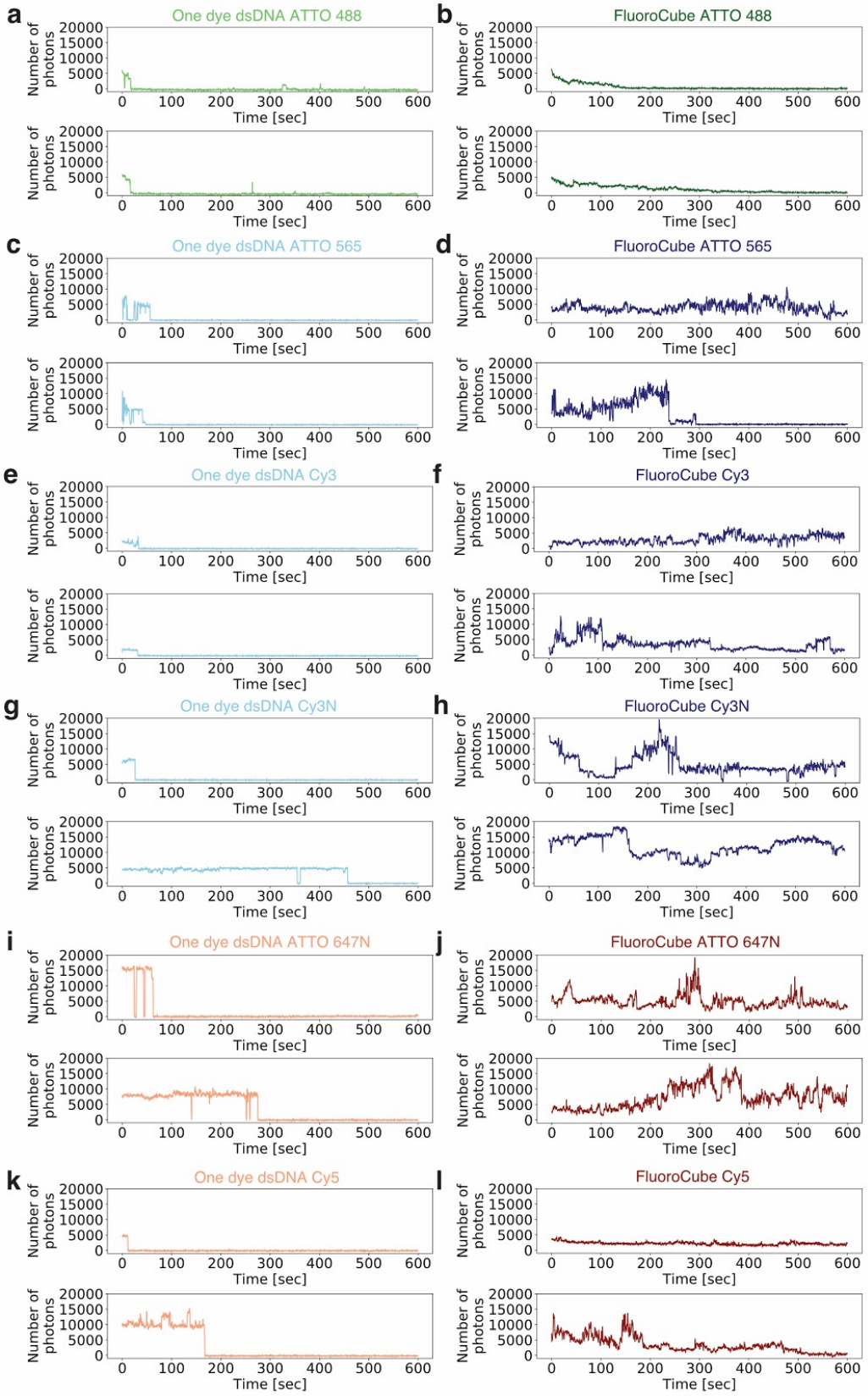
a
One dye dsDNA ATTO 488
b
FluoroCube ATTO 488
c
One dye dsDNA ATTO 565
d
FluoroCube ATTO 565
e
One dye dsDNA Cy3
f
FluoroCube Cy3
g
One dye dsDNA Cy3N
h
FluoroCube Cy3N
i
One dye dsDNA ATTO 647N
j
FluoroCube ATTO 647N
k
One dye dsDNA Cy5
l
FluoroCube Cy5
Number of photons
Time [sec]

Figure S4.4 | Intensity traces of DNA FluoroCubes and one dye double-stranded DNA with various fluorophores. Example intensity traces of the first 600 seconds of FluoroCubes (cube with six dyes) and one dye double-stranded DNA (one dye dsDNA) used to quantify the photophysical properties shown in **Figure 4.1** and **Figure S4.5 and S4.7** are presented. (a) Two example intensity traces for ATTO 488 one dye dsDNA. (b) Two example intensity traces for six dye ATTO 488 FluoroCubes. (c) Two example intensity traces for ATTO 565 one dye dsDNA. (d) Two example intensity traces for six dye ATTO 565 FluoroCubes. (e) Two example intensity traces for Cy3 one dye dsDNA. (f) Two example intensity traces for six dye Cy3 FluoroCubes. (g) Two example intensity traces for Cy3N one dye dsDNA. (h) Two example intensity traces for six dye Cy3N FluoroCubes. (i) Two example intensity traces for ATTO 647N one dye dsDNA. (j) Two example intensity traces for six dye ATTO 647N FluoroCubes. (k) Two example intensity traces for Cy5 one dye dsDNA. (l) Two example intensity traces for six dye Cy5 FluoroCubes. (a-l) These are example intensity traces (representative) from the same dataset as quantified in **Figure 4.1** and **Figure S4.5 and S4.7**. Thus, these are traces selected from movies of the five or four repeats with freshly assembled six dye FluoroCubes or one dye double-stranded DNA, respectively, and on new microscope slides. Note, “Cy3” stands for the non-sulfonated version of Cy3 whereas “Cy3N” stands for the sulfonated version of Cy3.

We speculate that the intensity fluctuations (increase in brightness over time) (**Fig. S4.5**) of six dye FluoroCubes result from one or more dye(s) bleaching and therewith no longer quenching other dyes so that the overall intensity increases. This observation agrees well with the fact that FluoroCubes and one dye dsDNA have a similar average brightness (**Fig. S4.1**).

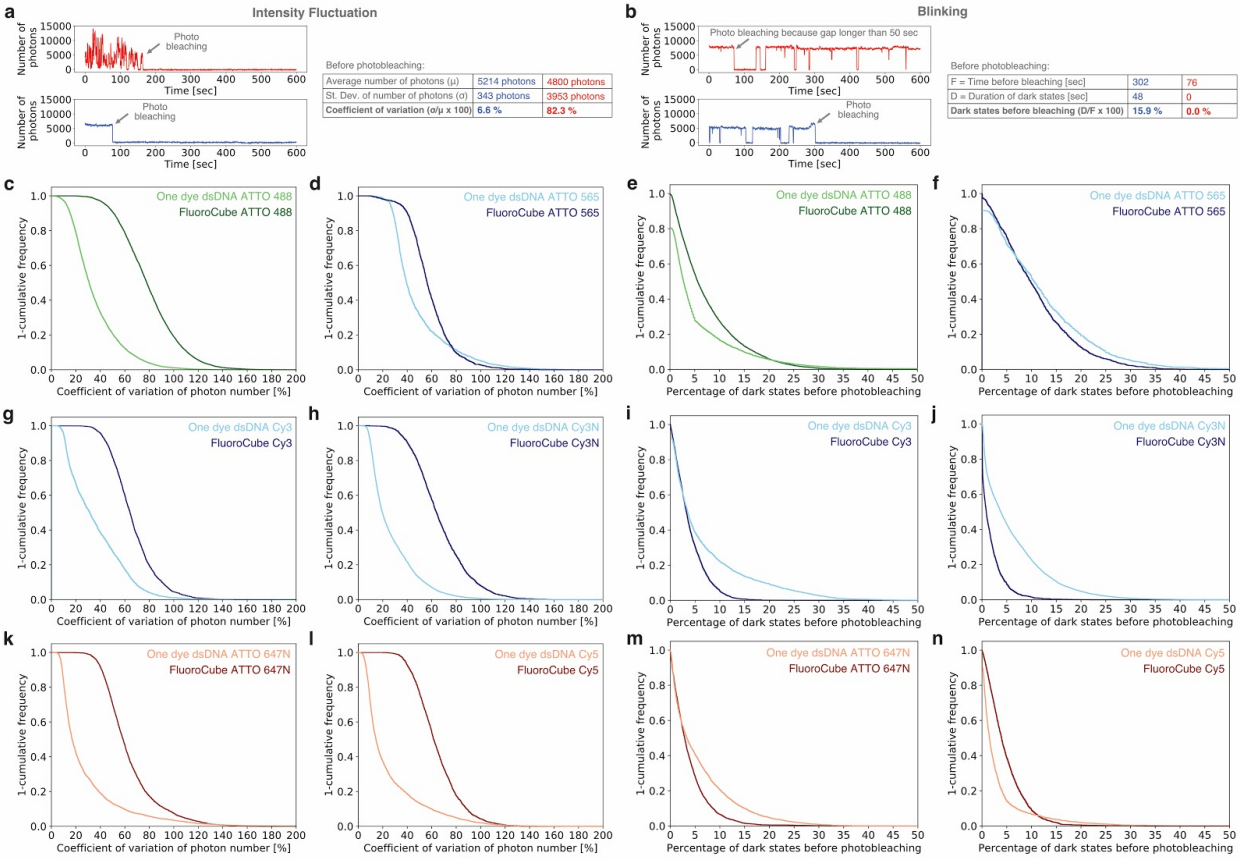

Figure S4.5 | Intensity fluctuation and blinking analysis of DNA FluoroCubes and one dye double-stranded DNA. (a) To quantify the intensity fluctuations of FluoroCubes we calculated the average number of photons and the standard deviation (St. Dev.) of number of photons per molecule up to the event of photobleaching. Using these values we determined the coefficient of variation as a measure of intensity fluctuations. The top, red trace shows a Single Dye Cube that blinks a lot, whereas the bottom, blue trace shows a Single Dye Cube with little blinking. Cumulative frequency plot of the coefficient of variation of FluoroCubes (cube with six dyes) and one dye double-stranded DNA (dsDNA) with (c) ATTO 488, (d) ATTO 565, (g) Cy3, (h) Cy3N, (k) ATTO 647N, and (l) Cy5 dyes.

(b) To quantify the blinking of FluoroCubes we calculated the time spent in dark states up to the event of photobleaching. Once a probe spent more than 50 seconds in a dark state we termed it photobleached (see red, upper trace). Both traces shown here are from a one dye dsDNA ATTO 647N. Cumulative frequency plot of the percentage of dark states before photobleaching of FluoroCubes (cube with six dyes) and one dye double-stranded DNA (dsDNA) with (e) ATTO 488, (f) ATTO 565, (i) Cy3, (j) Cy3N, (m) ATTO 647N, and (n) Cy5 dyes. (c-n) The data shown is pooled from all five or four repeats (six dye FluoroCubes or one dye double-stranded DNA, respectively) with more than 200 molecules each. Each experiment was performed with freshly assembled six dye FluoroCubes or one dye double-stranded DNA. For every experiment we prepared new microscope slides. Exact numbers (also of the sample size) are given in **Table S4.1**. Note, “Cy3” stands for the non-sulfonated version of Cy3 whereas “Cy3N” stands for the sulfonated version of Cy3.

Overall, the six dye FluoroCubes fluctuate more in intensity than one dye dsDNA. This is likely because the six dye FluoroCubes are getting brighter or dimmer over time, while single dyes typically keep a constant intensity until they photobleach (**Fig. S4.4**). In addition, six dye FluoroCubes blink less (enter dark states) than single dyes attached to dsDNA. This might be

because six dye FluoroCubes have multiple dyes which can compensate for one another (one turns dark, while the other dyes stay “on”) whereas when a single dye enters a dark state, the entire probe is dark.

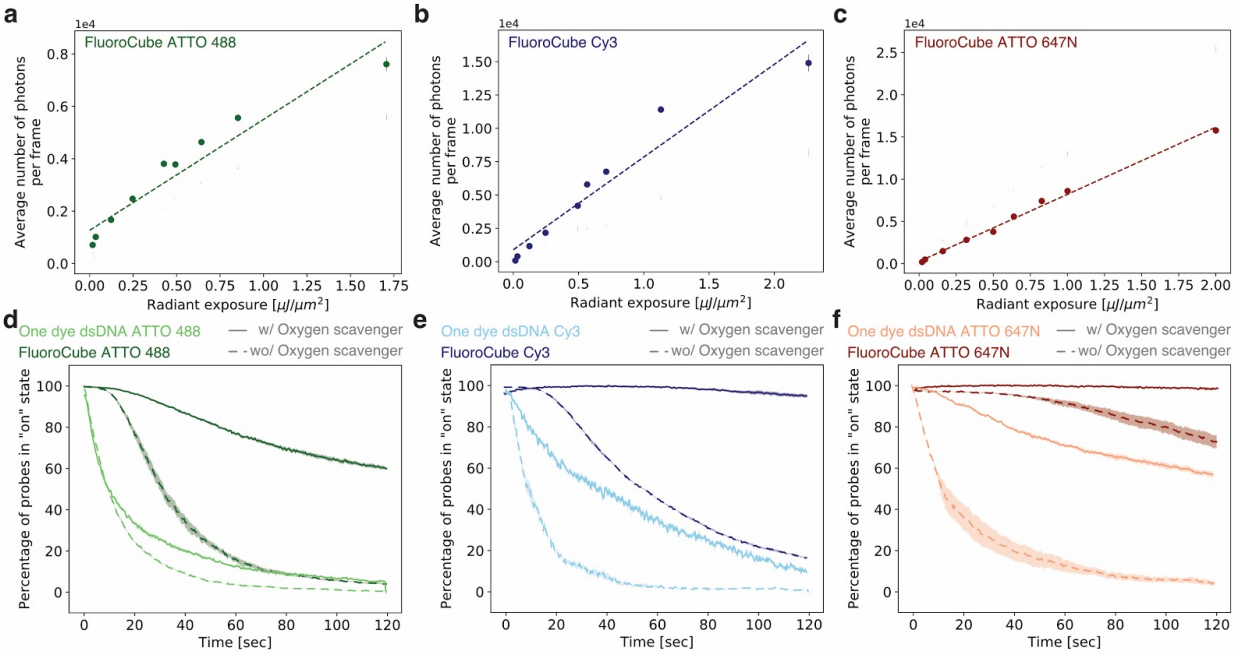

Figure S4.6 | Fluorescence intensity dependence on excitation power and effect of oxygen scavengers / triplet state quenchers. (a-c) Radiant exposure was changed by reducing/increasing the laser power and/or by adjusting the exposure time for the imaging of FluoroCubes (cube with six dyes). A detailed list of all imaging conditions is provided in **Table S4.8**. (a) Average number of photons per frame of three repeats as a function of radiant exposure for six dye ATTO 488 FluoroCubes (dark green dots). Dashed line is linear fit. Error bars show the standard error of the mean of three repeats (with freshly assembled six dye FluoroCubes on new microscope slides) with more than 1,000 molecules each. For most data points the error was around or less than 1% and thus the error bar is not visible. (b) Average number of photons per frame of three repeats as a function of radiant exposure for six dye Cy3 FluoroCubes (dark blue dots). Dashed line is linear fit. The error bars show the standard error of the mean of three repeats (with freshly assembled six dye FluoroCubes on new microscope slides) with more than 200 molecules each. For most data points the error was around or less than 1% and thus the error bar is not visible. (c) Average number of photons per frame of three repeats as a function of radiant exposure for six dye ATTO 647N FluoroCubes (dark red dots). Dashed line is linear fit. The error bars show the standard error of the mean of three repeats (with freshly assembled six dye FluoroCubes on new microscope slides) with more than 200 molecules each. For most data points the error was around or less than 1% and thus the error bar is not visible. (a-c) For the six ATTO 488 dye and the six Cy3 dye FluoroCube a nonlinear dependence is observed. (d) Photostability of one dye double-stranded DNA (light green) and six dye FluoroCubes with ATTO 488 (dark green) with the PCA/PCD oxygen scavenging[76] and the Trolox triplet state quenching system[136] present (solid line) or absent (dashed line). (e) Photostability of one dye double-stranded DNA (light blue) and six dye FluoroCubes with Cy3 (dark blue) with the PCA/PCD oxygen scavenging[76] and the Trolox triplet state quenching system[136] present (solid line) or absent (dashed line). (f) Photostability of one dye double-stranded DNA (light red) and six dye FluoroCubes with ATTO 647N (dark red) with the PCA/PCD oxygen scavenging[76] and the Trolox triplet state quenching system[136] present (solid line) or absent (dashed line). (d-f) The survival rate was quantified by counting the percentage of probes in the “on” state at any given time from 0 to 120 seconds. Opaque color is the standard error of the mean of three repeats (with freshly assembled six dye FluoroCubes on new microscope slides) with more than 80 molecules each.

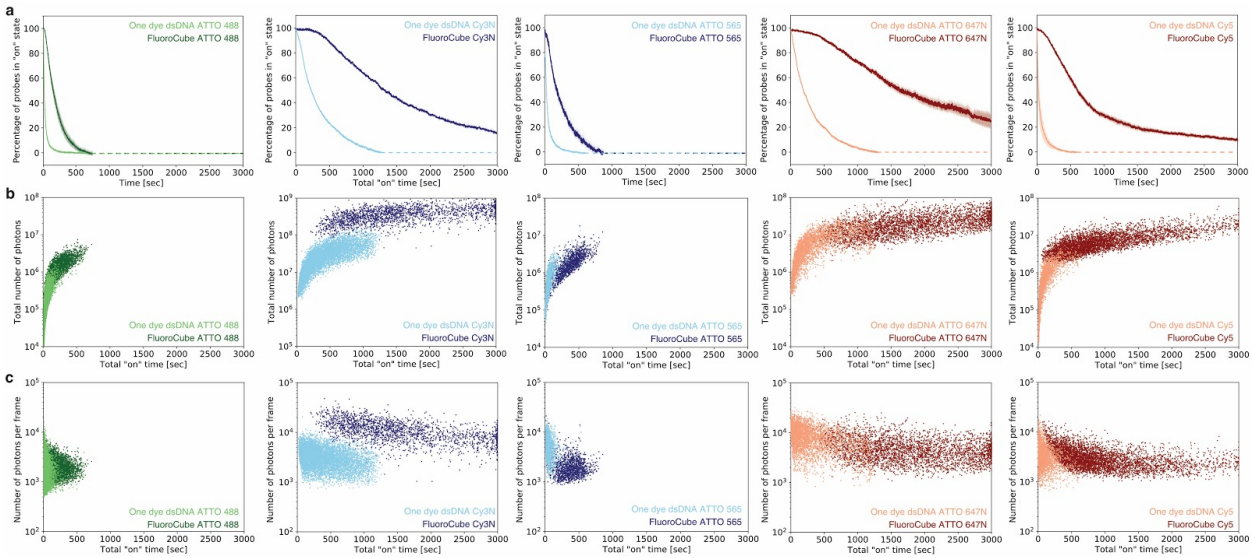

Figure S4.7 | Quantification of photophysical properties of DNA FluoroCubes and one dye double-stranded DNA with ATTO 488, Cy3N, ATTO 565, ATTO 647N, and Cy5. The experimental setup is as depicted in **Figure S4.1**. (a) Photostability of FluoroCubes (cube with six dyes) and one dye double-stranded DNA (one dye dsDNA) with different fluorophores. The survival rate was quantified by counting the percentage of probes in the "on" state at any given time from 0 to 3,000 seconds. Opaque color is the standard error of the mean of five or four repeats (six dye FluoroCubes or one dye double-stranded DNA, respectively) with more than 250 molecules each. Once all probes photobleached data analysis was terminated. This is indicated by the dashed line. (b) Total number of photons of six dye FluoroCubes and one dye dsDNA as a function of the total "on" time at the single-molecule level (pooled from all five or four experiments (six dye FluoroCubes or one dye double-stranded DNA, respectively)). (c) Average number of photons per frame of six dye FluoroCubes and one dye dsDNA as a function of the total "on" time at the single-molecule level (pooled from all five or four experiments (six dye FluoroCubes or one dye double-stranded DNA, respectively)). Note, "Cy3" stands for the non-sulfonated version of Cy3 whereas "Cy3N" stands for the sulfonated version of Cy3. (a-c) Each experiment was repeated five or four times with freshly assembled six dye FluoroCubes or one dye double-stranded DNA, respectively. For every experiment we prepared new microscope slides. Exact numbers (also of the sample size) are given in **Table S4.1**.

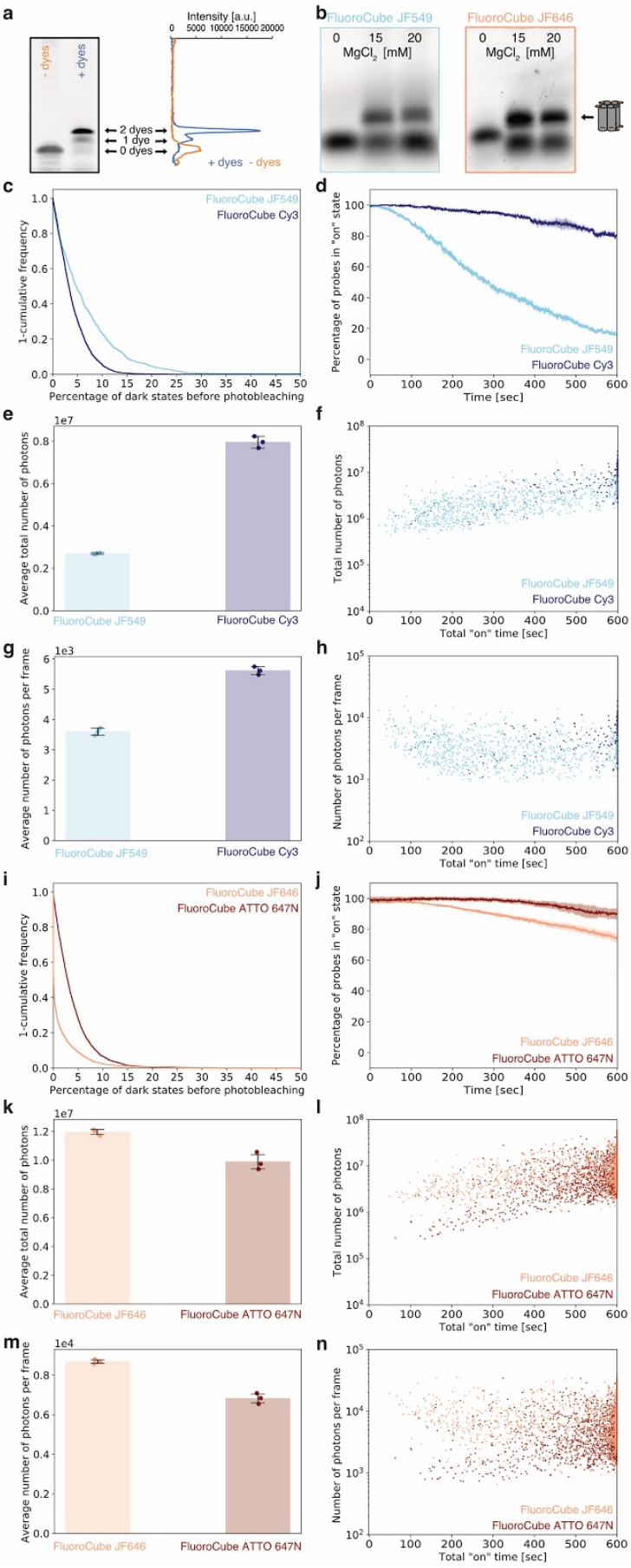
a
- dyes
+ dyes
Intensity [a.u.]
0 5000 10000 15000 20000
2 dyes
1 dye
0 dyes
+ dyes - dyes
b
FluoroCube JF549
FluoroCube JF646
0 15 20
MgCl2 [mM]
c
FluoroCube JF549
FluoroCube Cy3
1-cumulative frequency
Percentage of dark states before photobleaching
d
Percentage of probes in "on" state
Time [sec]
e
1e7
Average total number of photons
f
Total number of photons
Total "on" time [sec]
g
1e3
Average number of photons per frame
h
Number of photons per frame
i
FluoroCube JF646
FluoroCube ATTO 647N
j
k
1e7
l
m
1e4
n

Figure S4.8 | DNA FluoroCubes with Janelia Fluorophores JF549 and JF646. Since we noticed that the photophysical properties of six dye FluoroCubes depend on the dye, we asked if the widely-used and very photostable Janelia Fluorophores JF549 and JF646[135] can improve the performance of FluoroCubes even further. We conjugated NHS ester Janelia Fluorophores JF549 and JF646 to amine modified oligos, assembled them into six dye FluoroCubes and compared their photophysical properties to those of six dye FluoroCubes with Cy3 or ATTO 647N, respectively. We again observed dye dependent behavior. While the six dye JF646 FluoroCubes behaved equally well as the six dye ATTO 647N FluoroCubes, the six dye JF549 FluoroCubes performed significantly worse than the six dye Cy3 FluoroCubes.

(a) Labeling yield of amino group modified oligos with Janelia Fluorophores JF549 and JF646. Left PAGE column: Amino group modified oligos, which were not reacted with dyes. Right PAGE column: Amino group modified oligos, which were reacted with either Janelia Fluorophores JF549 or JF646. Labeling of ssDNA with one or two fluorophores causes a gel shift. Based on the intensity trace of a silver stained PAGE, we estimated the dual dye labeling efficiency to 76% using ImageJ[75]. More details about the labeling reaction are described in the **Materials and Methods**. (b) 2% agarose gel of six dye FluoroCubes with Janelia Fluorophores JF549 and JF646 after thermal annealing. The four ssDNA strands are annealed at different $MgCl_2$ concentrations. Negative stain TEM images are shown in **Figure S4.2**. (a, b) The oligo labeling with JF549 and JF646 was only performed once and the labeled oligos were used in all folding reactions used for the subsequent experiments. The PAGE was only run once whereas the agarose gel electrophoresis was repeated twice with very similar outcomes. (c-n) Note, that the data shown here is over 600 seconds and not over 3,000 seconds. (c) Cumulative frequency plot of the percentage of dark states before photobleaching to quantify blinking of six dye FluoroCube with JF549 (light blue) and six dye FluoroCube with Cy3 (dark blue). (d) Photostability of six dye FluoroCube with JF549 (light blue) and six dye FluoroCube with Cy3 (dark blue). The survival rate was quantified by counting the percentage of probes in the “on” state at any given time from 0 to 600 seconds. Opaque color is the standard error of the mean of three repeats with more than 100 molecules each. (e) Bar plot of the average of the total number of photons of three repeats of six dye FluoroCube with JF549 (light blue) and six dye FluoroCube with Cy3 (dark blue). The error bars show the standard error of the mean of three repeats with more than 100 molecules each. Dots show the values of individual experiments. Note, that the average of the total number of photons will be significantly higher than shown here because not all probes bleached within 600 seconds. (f) Total number of photons of six dye FluoroCube with JF549 (light blue) and six dye FluoroCube with Cy3 (dark blue) as a function of the total “on” time at the single-molecule level (pooled from all three experiments). (g) Bar plot of the average number of photons per frame of three repeats of six dye FluoroCube with JF549 (light blue) and six dye FluoroCube with Cy3 (dark blue). The error bars show the standard error of the mean of three repeats with more than 100 molecules each. Dots show the values of individual experiments. (h) Average number of photons per frame of six dye FluoroCube with JF549 (light blue) and six dye FluoroCube with Cy3 (dark blue) as a function of the total “on” time at the single-molecule level (pooled from all three experiments). (i-n) Same as in c-h but for six dye FluoroCube with JF646 (light red) and six dye FluoroCube with ATTO647N (dark red). (**c-n**) Each experiment was repeated three times with freshly assembled six dye FluoroCubes and on new microscope slides. Exact numbers (also of sample size) are given in **Table S4.2**.

Overall, the six dye FluoroCube with JF549 does not perform as well as the six dye FluoroCube with Cy3 whereas the six dye FluoroCube with JF646 performs slightly better than the six dye FluoroCube with ATTO647N. However, we note that only ~44% of the JF549 and JF646 FluoroCubes have six dyes total because the ssDNA dual labeling efficiency was 76%. Thus, with increased labeling efficiency the six dye FluoroCubes with JF549 and JF646 may perform even better.

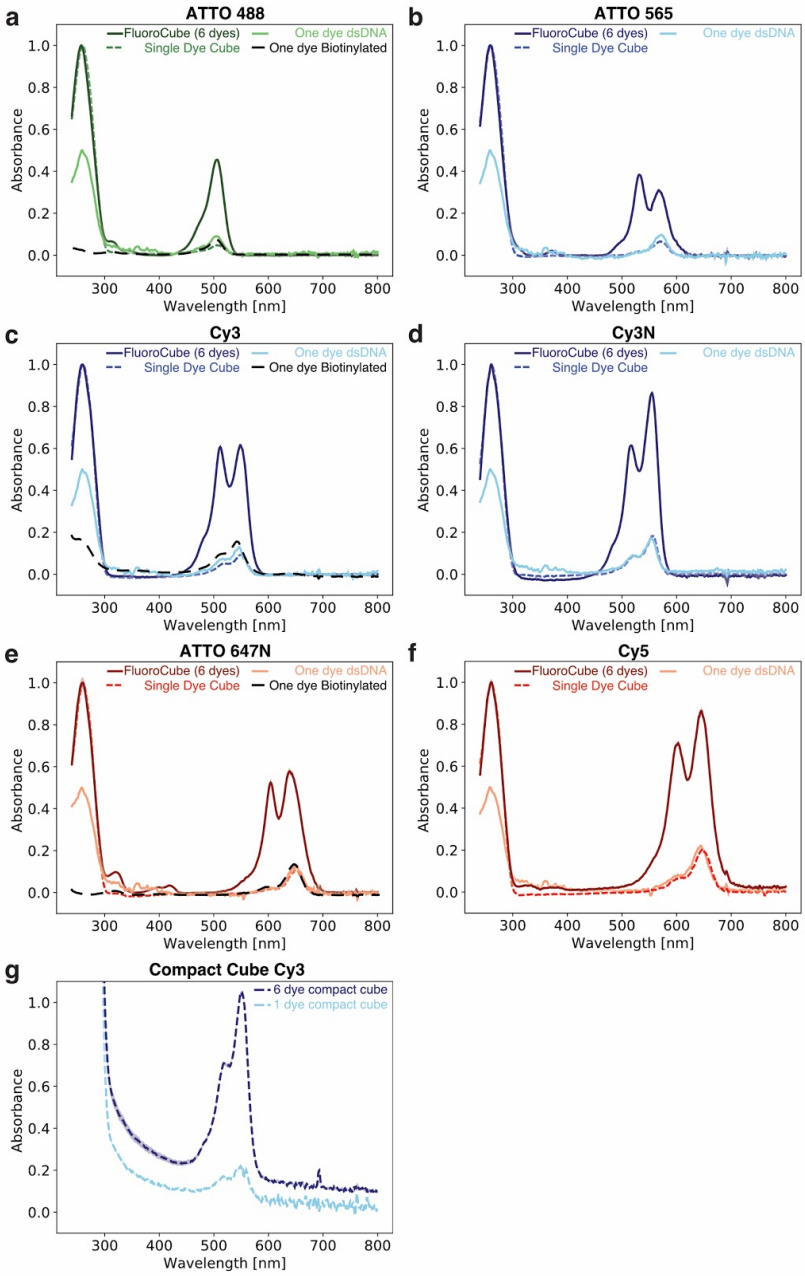

Figure S4.9 | Absorption spectra of DNA FluoroCubes and dyes. We determined the absorption spectra (this Figure) and excitation and emission spectra (**Fig. S4.12**) of FluoroCubes (cube with six dyes), Single Dye Cubes (cube with one dye), double-stranded DNA (dsDNA) with one dye and single biotinylated dyes.

For the absorption spectra we used an Eppendorf Spectrophotometer (UV-Vis BioSpectrometer) and measured the absorbance from 240 nm to 800 nm. To ensure that we use the same concentration among all DNA based samples, we normalized the spectra by measuring the 260 nm absorbance of DNA. Since the double-stranded DNA has half the amount of DNA of the FluoroCube and the Single Dye Cube it is normalized to 50% of the 260 nm absorbance. On the other hand, the Compact Cube[133] has eight fold more DNA than the FluoroCube and the Single Dye Cube and thus is normalized to 800% of the 260 nm absorbance. Note, that we could not apply the normalization for the biotinylated dye and therefore used a concentration of 500 nM which is roughly the same as for all other samples.

Absorption spectra for FluoroCubes (cube with six dyes), Single Dye Cubes (cube with one dye), and double-stranded DNA (dsDNA) with one dye with (a) ATTO 488, (b) ATTO 565, (c) Cy3, (d) Cy3N, (e) ATTO 647N, and (f) Cy5. We also measured the absorption spectra of single biotinylated dyes with (a) ATTO 488, (c) Cy3, and (e) ATTO 647N. (g) Absorption spectra of Compact Cube[133] with a single Cy3 dye and with six Cy3 dyes. (a-g) Opaque color is the standard error of the mean of three repeats with freshly assembled FluoroCubes, Single Dye Cubes, Compact Cubes, and double-stranded DNA. For the single, biotinylated dyes, we always used a new dye aliquot from the same stock that was previously aliquoted. All measurements are bulk measurements. Note, “Cy3” stands for the non-sulfonated version of Cy3 whereas “Cy3N” stands for the sulfonated version of Cy3.

While the absorption spectra of the single dye (biotinylated dye, dsDNA with one dye, Single Dye Cube) are almost identical, we observed significant differences for the six dye FluoroCubes. Positively charged and neutral dyes (Cy3, Cy5, ATTO 647N, and ATTO 565) show a large increase in absorbance in a “shoulder” blue shifted from the main peak, while negatively charged dyes (ATTO 488, Cy3N) have almost no increase in “shoulder” absorbance. This “shoulder” absorbance is often observed for face-to-face dimers of dyes[137] that may result from the flexibility of FluoroCubes in solution and the relatively long linker (up to 1.5 nm) between dye and oligo. Another possible explanation for the face-to-face dimer is dimerization of the FluoroCubes themselves, but we did not find any evidence for FluoroCube multimerization (**Fig. S4.10, Fig. S4.11**).

Negatively charged dyes may not be able to form face-to-face dimers as they are repelled by the negatively charged DNA so that they point away from the FluoroCube whereas the positively charged dyes may stack on the DNA bases or on top of each other. In agreement, the Compact Cubes with six dyes do not show any increase in shoulder absorbance and its dyes are more than 5 nm apart, hence physically unable to form face-to-face dimers. Interestingly, the shoulder absorbance of six dye FluoroCubes mainly represents non-fluorescent dyes (except for the six Cy3 dye FluoroCube) as no comparable shoulder is seen in the excitation spectra (**Fig. S4.12**).

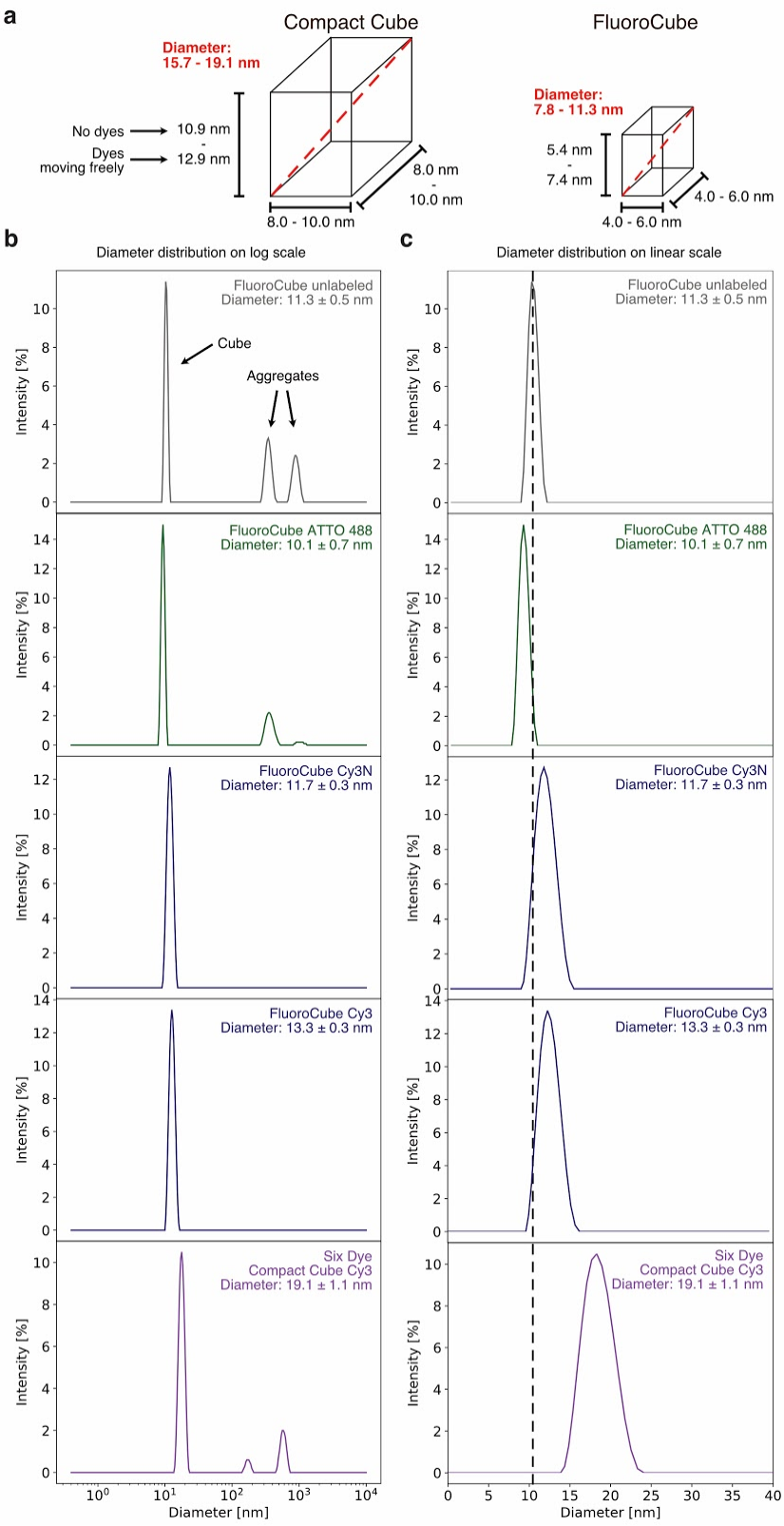

Figure S4.10 | Dynamic light scattering of FluoroCubes and Compact Cubes shows that FluoroCubes are predominantly monomeric. Even though FluoroCubes are monovalent by design, dimerization of FluoroCubes could result in undesirable multimerization of labeled

proteins, hence we deemed it important to ascertain monovalency. Here, we measured the size of FluoroCubes and Compact Cubes[133] with dynamic light scattering (DLS). In addition, we tested for the presence of dimers using a folding competition experiment and by measuring the number of photobleaching steps for the six dye FluoroCube (**Fig. S4.10**). All three experiments confirmed that the FluoroCubes are mainly monomeric.

Dynamic light scattering (DLS) allowed us to assess the state of FluoroCubes with a solution-based method. Since DLS has previously been successfully applied to measure the size distribution of DNA nanostructures[148–150], we adapted a protocol[150] to measure the diameter and amount of aggregates of FluoroCubes and Compact Cubes[133] using a Zetasizer ZS90.

The data presented in this figure shows that most FluoroCubes either form no aggregates or only very few. Note that we are showing the data as an intensity weighted distribution that over-represents the percentage of aggregates since the particle diameter “d” contributes with d^6 to the measured intensity. Taking this into account, we conclude that less than 1% of the FluoroCubes form aggregates. In addition, the DLS data shows that the measured diameter of FluoroCube and Compact Cube[133] agree well with the predicted diameter. Moreover, the diameter distributions of the FluoroCubes are symmetric (no shoulders visible), hence the FluoroCubes are monodisperse in size. Thus, together with the folding competition experiment (**Fig. S4.11**), the measurement of the number of photobleaching steps (**Fig. S4.11**), and the size distribution measured by negative stain electron microscopy (**Fig. S4.2, Table S4.1**), we conclude that the FluoroCubes are predominantly monomeric.

(a) Cartoon representation of the dimensions of FluoroCubes and Compact Cubes. Since DLS measurements assume that each particle has a sphere-like shape, we calculated the diameter (red dashed line) of FluoroCubes and Compact Cubes[133] based on their design. For the edge lengths we used either the shortest possible length, which assumes that no dyes are present, or we used the longest possible length, which assumes that the dyes move freely. However, in this calculation we did not account for any flexibility within the DNA nanostructures which would make the edge lengths even longer. (b) DLS analysis of an unlabeled FluoroCube, a FluoroCube with six ATTO 488 dyes, a FluoroCube with six Cy3N dyes, a FluoroCube with six Cy3 dyes, and a Compact Cube with six Cy3 dyes. The curves of the intensity weighted distribution values show the average of 30 measurements (one experiment). We repeated each experiment three times and found very consistent values (technical repeats; measurement with the same sample). The average diameter of these three repeats is given in the top right along with the standard error of the mean. Positions of cubes and aggregates are indicated with black arrows. (c) Same data as in b but now shown on a linear scale and over a shorter diameter range to highlight the different diameters of FluoroCubes and Compact Cube[133] (black dashed line is given as a reference to the diameter of an unlabeled FluoroCube).

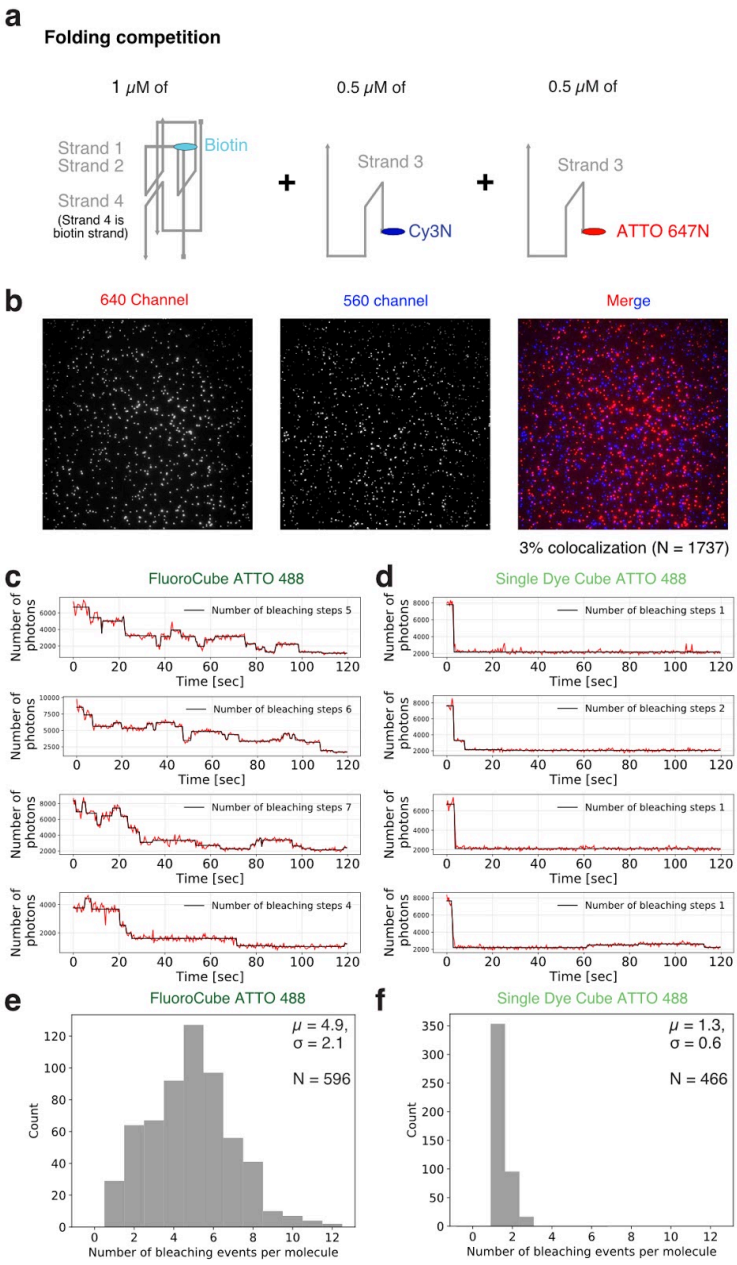

Figure S4.11 | DNA FluoroCubes are predominantly monomeric. To test whether DNA FluoroCubes are monovalent we tested for the presence of dimers using a folding competition experiment, by measuring the number of photobleaching steps for the six dye FluoroCube and the Single Dye Cube and by measuring the size of FluoroCubes and Compact Cubes with dynamic light scattering (DLS) (**Fig. S4.10**). All three experiments confirmed that the DNA FluoroCubes are mainly monomeric.

(a) Setup of the folding competition experiment. For this experiment we used the shape and design of a Single Dye Cube. We used 1 μM of the unlabeled strands 1 and 2 as well as the biotinylated strand 4. For strand 3, we used 0.5 μM of a Cy3N labeled oligo and 0.5 μM of an ATTO 647N oligo. Mixing all these strands together and starting the folding reaction, we predicted that the Single Dye Cubes will assemble into single colored cubes, if they are monomeric. If the cubes form dimers or higher oligomers, they will appear as two colored cubes

(colocalization). (b) Example TIRF images of the cubes created with the folding competition experiment described in a. Left: Image in the 640 channel. Middle: Image in the 560 channel. Right: Merge of the two images.

(a, b) We used these images from b to quantify the number of colocalizations which would indicate a dimeric or higher oligomeric structure. If all Single Dye Cubes formed dimers, we would predict to see 50% of the spots labeled in two colors. However, we only saw about 3% of the spots labeled in two colors indicating that almost all Single Dye Cubes are monomeric. We repeated this experiment twice and also used different fluorophores and always got a similar result for colocalization (~3%).

(c-f) Quantification of photobleaching steps of a six dye FluoroCube and a Single Dye Cube. Most six dye FluoroCubes show atypical photobleaching behavior (**Fig. S4.4**) that makes it impossible to determine the number of dyes by counting photobleaching steps. However, the six dye ATTO 488 FluoroCube shows stepwise photobleaching and we used this FluoroCube to estimate the number of fluorophores by counting photobleaching steps. In addition, we counted photobleaching steps for an ATTO 488 Single Dye Cube. We found on average ~5 photobleaching steps for the six dye ATTO 488 FluoroCube. This may indicate sub-stoichiometric labeling and/or undercounting caused by simultaneous bleaching of two dyes. For the Single Dye Cube we found mainly 1 step photobleaching. Both results confirm that the FluoroCubes and Single Dye Cubes are monomeric. To quantify photobleaching steps we used the Tdetector2 algorithm described by Chen et al.[151] For the analysis, we used movies from the same data used for quantification in **Figure 4.1**, **Figure S4.5 and Figure S4.7**. (c) Example intensity traces of six dye ATTO 488 FluoroCubes with detected photobleaching steps. (d) Example intensity traces of ATTO 488 Single Dye Cubes with detected photobleaching steps. (e) Histogram of number of the photobleaching steps from six dye ATTO 488 FluoroCubes. (f) Histogram of number of the photobleaching steps from ATTO 488 Single Dye Cubes. (e, f) Here, N is the sample number, μ is the average number of bleaching steps, and σ is the corresponding standard deviation.

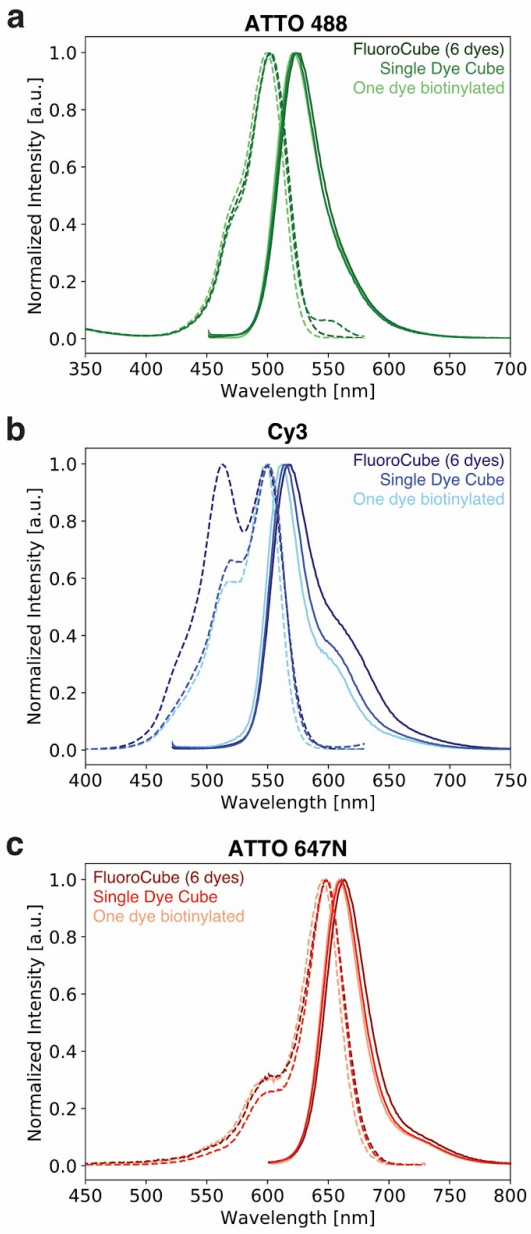

Figure S4.12 | Excitation and emission spectra of DNA FluoroCubes and dyes. (a-c) Excitation (dashed line) and emission (solid line) spectra of Single Dye Cubes, biotinylated dyes, and six dye FluoroCubes are shown for (a) ATTO 488, (b) Cy3, and (c) ATTO 647N. (a-c) All measurements are bulk measurements. Opaque color is the standard error of the mean of 10 measurements (technical repeats; measurement with the same sample). We repeated the experiment twice with freshly assembled FluoroCubes and Single Dye Cubes and got consistent results. Details about instrument settings are listed in **Table S4.5**. A discussion and interpretation of these results can be found in **Figure S4.9**.

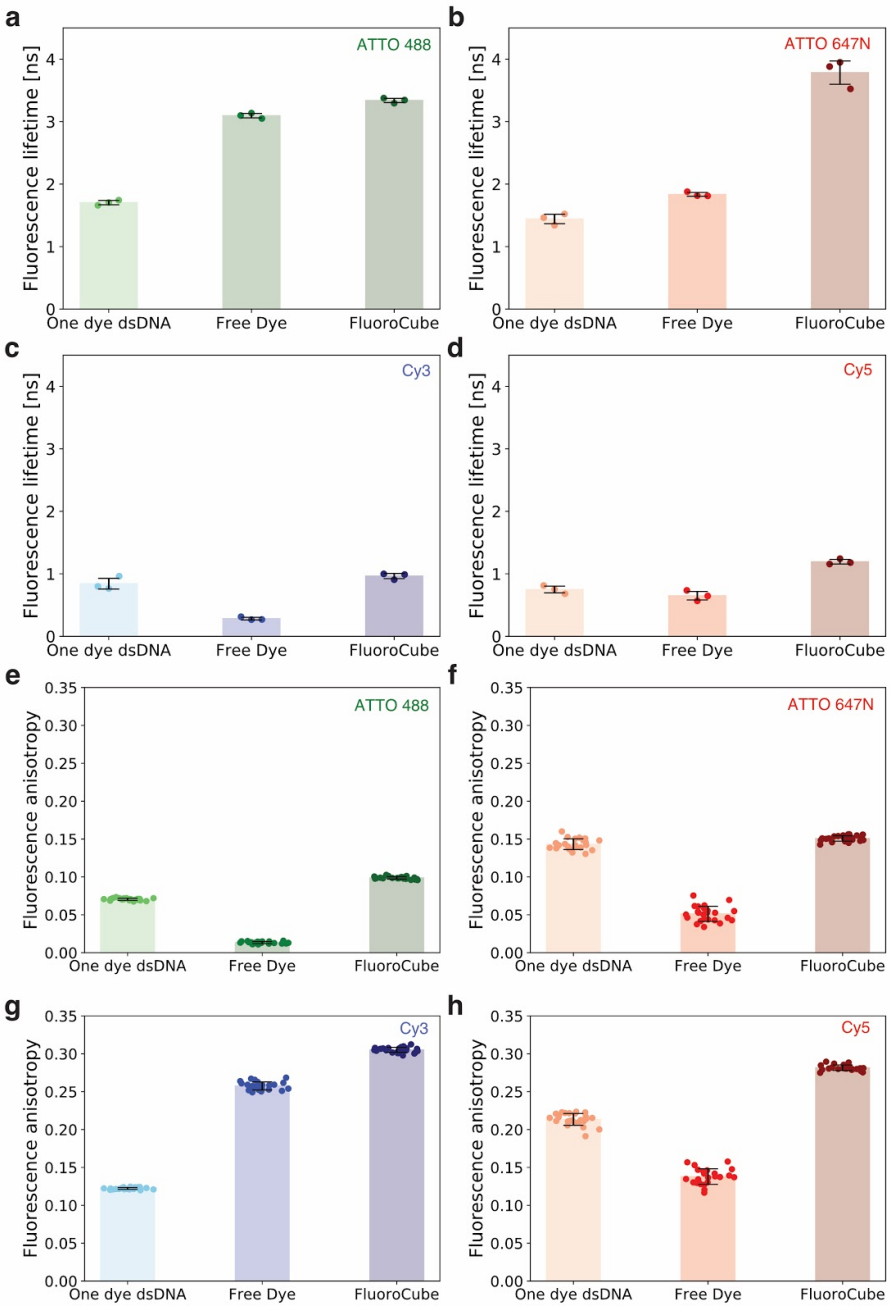

Figure S4.13 | Fluorescence lifetime and fluorescence anisotropy measurements of DNA FluoroCubes. To test whether the increased photostability of six dye FluoroCubes correlates with a changed excited state lifetime, we determined the fluorescence lifetime (a-d) and the fluorescence anisotropy (e-h) of FluoroCubes (cube with six dyes), one dye double-stranded (dsDNA), and single NHS ester dyes (Free dye). We found dye specific differences between six dye FluoroCubes and one dye double-stranded (dsDNA), but no correlation with increased photostability of FluoroCubes.

(a) Fluorescence lifetime of ATTO 488 one dye dsDNA (light green), NHS ester ATTO 488 dyes (medium green), and six dye ATTO 488 FluoroCubes (dark green). (b) Fluorescence lifetime of ATTO 647N one dye dsDNA (light red), NHS ester ATTO 647N dyes (medium red), and six dye ATTO 647N FluoroCubes (dark red). (c) Fluorescence lifetime of Cy3 one dye dsDNA (light blue), NHS ester Cy3 dyes (medium blue), and six dye Cy3 FluoroCubes (dark

blue). (d) Fluorescence lifetime of Cy5 one dye dsDNA (light red), NHS ester Cy5 dyes (medium red), and six dye Cy5 FluoroCubes (dark red). (a-d) Bars show the mean, the dots show values of each experiment and the error bars show the standard deviation of the three repeats performed with freshly assembled FluoroCubes and one dye double-stranded DNA. For the NHS ester dyes, we always used a new dye aliquot from the same stock that was previously aliquoted. All measurements are bulk measurements. The details about instrument settings are listed in **Table S4.6**.

(e) Fluorescence anisotropy measurements of ATTO 488 one dye dsDNA (light green), NHS ester ATTO 488 dyes (medium green), and six dye ATTO 488 FluoroCubes (dark green). (f) Fluorescence anisotropy measurements of ATTO 647N one dye dsDNA (light red), NHS ester ATTO 647N dyes (medium red), and six dye ATTO 647N FluoroCubes (dark red). (g) Fluorescence anisotropy measurements of Cy3 one dye dsDNA (light blue), NHS ester Cy3 dyes (medium blue), and six dye Cy3 FluoroCubes (dark blue). (h) Fluorescence anisotropy measurements of Cy5 one dye dsDNA (light red), NHS ester Cy5 dyes (medium red), and six dye Cy5 FluoroCubes (dark red). (e-h) Bars show the mean of 24 measurements. Values of each measurement are shown as dots. The error bars show standard deviation of 24 measurements performed with freshly assembled FluoroCubes and one dye double-stranded DNA. For the NHS ester dyes, we always used a new dye aliquot from the same stock that was previously aliquoted. All measurements are bulk measurements. Details about instrument settings are listed in **Table S4.7**. We successfully reproduced the fluorescence anisotropy measurements with each sample once.

Note, that we used slightly different constructs for this experiment than in the other experiments described in this manuscript. For the free dye, we used an NHS ester dye instead of a single, biotinylated dye and for the one dye dsDNA we used a 16 bp long version instead of a 32 bp long construct.

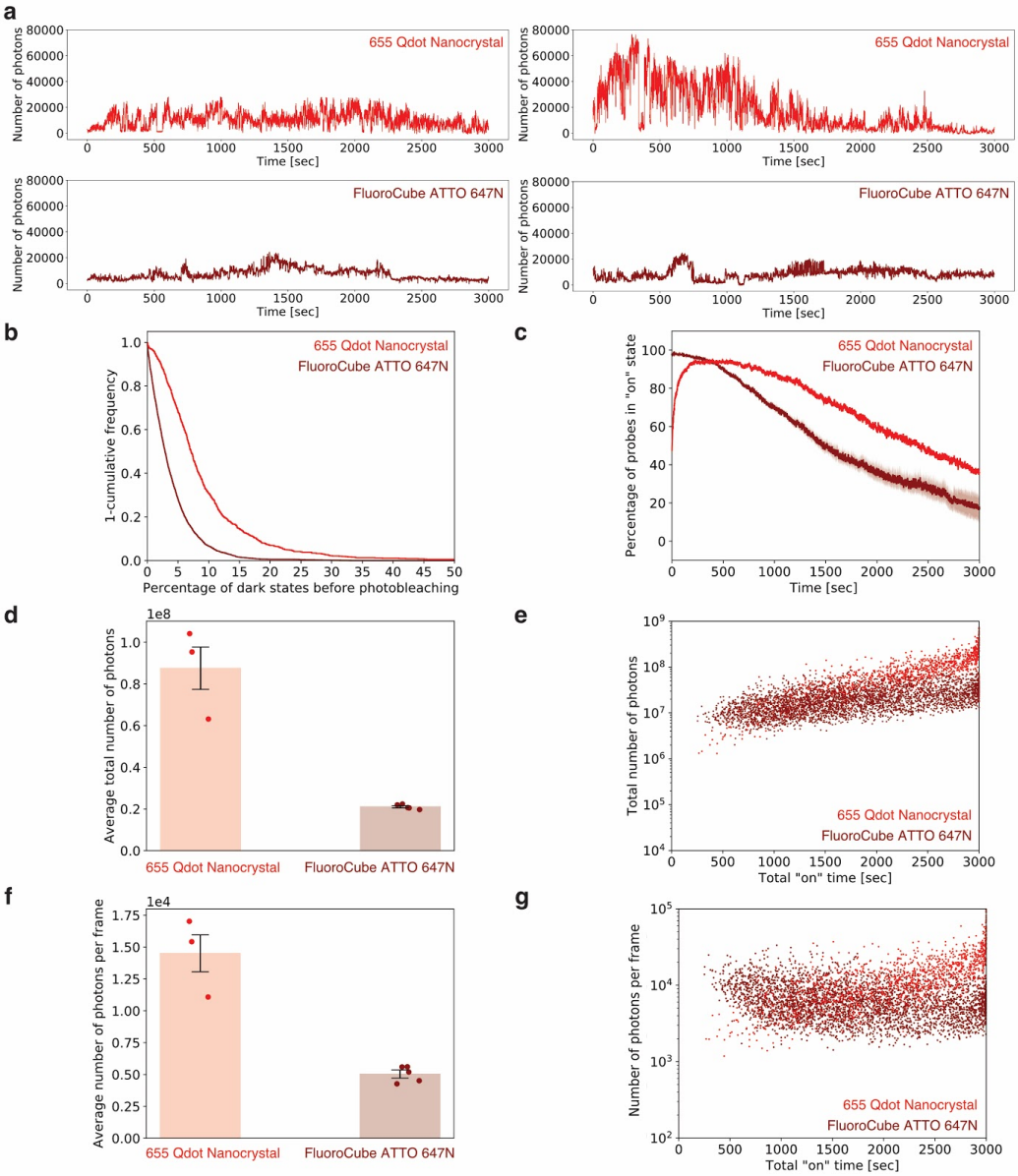

Figure S4.14 | Comparison of quantum dots with DNA FluoroCubes. (a) Two example intensity traces of Streptavidin modified 655 Qdot Nanocrystal (top, light red) and six dye ATTO 647N FluoroCube with one biotin (bottom, dark red). (b) Cumulative frequency plot of the percentage of dark states before photobleaching to quantify blinking of Streptavidin modified 655 Qdot Nanocrystal (light red) and six dye ATTO 647N FluoroCube with one biotin (dark red). (c) Photostability of Streptavidin modified 655 Qdot Nanocrystal (light red) and six dye ATTO 647N FluoroCube with one biotin (dark red). The survival rate was quantified by counting the percentage of probes in the “on” state at any given time from 0 to 3,000 seconds. Opaque color is the standard error of the mean of five or three repeats (six dye FluoroCubes or 655 Qdot, respectively) with more than 500 molecules each. (d) Bar plot of the average of the total number of photons of five or three repeats of Streptavidin modified 655 Qdot Nanocrystal (light red) and six dye ATTO 647N FluoroCube with one biotin (dark red), respectively. The error bars show the standard error of the mean. Dots show the values of individual experiments. Note, that the average of the total number of photons will be slightly higher than shown here because not all probes bleached within 3,000 seconds. (e) Total number of photons of Streptavidin modified 655

Qdot Nanocrystal (light red) and six dye ATTO 647N FluoroCube with one biotin (dark red) as a function of the total “on” time at the single-molecule level (pooled from all five or three experiments (six dye FluoroCubes or 655 Qdots respectively)). (f) Bar plot of the average number of photons per frame of five or three repeats with Streptavidin modified 655 Qdot Nanocrystal (light red) and six dye ATTO 647N FluoroCube with one biotin (dark red), respectively. The error bars show the standard error of the mean. Dots show the values of individual experiments. (g) Average number of photons per frame of Streptavidin modified 655 Qdot Nanocrystal (light red) and six dye ATTO 647N FluoroCube with one biotin (dark red) as a function of the total “on” time at the single-molecule level (pooled from all five or three experiments (six dye FluoroCubes or 655 Qdots respectively)). (b-g) The six dye ATTO 647N FluoroCube experiment was repeated five times with freshly assembled six dye FluoroCubes and on new microscope slides. For the six dye ATTO 647N FluoroCube we are showing the same data as shown in **Figure S4.5 and Figure S4.7**. For the 655 Qdot, we repeated the experiment three times with Qdots from the same stock but on freshly prepared microscope slides. Exact numbers (also of the sample size) are given in **Table S4.1**.

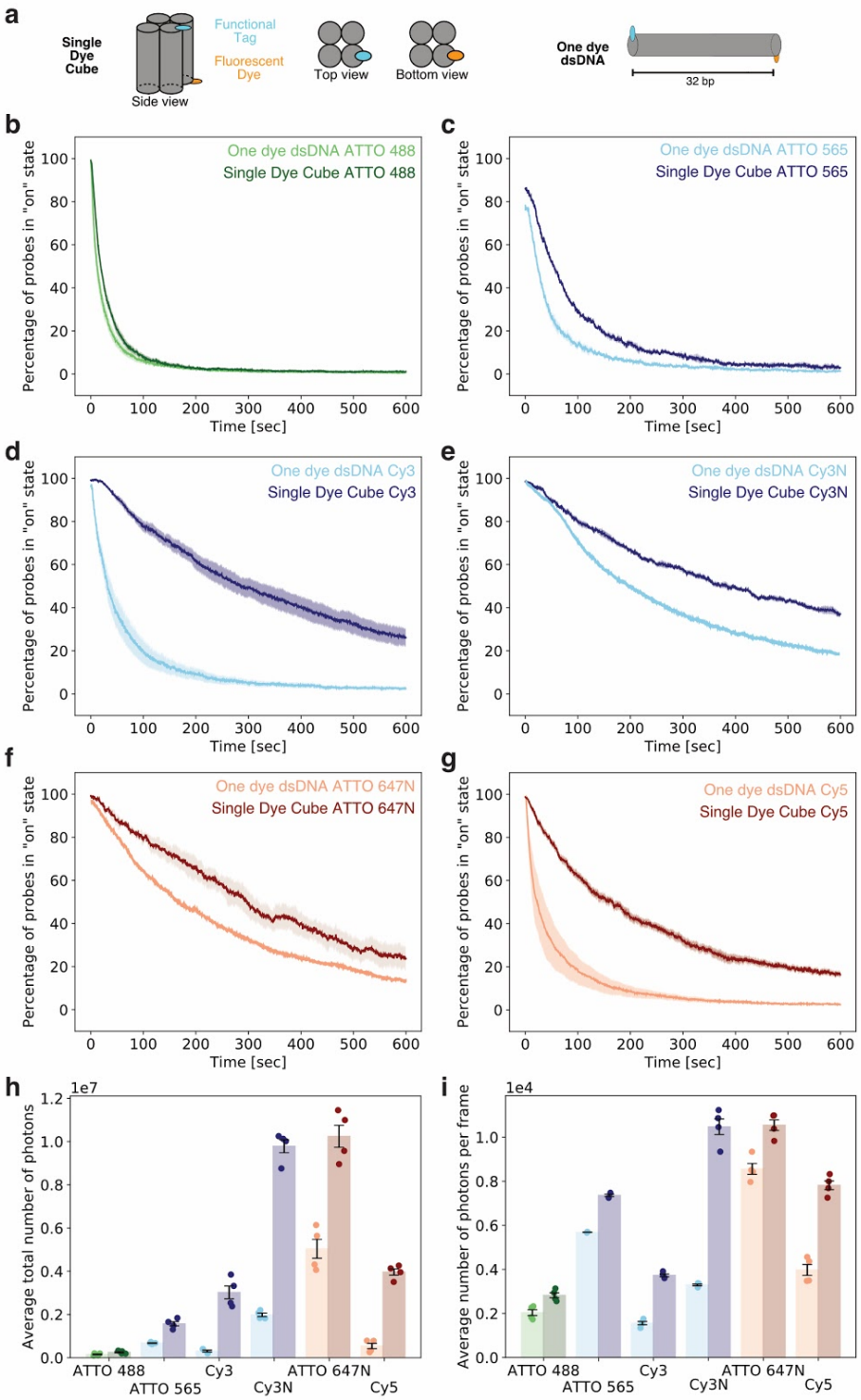

Figure S4.15 | Comparison of photophysical properties of Single Dye Cube and one dye double-stranded DNA. (a) Design of FluoroCubes with a single dye (Single Dye Cubes) compared to the double-stranded DNA with one dye (One dyes dsDNA). In the next panels we show the Single Dye Cubes in the darker colors while the one dye dsDNA are shown in lighter colors. (b-g) Photostability of Single Dye Cubes and one dye dsDNA with (b) ATTO 488, (c) ATTO 565, (d) Cy3, (e) Cy3N, (f) ATTO 647N, and (g) Cy5. The survival rate was quantified by

counting the percentage of probes in the “on” state at any given time from 0 to 600 seconds. Opaque color is the standard error of the mean of four repeats with more than 200 molecules each. (h) Bar plot of the average of the total number of photons of Single Dye Cubes and one dye dsDNA with dyes listed above. The error bars show the standard error of the mean of four repeats with more than 200 molecules each. Dots show the values of individual experiments. (i) Bar plot of the average number of photons per frame of Single Dye Cubes and one dye dsDNA with dyes listed above. The error bars show the standard error of the mean of four repeats with more than 200 molecules each. Dots show the values of individual experiments. (b-i) Each experiment was repeated four times with freshly assembled Single Dye Cubes or one dye double-stranded DNA and on new microscope slides.

Exact numbers (also of the sample size) are given in **Table S4.1 and Table S4.12** for one dye dsDNA and Single Dye Cubes, respectively. The data for the one dye dsDNA is the same as in **Figure 4.1** and **Figure S4.7**. Note that values (average total number of photons and average number of photons) for the ATTO 647N and Cy3N one dye double-stranded DNA are slightly different than in **Table S4.1** because these two one dye double-stranded DNA samples did not bleach over the course of 600 sec. Especially the average total number of photons for the ATTO 647N and Cy3N one dye double-stranded DNA is slightly higher than reported in this figure. Here, “Cy3” stands for the non-sulfonated version of Cy3 whereas “Cy3N” stands for the sulfonated version of Cy3.

A possible explanation for the strong increase in photostability of the Single Dye Cubes could be the local environment of the dye attachment. We speculate that the dye may be hidden in a protective pocket within the Cube so that it is more protected from solvent and oxygen while the single dye is more exposed to oxygen on the double-stranded DNA.

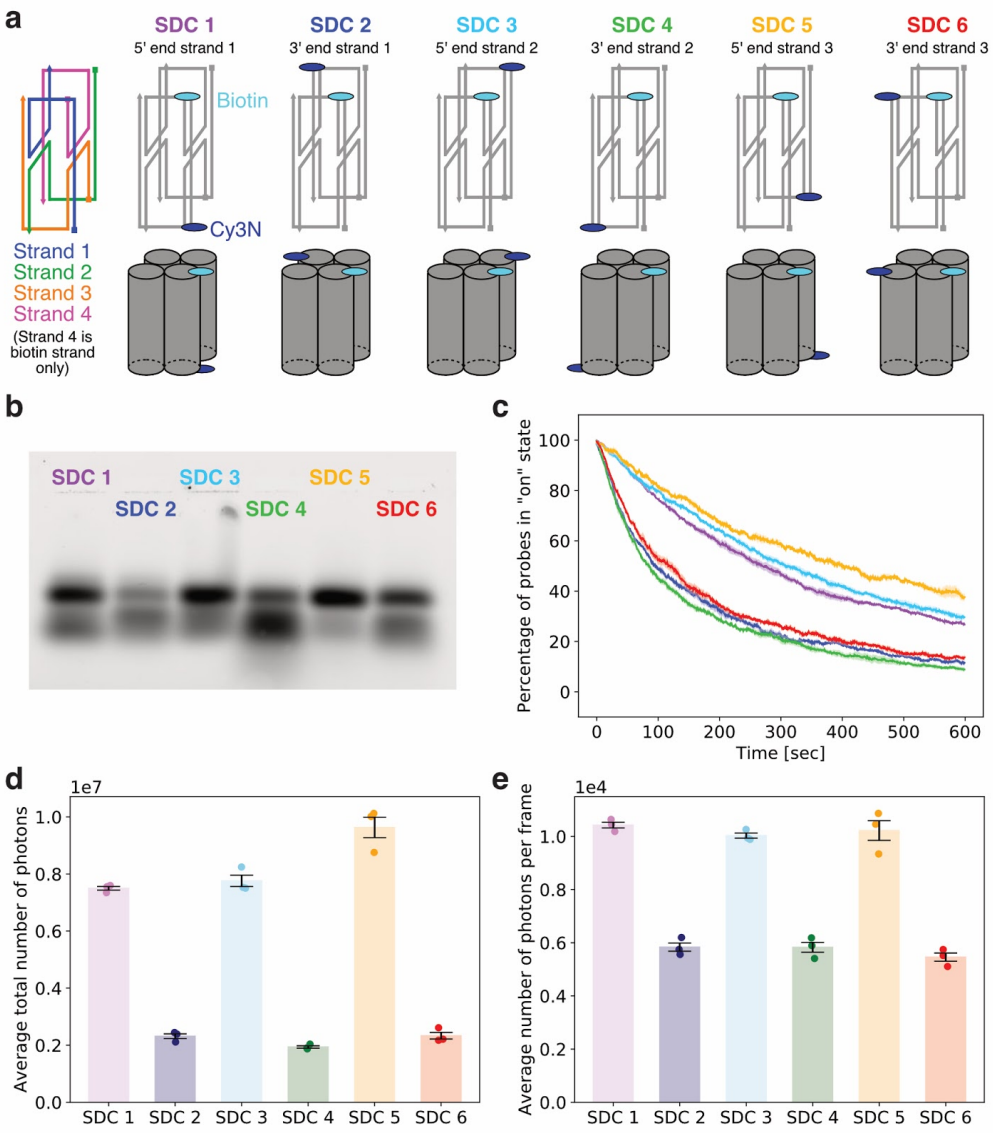

Figure S4.16 | Dye position on FluoroCube influences photophysical properties. (a) Design of Single Dye Cubes with one dye at different positions. Cyan indicates the position of biotin, which was the same for all six constructs while blue shows the position of the single dye (Cy3N), which was permuted for all six constructs. The names of the six different designs are color-coded as shown and this color code is used in all other panels of this figure. (b) 2% agarose gel with the six different designs for the Single Dye Cube shows that all cubes assembled well, but that the cubes with a dye at the 5' end assembled with higher yield. We repeated the gel ones and saw a very similar migration pattern. (c) Photostability of all six different designs for the Single Dye Cube. The survival rate was quantified by counting the percentage of probes in the "on" state at any given time from 0 to 600 seconds. Opaque color is the standard error of the mean of three repeats with more than 250 molecules each. (d) Bar plot of the average of the total number of photons of all six different designs for the Single Dye Cube. The error bars show the standard error of the mean of three repeats with more than 250 molecules each. Dots show the values of individual experiments. (e) Bar plot of the average number of photons per frame of all six different designs for the Single Dye Cube. The error bars show the standard error of the mean of three repeats with more than 250 molecules each. Dots show the values of individual experiments. (c-e) Each experiment was repeated three times with

freshly assembled Single Dye Cubes and on new microscope slides. Exact numbers (also of the sample size) are given in **Table S4.12**.

We observed a strong dependence of photostability on the position of the dye on the Single Dye Cubes when we permute the dye through all six possible positions. While some Single Dye Cubes almost behaved like one dye dsDNA (dyes on the 3' end), other Single Dye Cubes were more photostable (dyes on the 5' end) than one dye dsDNA. This shows that there is a dependence of photostability on dye position and local environment.

Note that we used the Single Dye Cubes with the most photostable position for our experiments in this study, which is on the 5' end of strand 3 (version SDC 5).

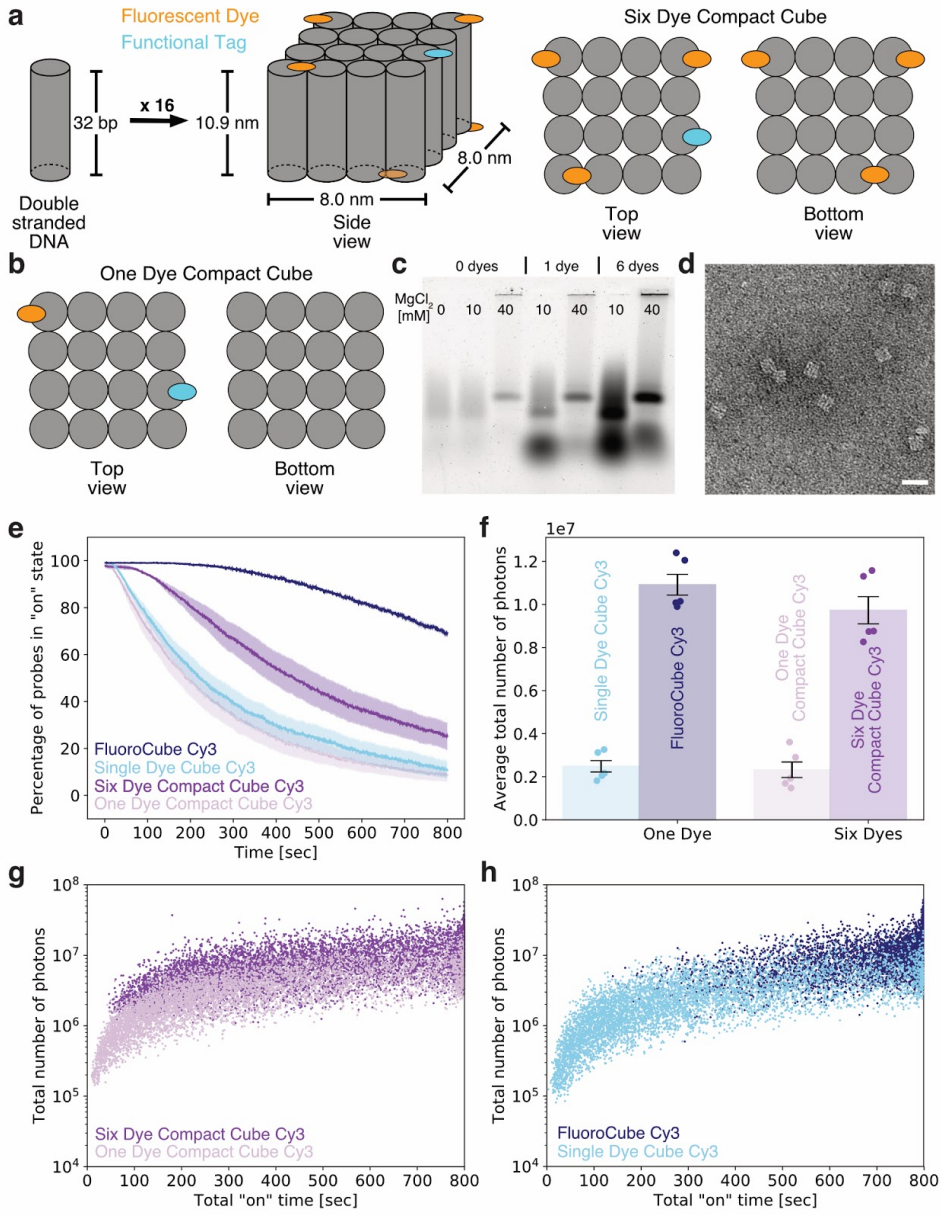

Figure S4.17 | Photophysical properties of Compact Cube with one and six dyes. (a) Cartoon of the design and dimensions of the Compact Cube with six dyes. A more detailed description of the Compact Cube can be found in Scheible et al.[133]. (b) Cartoon of the design of the Compact Cube with one dye. (c) 2% agarose gel stained with Ethidium Bromide with the Compact Cube without dyes and with one or six dyes assembled at indicated $MgCl_2$ concentrations. We repeated the gel twice and saw a very similar migration pattern. (d) Negative stain micrograph of the Compact Cube with a single Cy3 dye. Scale bar is 20 nm. This micrograph looks very similar to the one shown in Scheible et al.[133] and we therefore concluded that the Compacted Cubes assembled in the predicted shape. We performed the negative stain imaging with these Compact Cubes ones (n=1). We also imaged the Compact Cube with six Cy3 dyes and without any dyes and saw very similar images. (e) Photostability of the Cy3 labeled six dye FluoroCube, Single Dye Cube, six dye Compact Cube and one dye Compact Cube. The survival rate was quantified by counting the percentage of probes in the “on” state at any given time from 0 to 800

seconds. Opaque color is the standard error of the mean of five repeats with more than 700 molecules each. (f) Bar plot of the average of the total number of photons of the Cy3 labeled six dye FluoroCube, Single Dye Cube, six dye Compact Cube and one dye Compact Cube. The error bars show the standard error of the mean of five repeats with more than 700 molecules each. Dots show the values of individual experiments. Note that the total number of photons for the six dye FluoroCube is much higher than shown here because about 75% of the FluoroCubes were not bleached at the end of acquisition. The actual total number of photons for the six dye FluoroCube is shown in Figure 1 m and about 2-fold higher than the total number of photons for the six dye Compact Cube. (g) Total number of photons of the Cy3 labeled one and six dye Compact Cube as a function of the total “on” time at the single-molecule level (pooled from all five experiments). (h) Total number of photons of the Cy3 labeled six dye FluoroCube and Single Dye Cube as a function of the total “on” time at the single-molecule level (pooled from all five experiments). (e-h) Each experiment was repeated five times with freshly assembled six dye FluoroCubes, Single Dye Cubes, and Compact Cubes with one or six dyes and on new microscope slides. Exact numbers (also of sample size) are given in **Table S4.13**.

This data shows that Compact Cubes assemble well with 40 mM $MgCl_2$. Moreover, we see that the Compact Cube with one dye behaves very similar to a Single Dye Cube, and both are more photostable than the double-stranded DNA with one dye. A possible explanation for the increased photostability of the Single Dye Cubes and the one dye Compact Cubes compared to the one dye dsDNA is that the cubes act as protecting reagents either through geometric means (shielding) or resonance energy transfer between dyes and DNA.

Comparing the total number of photons of the six dye Compact Cube to the single dye Compact Cube we find a ~5-fold increase for the six dye Compact Cube. This is slightly lower than we would expect based on a linear increase in intensity with the number of dyes[128] and might either be the result of a suboptimal labeling efficiency or, more likely, because not all dyes of the six dye Compact Cube bleached during the time of acquisition.

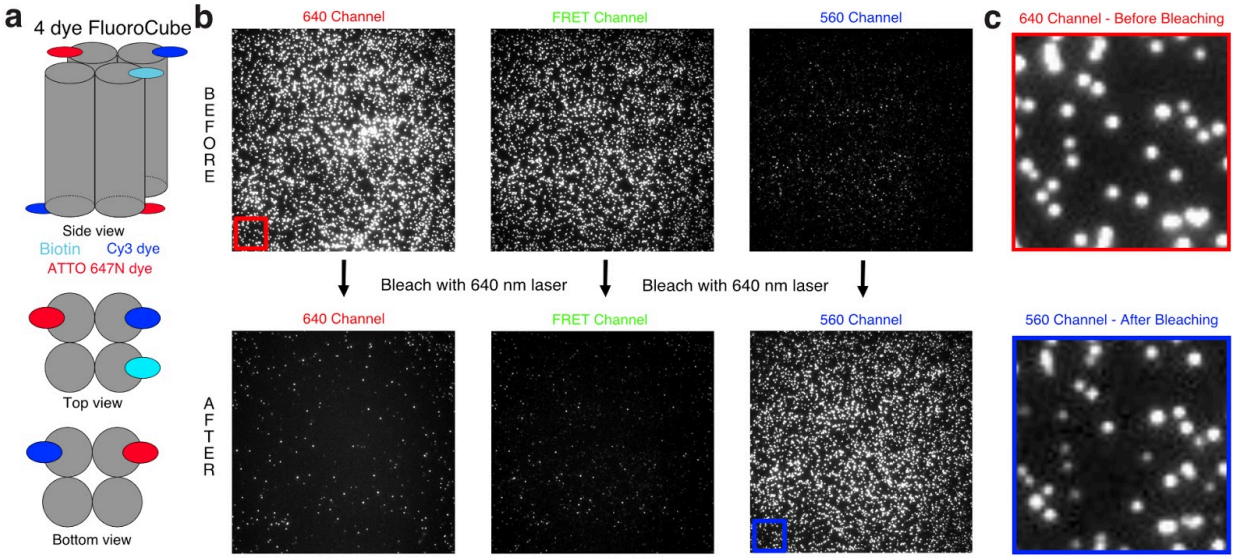

Figure S4.18 | Foerster resonance energy transfer (FRET) between dyes on four dye FluoroCube. (a) Design of four dye FluoroCube with two ATTO 647N dyes and two Cy3 dyes labeled with biotin. (b) Top: Micrographs in the 640 channel (640 nm laser with ET700-75m filter), FRET channel (561 nm laser with ET700-75m filter), and 560 channel (561 nm laser with ET600-50m filter). Bottom: Micrographs in the 640 channel, FRET channel, and 560 channel after bleaching with a 640 nm laser for 15 minutes. Blue and red square in left bottom corner show the part enlarged in c. (c) Zoom-in on the 640 channel before photobleaching (top) and the 560 channel after photobleaching (bottom) showing that the 560 and 640 signals come from the same FluoroCubes.

As expected based on the distance (~ 3-4 nm) between the Cy3 and ATTO 647N dye, we observe a high signal in the FRET channel, and low signal of the Cy3 donor in the 560 channel. After bleaching most of the ATTO 647N acceptor dyes, signal of the Cy3 donor is recovered in the 560 channel. These observations demonstrate Foerster Resonance Energy Transfer for these constructs, and suggest that Resonance Energy Transfer may also take place in the six dye FluoroCubes. Note, we repeated this experiment twice and saw similar effects for all three experiments.

This data also shows that more than 95% of the four dye FluoroCubes have at least three of the four oligos (used to fold the FluoroCube) incorporated because the FluoroCubes would not attach to the cover slide without the biotin (St_02 strand), and because there is a FRET signal at almost every spot visible in the 640 channel. Thus, both Cy3 and ATTO647N are present, hence both the SC_01 and SC_02 strands are present.

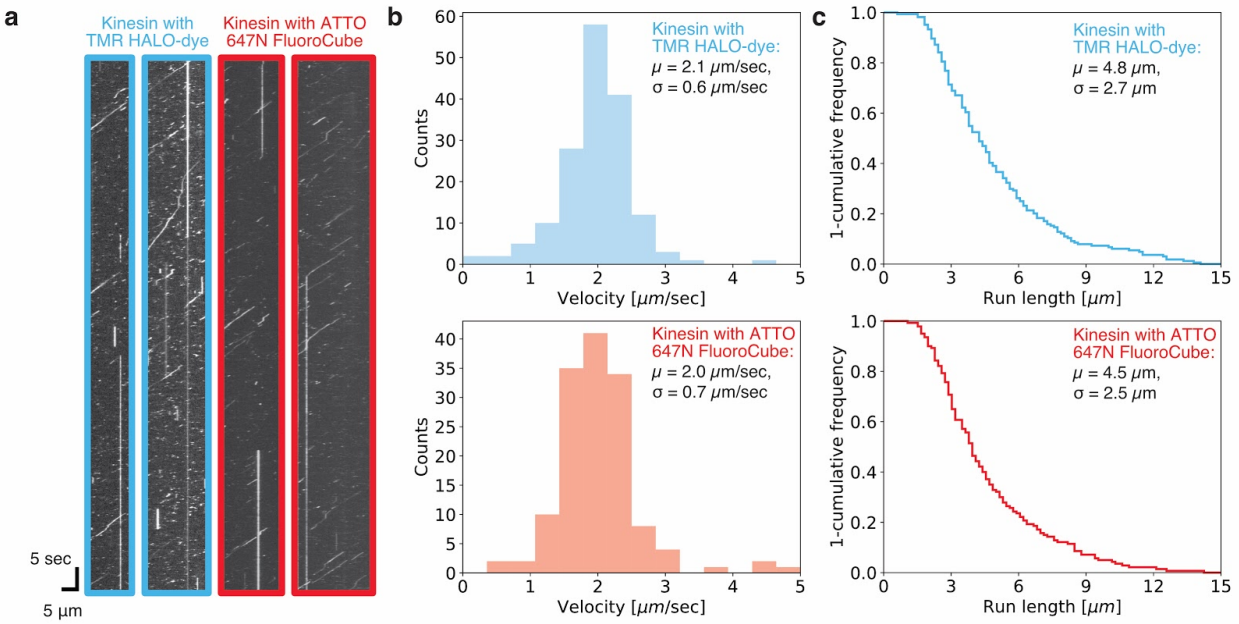

Figure S4.19 | Single HALO dye and six dye FluoroCube labeled kinesin have similar velocity and processivity. (a) Example kymographs of kinesin labeled with HALO-tag TMR dye (blue frame) and kinesin labeled with six dye ATTO 647N FluoroCube (red frame). (b) Velocity histogram with average velocity (μ) and its standard deviation (σ) for kinesin labeled with HALO-tag TMR dye (top) and kinesin labeled with six dye ATTO 647N FluoroCube (bottom). Kymographs are from many movies with motors from the same preparation but with freshly prepared microscope slides (n=3) (c) A '1-cumulative frequency distribution plot' of run length with average length (μ) and its standard deviation (σ) for kinesin labeled with HALO-tag TMR dye (top) and kinesin labeled with six dye ATTO 647N FluoroCube (bottom). (b, c) The data is pooled from many movies with motors from the same preparation but with freshly prepared microscope slides (n=3) and the sample size for the kinesin labeled with HALO-tag TMR dye is n = 164 and kinesin labeled with six dye ATTO 647N FluoroCube is n = 140.

Comparing the velocity and processivity of kinesin labeled with HALO-tag TMR dye and kinesin labeled with six dye ATTO 647N FluoroCube we found almost identical values indicating that FluoroCubes do not interfere with protein function in this assay. However, we observed that the labeling efficiency with the six dye ATTO 647N FluoroCubes was about 30% lower than the labeling efficiency with the HALO-tag TMR dye.

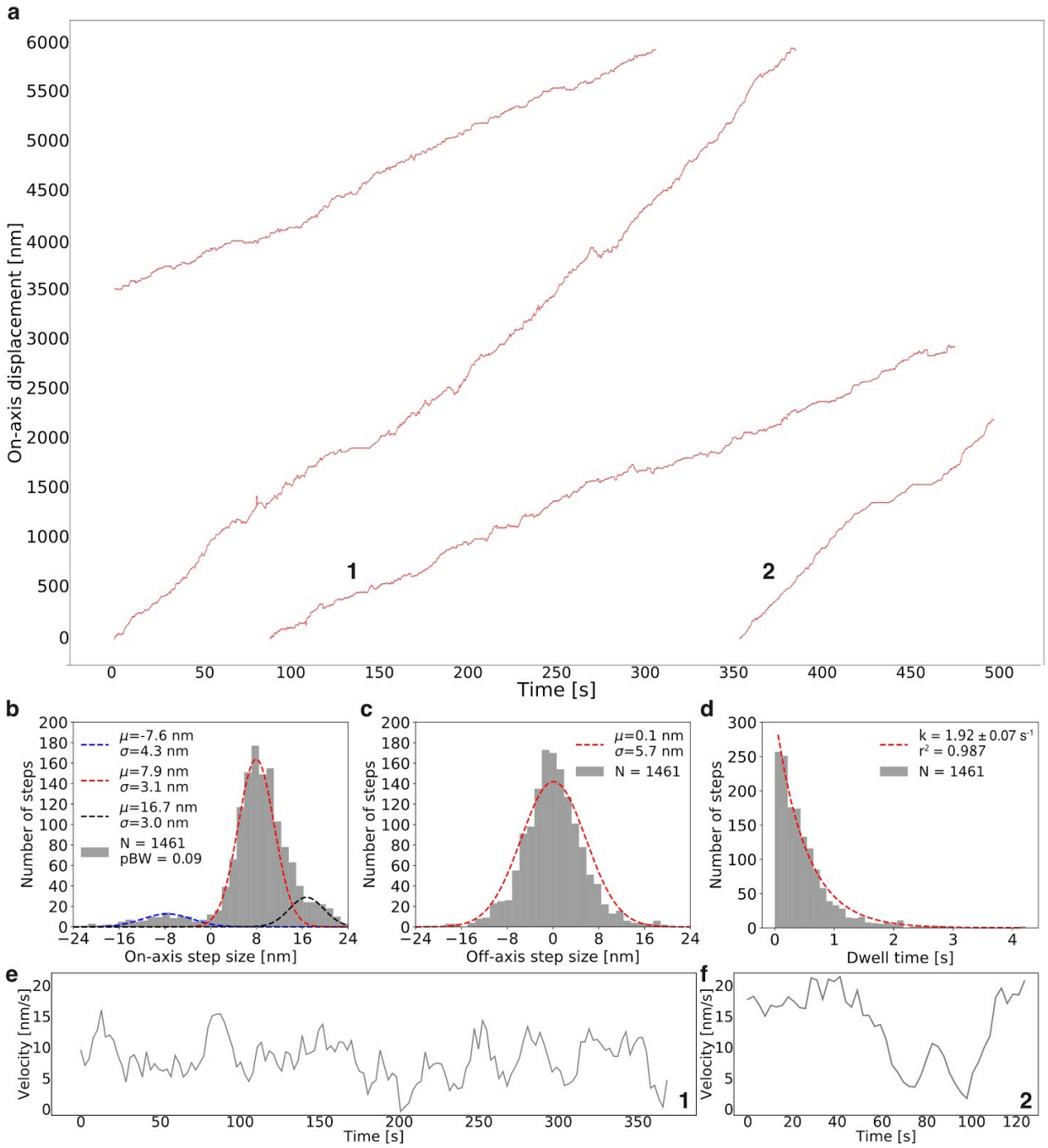

Figure S4.20 | Additional stepping data of individual kinesins. (a) Raw stepping data with position versus time of four kinesins (grey dots) with detected steps (red line) along an axoneme. The opaque red line shows the standard deviation for each step. The numbers 1 and 2 indicated traces for which the velocity over time was analyzed as shown in e and f, respectively. (b) Histogram of the on-axis step size distribution of the combined data shown in a. The data was split into positive and negative steps and fit with Gaussians. For the negative steps a single Gaussian was used (blue) whereas for the positive steps two Gaussians were used (red, black). pBW is the fraction of backward steps. We mainly measured 7.9 nm forward steps which is in good agreement with previous findings for conventional kinesin 1[99] and KIF1A[139]. The 16 nm forward steps are likely two 8 nm steps which happened during a single

exposure and thus could not be detected as individual steps. The observed backward steps of this artificially dimerized KIF1A[138] might be due to its properties as a monomeric motor for which backward steps have been observed[139]. In addition, the dimerization of the KIF1A motor domain using the coiled-coil of conventional kinesin 1[138], may have altered the neck linker length and alterations in neck linker length have been observed to result in few backward steps[152]. (c) Histogram of the off-axis step size distribution of the combined data shown in a fitted with a single Gaussian. The average of 0.1 nm shows that the motor moves along the axoneme with no bias to either side along the off-axis. This agrees well with previous findings that kinesin 1 prefers to move along a single protofilament without side steps[153]. (d) Histogram of the dwell-time distribution of the combined data shown in a fitted with a single exponential. The single exponential decay shows that both kinesin heads step at a similar rate, which in this case is limited by the ATP concentration[140]. (e, f) Velocity over time for stepping traces of a single kinesin as shown in a. The grey line shows a moving average of velocity binned into 15.6 sec (for details see **Materials and Methods**). The numbers 1 and 2 indicate which traces in a where chosen. (a-f) All traces were collected with motors from the same preparation but with freshly prepared microscope slides (n=4).

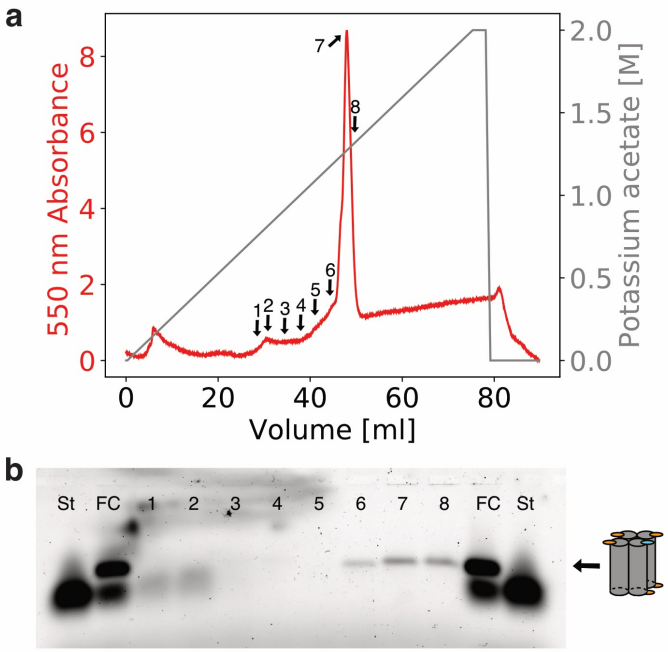

Figure S4.21 | Ion exchange chromatography separates six dye DNA FluoroCubes from excess oligos. (a) 550 nm absorbance trace (red) from ion exchange chromatography with six dye Cy3 FluoroCubes with one biotin. The grey trace shows the linear increase of potassium acetate from 0 M to 2 M over a volume of 80 ml. The arrows with numbers indicate fractions that were run on a 2% agarose gel to evaluate elution fractions. (b) 2% agarose gel with elution fractions from ion exchange chromatography (1-8) as shown in a. "St" refers to a single of the four ssDNA (FC_St_02) used to fold the six dye FluoroCubes (**Table S4.3**). "FC" refers to a six dye Cy3 FluoroCube with one biotin that was not purified by ion exchange chromatography. (a, b) We performed this experiment once.

Based on the agarose gel we can conclude that most of the FluoroCubes elute at approximately 1.1 M potassium acetate. Moreover, oligos that were not incorporated into a structure (FluoroCube) are clearly separated from fully folded FluoroCubes. We verified FluoroCube integrity by negative stain electron microscopy after ion exchange chromatography. Taken together, ion exchange chromatography can be used to further purify FluoroCubes.

Table S4.1 | Photophysical properties of quantum dots, DNA FluoroCubes, and one dye double-stranded DNA with different fluorophores. Here “One dye dsDNA” refers to a single dye attached to a double-stranded DNA (dsDNA) whereas “FluoroCube” refers to a cube with six dyes. In all cases the probes had a single biotin. Here “Cy3” stands for the non-sulfonated version of Cy3 whereas “Cy3N” stands for the sulfonated version of Cy3. Note, that the average of the total number of photons for some six dye FluoroCubes shown here is an underestimate because not all probes bleached within 3,000 seconds. Errors (±) are the standard error of the mean of five or four repeats (six dye FluoroCubes or one dye double-stranded DNA, respectively), which is recording a movie with freshly assembled six dye FluoroCubes or double-stranded DNA. For the 655 Qdot, we repeated the experiment three times with Qdots from the same stock but on freshly prepared microscope slides. “n” is the sample size number. “n.m.” is not measured and “N.A.” is not available.

	Photo-bleaching half-life time in seconds	**Total number of photons (10^6)**	**Average number of photons per frame (10^3)**	**Blinking - Percentage of dark states before photo-bleaching**	**Average outside diameter of FluoroCube by negative stain [nm]**	**Charge per dye**
One dye dsDNA (ATTO 488) n = 6292	13 ± 2	0.15 ± 0.03	2.0 ± 0.1	5.9 ± 5.0	n.m.	-1
FluoroCube (ATTO 488) n = 7916	123 ± 11	0.8 ± 0.1	2.0 ± 0.1	9.0 ± 6.0	6.8 ± 1.3 (n = 141)	-1
One dye dsDNA (ATTO 565) n = 1575	23 ± 2	0.7 ± 0.1	5.7 ± 0.1	14.1 ± 7.7	n.m.	0
FluoroCube (ATTO 565) n = 1368	179 ± 15	2.5 ± 0.1	2.5 ± 0.1	11.7 ± 5.5	7.8 ± 1.3 (n = 98)	0
One dye dsDNA (ATTO 647N) n = 3518	188 ± 64	5.6 ± 0.1	8.7 ± 0.1	6.2 ± 3.8	n.m.	+1
FluoroCube (ATTO 647N) n = 3495	1834 ± 177	21.0 ± 0.4	5.0 ± 0.3	3.9 ± 1.9	6.2 ± 1.2 (n = 189)	+1
One dye dsDNA (Cy3) n = 2841	24 ± 8	0.3 ± 0.1	1.6 ± 0.1	8.3 ± 6.8	n.m.	+1
FluoroCube (Cy3) n = 2654	1309 ± 80	12.9 ± 0.6	3.5 ± 0.1	4.0 ± 1.6	9.2 ± 2.2 (n = 146)	+1
One dye dsDNA (Cy3N) n = 7263	156 ± 3	2.9 ± 0.2	3.3 ± 0.1	6.2 ± 4.2	n.m.	-1

	Photo-bleaching half-life time in seconds	Total number of photons (10^6)	Average number of photons per frame (10^3)	Blinking - Percentage of dark states before photo-bleaching	Average outside diameter of FluoroCube by negative stain [nm]	Charge per dye
FluoroCube (Cy3N) n = 1966	1404 ± 43	39.4 ± 1.3	11.0 ± 0.5	1.8 ± 1.2	6.8 ± 1.4 (n = 128)	-1
One dye dsDNA (Cy5) n = 3430	18 ± 11	0.5 ± 0.1	4.0 ± 0.2	3.3 ± 3.1	n.m.	+1
FluoroCube (Cy5) n = 4910	603 ± 26	7.9 ± 0.2	3.3 ± 0.1	4.8 ± 1.9	10.0 ± 2.3 (n = 119)	+1
655 Qdot n = 1341	2022 ± 282	87.1 ± 1.0	14.4 ± 1.3	8.5 ± 3.8	n.m.	N.A.

Table S4.2 | Photophysical properties of DNA FluoroCubes with Janelia fluorophores. Here "FluoroCube" refers to a cube with six dyes. In all cases the probes had a single biotin. Note, that the average total number of photons shown here is an underestimate because most probes did not bleach within 600 seconds. Errors (±) are the standard error of the mean of three repeats, which is recording a movie with freshly assembled six dye FluoroCubes. "n" is the sample size number. "n.m." is not measured.

	Photo-bleaching half-life time in seconds	**Total number of photons (10^6)**	**Average number of photons per frame (10^3)**	**Blinking - Percentage of dark states before photo-bleaching**	**Average outside diameter of FluoroCube by negative stain in nanometer**	**Charge per dye**
FluoroCube (Cy3) n = 325	n.m. (See Table S4.1)	8.0 ± 0.2	5.6 ± 0.1	4.0 ± 1.6	See Table S4.1	+1
FluoroCube (JF549) n = 918	282 ± 7	2.69 ± 0.03	3.6 ± 0.1	6.7 ± 3.7	7.6 ± 1.7 (n = 133)	0
FluoroCube (ATTO 647N) n = 3025	n.m. (See Table S4.1)	9.9 ± 0.3	6.8 ± 0.1	3.9 ± 1.9	See Table S4.1	+1
FluoroCube (JF646) n = 2518	969 ± 16	12.0 ± 0.1	8.7 ± 0.1	1.4 ± 1.3	7.2 ± 1.7 (n = 103)	0

Table S4.3 | Sequences and corresponding modifications of all oligonucleotides used in this study. Nomenclature: “FC” stands for a single-stranded DNA (ssDNA) strand that was used to fold FluoroCubes (cube with six dyes). “SD” stands for a ssDNA strand that was used to fold Single Dye Cubes (cube with one dye). “dsDNA” stands for single-stranded DNA (ssDNA) strand that was used to fold the one dye double-stranded DNA (dsDNA). “NH2” stands for amino group modification. “UN” stands for unlabeled oligonucleotide. “LC” stands for single-stranded DNA (ssDNA) strand that was used to fold the Compact Cube[133].

For each FluoroCube and Single Dye Cube four ssDNA strands are required: SC_01, SC_02, St_01, and St_02. Both Single Dye Cubes (light gray part of the table) and FluoroCubes (white part of the table) need a functionalized oligo strand, which is always St_01 (dark gray part of the table), and either has a biotin or a HALO-ligand[103]. Single Dye Cubes, irrespective of the dye, always require two unlabeled strands “SD_SC_01_UN” and “SD_SC_02_UN” as well as one strand with a single dye “SD_St_02” (except for the Single Dye Cubes with Cy3N permuted through all six positions (see **Figure S4.16**)). Thus, for example, to assemble a Single Dye Cube with ATTO488 and biotin, one uses: SD_SC_01_UN, SD_SC_02_UN, FC_St_01_Biotin, and SD_St_02_ATTO488. For a FluoroCube with biotin one uses: FC_SC_01_ATTO647N, FC_SC_02_ATTO647N, FC_St_01_Biotin, and FC_St_02_ATTO647N. A detailed overview of strand combinations used for Single Dye Cubes, FluoroCubes, one dye double-stranded DNA, and the Compact Cube with one or six dyes can be found in **Table S4.4**. Note that amino group modified oligos were used to label with either JF549 or JF646. Here “Cy3” stands for the non-sulfonated version of Cy3 whereas “Cy3N” stands for the sulfonated version of Cy3.

Name	Sequence and modification	Vendor
FC_SC_01_NH2	/5AmMC6/ATGAGGTGTATGTGTAGAGTGATGGATGTAGT/3AmMO/	IDT
FC_SC_02_NH2	/5AmMC6/AGGATGAGTGAGAGTGAGATGAGAGTAGATGT/3AmMO/	IDT
FC_St_02_NH2	/5AmMC6/CACTCTCACACCTCATACATCTACCATCACTC/3AmMO/	IDT
FC_SC_01_ATTO488	/5ATTO488N/ATGAGGTGTATGTGTAGAGTGATGGATGTAGT/3ATTO488N/	IDT
FC_SC_02_ATTO488	/5ATTO488N/AGGATGAGTGAGAGTGAGATGAGAGTAGATGT/3ATTO488N/	IDT
FC_St_02_ATTO488	/5ATTO488N/CACTCTCACACCTCATACATCTACCATCACTC/3ATTO488N/	IDT
FC_SC_01_ATTO565	/5ATTO565N/ATGAGGTGTATGTGTAGAGTGATGGATGTAGT/3ATTO565N/	IDT
FC_SC_02_ATTO565	/5ATTO565N/AGGATGAGTGAGAGTGAGATGAGAGTAGATGT/3ATTO565N/	IDT
FC_St_02_ATTO565	/5ATTO565N/CACTCTCACACCTCATACATCTACCATCACTC/3ATTO565N/	IDT
FC_SC_01_ATTO647N	/5ATTO647NN/ATGAGGTGTATGTGTAGAGTGATGGATGTAGT/3ATTO647NN/	IDT
FC_SC_02_ATTO647N	/5ATTO647NN/AGGATGAGTGAGAGTGAGATGAGAGTAGATGT/3ATTO647NN/	IDT
FC_St_02_ATTO647N	/5ATTO647NN/CACTCTCACACCTCATACATCTACCATCACTC/3ATTO647NN/	IDT
FC_SC_01_Cy3	/5Cy3/ATGAGGTGTATGTGTAGAGTGATGGATGTAGT/3Cy3Sp/	IDT
FC_SC_02_Cy3	/5Cy3/AGGATGAGTGAGAGTGAGATGAGAGTAGATGT/3Cy3Sp/	IDT
FC_St_02_Cy3	/5Cy3/CACTCTCACACCTCATACATCTACCATCACTC/3Cy3Sp/	IDT
FC_SC_01_Cy3N	/5Cy3N/ATGAGGTGTATGTGTAGAGTGATGGATGTAGT/3Cy3N/	IDT
FC_SC_02_Cy3N	/5Cy3N/AGGATGAGTGAGAGTGAGATGAGAGTAGATGT/3Cy3N/	IDT
FC_St_02_Cy3N	/5Cy3N/CACTCTCACACCTCATACATCTACCATCACTC/3Cy3N/	IDT

Name	Sequence and modification	Vendor
FC_SC_01_Cy5	/5Cy5/ATGAGGTGTATGTGTAGAGTGATGGATGTAGT/3Cy5Sp/	IDT
FC_SC_02_Cy5	/5Cy5/AGGATGAGTGAGAGTGAGATGAGAGTAGATGT/3Cy5Sp/	IDT
FC_St_02_Cy5	/5Cy5/CACTCTCACACCTCATACATCTACCATCACTC/3Cy5Sp/	IDT
FC_St_01_Biotin	/5Biosg/TACACATACTCATCCTACTACATCTCTCATCTTT	IDT
FC_St_01_HALO	Halotag Ligand (O2) TACACATACTCATCCTACTACATCTCTCATCT	Biomers
dsDNA_Biotin	/5Biosg/AAGAGTGATGGTAGATGTATGAGGTGTGAGAGTG	IDT
SD_SC_01_UN	TTATGAGGTGTATGTGTAGAGTGATGGATGTAGTTT	IDT
SD_SC_02_UN	TTAGGATGAGTGAGAGTGAGATGAGAGTAGATGTTT	IDT
SD_St_02_UN	TTCACTCTCACACCTCATACATCTACCATCACTCTT	IDT
SD_St_02_ATTO488	/5ATTO488N/CACTCTCACACCTCATACATCTACCATCACTCTT	IDT
SD_St_02_ATTO565	/5ATTO565N/CACTCTCACACCTCATACATCTACCATCACTCTT	IDT
SD_St_02_ATTO647N	/5ATTO647NN/CACTCTCACACCTCATACATCTACCATCACTCTT	IDT
SD_St_02_Cy3	/5Cy3/CACTCTCACACCTCATACATCTACCATCACTCTT	IDT
SD_St_02_Cy5	/5Cy5/CACTCTCACACCTCATACATCTACCATCACTCTT	IDT
SD_St_02_5pr_Cy3N	/5Cy3N/CACTCTCACACCTCATACATCTACCATCACTCTT	IDT
SD_St_02_3pr_Cy3N	TTCACTCTCACACCTCATACATCTACCATCACTC/3Cy3N/	IDT
SD_SC_01_5pr_Cy3N	/5Cy3N/ATGAGGTGTATGTGTAGAGTGATGGATGTAGTTT	IDT
SD_SC_01_3pr_Cy3N	TTATGAGGTGTATGTGTAGAGTGATGGATGTAGT/3Cy3N/	IDT
SD_SC_02_5pr_Cy3N	/5Cy3N/AGGATGAGTGAGAGTGAGATGAGAGTAGATGTTT	IDT
SD_SC_02_3pr_Cy3N	TTAGGATGAGTGAGAGTGAGATGAGAGTAGATGT/3Cy3N/	IDT
	Oligos for Compact Cube below	
LC_SC_01	TTGAAAATTATCTCGATAAGCAGAAGGACCTGTATAACTGGCAAGAGACAAGGCCGCTTCAGAA	IDT
LC_SC_02	AGGATAGCCGGACCGTATTAATGCCGCGCCAACGGTTTCCCGGACCTAGTGTCTATCAAGTCTA	IDT
LC_SC_03	TTCTATGAAACCATTCTCGGGTCGAGCGGGTCACTGTTGTGACCTACGAGAAGCGTATAGATGT	IDT
LC_SC_04	TCCGCGCGAATAGCTCACAGGCGAACTACGTATGAATTGGTTTAAACGCTCCTCGGGAATTAAT	IDT
LC_SC_05	ACGACAGGTGGCAAACCACCTCCGATGTCAGCGCCGCATACCCATTCACTGTGAATTTCCACCAC	IDT
LC_SC_06	CGAGGATTCGCAGGTCCATGGGATTCACCAAGCTCGTATACACCCTGATTCTCCATGGCAGCGC	IDT
LC_SC_07	GTAAGTTGAAGTAGGAAGCTTTTTCTAGCCATAGCATCGACACTACGACCTGCTTTTCGACACA	IDT

Name	Sequence and modification	Vendor
LC_SC_08	GGACTGCATTCTGGACAGTAACTGCATTAACTACGTGCTCCCAACATAAGTGACGTCCTCAGCA	IDT
LC_St_01	TTTGCTGAGGTGGAAATTTT	IDT
LC_St_02	TTCCGGGAAACCGTTGGCCCTTCTGCTCGCCTGTCGTAGGTCGGGT	IDT
LC_St_03	GGTTCTGCGAATCCTCGGTGACGTCACTTCCTACTTCAACTTACTT	IDT
LC_St_04	GTATGCGGCGCTCAGTTACTTCGTAGTGTCGATGCTTT	IDT
LC_St_05_Biotin	/5Biosg/TTCCATGGACTCATAGAATT	IDT
LC_St_06	TTGAGAATCAACAACAGTTT	IDT
LC_St_07_Cy3	TTACATCTATCACTAGGTTT/Cy3	IDT
LC_St_08	TTTACGTAGTTTATCGAGTT	IDT
LC_St_09	TTCCGGCTATCCTTTCTGAAGCGGCCCCGAGGAGGAAT	IDT
LC_St_10	GTATACGAGCTTAAAAAGCTTATGTTGGGAGCACGTTT	IDT
LC_St_11	TTTGCCAGTTATACAGGTGCGGCATTCGACCCGACGTTTAAAATGG	IDT
LC_St_12	TTAGGTGGTTCGCGCGGATT	IDT
LC_St_13	TTAGTTAATGGACATCGGTT	IDT
LC_St_14	TTATAATTTTCAATAGACTTGATAGAACGCTTCTGAGCTATTTGCC	IDT
LC_St_15	TTGACCCGCTAATACGGTTT	IDT
LC_St_16	ACCTGTCGTGCGAAAGCAGGGTCCAGAATGCAGTCCTT	IDT
LC_St_17	TTATGGCTAGGGTGAATCTT	IDT
LC_St_18	TTCACAGTGACCAATTCATT	IDT
LC_St_19	TTTGTGTCGACTGCCATGTT	IDT
LC_St_20	TTATTAATTCTTGTCTCTTT	IDT
LC_St_03_Cy3	GGTTCTGCGAATCCTCGGTGACGTCACTTCCTACTTCAACTTACTT/Cy3	IDT
LC_St_09_Cy3	Cy3/TTCCGGCTATCCTTTCTGAAGCGGCCCCGAGGAGGAAT	IDT
LC_St_14_Cy3	Cy3/TTATAATTTTCAATAGACTTGATAGAACGCTTCTGAGCTATTTGCC	IDT
LC_St_16_Cy3	ACCTGTCGTGCGAAAGCAGGGTCCAGAATGCAGTCCTT/Cy3	IDT
LC_St_20_Cy3	TTATTAATTCTTGTCTCTTT/Cy3	IDT

Table S4.4 | Combination of oligonucleotide strands used to assemble all DNA FluoroCubes, Single Dye Cubes, one dye double-stranded DNA and Compact Cubes with one or six dyes used in this study. Nomenclature: “FC” stands for FluoroCubes with six dyes and “SD” stands for Single Dye Cubes. “dsDNA” stands for one dye double-stranded DNA (dsDNA). “LC” stands for the Compact Cube[133]. The exact sequences with modifications are given in **Table S4.3**. Here “Cy3” stands for the non-sulfonated version of Cy3 whereas “Cy3N” stands for the sulfonated version of Cy3. The detailed design of the Cy3N Single Dye Cubes (SDC 1-6) is shown in **Figure S4.16**. The SDC 5 design of the Cy3N Single Dye Cubes has the dye at the same position as all other Single Dye Cubes with different dyes. Note that for FluoroCubes with either Janelia Fluorophores JF549 or JF646 amino group modified oligos have been used which were labeled with either dye as described in the **Materials and Methods** and shown in **Figure S4.8**. A protocol for annealing the oligonucleotide strands to fold DNA FluoroCubes, Single Dye Cubes, one dye double-stranded DNA and Compact Cubes with one or six dyes is given in the **Materials and Methods**.

Fluorocube / Single Dye Cube/ One dye dsDNA/ Compact Cube name	**Oligonucleotide strands used**
FC_ATTO488_Biotin	FC_SC_01_ATTO488, FC_SC_02_ATTO488, FC_St_01_Biotin, FC_St_02_ATTO488
FC_ATTO565_Biotin	FC_SC_01_ATTO565, FC_SC_02_ATTO565, FC_St_01_Biotin, FC_St_02_ATTO565
FC_ATTO647N_Biotin	FC_SC_01_ATTO647N, FC_SC_02_ATTO647N, FC_St_01_Biotin, FC_St_02_ATTO647N
FC_ATTO647N_HALO	FC_SC_01_ATTO647N, FC_SC_02_ATTO647N, FC_St_01_HALO, FC_St_02_ATTO647N
FC_Cy3_Biotin	FC_SC_01_Cy3, FC_SC_02_Cy3, FC_St_01_Biotin, FC_St_02_Cy3
FC_Cy3N_Biotin	FC_SC_01_Cy3N, FC_SC_02_Cy3N, FC_St_01_Biotin, FC_St_02_Cy3N
FC_Cy5_Biotin	FC_SC_01_Cy5, FC_SC_02_Cy5, FC_St_01_Biotin, FC_St_02_Cy5
FC_JF549_Biotin	FC_SC_01_NH2, FC_SC_02_NH2, FC_St_01_Biotin, FC_St_02_NH2
FC_JF646_Biotin	FC_SC_01_NH2, FC_SC_02_NH2, FC_St_01_Biotin, FC_St_02_NH2
SD_ATTO488_Biotin	SD_SC_01_UN, SD_SC_02_UN, FC_St_01_Biotin, SD_St_02_ATTO488
SD_ATTO565_Biotin	SD_SC_01_UN, SD_SC_02_UN, FC_St_01_Biotin, SD_St_02_ATTO565
SD_ATTO647N_Biotin	SD_SC_01_UN, SD_SC_02_UN, FC_St_01_Biotin, SD_St_02_ATTO647N
SD_Cy3_Biotin	SD_SC_01_UN, SD_SC_02_UN, FC_St_01_Biotin, SD_St_02_Cy3
SD_Cy5_Biotin	SD_SC_01_UN, SD_SC_02_UN, FC_St_01_Biotin, SD_St_02_Cy5
SD_Cy3N_Biotin_SDC1	SD_SC_01_5pr_Cy3N, SD_SC_02_UN, FC_St_01_Biotin, SD_St_02_UN
SD_Cy3N_Biotin_SDC2	SD_SC_01_3pr_Cy3N, SD_SC_02_UN, FC_St_01_Biotin, SD_St_02_UN
SD_Cy3N_Biotin_SDC3	SD_SC_01_UN, SD_SC_02_5pr_Cy3N, FC_St_01_Biotin, SD_St_02_UN

Fluorocube / Single Dye Cube/ One dye dsDNA/ Compact Cube name	Oligonucleotide strands used
SD_Cy3N_Biotin_SDC4	SD_SC_01_UN, SD_SC_02_3pr_Cy3N, FC_St_01_Biotin, SD_St_02_UN
SD_Cy3N_Biotin_SDC5	SD_SC_01_UN, SD_SC_02_UN, FC_St_01_Biotin, SD_St_02_5pr_Cy3N
SD_Cy3N_Biotin_SDC6	SD_SC_01_UN, SD_SC_02_UN, FC_St_01_Biotin, SD_St_02_3pr_Cy3N
dsDNA_ATTO488_Biotin	dsDNA_Biotin, SD_St_02_ATTO488
dsDNA_ATTO565_Biotin	dsDNA_Biotin, SD_St_02_ATTO565
dsDNA_ATTO647N_Biotin	dsDNA_Biotin, SD_St_02_ATTO647N
dsDNA_Cy3_Biotin	dsDNA_Biotin, SD_St_02_Cy3
dsDNA_Cy5_Biotin	dsDNA_Biotin, SD_St_02_Cy5
dsDNA_Cy3N_Biotin	dsDNA_Biotin, SD_St_02_5pr_Cy3N
LC_one-dye_Cy3_Biotin	LC_SC_01, LC_SC_02, LC_SC_03, LC_SC_04, LC_SC_05, LC_SC_06, LC_SC_07, LC_SC_08, LC_St_01, LC_St_02, LC_St_03, LC_St_04, LC_St_05_Biotin, LC_St_06, LC_St_07_Cy3, LC_St_08, LC_St_09, LC_St_10, LC_St_11, LC_St_12, LC_St_13, LC_St_14, LC_St_15, LC_St_16, LC_St_17, LC_St_18, LC_St_19, LC_St_20
LC_six-dyes_Cy3_Biotin	LC_SC_01, LC_SC_02, LC_SC_03, LC_SC_04, LC_SC_05, LC_SC_06, LC_SC_07, LC_SC_08, LC_St_01, LC_St_02, LC_St_03_Cy3, LC_St_04, LC_St_05_Biotin, LC_St_06, LC_St_07_Cy3, LC_St_08, LC_St_09_Cy3, LC_St_10, LC_St_11, LC_St_12, LC_St_13, LC_St_14_Cy3, LC_St_15, LC_St_16_Cy3, LC_St_17, LC_St_18, LC_St_19, LC_St_20_Cy3

Table S4.5 | Settings for excitation and emission spectra measurements. These settings were used for all samples, DNA FluoroCubes (cube with six dyes), one dye dsDNA, and single, biotinylated dyes. We used an interval of 1 nm between the measurements. All measurements here are bulk measurements.

	Excitation spectra - Excitation Wavelength	**Excitation spectra - Emission Wavelength (fixed)**	**Emission spectra - Excitation Wavelength (fixed)**	**Emission spectra - Emission Wavelength**
ATTO 488	350 to 580 nm	600 nm	430 nm	450 to 700 nm
ATTO 647N	450 to 730 nm	750 nm	580 nm	600 to 800 nm
Cy3	400 to 630 nm	650 nm	450 nm	470 to 750 nm

Table S4.6 | Settings for fluorescence anisotropy measurements. These settings were used for all samples, FluoroCubes (cube with six dyes), one dye dsDNA, and single NHS ester dyes. All measurements are bulk measurements.

	Iterations	**Excitation Wavelength (fixed)**	**Emission Wavelength (fixed)**
ATTO 488	24	500 nm	520 nm
ATTO 647N	24	647 nm	665 nm
Cy3	24	550 nm	565 nm
Cy5	24	649 nm	665 nm

Table S4.7 | Settings for fluorescence lifetime measurements. These settings were used for all samples, FluoroCubes (cube with six dyes), one dye dsDNA, and single NHS ester dyes. All measurements are bulk measurements.

	Excitation Wavelength (fixed)	**Emission Longpass filter**	**Modulation frequencies**
ATTO 488	470 nm	500 nm	400,000 Hz, 797,895 Hz, 1,591,590 Hz, 3,174,802 Hz, 6,332,894 Hz, 12,632,455 Hz, 25,198,421 Hz, 50,264,213 Hz, 100,263,864 Hz, and 200,000,000 Hz
ATTO 647N	620 nm	650 nm	See ATTO 488
Cy3	475 nm	520 nm	See ATTO 488
Cy5	620 nm	650 nm	See ATTO 488

Table S4.8 | Calculation of radiant exposures as used in Figure S4.6. Laser power was measured after the objective. The field of illumination has a 2D Gaussian shape (reflecting the Gaussian shape of the laser beam), causing the radiant exposure to vary over the field of view. We calculated an average radiant exposure by assuming a field of illumination of 60 x 60 µm.

Laser power 488 nm [mW]	**Laser power 561 nm [mW]**	**Laser power 640 nm [mW]**	**Exposure time [ms]**	**Radiant exposure 488 nm [µJ/µm^2]**	**Radiant exposure 561 nm [µJ/µm^2]**	**Radiant exposure 640 nm [µJ/µm^2]**
0.31	0.29	0.36	100	0.01	0.01	0.01
0.31	0.29	0.36	200	0.02	0.02	0.02
0.31	0.29	0.36	400	0.03	0.03	0.04
4.44	4.45	5.75	100	0.12	0.12	0.16
4.44	4.45	5.75	200	0.25	0.25	0.32
11.58	12.82	14.89	100	0.32	0.36	0.41
11.58	12.82	14.89	200	0.64	0.71	0.83
11.58	12.82	14.89	400	1.29	1.42	1.65
15.36	20.36	18.01	100	0.43	0.57	0.50
15.36	20.36	18.01	200	0.85	1.13	1.00
15.36	20.36	18.01	400	1.71	2.26	2.00

Table S4.9 | Number of first frames to check for Spot Intensity Analysis Plugin. The “Spot Intensity Plugin” finds spot coordinates by averaging a user-definable number of frames and detecting local maxima within this averaged image. Intensities at these coordinates are then measured in the complete data set. The number of frames to check varies for each sample depending on how fast they bleach. If for example a molecule bleaches early (as for the one dye double-stranded DNA), many dark frames will be used for the average and very few molecules will be found since the average intensity will be lower than the threshold (Noise). In a similar way, if too few frames are used and a molecule gets brighter over time (as for the six dye FluoroCubes), then it may not be considered. Thus, we typically used only a few frames for the one dye double-stranded DNA, single, biotinylated dyes, and the Single Dye Cube samples and more frames for the six dye FluoroCube samples. However, this also depended on how fast the six dye FluoroCubes bleached. “Single Dye Cube” refers to a cube with a single dye whereas “FluoroCube” refers to a cube with six dyes. “Cy3” stands for the non-sulfonated version of Cy3 whereas “Cy3N” stands for the sulfonated version of Cy3.

Figure	**Dataset**	**Number of frames to check**
Fig. 4.1, Fig. S4.3, Fig. S4.5, Fig. S4.7, Fig. S4.15	One dye dsDNA (ATTO 488)	10
Fig. S4.3	Single, biotinylated dye (ATTO 488)	10
Fig. S4.15	Single Dye Cube (ATTO 488)	20
Fig. 4.1, Fig. S4.5, Fig. S4.7	FluoroCube (ATTO 488)	500
Fig. 4.1, Fig. S4.5, Fig. S4.7, Fig. S4.15	One dye dsDNA (ATTO 565)	50
Fig. S4.15	Single Dye Cube (ATTO 565)	100
Fig. 4.1, Fig. S4.5, Fig. S4.7	FluoroCube (ATTO 565)	500
Fig. 4.1, Fig. S4.3, Fig. S4.5, Fig. S4.7, Fig. S4.15	One dye dsDNA (ATTO 647N)	100
Fig. S4.3	Single, biotinylated dye (ATTO 647N)	100
Fig. S4.15	Single Dye Cube (ATTO 647N)	100
Fig. 4.1, Fig. S4.5, Fig. S4.7, Fig. S4.8, Fig. S4.14	FluoroCube (ATTO 647N)	4,000
Fig. 4.1, Fig. S4.3, Fig. S4.5, Fig. S4.15	One dye dsDNA (Cy3)	10
Fig. S4.3	Single, biotinylated dye (Cy3)	10
Fig. S4.15	Single Dye Cube (Cy3)	100
Fig. 4.1, Fig. S4.5, Fig. S4.8	FluoroCube (Cy3)	2,000
Fig. 4.1, Fig. S4.5, Fig. S4.7, Fig. S4.15	One dye dsDNA (Cy3N)	100
Fig. S4.15, Fig. S4.16	Single Dye Cube (Cy3N)	100
Fig. 4.1, Fig. S4.5, Fig. S4.7	FluoroCube (Cy3N)	4,000
Fig. 4.1, Fig. S4.5, Fig. S4.7, Fig. S4.15	One dye dsDNA (Cy5)	10
Fig. S4.15	Single Dye Cube (Cy5)	20

Figure	Dataset	Number of frames to check
Fig. 4.1, Fig. S4.5, Fig. S4.7	FluoroCube (Cy5)	1,000
Fig. S4.8	FluoroCube (JF 549)	1,000
Fig. S4.8	FluoroCube (JF 646)	4,000
Fig. S4.14	Q-dot	4,000
Fig. S4.17	One dye Compact Cube	100
Fig. S4.17	Six dye Compact Cube	1000
Fig. S4.17	Single Dye Cube (Cy3)	100
Fig. S4.17	FluoroCube (Cy3)	2000

Table S4.10 | Fitting parameters used in μManager's[70] 'Localization Microscopy' plug-in.

Imaging Parameters	
Photon conversion factor	1.84
Linear (EM) gain	1.0
Pixel size [nm]	159.0
Time interval [ms]	103
Z-step [nm]	50.0
Camera offset [electron counts]	91.0
Read noise [electron counts]	9.84
Find Maxima	
Pre-Filter	None
Noise tolerance	80
Fit Parameters	
Dimensions	1
Filter	Simplex-MLE
Max Iterations	500
Box size [pixel]	12.0
Fix width	Not selected
Filter Data	Nothing selected
Positions	Only imaged at one position
Skip Channels	Not selected

Table S4.11 | Photophysical properties of one dye double-stranded DNA and single, biotinylated dyes. Note, that the average total number of photons shown here is a slight underestimate because not all probes bleached within 600 seconds. Errors (±) are the standard error of the mean of four repeats, which is recording a movie with freshly assembled double-stranded DNA. For the single, biotinylated dyes, we always used a new dye aliquot from the same stock that was previously aliquoted. “n” is the sample size number.

	Photo-bleaching half-life time in seconds	**Total number of photons (10^6)**	**Average number of photons per frame (10^3)**
One dye dsDNA (ATTO 488) n = 5347	20 ± 6	0.08 ± 0.01	2.2 ± 0.3
Single, biotinylated dye (ATTO 488) n = 7260	7 ± 2	0.13 ± 0.01	1.4 ± 0.2
One dye dsDNA (Cy3) n = 2291	25 ± 3	0.20 ± 0.03	1.6 ± 0.1
Single, biotinylated dye (Cy3) n = 4447	9 ± 1	0.16 ± 0.01	2.5 ± 0.2
One dye dsDNA (ATTO 647N) n = 3071	92 ± 9	2.8 ± 0.3	9.0 ± 0.3
Single, biotinylated dye (ATTO 647N) n = 2711	54 ± 3	1.6 ± 0.1	7.1 ± 0.5

Table S4.12 | Photophysical properties of Single Dye Cubes. Note, that the average total number of photons shown here is a slight underestimate because not all probes bleached within 600 seconds. The white part of the table (top) shows values corresponding to **Figure S4.15** and the grey part (bottom) shows values corresponding to **Figure S4.16**. Errors (±) are the standard error of the mean of four (three for the Cy3N Single dye Cubes) repeats, which is recording a movie with freshly assembled Single Dye Cubes. "n" is the sample size number. The detailed design of the Cy3N Single Dye Cubes (SDC 1-6) is shown in **Figure S4.16**. The SDC 5 design of the Cy3N Single Dye Cubes has the dye at the same position as all other Single Dye Cubes labeled with different dyes.

	Photo-bleaching half-life time in seconds	**Total number of photons (10^6)**	**Average number of photons per frame (10^3)**
Single Dye Cube (ATTO 488) n = 4541	19 ± 1	0.3 ± 0.1	2.8 ± 0.1
Single Dye Cube (ATTO 565) n = 1172	54 ± 2	1.6 ± 0.1	7.4 ± 0.1
Single Dye Cube (Cy3) n = 1915	308 ± 46	3.0 ± 0.3	3.7 ± 0.1
Single Dye Cube (ATTO 647N) n = 2507	346 ± 51	10.2 ± 0.5	10.6 ± 0.2
Single Dye Cube (Cy5) n = 1194	157 ± 13	4.0 ± 0.1	7.8 ± 0.2
Single Dye Cube (Cy3N) (Supp. Figure 15 - like SDC 5) n = 1282	420 ± 14	9.8 ± 0.3	10.5 ± 0.4
Single Dye Cube (Cy3N) - SDC 1 n = 3094	271 ± 12	7.5 ± 0.1	10.4 ± 0.1
Single Dye Cube (Cy3N) - SDC 2 n = 1919	96 ± 1	2.3 ± 0.1	5.8 ± 0.2
Single Dye Cube (Cy3N) - SDC 3 n = 2074	307 ± 14	7.8 ± 0.2	10.0 ± 0.1
Single Dye Cube (Cy3N) - SDC 4 n = 3459	83 ± 4	1.9 ± 0.1	5.8 ± 0.2

	Photo-bleaching half-life time in seconds	Total number of photons (10^6)	Average number of photons per frame (10^3)
Single Dye Cube (Cy3N) - SDC 5 n = 990	435 ± 7	9.6 ± 0.4	10.2 ± 0.4
Single Dye Cube (Cy3N) - SDC 6 n = 3155	114 ± 10	2.3 ± 0.1	5.5 ± 0.2

Table S4.13 | Photophysical properties of Single Dye Cubes, six dye FluoroCubes, Compact Cube with one and six dyes. Note, that the average total number of photons shown here is an underestimate because not all probes bleached within 800 seconds. This is particularly true for the six Cy3 dye FluoroCube. Errors (±) are the standard error of the mean of five repeats, which is recording a movie with freshly assembled six dye FluoroCubes, Single Dye Cubes, or Compact Cubes with one or six dyes. “n” is the sample size number. N.m. stands for not measurable since the six Cy3 dye FluoroCubes did not photobleach to 50%.

	Photo-bleaching half-life time in seconds	**Total number of photons (10^6)**	**Average number of photons per frame (10^3)**
FluoroCube (Cy3) n = 6629	n.m.	10.9 ± 0.5	5.4 ± 0.2
Single Dye Cube (Cy3) n = 6319	243 ± 41	2.5 ± 0.3	3.8 ± 0.1
One dye Compact Cube (Cy3) n = 6451	214 ± 37	2.3 ± 0.4	4.7 ± 0.1
Six Dye Compact Cube (Cy3) n = 7740	480 ± 75	9.9 ± 0.6	7.4 ± 0.1

Materials and Methods

Flow-cell preparation

Flow-cells were assembled as previously described[78]. Briefly, we made custom three-cell flow chambers using laser-cut double-sided adhesive sheets (Soles2dance, 9474-08x12 - 3M 9474LE 300LSE), glass slides (Thermo Fisher Scientific, 12-550-123), and 170 µm thick coverslips (Zeiss, 474030-9000-000). The coverslips were cleaned in a 5% v/v solution of Hellmanex III (Sigma, Z805939-1EA) at 50° C overnight and washed at least ten times with the same amount of Milli-Q water.

Assembly and analysis of the DNA FluoroCubes, Single Dye Cubes, double-stranded DNA, and of Compact Cubes

For each six dye FluoroCube and Single Dye Cube four 32 bp long oligonucleotide strands are required, each modified either with dyes or a functional tag such as biotin or HALO-ligand[103] (**Fig. S4.1, Table S4.3, Table S4.4**). These four oligos are connected using crossovers resulting in four connected 16 bp long double-stranded DNAs (dsDNA) with a size of approximately 5.4 x 4.0 x 4.0 nm. A detailed map of oligonucleotide routing and the bases is depicted in **Figure S4.1**. Two oligos were used for the double-stranded DNA with one dye and 28 oligos were used for the Compact Cubes[133] (**Table S4.3, Table S4.4**). For each of the four samples oligos were mixed to a final concentration of 10 µM (if not stated otherwise) in folding buffer (5 mM Tris pH 8.5, 1 mM EDTA and 40 mM $MgCl_2$ (if not stated otherwise)) and annealed by denaturation at 85° C for 5 min followed by cooling from 80° C to 65° C with a decrease of 1° C per 5 min. Afterwards the samples were further cooled from 65° C to 25° C with a decrease of 1° C per 20 min and then held at 4° C. Folding products were analyzed by 3.0% agarose gel electrophoresis (if not stated otherwise) in TBE (45 mM Tris-borate and 1 mM EDTA) with 12 mM $MgCl_2$ at 70 V for 2.5 hours on ice and purified by extraction and centrifugation in Freeze 'N Squeeze columns (BioRad Sciences, 732-6165). The gels were scanned using a Typhoon 9400

scanner (GE Healthcare). A step-by-step protocol on FluoroCube assembly can be found on protocols.io (dx.doi.org/10.17504/protocols.io.8k2huye)[154].

Agarose gel-based yield estimation was carried out using ImageJ[75]. The percentage of FluoroCubes that ran as a monomeric band was estimated as the background-subtracted integrated intensity value divided by the background-subtracted integrated intensity value enclosing the material from the well, down to the bottom of the leading band (single oligos). Note, that the different brightness of FluoroCube bands in the agarose gels is mainly due to the variation of material loaded into the gel.

Negative stain electron microscopy data collection and processing

For negative-stain EM, unpurified, but folded FluoroCubes at 300 nM (diluted in FluoroCube Buffer: 20 mM Tris pH 8.0, 1 mM EDTA, 20 mM Mg-Ac, and 50 mM NaCl) were incubated on freshly glow discharged carbon coated 400 mesh copper grids for 1 min and blotted off. Immediately after blotting, a 0.75% uranyl formate solution was applied for staining and blotted off without incubation. This staining was repeated four times and followed by a last incubation for which the stain was incubated for 45 sec before blotting. Samples were allowed to air dry before imaging. Data were acquired at UCSF, on a Tecnai T12 microscope operating at 120 kV, using a 4k×4k CCD camera (UltraScan 4000, Gatan) and a pixel size of 1.7 Å/pixel. For the class average in **Figure 4.1**, 1,743 Particles were picked and boxed using EMAN 2.21[155]. Then a 2D classification was performed to remove junk and noisy particles, leading to 983 particles selected.

Mono-Q clean-up of DNA FluoroCubes

Thermally annealed DNA FluoroCubes were purified using anion exchange chromatography with a GE Source 15Q 4.6/100 PE column (**Fig. S4.21**). DNA FluoroCubes were bound to the column in Buffer A (20 mM Tris pH 8.0, 1 mM EDTA, 10 mM Mg-Ac, and 10%

Glycerol) and afterwards the ionic strength was increased linearly by adding Buffer B (20 mM Tris pH 8.0, 2 M K-Ac, 1 mM EDTA, 10 mM Mg-Ac, and 10% Glycerol) to 100% over 80 min.

Labeling of oligonucleotides with Janelia Fluorophores

We mixed 5' and 3' amino modified oligos (**Table S4.3**) at a final concentration of 500 μM (in water) with NHS ester modified Janelia Fluorophores JF549 or JF646[135] at a final concentration of 5 mM (in DMSO) in 15 mM HEPES pH 8.5 buffer. These solutions were incubated for 4 h at room temperature. We then removed excess dye by four subsequent spins of the solution over Micro Bio-Spin 6 Columns (Bio-Rad) at 700 g for 2 min. The final oligo concentration was determined with a UV spectrophotometer. Afterwards six dye FluoroCubes were assembled as described above.

Preparation of flow-cells with DNA FluoroCubes, Single Dye Cubes, double-stranded DNA, Compact Cubes, biotinylated dyes and quantum dots

The preparation of flow cells is identical for 6-dye Cubes (FluoroCubes), 1-dye Cubes (Single Dye Cubes), the double-stranded DNA with one dye, biotinylated dyes, and the one and six dye Compact Cubes[133]. In either case, samples were folded with biotin as the functional tag (except the single, biotinylated dye) and we used unpurified, but folded samples. We first added 10 μl of 5 mg/ml Biotin-BSA (Thermo Scientific, 29130) in BRB80 to the flow-cell and incubated for 2 min. Afterwards, we added another 10 μl of 5 mg/ml Biotin-BSA in BRB80 and incubated for 2 min. Then we washed with 20 μl of FluoroCube Buffer (20 mM Tris pH 8.0, 1 mM EDTA, 20 mM Mg-Ac, and 50 mM NaCl) with 2 mg/ml β-casein (Sigma, C6905), 0.4 mg/ml κ-casein (Sigma, C0406). This was followed by addition of 10 μl of 0.5 mg/ml Streptavidin (Vector Laboratories, SA-5000) in PBS (pH 7.4) and a 2 min incubation. We then washed with 20 μl of FluoroCube Buffer with 2 mg/ml β-casein, and 0.4 mg/ml κ-casein. Next, we either added DNA based samples or the single, biotinylated dye in FluoroCube Buffer or Quantum dots (Qdot™

655 Streptavidin Conjugate, ThermoFisher Scientific, Q10121MP) and incubated for 5 min. Finally, we washed with 30 µl of FluoroCube Buffer with 2 mg/ml β-casein, and 0.4 mg/ml κ-casein. We then added the PCA/PCD/Trolox oxygen scavenging system[76,136] in FluoroCube Buffer with 2 mg/ml β-casein, and 0.4 mg/ml κ-casein for the DNA based samples and or the single, biotinylated dye. For the Quantum dots we added the PCA/PCD oxygen scavenging system[76] and 1% β-mercaptoethanol (BME) in FluoroCube Buffer with 2 mg/ml β-casein, and 0.4 mg/ml κ-casein.

We note that the concentration of the PCA/PCD/Trolox oxygen scavenging system[76,136] is critical and small deviations had large effects on the performance of all samples used in our experiments. We used the following concentrations in all our experiments: 2.5 mM of protocatechuic acid (PCA) (Sigma: 37580) at pH 9.0, 5 units of protocatechuate-3,4-dioxygenase (PCD) (Oriental yeast company Americas Inc.: 46852004), and 1 mM Trolox (Sigma: 238813) at pH 9.5.

Measurements of fluorescence anisotropy, fluorescence lifetime, as well as absorption, excitation and emission spectra

We determined fluorescence anisotropy, fluorescence lifetime, as well as excitation and emission spectra using an ISS K2 multifrequency fluorometer in bulk measurements. All experiments were performed at room temperature (21-23° C). Instrument settings for the excitation and emission spectra are listed in **Table S4.5,** settings for the fluorescence anisotropy measurements are listed in **Table S4.6**, and settings for the fluorescence lifetime measurements are listed in **Table S4.7**. For the absorption spectra we used an Eppendorf Spectrophotometer (UV-Vis BioSpectrometer) and measured the absorbance from 240 nm to 800 nm. For all samples we used a concentration of 500 nM. In addition, we normalized the absorption spectra based on the 260 nm absorbance.

Dynamic light scattering (DLS) of DNA FluoroCubes and Compact Cubes

Dynamic light scattering measurements were performed using a Zetasizer ZS90 (Malvern Panalytical) at a wavelength of 633 nm. 60 µl of unpurified FluoroCubes or Compact Cubes were measured at 25°C at a concentration of 5 µM in FluoroCube Buffer (20 mM Tris pH 8.0, 1 mM EDTA, 20 mM Mg-Ac, and 50 mM NaCl).

Kinesin cloning, purification and labeling

The kinesin construct was cloned and purified as previously described[138] except that the GFP was replaced with a HALO-tag[103].

The plasmid was transfected and expressed in Agilent BL21(DE3) cells. Cells were grown in LB at 37° C until they reached 1.0 OD_{600} and the expression was induced by addition of 0.2 mM IPTG. Then the cells were incubated overnight at 20° C. Cells were pelleted and harvested in lysis buffer (25 mM Pipes (pH 6.8), 2 mM $MgCl_2$, 250 mM NaCl, 20 mM imidazole, 1 mM BME, 0.1 mM ATP, and 0.4 mM PMSF), and lysed in the EmulsiFlex homogenizer (Avestin). After a spin in a Sorvall SS-34 rotor for 30 min at 30,000 x g, the supernatant was loaded onto a Ni-NTA resin (QIAGEN, 30210) and washed with additional lysis buffer. We then took 500 µl of beads slur in lysis buffer supplemented with 10 mM $MgCl_2$ and added either six dye ATTO 647N FluoroCubes with a HALO-tag[103] to 5 µM final or 5 µM final of HALO-tag TMR dye (Promega). These mixtures were incubated on a Nutator for 3 h at 4 ° C. Afterwards we washed with additional lysis buffer supplemented with 10 mM $MgCl_2$. Then the protein of both labeling reactions was eluted by adding 300 mM of imidazole to the lysis buffer supplemented with 10 mM $MgCl_2$. Subsequently the samples were purified by gel filtration over a S200 10/300GL column from GE Healthcare. Gel filtration buffer was composed of 25 mM Pipes (pH 6.8), 10 mM $MgCl_2$, 200 mM NaCl, 1 mM EGTA, 1 mM DTT, and 10% sucrose. Finally the samples were flash frozen and stored at -80° C.

Preparation of flow-cells with kinesin

Single-molecule assays with kinesin in flow-cells were prepared as previously described[138,140]. We first added 10 µl of Alexa 488 labeled axonemes in BRB80 (80 mM Pipes (pH 6.8), 1 mM $MgCl_2$, 1 mM EGTA) and incubated for 5 min. Then, we washed with 60 µl of BRB80 with 1.0 mg/ml κ-casein (Sigma, C0406) supplemented with 5 mM $MgCl_2$. For the comparison between six dye ATTO 647N FluoroCubes labeled kinesin and HALO-tag TMR dye labeled kinesin, we added 10 µl of labeled motor in BRB80 with additional 5 mM $MgCl_2$, 1.0 mg/ml κ-casein, 1 mM ATP, and the PCA/PCD/Trolox oxygen scavenging system[76,136]. For the high resolution stepping data acquisition, we added 10 µl of six dye ATTO 647N FluoroCubes labeled kinesin in BRB80 with additional 5 mM $MgCl_2$, 1.0 mg/ml κ-casein, 1.5 µM ATP, an ATP regeneration system (1 mM phosphoenolpyruvate (Sigma, 860077), ~0.01 U pyruvate kinase (Sigma, P0294), ~0.02 U lactate dehydrogenase (Sigma, P0294)), and the PCA/PCD/Trolox oxygen scavenging system[76,136].

Microscope setup

All data collections were carried out at room temperature (~23° C) using a total internal reflection fluorescence (TIRF) inverted microscope (Nikon Eclipse Ti microscope) equipped with a 100× (1.45 NA) oil objective (Nikon, Plan Apo ƛ). We used an Andor iXon 512x512 pixel EM camera, DU-897E and a pixel size of 159 nm. We used two stepping motor actuators (Sigma Koki, SGSP-25ACTR-B0) mounted on a KS stage (KS, Model KS-N) and a custom-built cover to reduce noise from air and temperature fluctuations. A reflection based autofocus unit (FocusStat4) was custom adapted to our microscope (Focal Point Inc.). For the data collection we used a 488 nm laser (Coherent Sapphire 488 LP, 150 mW), a 561 nm laser (Coherent Sapphire 561 LP, 150 mW), and a 640 nm laser (Coherent CUBE 640-100C, 100 mW). A TIRF cube containing excitation filter (Chroma, zet405/491/561/638x), dichroic mirror (zt405/488/561/638rpc), and emission filter (Chroma, zet405/491/561/647m) was mounted in

the upper turret of the microscope. The lower turret contained an ET450/50m (Chroma) filter for the 488 nm laser, an ET600/50m (Chroma) filter for the 561 nm laser, and an ET700/75m (Chroma) filter for the 640 nm laser.

Single-molecule TIRF data collection and analysis of DNA FluoroCubes, Single Dye Cubes, double-stranded DNA, biotinylated dyes, Compact Cubes and quantum dots

The TIRF data of surface immobilized six dye DNA FluoroCubes, Single Dye Cubes, double-stranded DNA with one dye, biotinylated dyes, quantum dots or one and six dye Compact Cubes[133] was acquired under continuous laser illumination with an intensity (irradiance) of 120 W/cm^2 (488 nm laser), 120 W/cm^2 (561 nm laser), and 160 W/cm^2 (640 nm laser) and an exposure of 400 ms if not specified otherwise. The acquisition length varied based on the experiment and how fast the respective probe bleached. Thus, before conducting an experiment we pre-established the acquisition length. Typically we either recoded 7,500 frames (3,000 sec), 2,000 frames (800 sec), 1,500 frames (600 sec), or 300 frames (120 sec). We used the camera in conventional CCD mode (i.e., no EM gain). All datasets were acquired with a '16 bit, conventional, 3 MHz' setting and a preamp gain of 5x. All experiments were performed at room temperature (21-23° C). The acquisition software was μManager[70] 2.0 and data was analyzed in ImageJ[75]. Single molecules were located and traced using the Spot Intensity Analysis plugin in ImageJ[75] (https://imagej.net/Spot_Intensity_Analysis) with the following settings: Time interval of 0.4 sec (except for data in **Figure S4.6** for which the exposure time was used as listed in **Table S4.8**), Electron per ADU of 1.84, Spot radius of 3, Noise tolerance of 100 (except for the Cy3 one dye dsDNA and the single, biotinylated Cy3 dye for which we used a Noise tolerance of 50), and a Median background estimation. The number of frames to check is shown in **Table S4.9** since it varies for each sample depending on how fast they bleach. Afterwards the data were further analyzed and plotted with a custom written python script and only localized particles with >500 photons were counted as in the "on" state. Note,

that in some cases the average total number of photons is an underestimate since not all samples fully bleached within the acquisition time.

Single-molecule TIRF data collection and analysis of kinesin stepping

For the comparison between six dye ATTO 647N FluoroCubes labeled kinesin and TMR dye HALO-tag labeled kinesin, motors were continuously illuminated with an effective exposure time of 0.103 s with a 640 nm laser (160 W/cm^2) or a 561 nm laser (120 W/cm^2), respectively.

For the high resolution stepping data acquisition, kinesins labeled with six dye ATTO 647N FluoroCubes with a HALO-tag[103] were continuously illuminated with a 640 nm laser (160 W/cm^2) with an effective exposure time of 0.103 s. We used the camera in conventional CCD mode (i.e., no EM gain). All datasets were acquired with a '16 bit, conventional, 3 MHz' setting and a preamp gain of 5x. All experiments were performed at room temperature (21-23° C). The acquisition software was μManager[70] 2.0. All emitters were fitted and localized using μManager's[70] "Localization Microscopy' plug-in as previously described[78]. Parameters for analysis are shown in **Table S4.10**. Tracks of individual motors were extracted using the μManagers[70] "Localization Microscopy' plug-in. We set the minimum frame number to 1000, the maximum number of missing frames to 100, the maximum distance between frames to 100 nm and the total minimum distances of the full track to 500 nm. Then tracks of individual motors were rotated using a principal component analysis (PCA) implemented in python. Afterwards we used a custom Matlab (Matlab R2016b) script to identify individual steps using Chung-Kennedy edge-detecting algorithm as previously described[48] and further analyzed the data in a custom written python script. Only steps for which the step itself and the previous as well as following step had a standard deviation of less than 4 nm were considered for further quantification. The velocity over time for the stepping trace of a single kinesin was analyzed with a moving average for which we first binned the data into 2.6 sec bins and then grouped six of these 2.6 sec bins

into 15.6 sec bins. We used these 15.6 sec bins to calculate the average velocity at any given point, but used the 2.6 sec intervals to move along the time axis.

Figure and graph preparation

Figures were created using ImageJ[75] (light microscopy data), Affinity designer (version 1.6.1, Serif (Europe) Ltd) and Python (version 2.7, Python Software Foundation).

Statistics and error calculation

For each result the inherent uncertainty due to random or systematic errors and their validation are discussed in the relevant sections of the manuscript. Details about the sample size, number of independent calculations, and the determination of error bars in plots are included in the figures and figure captions.

Acknowledgements

We are grateful to Jongmin Sung (University of California, San Francisco) for critical discussions of the manuscript. We thank Dyche Mullins (University of California, San Francisco) for teaching us how to use the ISS K2 multifrequency fluorometer. We are thankful to Young-wook Jun and Yuetao Zhao (University of California, San Francisco) for teaching us how to use the Malvern Zetasizer ZS90. We thank Luke Lavis (Janelia Research Campus) for the suggestion of comparing sulfonated versus non-sulfonated dyes and for providing the JF549 and JF646 dyes. We are thankful to Shawn Douglas (University of California, San Francisco) and Andrew G. York (Calico Labs) for feedback on the manuscript after pre-printing. Andrew Carter (MRC Laboratory of Molecular Biology) and Elizabeth Villa (University of California, San Diego) supplied the Matlab script for step detection of kinesin. The authors gratefully acknowledge funding from the National Institutes of Health: R01GM097312, 1R35GM118106 (R.D.V., S.N.), and the Howard Hughes Medical Institute (R.D.V. and N.S.).

CHAPTER 5

Three-color single-molecule imaging reveals conformational dynamics and minimal requirements for directed motility of dynein

Abstract

The homodimeric AAA+ motor protein dynein has to precisely coordinate the motion among its many domains to achieve directed and continuous motility along microtubules. While recent structural and biochemical studies uncovered key molecular mechanisms contributing to dynein motility, a comprehensive understanding of how dynein coordinates the movement of its many domains when stepping along microtubules is lacking. Here, we used three-color, single-molecule imaging to track multiple domains of dynein simultaneously with nanometer precision. We observed that the AAA ring and the microtubule-binding domain (MTBD) move relative to each other leading to both domains not always stepping simultaneously and to both domains taking differently sized steps. Moreover, using Monte Carlo simulations we found that this flexibility within the motor domain is important for dynein motility and enables dynein to adopt a large variety of conformations. Thus, we propose that dynein is a highly flexible molecule whose directional motility depends on the relative movement between AAA ring and microtubule-binding domain.

Introduction

The microtubule-based motor protein dynein belongs to the AAA+ family (ATPases Associated with diverse cellular Activities) motors and is responsible for almost all minus end directed motility along microtubules[11,34]. Dyneins play key roles in cellular processes and architecture including cargo transport, mitosis, and cilia motility[1–4]. Mutations or defects in dyneins are linked to several pathologies including cancers and neurological diseases[5,6].

Compared to other cytoskeletal motors, kinesin[15,16] and myosin[17,18], which have a globular and compact motor domain, dynein is the largest and most complex cytoskeletal motor protein with a size of ~1.4 MDa. This large machinery is composed of two heavy chains and several associated polypeptide chains that primarily bind to the N-terminal tail region to dimerize the heavy chains, regulate dynein's function and attach it to cargo[2,54,156]. The remaining two-thirds of the dynein heavy chain constitute the motor domain which is the main driver of dynein motility and sufficient for processive movement along microtubules[60]. The motor domain consists of six different AAA domains that are linked together as an asymmetric hexameric ring (AAA1–AAA6) of which only AAA1-4 can bind or hydrolyze ATP[27,30,33,37]. On top of the AAA ring lies the N-terminal linker which serves as the mechanical element. Upon ATP binding to AAA1 dynein releases from microtubules and the linker bends. After ATP hydrolysis, dynein rebinds to microtubules while the linker undergoes the force-generating power stroke by straightening back to its initial conformation[29,34–36,39]. The large catalytic AAA ring of dynein is separated from the small microtubule-binding domain (MTBD) by a ~15 nm long, coiled-coil extending from AAA4 called the stalk[40–42]. The conservation of the stalk length combined with the conserved direction in which the dynein linker swings make dynein a microtubule motor that moves exclusively towards the minus end[11,157].

Initial dynein stepping experiments with a single fluorescent probe revealed that dynein, unlike kinesin, takes side- and backward steps[60]. In addition, dynein was observed to take variable step sizes compared to kinesin which only takes 16 nm steps[60,140]. Later, two-color

single-molecule experiments showed that the two AAA rings of dynein move in an uncoordinated manner, different from the hand-over-hand stepping of kinesin and myosin[47,48,140,158]. Moreover, one active motor domain and an additional microtubule anchor were shown to be sufficient to achieve processive and directed motility since the linker tension gates microtubule release of dynein[67].

However, all these observations stem from experiments in which the movement of the AAA rings of dynein were followed and it is unclear whether the MTBDs of dynein move in the same way as the AAA ring. Moreover, it is unknown how the AAA ring and the MTBD of dynein move relative to each other while dynein steps along microtubules. This is particularly interesting as the AAA ring and the MTBD have been observed to move relative to each other when bound to microtubules, indicating flexible elements within the dynein motor domain[11,49,50]. While cryo-electron microscopy studies showed that a flexible hinge between the MTBD and stalk gives rise to this relative movement[50], it is unknown to what extent this holds true when dynein is moving along microtubules and what influence this flexibility has on dynein's stepping.

Here, we developed a three-color total internal reflection fluorescence (TIRF) microscopy single-molecule experiment that allowed us to track the movement of one AAA ring and two MTBDs simultaneously. We show that the AAA ring and the MTBD step in a slightly different manner with the AAA ring taking larger forward and less backward steps than the MTBD. The difference in step sizes of the MTBD and the AAA ring is further supported by the observation that the AAA ring and the MTBD on the same motor domain do not always step at the same time. Furthermore, we found a large flexibility within dynein's motor domain which permits the AAA ring and MTBD on the same motor domain to move relative to each other in an inter-MTBD distance dependent manner. Moreover, we find that this flexibility within dynein's motor domain not only allows the AAA ring and the MTBD to step at different times and take differently sized steps, but also gives rise to a large variety of conformations that dynein can adopt. Using Monte Carlo simulations combined with our experimental data, we show that

dynein can adopt many previously undescribed conformations and we identify minimal requirements for directed motility. Taken together, we propose that dynein is a highly flexible molecule whose directional motility depends on the relative movement between AAA ring and microtubule-binding domain.

Results

Stepping analysis of a three-color dynein

To determine how the AAA ring and the MTBD of dynein move relative to each other while dynein is stepping along microtubules, we tracked the stepping of a three-color labeled dynein in which one AAA ring and two MTBDs are fluorescently labeled with high spatiotemporal resolution. Therefore, we designed a three-color TIRF microscopy single-molecule experiment and first extended our previously developed two-color image registration routine[78] to a three-color system (**Fig. S5.1**). We validated this approach by measuring the distance between three differently colored dyes that were placed at well-defined distances on a DNA-origami nanoruler[100,159] (**Fig. S5.2**) and found that we can recover the expected distances among all three dyes with one nanometer accuracy.

To create a three-color labeled dynein dimer in which one AAA ring and two MTBDs are fluorescently labeled, we used the well-studied, truncated yeast cytoplasmic dynein and added a N-terminal SNAP-tag[160], a C-terminal HALO-tag[103] and an internal YBBR-tag[104]. In this design, the HALO-tag is positioned on top of the AAA ring and the YBBR-tag is placed in a flexible loop (loop 5) of the MTBD enabling us to simultaneously label the AAA ring and the MTBD on the same motor domain.

To label dynein with three colors an optimal fluorescent probe should not only be small enough to not perturb motor function but also be bright and photostable to enable tracking with high spatiotemporal resolution for multiple steps. While quantum dots would provide brightness and photostability for high resolution tracking, their size of ~15 nm would have likely interfered with motor function if three quantum dots were attached to a single dynein (~23 nm tall). On the other hand, single organic dyes are small (~1.5 nm), but bleach significantly faster making it impossible to track a three-color dynein for many steps with nanometer resolution because bleaching of one of the three fluorescent probes would end the three-color trace. DNA FluoroCubes are relatively small (~6 nm) and provide an intermediate brightness as well as

photostability compared to quantum dots and single organic dyes[161]. Specifically, when we compared a three-color dynein labeled with single organic dyes to a three-color dynein labeled with FluoroCubes, we found that 4% of the single dye labeled dynein had a signal in all three channels after 50 frames while for the FluoroCube labeled dynein still more than 75% of the three-color dynein emitted a signal in all three channels (**Fig. S5.3**). Moreover, the FluoroCube labeled dynein yielded more precise localizations with average localization errors between 2.4 and 4.1 nm (**Fig. S5.3**). Thus, we decided to use FluoroCubes as fluorescent labels to create a three-color dynein. To ensure that only one AAA ring in a dynein dimer got labeled, we labeled the two motor domains separately before artificially dimerizing them using the previously described DNA-based dimerization[48]. Thus, for one motor domain we labeled the HALO-tag with a six dye ATTO 488 FluoroCube[161] and the YBBR-tagged MTBD with a six dye ATTO 674N FluoroCube. For the other motor domain, we only labeled the YBBR-tagged MTBD with a six dye Cy3N FluoroCube (**Fig. 5.1**). Finally, the N-terminal SNAP-tag on either motor domain was labeled with reverse-complement single stranded DNA to dimerize both motor domains after labeling. This three-color FluoroCube labeled dynein had a similar velocity and processivey as a GFP-tagged wild-type dynein (**Fig. 5.1, Fig. S5.4**), demonstrating that the labeling did not perturb wild-type function.

Next, we tracked the stepping of many three-color dyneins at rate-limiting ATP (3 μM) along microtubules to resolve individual steps of all three domains (**Materials and Methods**). Therefore we acquired images in all three channels in an alternating fashion. However, in order to enable a fast acquisition with no dead time, we skipped the 488 channel every other round (see **Materials and Methods**). Using this three-color acquisition approach, we could clearly resolve separate steps for all three domains along the on-axis, dynein's main direction of movement (**Fig. 5.1, Fig. S5.5**) and in x- and y-space (**Fig. 5.1**). Taken together, we created a three-color labeled dynein that enabled us to track the steps of one AAA ring and two MTBDs simultaneously with nanometer resolution.

The AAA ring takes larger forward and fewer backward steps than the MTBD

To compare the stepping of the AAA ring and the MTBD, we first analyzed the step sizes of both domains. The AAA ring steps we measured were similar to previous observations[47,48,60] , with a large variety of step sizes, including backward and sideward steps to adjacent protofilaments (**Fig. 5.2, Fig. S5.6, Fig. S5.7**). When we compared the on-axis step-size distribution of the AAA ring to both MTBDs (**Fig. 5.2**), we noticed that the AAA ring not only took slightly larger forward steps (22.2 nm for the AAA ring compared to 19.5 nm and 18.2 nm for the blue and red labeled MTBD, respectively) but also less frequent backward steps than either MTBD (14% for the AAA ring compared to 21% and 19% for the blue and red labeled MTBD, respectively) while the step size distribution of both MTBDs was almost identical (**Fig. 5.2**). Moreover, while the on-axis step size distribution for the AAA ring was different from the on-axis step size distribution of the MTBDs, the off-axis step sizes were very similar (**Fig. 5.2, Fig. S5.7**). Besides the difference in on-axis stepping, we found very similar properties for the stepping of the two MTBDs when compared to previous stepping analysis of two-colored AAA rings[47,48] (**Fig. S5.8**). However, given the difference in on-axis stepping between the AAA ring and the MTBDs, we wondered whether this might indicate that the AAA ring and the MTBD on the same motor domain do not always step simultaneously.

The AAA ring and the MTBD on the same motor domain do not always step simultaneously

To test if and when the AAA ring and the MTBD on the same motor domain step simultaneously, we quantified the number of steps during which the green labeled AAA ring and the MTBD on the same motor domain (red, associated MTBD) or the MTBD on the other motor domain (blue, opposite MTBD) step at the same time (**Fig. 5.1**). Interestingly, we found that the probability for either MTBD to step at the same time as the AAA ring increased with an increasing on-axis MTBD step size (**Fig. 5.2**). In addition, we observed that not only the on-axis

step size influenced the probability for the MTBD and the AAA ring to step simultaneously but also the on-axis distance between both MTBDs as well as the stepping direction (**Fig. S5.9**).

Observed distance between AAA ring and MTBD domain is variable

We next asked if the MTBD and the AAA ring have the same step size and direction if both step simultaneously. Therefore, we compared the step sizes of either the opposite MTBD (**Fig. 5.2**) or the associated MTBD (**Fig. 5.2**) with the step sizes of the green-labeled AAA ring. For either case, we noticed that the AAA ring takes on average larger steps than either MTBD suggesting that the AAA ring and the MTBD on the same motor domain move relative to each other. To further investigate if and how the AAA ring and the MTBD move relative to each other, we focused on the motor domain for which both, the AAA ring and the MTBD were labeled (**Fig. 5.3**). We first looked at the relative position between the AAA ring and the MTBD at any given time and found that on average the MTBD is leading the AAA ring along the on-axis, while we did not observe any difference along the off-axis (**Fig. 5.3**). As a control, we also looked at the relative position of both MTBDs and found that they are almost identical (**Fig. 5.3**) as one would expect for a homodimeric motor. This continuous, rather than bimodal distribution of on-axis distances between AAA ring and MTBD further supports the notion that the AAA ring and the MTBD adopt a large variety of distances between them rather than one fixed distance.

Angle between stalk and microtubule is inter-MTBD distance dependent

Since we observed a variable distance between the AAA ring and MTBD on the same motor domain, we asked how the angle between the stalk and the microtubule on-axis changes when dynein walks. Therefore we focused on the motor domain for which we have both, the AAA ring (green) and the MTBD (red), labeled and only calculated the angle ω for this dual-labeled motor domain (**Fig. 5.3**). To calculate the angle ω, we used the on-axis distance between the green-labeled AAA ring and the red-labeled MTBD at any given time and assumed

a fixed length between the MTBD and center of the AAA ring (hypotenuse). In addition, we used the MTBD on the opposite motor domain (blue) and compared it to the relative position of the red-labeled MTBD in order to determine which MTBD is leading (closer to the microtubule minus end) and which MTBD is trailing. Using these definitions, we first calculated the angle ω for two different cases - for the leading motor domain (red MTBD leading) or for the trailing MTBD (red MTBD trailing). Comparing the average angle in both cases, we found that the angle ω for the leading motor domain was smaller (71.8°) than for the trailing motor domain (90.0°) (**Fig. 5.3**). To investigate the influence of the relative position between motor domains on the stalk-microtubule on-axis angle in more detail, we calculated the angle ω as a function of inter-MTBD on-axis distance and observed a correlation (**Fig. 5.3**) revealing that the angle increases the more trailing (or less leading) the motor domain is.

We then used this stalk-microtubule on-axis angle information to reanalyze the step size distributions of the MTBD (red) and corresponding AAA ring (green) when they step simultaneously. To do so, we calculated how much the stalk-microtubule on-axis angle ω changed from before to after a step and found that the motor domain often pivots either increasing or decreasing the angle ω (**Fig. S5.10**). Taken together, we found that dynein's motor domain is very flexible, allowing the AAA ring and MTBD on the same motor to move relative to each other in a manner that varies with inter-MTBD distance, which typically results in a leading motor domain to adopt a more shallow angle than the trailing motor domain.

Dynein adopts a large variety of conformations

Observing this flexibility between AAA ring and MTBD made us wonder how many different conformations dynein adopts. Since we can measure the relative position of all three colors, we can ask which of the three domains is closest towards the microtubule minus end. For instance, for one domain order the red-labeled MTBD might be closest to the minus end followed by the green-labeled AAA ring, followed by the blue-labeled MTBD. Permuting through

all possible orders leads to a total of six different domain orders (**Fig. 5.4**). When we quantified how often each of the six domain orders is occupied during all stepping traces, we found that dynein can adopt all six domain orders to a varying degree (**Fig. 5.4**). For instance, the two domain orders in which the green-labeled AAA ring is leading is the least frequent, making up less than 18% of all domain orders compared to domain orders in which either the red-labeled or blue-labeled MTBD are leading, which make up ~40% and ~43%, respectively. However, the domain orders of the three colors only serve as a proxy for possible dynein conformations as we do not have any data on the second AAA ring. Nevertheless, we can assign some possible dynein conformations to each of the six domain orders using information about dynein's structure. If we consider that dynein is a homodimer, that relative movement along the on-axis can only occur between both motor domains and among the AAA rings and MTBDs within each motor domain, and if we only count the relative position towards the microtubule minus end of these four moving parts as differences, then dynein can adopt a maximum of 12 conformations (**Fig. S5.11**). For instance, there are two possible conformations for an order in which a AAA ring is furthest away from the microtubule minus end, lead by a MTBD, lead by another AAA ring, and finally lead by another MTBD (Ring-MTBD-Ring-MTBD). Applying this logic, we could assign these 12 possible dynein conformations to the three-color domain orders to gain some insight into which conformations dynein is more likely to adopt. For instance, we found that dynein conformations in which both AAA rings are leading both MTBDs (conformations IX and X in **Figure S5.11**) have a low probability as they only coincide with three-color domain orders that have the lowest abundance (green-labeled AAA ring leading - top two rows in **Figure S5.11**).

Returning to the three-color domain orders, we next asked how likely it is for dynein to transition between domain orders. For this, we measured the frequencyof domain orders after at least one of the three domains took a step. In addition to a single domain stepping at a given time, we also allowed cases in which two domains stepped simultaneously such as a AAA ring and a MTBD. We then measured into which domain orders a dynein from an initial domain order

transitioned after at least one domain took a step. We found that for any of the six domain orders it was most likely to stay in the same order (**Fig. 5.4**). However, the two domain orders with the green-labeled AAA ring leading were the least stable and more likely to transition to other domain orders. Observing that dynein often remained in its current state prompted us to ask for how many steps dynein will retain a given domain order. Therefore, we determined the percentage of molecules that remained in the initial domain order after one or two steps. If this process were random, we would have expected that ~17% will remain in the initial domain order after one step and only less than 3% will still have the same domain order after a second step (**Fig. 5.4**). However, since we found much larger numbers for retaining the same domain order, it appears that dynein tends to remain in domain orders in a similar way as the AAA rings of dynein tend to not pass each other[48]. We also measured how often a step of any of the labeled domains was followed by a step of the same or other domains. For instance, the blue MTBD would take a step after the red MTBD moved without anything else moving in between. We found that it is very unlikely that the same domain takes two consecutive steps without anything else moving and that it is most likely that one MTBD moves after the other (**Fig. 5.4**). This is again in agreement with the observation that the two dynein AAA rings tend to step alternatively[47,48]. In summary, dynein's two AAA rings and the two MTBDs often move in an alternating fashion and are less likely to pass each other, resulting in a retainment of a given domain order over multiple steps.

Minimal requirements for directed motility of dynein

The ability of dynein to adopt all six three-color domain orders (**Fig. 5.4**) shows that dynein adopts a large variety of conformations when moving along microtubules. However, since we did not have information regarding the location of the second AAA ring, we decided to turn to Monte Carlo simulations to obtain more insights on dynein conformations and motility. Using our experimentally obtained data as input, we simulated the stepping of both AAA rings

and both MTBDs along microtubules (**Fig. 5.5, Fig. S5.12**). We applied a few rules that are based on previous studies[11,34,47,48,60,67] and our observations of movement of three-color dynein. Specifically, a bias to take more forward than backward steps, a bias to close the gap between the motor domains along the on- and off-axis when taking a step, a higher probability for the trailing domain instead of the leading domain to take the next step, a bias towards alternating stepping behavior, and a relative movement between the AAA ring and the MTBDs (**Fig. 5.5**). However, we did not enforce specific distances between the two motor domains by setting cutoffs for on- and off-axis distance. If we ignored any of these rules during a Monte Carlo simulation, the simulated dynein motility did not match current or previous experimental observations (**Fig. 5.5 b-g, Fig. S5.13**). For instance, if we did not apply the tendency for the motor domains to step closer towards each other along the off-axis (**Fig. 5.5, Fig. S5.8**) but rather allowed the motor domains to move in either direction along the off-axis, we saw that both motor domains drifted apart to distances larger than 100 nm. However, if we applied all these rules during the simulation, we could reproduce the experimental data for dynein stepping very nicely (**Fig. S5.14**). Interestingly, certain parameters did not have to be provided but agreed well with previous experimental observations. For instance, we did not provide input into the simulations regarding the second AAA ring except the step sizes of the associated MTBD and the relative movement between that AAA ring and the MTBD (**Fig. S5.12**). Nevertheless, our simulation yielded inter-AAA ring distances (**Fig. 5.5**) very similar to those observed in stepping experiments in which both AAA rings were labeled[48]. Moreover, when we varied the angle flexibility, we found the best agreement with experimental inter-AAA ring distances (~18 nm) when we used the inter-MTBD on-axis distant-dependent angle distribution described in this study. For instance, using a fixed angle ω resulted in a larger inter-AAA ring distance (~27 nm) than using our distant-dependent angle distribution (~22 nm) (**Fig. S5.15**). In addition to the inter-AAA ring distances, we also found good agreement for passing and not passing motility of the AAA rings when comparing it to experimental data[48] without directly encoding this motion in

the simulation (**Fig. 5.5**). In summary, encoding a set of parameters and enforcing some biases in our Monte Carlo simulation for dynein stepping revealed minimal components required for dynein motility and enabled us to reproduce our three-color stepping data as well as stepping data collected by others.

Next, this Monte Carlo simulation let us predict the frequencies of possible dynein conformations. We found that conformations in which the two stalks cross are very unlikely compared to conformations with the same order of AAA rings and MTBDs in which the stalks did not cross (**Fig. S5.16**). The two most prominent conformations with an uncrossed stalk were Ring-MTBD-Ring-MTBD and MTBD-Ring-Ring-MTBD (**Fig. S5.16**). To test the influence of the relative movement between AAA ring and MTBD on the distribution of possible dynein conformations we ran Monte Carlo simulations with two other sets of allowed angle values for the stalk-microtubule on-axis angle (as shown in **Fig. S5.15**). While simulations allowing inter-MTBD distance dependent relative movement between AAA ring and MTBD, as shown experimentally in this study, occupied all 12 dynein conformations, allowing no flexible movement between AAA ring and MTBD predicted only two dynein conformations in the uncrossed stalk state, unlike the experimental observations(**Fig. 5.4, Fig. S5.11**). Simulations allowing flexible movement between AAA ring and MTBD but only using an inter-MTBD distance-independent angle distribution, we observed a conformation distribution more similar to the distance-dependent angle (**Fig. S5.16**). Taken together, our Monte Carlo simulation of dynein stepping suggests that the inter-MTBD on-axis distance-dependent relative movement between AAA ring and MTBD is important for dynein motility and enables dynein to adopt a large variety of conformations.

Discussion

By developing a three-color, single-molecule TIRF microscopy routine, we were able to track the movement of one AAA ring and two MTBDs of a dynein homodimer simultaneously and showed that the AAA ring and MTBD on the same motor domain move relative to each other in an inter-MTBD distance dependent manner. Furthermore, we observed that the AAA ring and the MTBD do not always step at the same time and often take differently sized steps if they step simultaneously. Strikingly, our data suggest that the dynein motor domain often pivots during a step leading to different distances between AAA ring and MTBD before and after a step. Using Monte Carlo simulations, our study also provides insight into the minimal requirements for directed and continuous motility and highlights the influence of the flexible motor domain on dynein stepping and dynein's ability to adopt a large variety of conformations (**Fig. 5.5, Fig. S5.17**). Based on these observations we propose an updated model for dynein stepping (**Fig. 5.6**) which we discuss below.

Inherent flexibility of the motor domain allows dynein to adopt a large variety of conformations

Applying our three-color single-molecule imaging to a moving dynein, we observed flexible movement between the AAA ring and MTBD of the same motor domain. This flexibility within dynein's motor domain has also been observed by others[11,49,50]. For instance, a cryo-electron microscopy study of a rigor-bound dynein by Imai et al.[50] has shown that this flexible motion between AAA ring and MTBD is caused by a hinge located at the interface between stalk and MTBD. The average angles for the stalk-microtubule on-axis measured by Imai et al.[50] and Can et al.[11] of ~42° and ~55°, respectively, were smaller than the angles we measured for the leading (72°) and trailing (90°) motor domain. One reason for this difference in average angles might be that our C-terminal fluorescent label on the AAA ring is not in the center but rather on the side of the AAA ring which is closer towards the minus end therewith biasing the angle towards larger values. In addition, the HALO tag and the attached FluorCube

can move freely at the C-Terminus contributing to a widening of angle distributions. Nevertheless, this potential offset does not change our observation that the leading motor domain tends to adopt a more shallow angle than the trailing motor domain.

The flexibility within the motor domain of dynein can also explain some of our other observations such as the ability of a MTBD to move without the AAA ring and the difference in step sizes for the AAA ring and MTBD. For example, the relative movement between AAA ring and MTBD might allow the MTBD to take a short step while the AAA ring does not move significantly (two most right examples in **Figure 5.5**). In this case the MTBD might release from the microtubule, perform a Brownian search[34] and rebind to a tubulin dimer close by. The possibility that the MTBD takes short steps without the AAA ring moving also agrees well with our data showing that the likelihood of AAA ring and MTBD moving simultaneously increases with increasing MTBD step size as well as with increasing inter-MTBD distance (**Fig. S5.17**). Moreover, these short "exploration" steps of the MTBD without the AAA ring movement can also explain why we observed more backward steps and a lower average forward step size for the MTBD compared to the AAA ring (**Fig. S5.17**) as these short "exploration" steps of the MTBD might shift the MTBD step size distribution towards more backward steps and shift the average forward step size to smaller values than the AAA ring. In addition, these short "exploration" steps might provide an explanation for why we see a retainment of the three-color domain orders over multiple steps, as these short steps of the MTBD are often not large enough to alter domain order. Taken together, we propose that the microtubule-binding domain can perform short "exploration" steps if the inter-MTBD distance is short without the AAA ring of the same motor domain having to move.

We also showed by combining our experimental data with Monte Carlo simulations, that the observed flexible movement of the AAA ring and the MTBD allows dynein to adopt a large variety of conformations (**Fig. 5.5, Fig. S5.16**). When we restricted this relative movement in our simulations, we only observed two out of twelve possible conformations. Moreover, within the

limits of our simulation, we noticed that restricting the flexibility of dynein's motor domain resulted in an inter-AAA ring distance significantly larger than the distance measured in two-color stepping experiments in which bothAAA rings were labeled[48], whereas allowing flexible movement predicted a distance much closer to the experimental value. Thus, our data suggests that dynein can step in even more different ways than previously described (**Fig. 5.5, Fig. S5.16**) and adopt a large variety of conformations.

The short "exploration" steps of the MTBD and the large variety of ways dynein can step along microtubules are strikingly different compared to other motor proteins such as kinesins, which have been shown to take regular, 16-nm steps and to almost exclusively step forward without side- or backward steps[140,153]. Dynein's ability to step in so many different ways might provide an advantage over kinesin, when they undergo a tug-of-war[13,14] to determine in which direction cargo will be transported. For instance, utilizing the inherent flexibility and the ability to step in many different ways might explain why a single dynein is better than a single kinesin in circumventing obstacles such as microtubule associated proteins (MAPs)[14,162].

An updated model for dynein stepping

Flexibility within the dynein motor domain not only enables a much larger range of conformations among dynein's many steps, but also might influence how a single step of dynein is carried out under load. Previous studies have shown that dynein linker tension gates dynein release from microtubules[67,163,164]. Based on our observation of the tilting of the two motor domains towards each other at larger inter-MTBD distance, we speculate that the motor domains can generate tension / torque among each other as has been suggested by others[49]. Combined with the study that dynein is more likely to release from microtubules under forward or lower backward force[48,67], we speculate that tension between both AAA rings at larger distances could act as an assisting, forward pulling force on the trailing motor domain and as an additional backward force on the leading domain (**Fig. 5.6**). These additional inter-dynein

tensions could explain why the trailing motor domain is more likely to release than the leading motor domain as we observed in this study and as has been reported by others[47,48,67]. Interestingly, when we ran Monte Carlo simulations of dynein stepping, we did not have to apply any physical constraints to keep the two motor domains together besides providing inter-MTBD distant dependent stepping directions which biased the stepping direction of the moving motor domain towards the other, bound motor domain to close an on- or off axis gap if the distance became to large (**Fig. S5.12**). For instance, a motor domain left of the other motor domain would prefer to step towards the right (**Fig. S5.7**). However, if we did not apply this bias, the motor domains would drift apart. This observation further supports the model of tension sensing between both motor domains.

After the motor domain is released from the microtubule and according to the load sharing model for dynein[165], the bound motor domain would carry all the load and the released motor domain would be “free” to perform a Brownian search[34]. In addition to releasing from the microtubule, the motor domain would also undergo the priming stroke (bending of the linker), which biases the stepping direction towards the minus end[166]. However, we speculate that in addition to the priming stroke propelling the motor forward, the release of inter-AAA ring tension and a potential rotation of the motor domain[34] might also contribute to the forward movement of the trailing motor domain (**Fig. 5.6**). Once the MTBD rebinds, load sharing continues[165]. With phosphate release, the motor domain undergoes a power stroke pulling the cargo forward[165]. However, based on our observation of the flexible motion between AAA ring and MTBD, we suggest that the two AAA rings will also be pulled towards each other in addition to the pulling of the cargo (**Fig. 5.6**). Interestingly, movement of the two AAA rings towards each other after microtubule rebinding has also been suggested by Lippert et al.[49] and agrees with our observation (**Fig. 5.2**) that the AAA ring of the opposite motor domain that did not release from the microtubule can still undergo movement if the inter-MTBD distance is large.

In future studies it will be interesting to test whether this flexible movement between AAA ring and MTBD can be observed if load is applied to dynein[41,163–165,167–169]. Another interesting area for future studies will be to investigate how the different domains among multiple motors coordinate their stepping and if the flexible movement within the dynein motor domain can also be observed for mammalian dynein for which two dynein homodimers can be recruited to the same complex[22,23]. Lastly, we anticipate that the three-color single-molecule approach used in this study can also be applied to other proteins to explore conformational dynamics.

Figures and figure legends

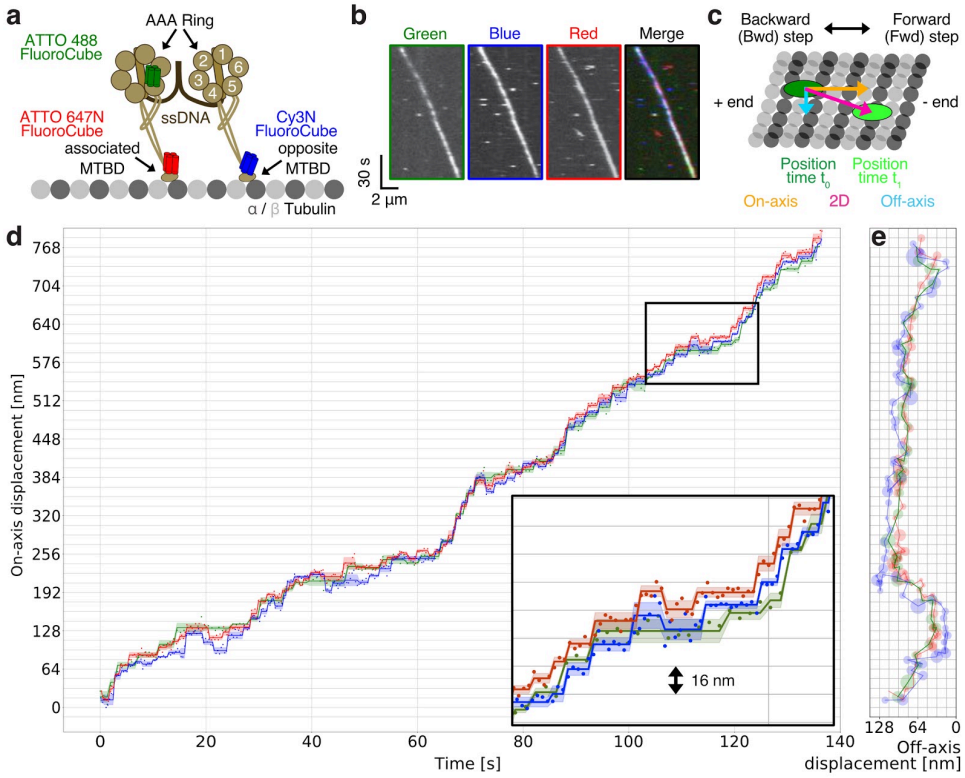

Figure 5.1 | Three-color stepping trace of dynein. (a) Schematic showing structure and design of three-color dynein. Each of the two motor domains of dynein is labeled individually and dimerized using reverse-complementary single-stranded DNA (black, attachment via SNAP-tag[104,160]). The MTBD of each motor domain and one of the two AAA rings are labeled with FluoroCubes[161]. For one motor domain the AAA ring is labeled with a six dye ATTO 488 FluoroCube (green, attachment via HALO-tag[103]) and the MTBD is labeled (associated MTBD) with a six dye ATTO 647N FluoroCube (red, attachment via YBBR-tag[104]). For the other motor domain only the MTBD is labeled (opposite MTBD) with a six dye Cy3N FluoroCube (blue, attachment via YBBR-tag[104]). More details about construct design and labeling can be found in **Materials and Methods**. (b) Example kymograph of a three-color dynein visualized in all three channels and merged. More kymographs of three-color dynein can be found in **Figure S5.3**. (**c**) Microtubule lattice (grey circles) with plus and minus ends and the definition for forward and backward as well as 2D, on- and off-axis steps. (**d**) Raw stepping data with position along the on-axis versus time of a three-color dynein heterodimer (colored dots) with detected steps (colored lines). The opaque lines show the standard deviation along the on-axis for each step. Insert is a magnified view of the area in the black box. More stepping traces are shown in **Figure S5.5**. (**e**) The same trace as in **d** but in xy space. The opaque, colored circles show the fitted position for which the radius corresponds to the standard error of the mean of the combined on- and off-axis.

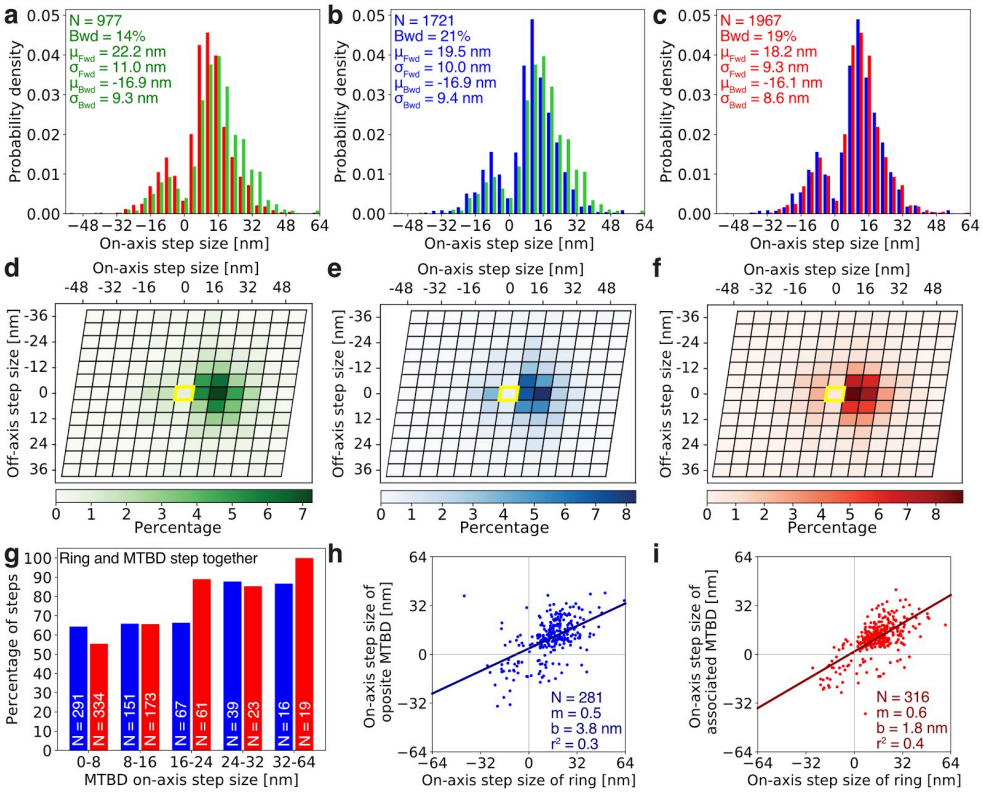

Figure 5.2 | Two-dimensional stepping analysis of AAA ring and MTBD stepping. (a) Histogram of on-axis step sizes of dynein's AAA ring (green) and the MTBD (red) of the same motor domain (associated MTBD). (b) Histogram of on-axis step sizes of dynein's AAA ring (green) and the MTBD (blue) on the opposite motor domain. (c) Histogram of on-axis step sizes of dynein's MTBDs (blue and red). (a-c) Number of steps detected (N), percentage of backward steps (Bwd), average forward step size (μ_{Fwd}) and its standard deviation (σ_{Fwd}), and average backward step size (μ_{Bwd}) and its standard deviation (σ_{Bwd}) are shown for AAA ring (green), opposite MTBD (blue) and associated MTBD (red) in a, b, and c, respectively. (d-f) Same data as in a-c shown as a heatmap of the on-and off-axis step sizes of (d) dynein's AAA ring (green), (e) the opposite MTBD (blue), and (f) the associated MTBD (red) mapped on a microtubule mattice. The microtubule lattice is based on a 13 protofilament microtubule and was derived as described in **Figure S5.6**. Here, each parallelogram represents a tubulin dimer consisting of one copy of α and β tubulin. The yellow parallelogram represents the tubulin dimer from at which the domain is located prior to the step. (g) Histogram showing how often the AAA ring steps at the same time as the opposite MTBD (blue) and the associated MTBD (red) as a function of the MTBD on-axis step size. The sample size N refers to the total number of steps for the respective condition. (h-i) Correlation of on-axis step sizes of the AAA ring and (h) the opposite MTBD (blue) and (i) associated MTBD (red) if they step at the same time. Each dot represents a single step. Blue and red lines show linear fit.

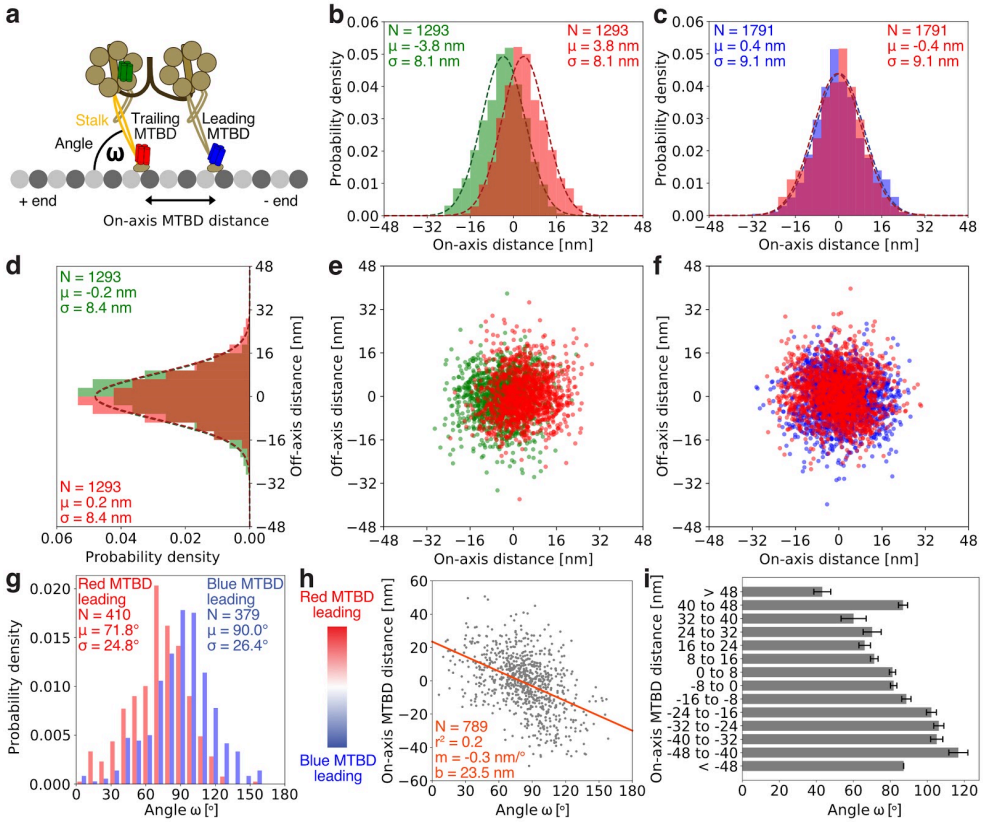

Figure 5.3 | Relative position of AAA ring and MTBD on the same motor domain. (a) Schematic showing the definition of leading and trailing MTBD as well as the definition of the angle ω between stalk (orange) and on-axis microtubule lattice (small, grey circles). Note, the angle is only calculated for the motor domain for which the AAA ring (green) and the MTBD (red) are both labeled. To calculate the angle ω we used trigonometry and the on-axis distance between the AAA ring (green) and the MTBD (red) as adjacent side and the fixed and known distance from the MTBD to the AAA ring as hypotenuse (see **Materials and Methods**). (b) Histogram of on-axis distances between AAA ring (green) and the MTBD (red) of the same motor domain. (c) Histogram of on-axis distances between both MTBDs (blue and red) on opposite motor domains. (d) Histogram of off-axis distances between AAA ring (green) and the MTBD (red) of the same motor domain. (e-f) Scatter plot of the relative position between (e) AAA ring (green) and the MTBD (red) of the same motor domain and (f) both MTBDs (blue and red) on opposite motor domains. Here, the centroid position of either (e) AAA ring and MTBD or (f) both MTBDs is fixed in the origin and the position of the domains relative to the centroid is shown as dot. (g) Histogram of angles ω between dynein's stalk and the on-axis microtubule lattice for the motor domain for which the AAA ring (green) and the MTBD (red) are both labeled if either the red or blue MTBD is leading. (h) Correlation between stalk-microtubule on-axis angles ω and inter-MTBD on-axis distances at a single-molecule level (grey dots). Here, a positive value refers to a state in which the red MTBD is leading and a negative value refers to a state where the blue MTBD is leading. Orange line shows linear regression. (i) Same data as in h shown as histogram. Black error bars show the standard error of the mean.

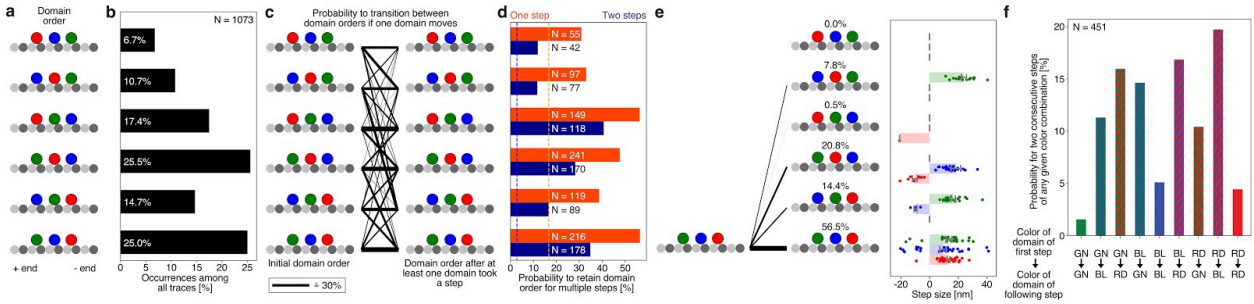

Figure 5.4 | Frequency of domain orders and order of stepping of AAA ring and both MTBDs. (a) Schematic of all six possible domain orders along the microtubule on-axis. Small, grey circles show tubulin while the larger green, blue, and red circles represent the AAA ring, the opposite MTBD, and the associated MTBD, respectively. For instance, to be classified as the top domain order, the AAA ring (green) has to be closest to the microtubule minus end, followed by the opposite MTBD (blue) and followed by the associated MTBD (red). Note that the absolute distance between domains is irrelevant. Only the relative position towards the microtubule minus end matters. (b) Histogram of occurrence of each of the six possible domain orders. (c) Probability to transition from one domain order to another. A transition is counted if at least one domain took a step. The thickness of the black lines shows frequency. If no black line is drawn between to domain orders, this transition was not observed. (d) Probability to retain domain order after one (orange) or two (blue) steps. Here, a step refers to the movement of at least one of the three domains. The orange and blue dotted lines indicate the probability to retain the domain order after one (orange) or two (blue) steps if transitions were random. The sample size N refers to the total number of all domain order transitions that occurred after the motor took a step out of its current domain order. (e) Observed on-axis step sizes for transitions out of one domain order. The bars show the average step sizes and the dots the distribution at the single-molecule level for the AAA ring (green), the opposite (blue) and associated (red) MTBD. Error bars show the standard error of the mean. Note, sometimes two domains might be moving during a single transition. (f) Frequency of two consecutive domain steps for any possible order. For instance, the most left, green bar shows the frequency of how often a green-labeled AAA ring step is followed by another green-labeled AAA ring step without the movement of any other domain in between or at the same time. GN stands for green (AAA ring), BL stands for blue (opposite MTBD), and RD stands for red (associated MTBD).

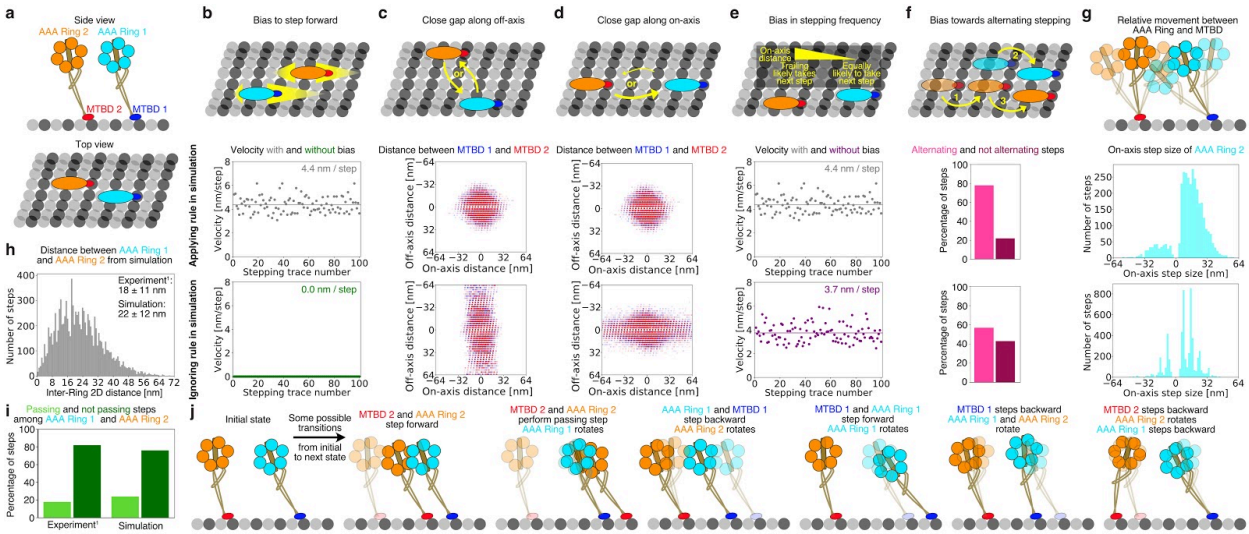

Figure 5.5 | Experimental data combined with simulations reveal minimal requirements for continuous and directed motility of dynein. (a) Schematic showing side and top view of dynein used in Monte-Carlo Simulations. One motor domain is represented by a cyan AAA ring and a blue MTBD while the other motor domain is represented by an orange AAA ring and a red MTBD. Note, there is no tail linking both motor domains together and therewith no physical constraint holding both motor domains together. Small, grey circles show tubulin. (b-g) Schematics on the top represent requirements for dynein motility. The graphs below show an example of what happens to dynein motility if the requirement is applied (top graph) or ignored (bottom graph) during the simulation. (b) If the bias to step forward is ignored, dyneins performs random walks with no positional net gain. (c) If the bias of the stepping direction along the off-axis is ignored, both motor domains will drift apart along the off-axis. (d) If the bias of the stepping direction along the on-axis is ignored, both motor domains will drift apart along the on-axis. (e) If the bias in stepping frequency of leading and trailing motor domain is ignored, dynein will move more slowly towards the microtubule minus end. (f) If no bias towards alternating stepping is encoded, dynein will have a lower tendency to alternate. (g) If there is no relative movement between AAA ring and MTBD, the AAA ring will step exactly as the MTBD and follow the microtubule lattice. Moreover, the inter-AAA ring distance will change (**Fig. S5.15**). (h) 2D distance between both AAA rings based on 100 simulations with more than 10,000 steps compared to previously measured inter-ring 2D distance[47,48] shows a good agreement. (i) Passing and not passing steps among the two AAA rings based on 100 simulations with more than 10,000 steps compared to previously measured inter-ring 2D distance shows a good agreement. (a-i) 100 simulations for each condition with more than 10,000 steps were performed. More details on the set up of the Monte Carlo Simulation can be found in **Materials and Methods**, and **Figures S5.12-S5.16**. (j) Example model showing the many possible transitions dynein can undergo during one step highlighting the high flexibility of dynein's motor domains. More details about the stepping model can be found in **Figures S5.17**.

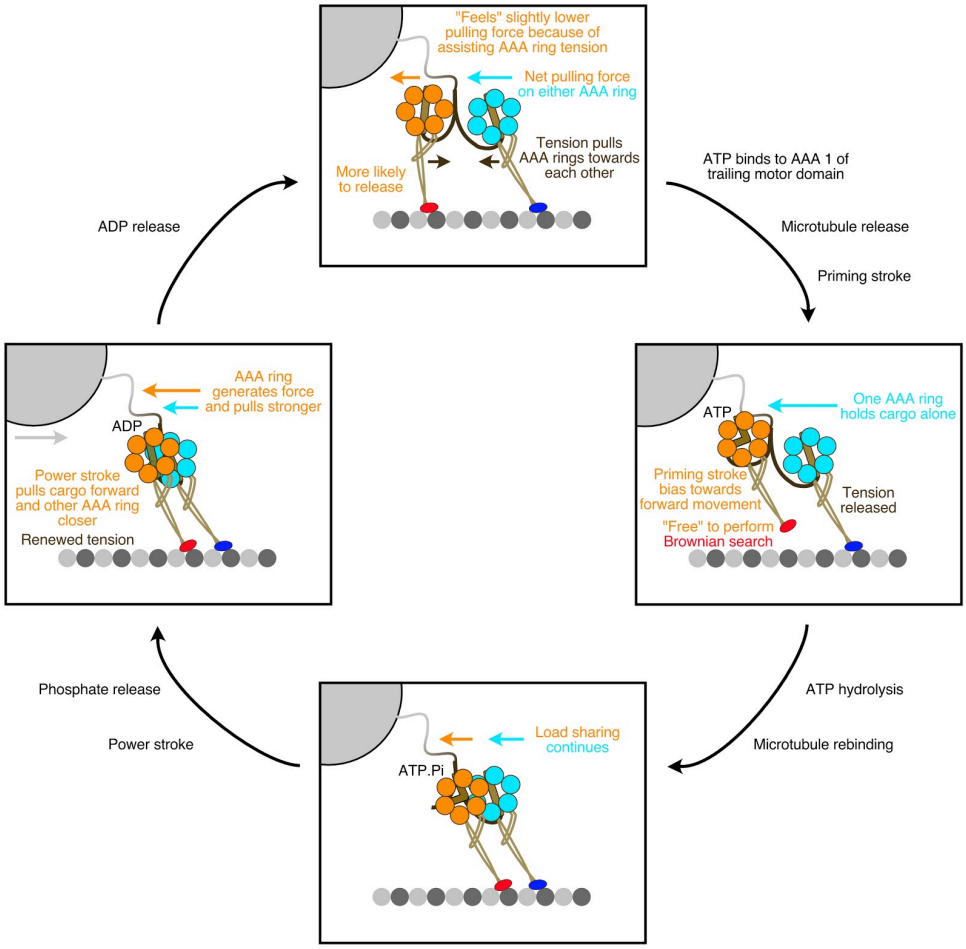

Figure 5.6 | An updated model for the dynein stepping cycle. If the two motor domains are separated along the on-axis, inter-AAA ring tension might pull both closer towards each other. This inter-AAA ring tension in turn might provide an assisting, forward force for the trailing motor domain (here orange) slightly reducing the pulling force of the grey cargo and therewith increasing the probability to release from the microtubule. Once ATP bound to the trailing motor domain, it will release from the microtubule and perform the priming stroke. The priming stroke together with assistance from the forward pulling inter-AAA ring tension will bias the motor to step forward. After ATP hydrolysis and microtubule rebinding, the load will once again be shared among the two motor domains. Once the phosphate is released, the linker will straighten and carry out the force generating power stroke. This power stroke will then pull the cargo forward and pull the two AAA rings closer together. Depending on the new inter-motor domain distance, the tension between AAA rings is renewed.

We note that this particular example is more likely to occur when the motor domains are separated along the on-axis as we would expect little tension between motor domains when they are in close proximity and therewith a similar probability for either motor domain to release from the microtubule. However, once one motor domain stepped and rebound further away from the other, we would expect to see the described tilting of AAA rings towards each other after the power stroke occured.

Supplemental figures and tables with legends

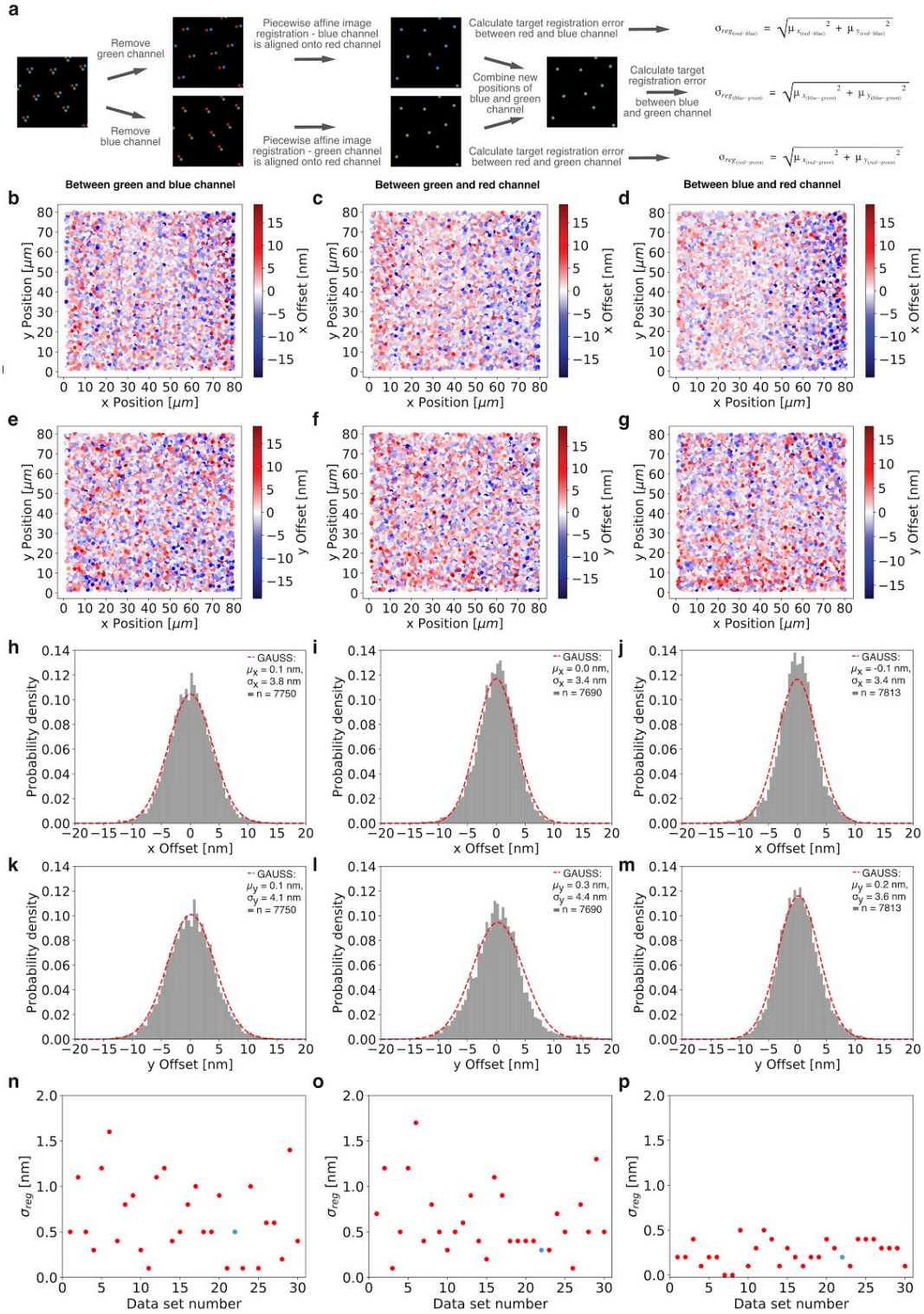

Figure S5.1 | Workflow and example results of three-color image registration. (a) Workflow for three-color image registration. A data set for which tetraspeck beads were imaged in three

channels (green, blue, and red) is divided into a channel that only contains blue and red (top) or only contains green and red (bottom). Then, both two-color datasets are aligned as previously described[78]. For both, the red channel serves as the reference and only blue and green positions are shifted. Afterwards the target registration error for all three color combinations is calculated. Note, for the registration error between green and blue, the two split, registered data sets are combined and the red channel is removed. (b-p) Example results of image registration for all three color combinations are shown: Between the green and blue channel (left panels), between the green and red channel (middle panels), and between the blue and red channel (right panels). (b-d) Target registration error after registration along the x-axis. Each dot shows a single fiducial marker for which the distance offset between the two colors of the same fiducial marker is color-coded. Negative values (blue dots) mean that channel 1 has a smaller number for its x position whereas positive values (red dots) represent fiducials where channel 2 has a smaller number for its x position. (e-g) Same datasets as in b-d but the offset is along the y-axis. (h-j) Histogram of x-axis offset after registration with Gaussian fit (dashed red line) of data shown in b-d. (k-m) Histogram of y-axis offset after registration with Gaussian fit (dashed red line) of data shown in e-g. (n-p) Registration accuracy σ_{reg} is shown for 30 datasets. The blue dot is the registration error of the data shown in detail in b-m. For the three-color dynein stepping experiments we accepted datasets if $\sigma_{reg} < 1$nm. More details about image registration is given in **Materials and Methods**.

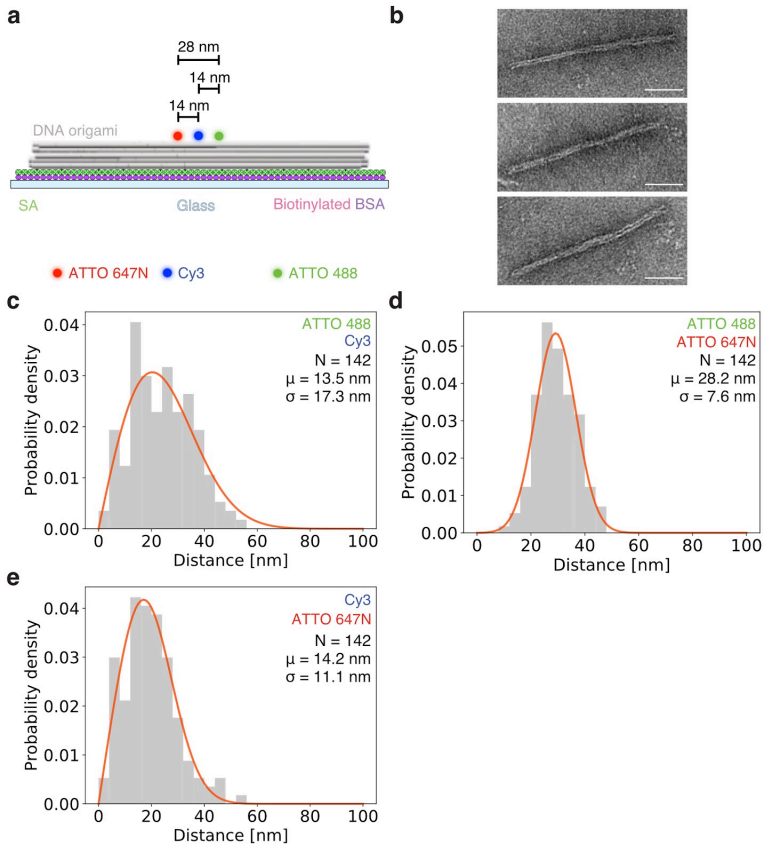

Figure S5.2 | Three-color distance measurements with DNA nanoruler. (a) Schematic showing the design of a three-color DNA-origami based nanoruler[100,159]. On this nanoruler, the three dyes ATTO 488, Cy3, and ATTO647N are placed with a well-defined distance. On the opposite side of the dyes, the nanoruler is functionalized with biotin to immobilize it on a glass coverslip via biotinylated BSA and streptavidin (SA). (b) Negative stain electron microscopy micrographs of three-color nanoruler. Scale bar is 50 nm. (c-e) Histogram of measured distances for all three color combinations. The orange line shows a fit with a probability distribution function described in[78] with the average distance (μ) and its standard deviation (σ). Note, the standard deviation of the ATTO 488 and Cy3 color combination is higher as for the two other color combinations because ATTO 488 and Cy3 yielded a larger localization error than color combinations that included the well-localized ATTO 647N dye. The data shown is for a single acquisition which was successfully reproduced five times (not shown).

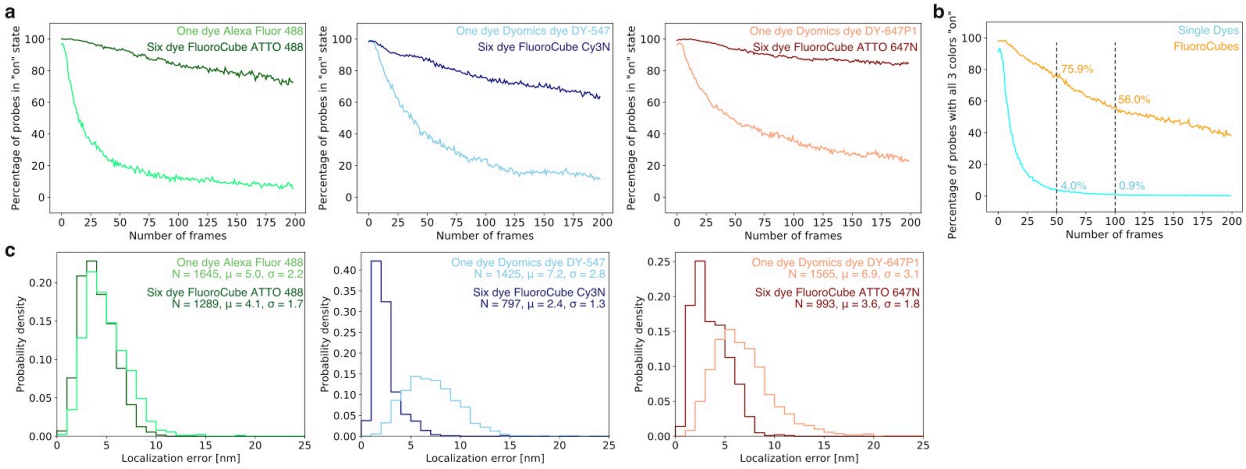

Figure S5.3 | Comparison of photostability and localization error of single, organic dyes and six dye FluoroCubes attached to rigor-bound dynein. (a-c) Labeling of three-color dynein heterodimers with FluoroCubes[161] and dyes was as follows: For one motor domain the AAA ring is labeled via HALO-tag[103] with a six dye ATTO 488 FluoroCube (dark green) or a an Alexa Fluor 488 (light green) and the MTBD is labeled via YBBR-tag[104] with a six dye ATTO 647N FluoroCube (dark red) or a Dyomics dye DY-647P1 (light red). For the other motor domain only the MTBD is labeled via YBBR-tag[104] with a six dye Cy3N FluoroCube (blue) or a Dyomics dye DY-547 (light blue). For the measurement of photostability and localization error a three-color dynein is rigorously bound to microtubules using 1 mM ADP. Note, that the photostability is likely slightly higher as some dyneins may have detached prior to photobleaching. (a) Photostability of single-organic dyes compared to DNA FluoroCubes. Here, the number of probes in the on state is shown as a function of frames recorded. (b) Cumulative photostability of all three-color dyneins either labeled with single-organic dyes or with DNA FluoroCubes. Here, the number of dyneins for which all probes are in the on state is shown as a function of frames recorded. (a-b) Number of probes measured is given in c. (c) Localization error for respective probes when attached to rigor-bound dynein. The data is pooled from many movies with motors from the same preparation but with freshly prepared microscope slides (n=3). Details about imaging conditions are given in **Materials and Methods**.[103]

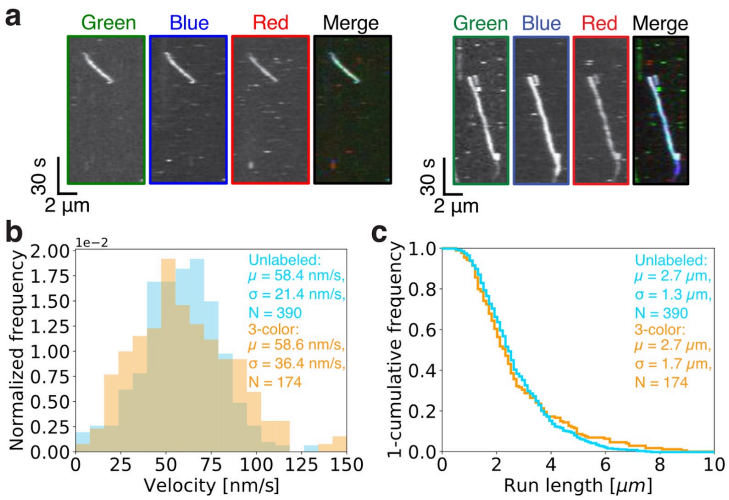

Figure S5.4 | Comparison of velocity and processivity of single, organic dye and six dye FluoroCube labeled three-color dynein. (a) Additional example kymographs of three-color dynein as shown in **Figure 5.1**. (b) Velocity histogram with average velocity (μ) and its standard deviation (σ) for three-color dynein labeled with six dye DNA FluoroCubes[161] (orange) or GFP-tagged wild-type dynein (cyan). (c) A '1-cumulative frequency distribution plot' of run length with average length (μ) and its standard deviation (σ) for three-color dynein labeled with six dye DNA FluoroCubes (orange) or GFP-tagged wild-type dynein (cyan). (b, c) The data is pooled from many movies with motors from the same preparation but with freshly prepared microscope slides (n=3) and the sample size N is given.

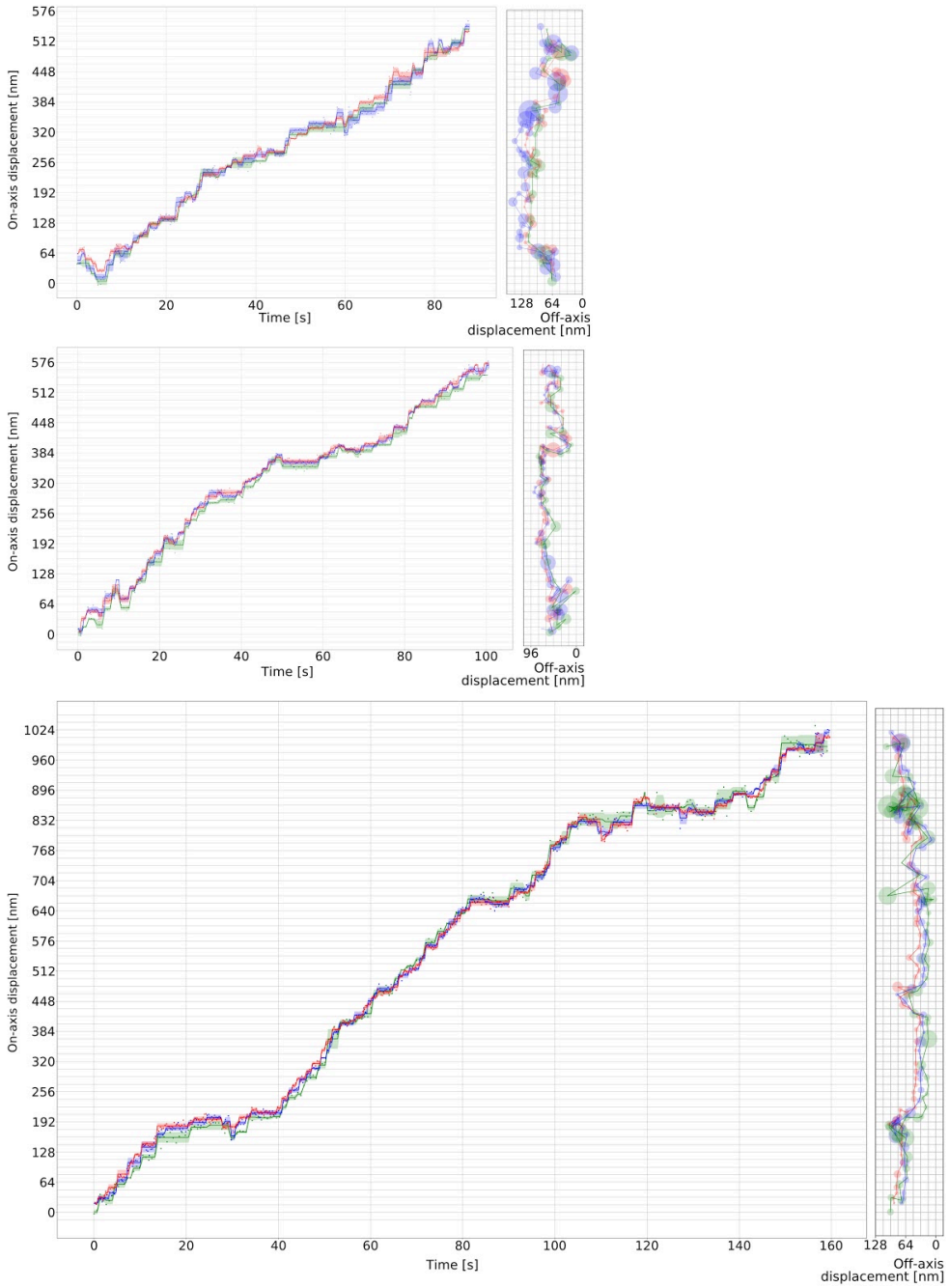

Figure S5.5 | Additional stepping traces of three-color dynein. Three additional stepping traces of three-color dynein similar to the one shown in **Figure 5.1**. Left: Raw stepping data with position along the on-axis versus time of a three-color dynein heterodimer (colored dots) with detected steps (colored lines). The opaque lines show the standard deviation along the on-axis for each step. Right: The same trace as on the left but in xy space. The colored circles show the fitted position for which the radius corresponds to the standard error of the mean of the combined on- and off-axis.

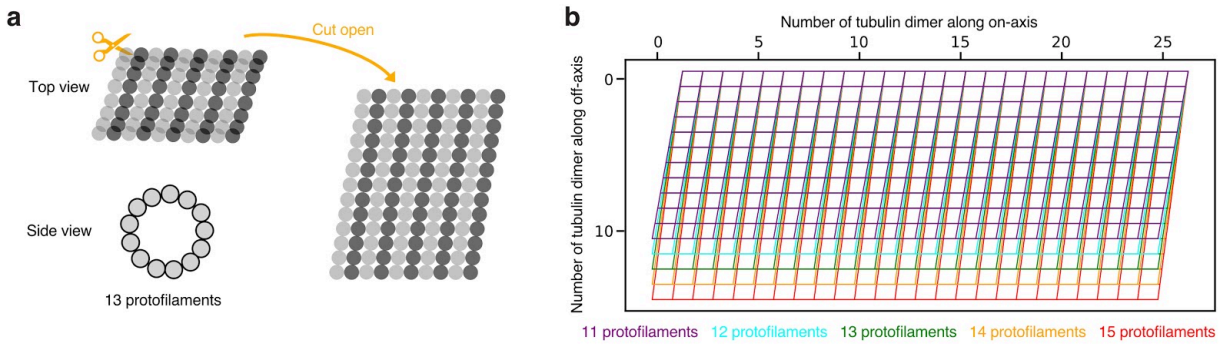

Figure S5.6 | Comparison of microtubule lattices with various protofilament numbers. (a) Left: Schematic of 13-protofilament microtubule as seen from the top and side. Right: Schematic of a flattened 13-protofilament microtubule lattice is shown. For plotting the experimentally determined as well as Monte Carlo simulated on- and off-axis steps of dynein onto a microtubule lattice, this flattened 13-protofilament microtubule lattice was used. (b) Since microtubule filaments made with purified tubulin can assemble into filaments with various protofilaments, we compared how similar the flattened out lattices of microtubule lattices with different numbers of protofilaments are. Each parallelogram represents a tubulin dimer consisting of one copy of α and β tubulin and is 8x6 nm (on-axis x off-axis) in size. Overall, the difference between lattices of microtubule lattices with different numbers of protofilaments is relatively small and smaller than our localization error. Thus, we reasoned that using the average protofilament number of 13 is a good approximation for our microtubule lattice. We note that using a flattened microtubule lattice is another approximation as the distance between protofilaments gets smaller the further one deviates from the center in the top view. However, since more than 60% of dynein's sideward steps are smaller than ±12 nm (**Fig. S5.7**), which is two protofilaments to the left or right and since two adjacent protofilaments almost do not overlap with each other (see center of top view), we reasoned that using a flattened lattice is a good approximation (given that our localization error is larger then the overlap between two adjacent protofilaments).

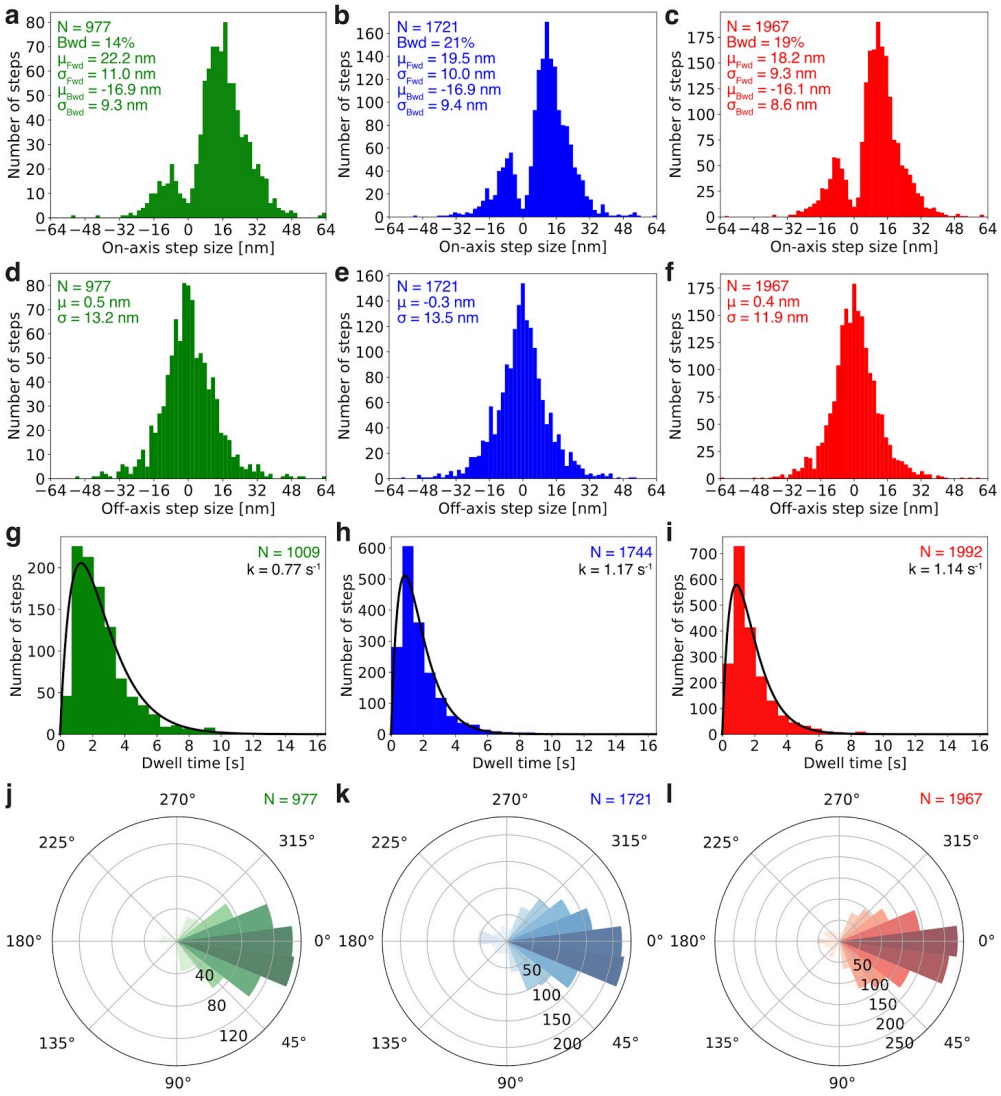

Figure S5.7 | Extended two-dimensional stepping analysis of AAA ring and MTBD stepping shows. (a-c) Histogram of on-axis step sizes of (a) dynein's AAA ring (green), (b) the opposite MTBD (blue), and (c) the associated MTBD (red). Number of steps detected (N), percentage of backward steps (Bwd), average forward step size (μ_{Fwd}) and its standard deviation (σ_{Fwd}), and average backward step size (μ_{Bwd}) and its standard deviation (σ_{Bwd}) are given. (d-f) Histogram of off-axis step sizes of (d) dynein's AAA ring (green), (e) the opposite MTBD (blue), and (f) the associated MTBD (red). Number of steps detected (N), average step size (μ) and its standard deviation (σ) are given. (g-i) Histogram of the dwell times of (g) dynein's AAA ring (green), (h) the opposite MTBD (blue), and (i) the associated MTBD (red). The black lines are fits of a convolution of two exponential functions with equal decay constants. (j-l) Angle histogram of the stepping angles for (g) dynein's AAA ring (green), (h) the opposite MTBD (blue), and (i) the associated MTBD (red). The stepping angle is defined as the angle between the 2D stepping vector and microtubule on-axis (See **Fig. 5.1**). A stepping angle between 0° and 90° refers to a forward to the right step, a stepping angle between 90° and 180° refers to a backward to the right step, a stepping angle between 180° and 270° refers to a backward to the left step, and a stepping angle between 270° and 360° refers to a forward to the left step.

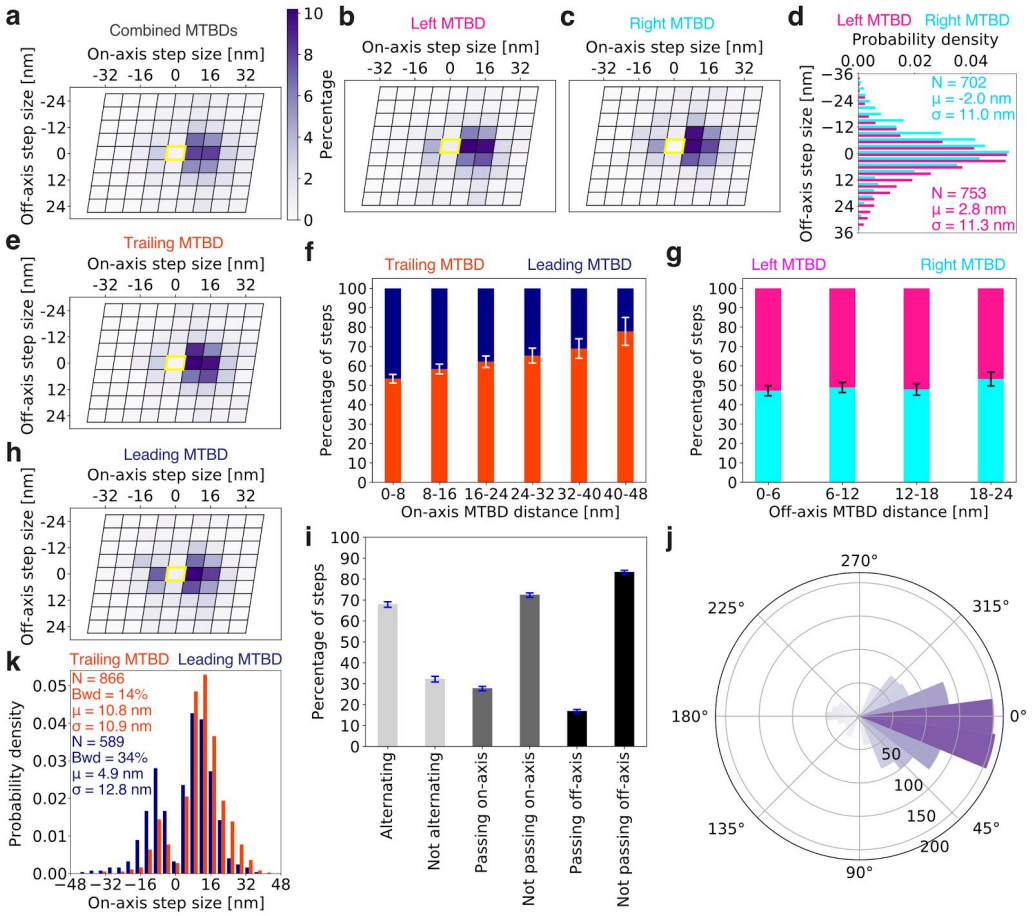

Figure S5.8 | Extended analysis of stepping parameters of both MTBDs. (a-c, e, h) Heatmaps of the on-and off-axis step sizes of dynein's MTBDs mapped on the microtubule lattice. Here, each parallelogram represents a tubulin dimer consisting of one copy of α and β tubulin. The yellow parallelogram represents the tubulin dimer from at which the domain is located prior to the step. For each heatmap more than 1,000 steps are analyzed. (a) Step size distribution of all MTBDs regardless of relative position. (b) Step size distribution of all MTBDs that are to the left of the other MTBD prior to their step. (c) Step size distribution of all MTBDs that are to the right of the other MTBD prior to their step. (d) Histogram of off-axis step sizes of all MTBDs that are to the left (pink) or right (cyan) of the other MTBD prior to their step. (e) Step size distribution of all MTBDs that are trailing the other MTBD prior to their step. (h) Step size distribution of all MTBDs that are leading the other MTBD prior to their step. (k) Histogram of on-axis step sizes of all MTBDs that are trailing (orange) or leading (dark blue) the other MTBD prior to their step. (d, k) Number of steps detected (N), percentage of backward steps (Bwd), average step size (μ) and its standard deviation (σ) is given. (f) Probability of the trailing (orange) or leading (dark blue) MTBD to take the next step as a function of the inter-MTBD on-axis distance. (g) Probability of the left (pink) or right (cyan) MTBD to take the next step as a function of the inter-MTBD off-axis distance. (i) Percentage of steps for which the MTBDs alternate in stepping (light grey), for which the MTBDs passed each other when one of them took a step along the on-axis (medium grey) and along the off-axis (dark grey). (j) Angle histogram of the stepping angles. The stepping angle is defined as the angle between the 2D stepping vector and microtubule on-axis (**Fig. 5.1**). A stepping angle between 0° and 90° refers to a forward to the right step, a stepping angle between 90° and 180° refers to a backward to the right step, a stepping angle between 180° and 270° refers to a backward to the left step, and a stepping

angle between 270° and 360° refers to a forward to the left step. (a-j) The data for both MTBDs (associated and opposite) was combined. (f, g, i, j) The total number of steps analyzed for these plots is N = 1,455.

For both, the leading and training as well as the left and right MTBD we can see that they prefer to step towards each other. For instance, a motor domain left of the other motor domain would prefer to step towards the right (b-d) while a trailing motor is more likely to step forward than the leading motor (e, h, k). However, we only observe a bias for the trailing motor domain to take a next step with increasing inter-MTBD distance along the on-axis, while we do not see such bias for the left and right MTBD with increasing off-axis distance (f, g).

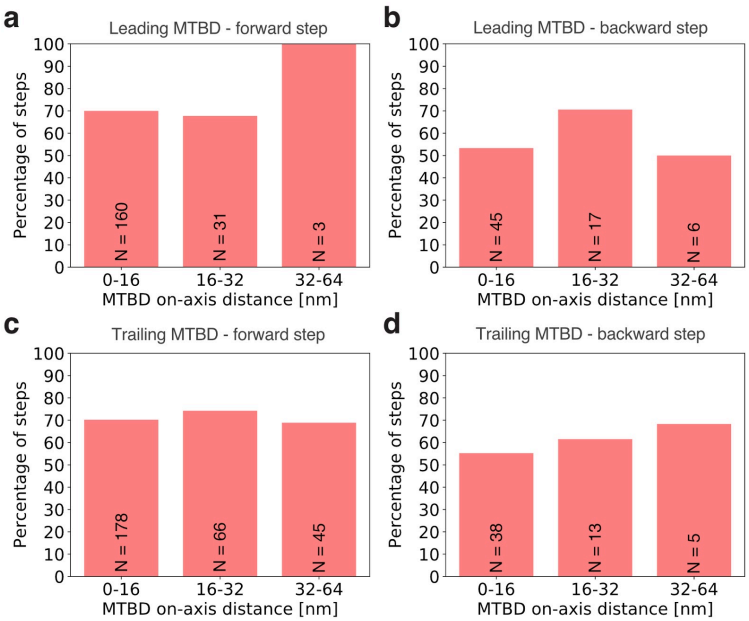

Figure S5.9 | Probability of AAA ring and associated MTBD stepping at the same time as a function of inter-MTBD on-axis distance. The probability that the AAA ring and the associated MTBD step at the same time as a function of inter-MTBD on-axis distance for (a) a leading MTBD that is taking a forward step, (a) a leading MTBD that is taking a backward step, (c) a trailing MTBD that is taking a forward step, and (d) a trailing MTBD that is taking a backward step. (a-d) The sample size N refers to the total number of steps for the respective condition.

This data shows that the probability for the AAA ring and the associated MTBD to step at the same time is not only a function of MTBD on-axis step size (**Fig. 5.2**) but also a function of inter-MTBD on-axis distance as well as the stepping direction (forward vs. backward step).

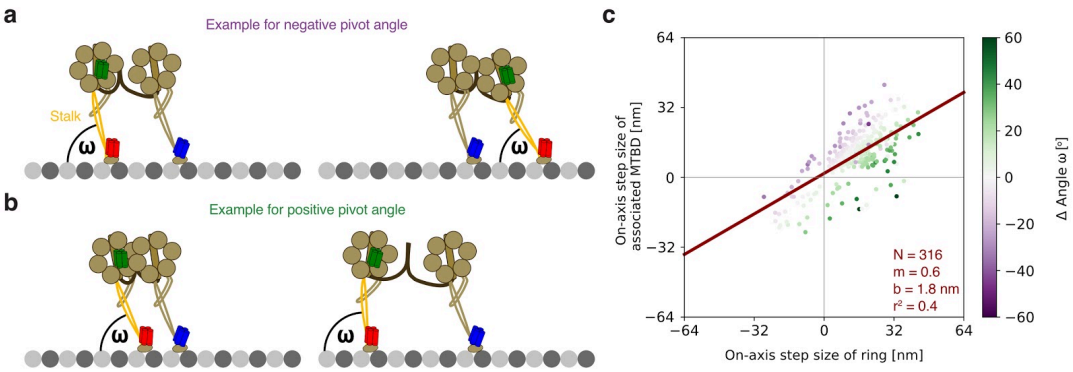

Figure S5.10 | Stalk-microtubule lattice angle often changes when AAA ring and associated MTBD are stepping at the same time. Schematic of a step in which the stalk-microtubule lattice angle ω gets (a) smaller or (b) larger. (c) Correlation of on-axis step sizes of the AAA ring and associated MTBD if they step at the same time (same data as in **Fig. 5.2**). Each dot represents a single step and dots are color-coded based on change in angle between dynein's stalk and the on-axis microtubule lattice for the motor domain for which the AAA ring (green) and the MTBD (red) are both labeled. Here, a negative value (purple) refers to a case in which the angle ω gets smaller (see example in a) and a positive value (green) refers to a case in which the angle ω gets larger (see example in b). Red lines show linear regression.

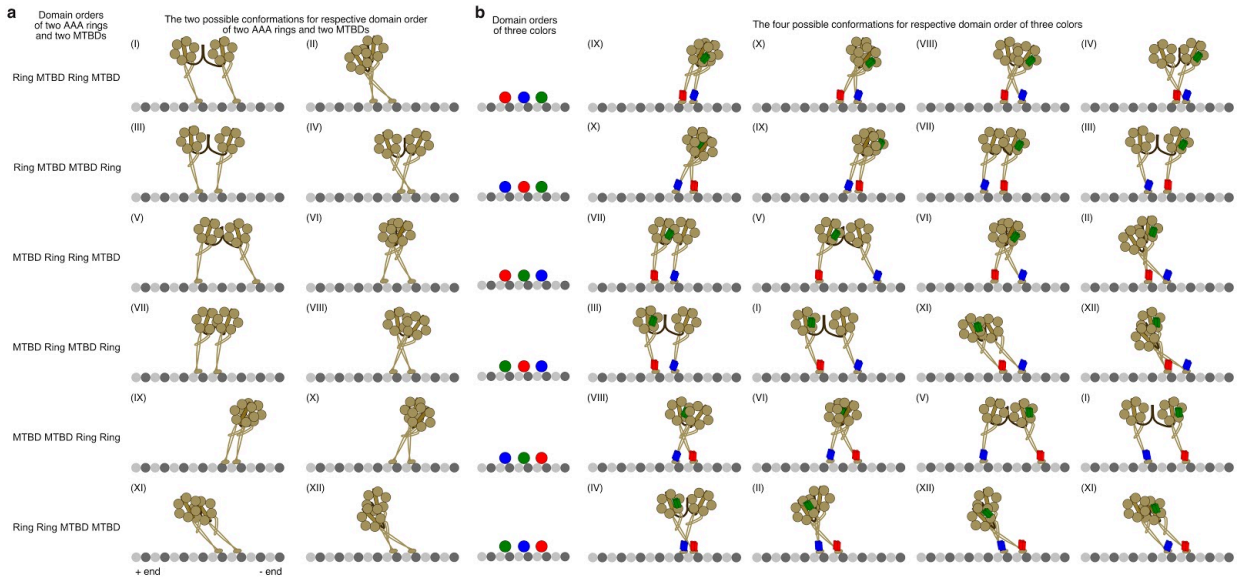

Figure S5.11 | Conformations dynein can adopt while moving along microtubules. For this figure we only show representative conformations. Note that these are only based on the proximity of the respective domains (both AAA rings and both MTBDs) towards the microtubule minus end. Thus, any conformation shown here can have many other appearances for which the stalk-microtubule lattice angle (**Fig. 5.3**) or the inter-domain distances might be different. Moreover, we only show conformations for changes along the on-axis and are ignoring differences along the off-axis. (a) Schematics showing all possible conformations dynein might be able to adopt if one allows both AAA rings to move relative to their respective MTBDs along the on-axis and ignores the absolute distance between these four domains but instead only focuses on the relative position towards the microtubule minus end. Since dynein is a homodimer, we can not distinguish the two motor domains and we end up with 12 possible conformations. These 12 conformations can be divided into 6 subcategories listed on the very left. Within each subcategory, the two stalks can either cross (right) or not be crossed (left). For instance, there are two possible conformations for an order in which a AAA ring is furthest away from the microtubule minus end, lead by a MTBD, lead by another AAA ring, and finally lead by another MTBD (Ring-MTBD-Ring-MTBD). (b) Based on the three labels that we used in our three-color stepping experiments, we can find 6 possible domain orders (very left and **Fig. 5.4**). Each of these 6 domain orders can correspond to four of the 12 different dynein conformations shown in a, since the unlabeled AAA ring can be at any position. The Latin Numbers shown in the top left corner for any given conformation correspond to the 12 conformations shown in a. Note that any of the 12 conformations in a is associated with two different domain orders of the three colors because the green AAA ring label with the associated red MTBD could also be on the other motor domain (dynein is a homodimer) yielding two possible domain orders of colors for any of the 12 dynein conformations.

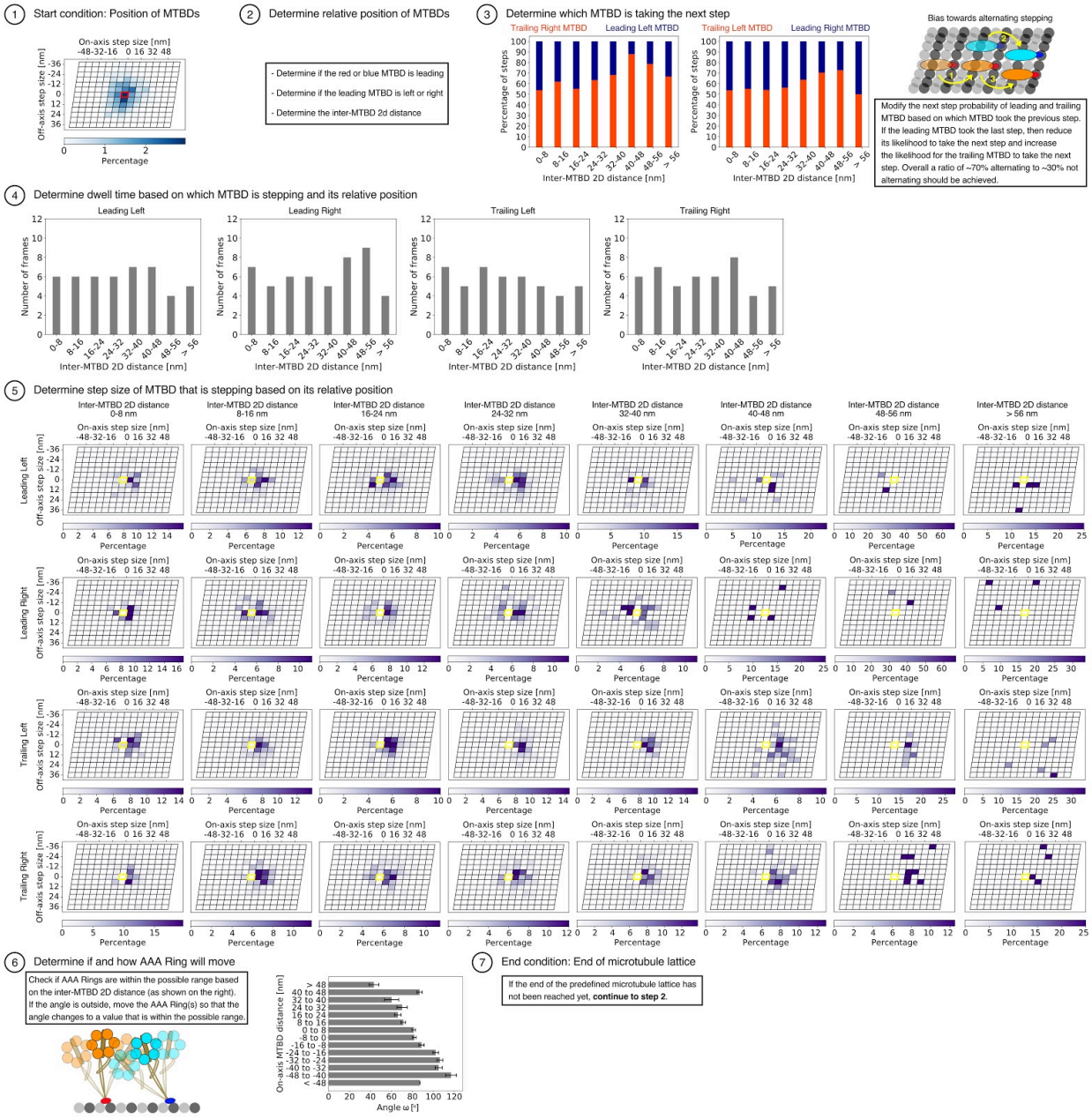

Figure S5.12 | Set up of Monte Carlo simulation for dynein stepping. For the Monte Carlo simulation we used our experimental data as input. For this simulation, we defined a start condition, followed by a loop of simulations for continuous stepping which ended as soon as dynein reached the end of the microtubule lattice. The parameters such as length and number of protofilaments of the microtubule lattice were predefined. For all our simulations we used a flattened lattice as shown in **Figure S5.6**. Note, that during the simulation the MTBDs are the main driver of motility and we let the AAA rings follow by a defined set of rules as detailed below. For this simulation, one motor domain is shown with a cyan AAA ring and with a blue MTBD while the other motor domain is shown with an orange AAA ring and a red MTBD (see **Fig. 5.5**). Also note, that the MTBD can only step between tubulin dimers and therefore will have a discrete step size while the ring will be allowed to move freely and is not bound to the microtubule lattice.

1. For the start condition, we set the red MTBD into the center of the microtubule lattice along the off-axis and towards the plus end of the microtubule along the on-axis. To determine the relative position of the other, blue MTBD we used the experimentally determined relative position of both MTBDs as shown in the panel for the starting condition. Here, each parallelogram represents a tubulin dimer consisting of one copy of α and β tubulin. The red parallelogram represents the tubulin dimer at which the red MTBD is located and the blue heatmap shows the distribution of possible relative positions of the blue MTBD. Now, to pick one of the possible blue positions we used a matrix for which we cumulatively added up the probabilities as one goes through the columns and rows of the microtubule lattice. Thus, any given position in this n x m matrix (on-axis x off-axis) will have an assigned probability range. For instance, position (5, 6) will be between 10.2% and 11.7%. To randomly select one position for the blue MTBD, we then drew a random number between 0.0 and 100.0.
   For the initial position of both AAA rings, we assigned the same off-axis position and an on-axis position that is 4 nm closer to the microtubule plus end than the corresponding microtubule-binding domains are.
2. Once the start condition was set, we determined whether the blue or red MTBD is leading, whether the blue or red MTBD is left, and calculated the 2D distance between both microtubule-binding domains.
3. Based on the 2D distance between both MTBDs, we determined whether the leading or trailing MTBD is taking the next step. Therefore, we again used experimental data as shown in the two panels in step 3 of the simulation. In addition, to account for the experimentally observed alternating stepping bias, we modified the probability for the leading or trailing MTBD to take the next step. For instance, if the currently leading MTBD took the previous step, the probability for the leading MTBD to take the next step is reduced by 0.5-fold. However, if the currently trailing MTBD took the previous step, the probability for the leading MTBD to take the next step is increased by 1.5-fold. With this, we might find that the probability for the leading MTBD is 32% (0 to 32) and for the trailing MTBD to take the next step is 68% (33 to 100). To finally decide if the currently leading or trailing MTBD is taking the next step, we again drew a random number between 0.0 and 100.0.
4. After determining which MTBD is taking the next step, but before determining what the next step is, we determined the dwell time of dynein in its current conformation. For this, we again used experimental data and picked the dwell time based on the relative position of the MTBD that is going to take the next step (e.g. leading left) and based on the inter-MTBD 2D distance (e.g. 24-32 nm). Note, that the dwell time here refers to the number of frames / images that are generated for the current conformation of dynein.
5. Next, we determined the step size along the on- and off-axis of the MTBD that is taking the next step. Based on the relative position of the MTBD that is going to take the next step (e.g. leading left) and based on the inter-MTBD 2D distance (e.g. 24-32 nm), we used the experimentally determined probabilities of where to step next as shown in the panels in step 5 of the simulation. Here, the probabilities for on-and off-axis step sizes of the MTBD that is taking the next step are mapped on the microtubule lattice in form of a heatmap. Each parallelogram represents a tubulin dimer consisting of one copy of α and β tubulin. The yellow parallelogram represents the tubulin dimer from at which the MTBD is located prior to the step. Then, as described in step 1, we cumulatively added up the probabilities as one goes through the columns and rows of the microtubule lattice and drew a random number between 0.0 and 100.0 to find the new position for the stepping microtubule-binding domain.
6. Having determined the new position of the MTBD, we next determined whether the AAA ring(s) are moving and if they are, how they are stepping. Therefore we first check

whether both AAA rings are in a position that yields a stalk-microtubule on-axis angle (see **Fig. 5.3**) within the possible range based on the inter-MTBD on-axis distance. Here, the possible range is $\mu \pm 2\sigma$. For the off-axis distance we set a cut-off of 6 nm between AAA ring and MTBD.

If one or both AAA rings are outside either the on- or off-axis range, the AAA ring position(s) need to be adjusted so that they land within the given range (the AAA ring is taking a step). To randomly select a new position of the AAA ring within the given range, we used the Cumulative Distribution Function (CDF) for which μ is the average angle for the given inter-MTBD on-axis distance and σ the corresponding standard deviation. Then, we drew a number between 0.0 and 1.0 to randomly select the new angle. In order for this new angle to be achieved, the AAA ring has to step to a new position. Note, that we placed one additional constraint, which is that if the AAA ring on the opposite motor domain of the MTBD that took the last step, has to adjust its position, we always also make the associated AAA ring move.

7. After moving the MTBD and potentially moving the AAA ring(s), we checked if we reached the end condition which is reaching the end of the predefined microtubule lattice. If the end was reached, the simulation was terminated. If the end was not reached, the simulation jumped to step 2 to cycle through another round of stepping.

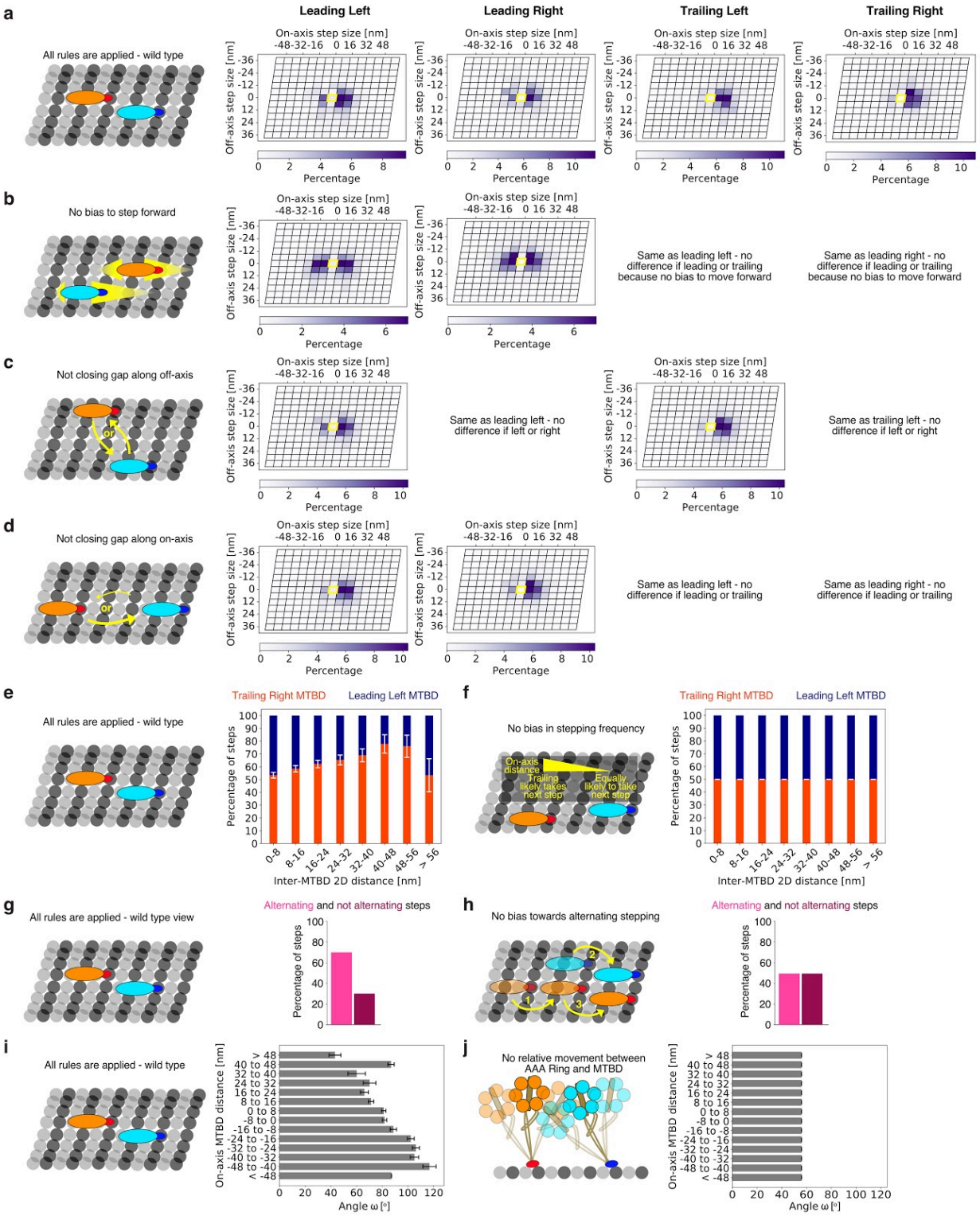

Figure S5.13 | Input data used for Monte Carlo simulations in which we change perturbations for dynein stepping. (a-d) To remove the bias (b) to step forward, (c) of the stepping direction along the off-axis, and (d) of the stepping direction along the on-axis we change the probabilities for the step size along the on- and off-axis for the MTBD that is taking the step (see step 5 in **Fig. S5.12**). We distinguish between four positions of the stepping MTBD relative to the MTBD

that is not stepping: Leading Left, Leading Right, Trailing Left, and Trailing Right. Note, that we only show the average probabilities for all four relative positions and not the inter-MTBD distance dependent heatmaps as shown in step 5 of **Figure S5.12** for the wild type condition. Here, the probabilities for on-and off-axis step sizes of the MTBD that is taking the next step are mapped on the microtubule lattice in form of a heatmap. Each parallelogram represents a tubulin dimer consisting of one copy of α and β tubulin. The yellow parallelogram represents the tubulin dimer from at which the MTBD is located prior to the step. (a) Average step size heatmaps for all four relative positions for the wild type condition for which all rules as described in **Figure 5.5** and **Figure S5.12** are applied. (b) Average step size heatmaps for all four relative positions if the bias to step forward is removed. Note, that there is no difference between the leading or trailing position as there is no bias along the on-axis for this condition. (c) Average step size heatmaps for all four relative positions if the bias of the stepping direction along the off-axis is removed. Note, that the left and right positions are combined into one as the difference between left and right MTBD was ignored for this condition. (d) Average step size heatmaps for all four relative positions if the bias of the stepping direction along the on-axis is removed. Note, that the leading and trailing positions are combined into one as the difference between leading and trailing MTBD was ignored for this condition. (e, f) Difference in input data for the frequency of stepping for leading and trailing MTBD if the bias is (e) applied or (f) ignored. (g, h) Difference in input data for the frequency of alternating stepping if the bias is (g) applied or (h) ignored. (i, j) Difference in input data for the flexibility of the AAA ring relative to the MTBD if the bias is (i) applied or (j) ignored. For the fixed angle in j, we used a previously reported average value based on electron microscopy data of monomeric dynein[11]. (a-j) Note, that the wild type data for which the biases are applied is experimental data collected in this study and that the data for which biases were removed is modified as described above.

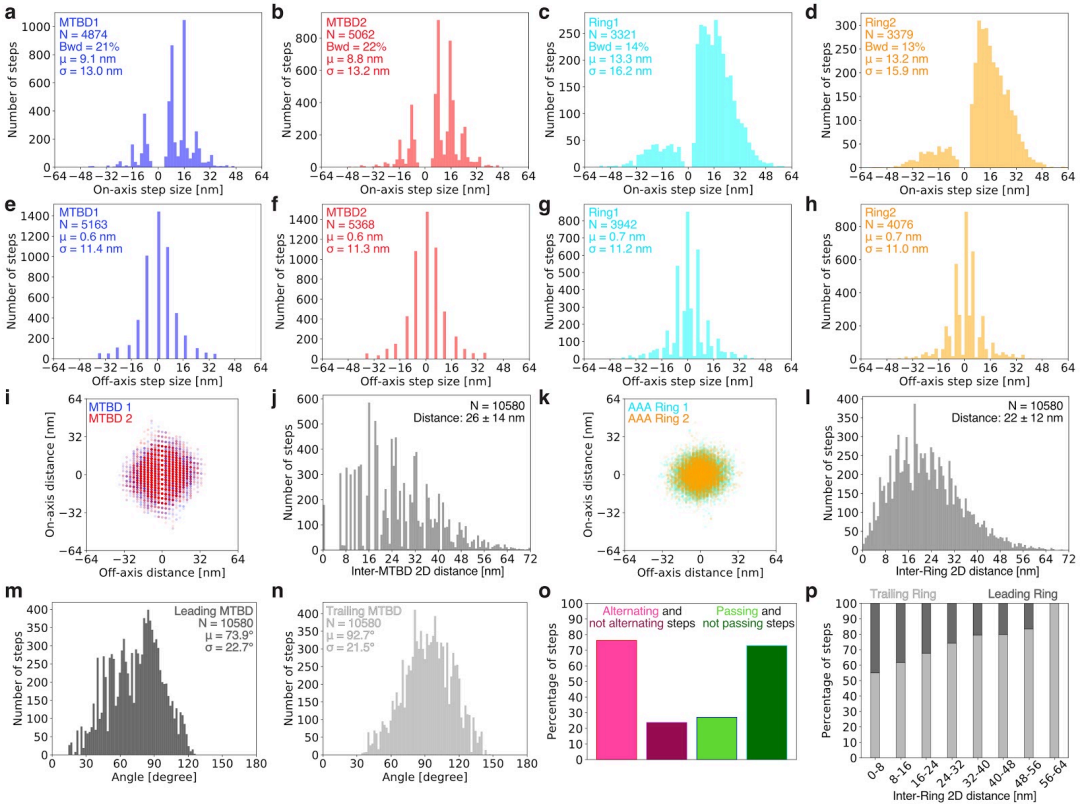

Figure S5.14 | Stepping analysis of AAA rings and MTBDs from Monte Carlo simulated data. (a-d) Histogram of on-axis step sizes for (a) MTBD 1, (b) MTBD 2, (c) AAA ring 2, and (d) AAA ring 2. Here, the number of steps detected (N), percentage of backward steps (Bwd), average step size (μ) and its standard deviation (σ) are given. (e-h) Histogram of off-axis step sizes for (e) MTBD 1, (f) MTBD 2, (g) AAA ring 2, and (h) AAA ring 2. Here, the number of steps detected (N), average step size (μ) and its standard deviation (σ) are given. (a-h) Note, that the step sizes for the MTBDs are discrete and that the step sizes for the AAA rings are more continuous since only the MTBDs follow the well defined microtubule lattice. (i, k) Scatter plot of the relative position between (i) both MTBDs and (k) both AAA rings. Here, the centroid position of either (i) MTBDs or (k) AAA rings is fixed in the origin and the position of the domains relative to the centroid is shown as a dot. (j) Histogram of the inter-MTBD 2D distance. (l) Histogram of the inter-AAA ring 2D distance. (m) Histogram of angles between dynein's stalk and the on-axis microtubule lattice for the motor domain for which the MTBD is leading. (n) Histogram of angles between dynein's stalk and the on-axis microtubule lattice for the motor domain for which the MTBD is trailing. (i-l) Overall, the AAA ring spans a smaller area than the MTBDs and the average distance between both MTBDs is larger than the average distance between the AAA rings. This agrees well with the fact that the two AAA rings are held together by the tail and that the MTBDs likely can move relative to their respective AAA ring and therefore explore a larger area. (o) Percentage of steps for which the AAA rings alternate in stepping (pink) or do not alternate in stepping (purple) and for which the AAA rings passed each other when one of them took a step along the on-axis (light green) or did not pass each other (dark green). (p) Probability of the trailing (light grey) or leading (dark grey) AAA ring to take the next step as a function of the inter-AAA ring on-axis distance. (o, p) These data agree well with previous observations for which both AAA rings were labeled while dynein was stepping along microtubules[48] showing that our Monte Carlo simulation recapitulates previous observations. (a-p) All this data is from 100 Monte Carlo simulations (as described in **Fig. S5.12**) for which we used a microtubule lattice with 13 protofilaments and a length of 79 tubulin dimers (~630 nm).

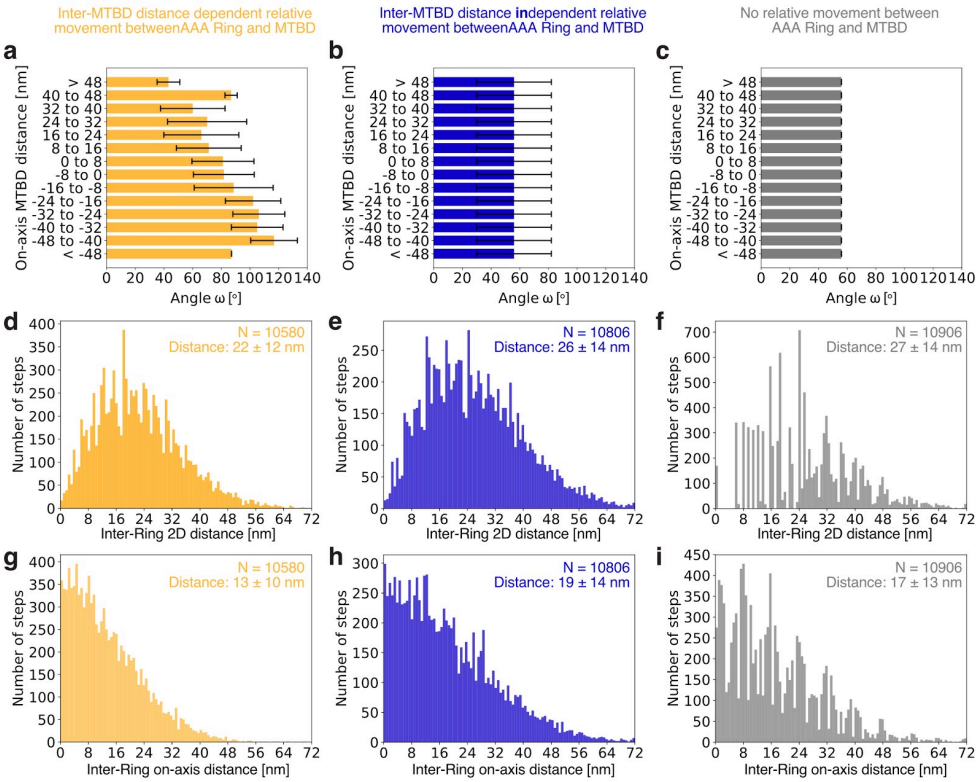

Figure S5.15 | Influence of relative movement between AAA ring and MTBD on inter-AAA ring distance. We used the Monte Carlo simulations to test how the relative movement between AAA ring and MTBD (see **Fig. 5.3**) influences the inter-AAA ring distance. Therefore we used different angles for the stalk-microtubule on-axis angle as input and looked at the inter-AAA ring distance as output. We compared the (a) inter-MTBD distance dependent movement between AAA ring and MTBD as observed in this study, the (b) inter-MTBD distance independent movement between AAA ring and MTBD based on average values from cryo-electron microscopy studies[11], and the case of (c) no relative movement between AAA ring and MTBD. For all three cases we ran 100 Monte Carlo simulations (as described in **Fig. S5.12**) for which we used a microtubule lattice with 13 protofilaments and a length of 79 tubulin dimers (~630 nm). (a-c) Input values for the stalk-microtubule on-axis angle. The error bars show the standard deviation. (d-f) 2D inter-AAA ring distances for all three conditions. (g-i) On-axis inter-AAA ring distances for all three conditions. (d-i) The distance values listed are the average distance with corresponding standard deviation.

Note that a previous study in which both AAA rings were labeled found a 2D inter-AAA ring distance of 18 ± 11 nm[48]. Thus, while the inter-MTBD distance dependent movement between AAA ring and MTBD agrees well with the experimental observed 2D inter-AAA ring distance, the other two cases yield larger inter-AAA ring distances showing that flexible motion between the AAA ring and microtubule-binding domain might be necessary to maintain a closer proximity between both AAA rings.

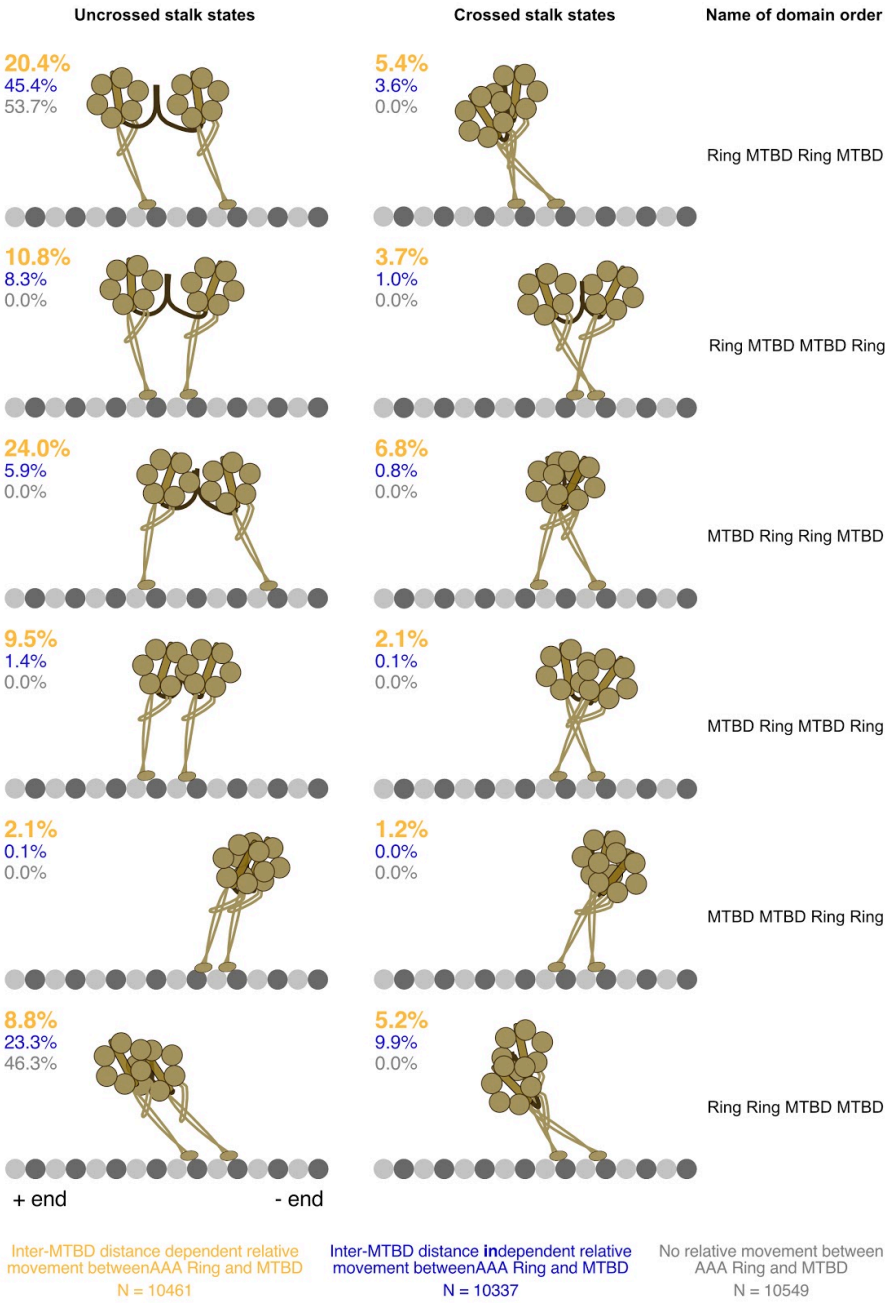

Figure S5.16 | Occurrence of dynein conformations based on Monte Carlo simulations. Schematics for all possible dynein conformations as introduced in **Figure S5.11** are shown. Using Monte Carlo simulations to simulate dynein stepping along microtubules as described in **Figure S5.12**, we quantified the occurrence of the 12 dynein conformations. We compared the occurrence of conformations for different regimes of stalk-microtubule on-axis angles (**Fig. S5.15**): for inter-MTBD distance dependent movement between AAA ring and MTBD as observed in this study (orange), for inter-MTBD distance independent movement between AAA ring and MTBD based on average values from cryo-electron microscopy studies[11] (blue), and for no relative movement between AAA ring and MTBD (grey). The percentages for all three cases and 12 possible conformations are listed in the top left. For all three cases we ran 100 Monte Carlo simulations (as described in **Fig. S5.12**) for which we used a microtubule lattice with 13 protofilaments and a length of 79 tubulin dimers (~630 nm).

The biggest difference can be observed between the case where no relative movement between AAA ring and MTBD is allowed and the other two cases as the no movement cases only allows for two of the twelve conformations. For the cases with flexible AAA ring movement, the crossed stalk conformations are far less prominent than the conformations in which the stalks do not cross. Moreover, the largest difference between the distance dependent relative movement (orange) and the distance independent relative movement (blue) is the occupancy among conformations 1, 5, 7, and 11 (counted from top left to bottom right).

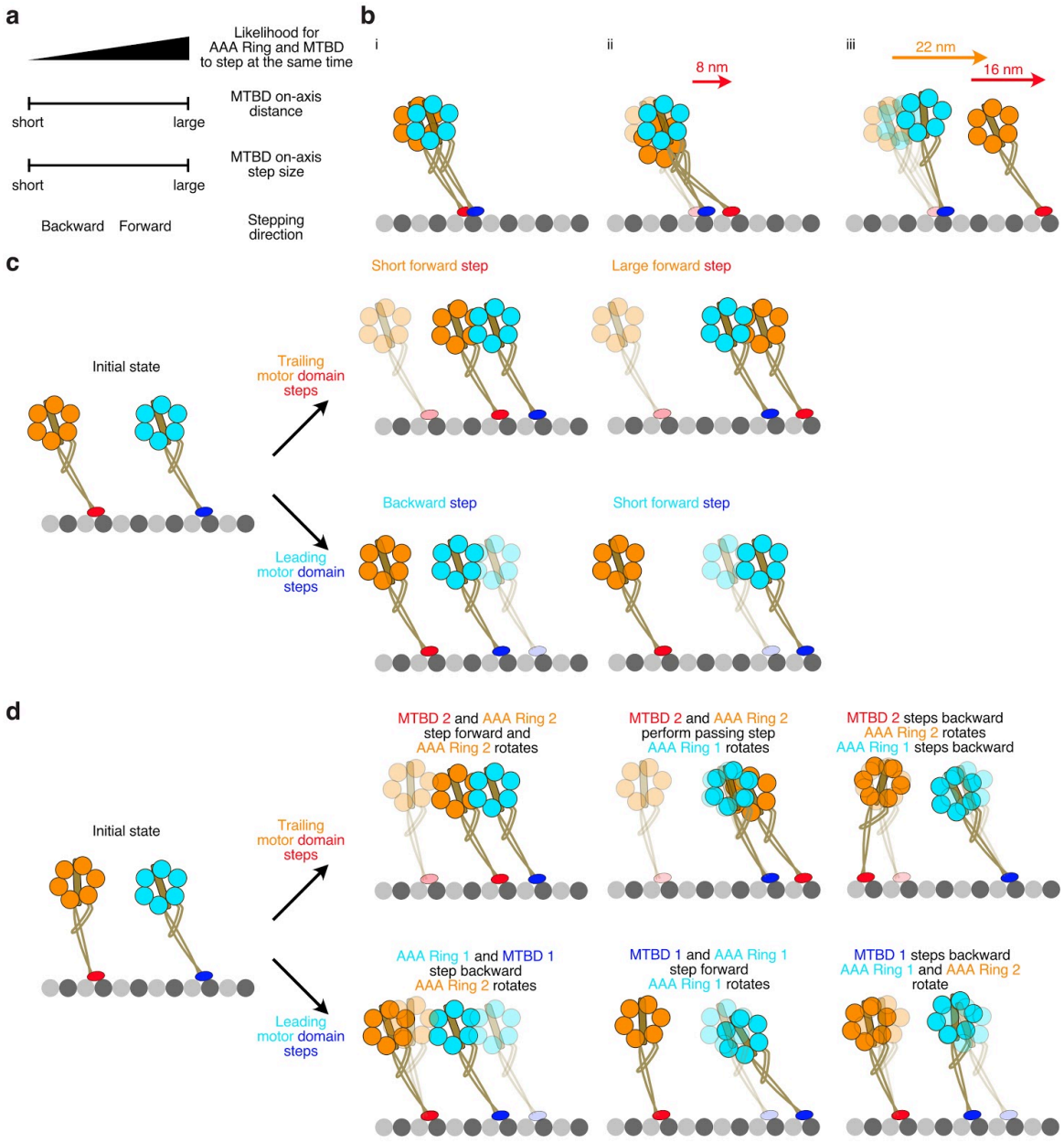

Supplementary Figure 17 | Models for dynein stepping. (a) Parameters that influence the likelihood of the AAA ring (green) and the associated MTBD (red) to step at same time. The larger the MTBD on-axis distance and the larger the MTBD step size the more likely the AAA ring and the associated MTBD will step at the same time (**Fig. 5.2, Fig. S5.9**). Also, if the MTBD is taking a forward step the likelihood to step together is increased (**Fig. S5.9**). (b) One explanation why the AAA ring on average might take larger steps than the associated MTBD when they are stopping at the same time (**Fig. 5.2**) is the following. The flexibility within the dynein motor domain may allow the MTBD to move without the AAA ring during the first step (i to ii) and then, during the second step of the MTBD, the tension on the AAA ring might become large enough so that it is forced to move (ii to iii). However, this time the AAA ring might make up some of the distance the MTBD covered during the first step (when they did not step at the same time) leading to a larger step of the AAA ring during the second step (when they step at the same time) compared to the MTBD. The stepping behavior depicted in this panel can also

explain or observation of more backward steps and shorter forward steps of the MTBD compared to the AAA ring. Under certain conditions, a short step of MTBD or a short inter-MTBD distance, the MTBD can move without the AAA ring (see a). Thus, these short “exploration” steps of the MTBD might shift the MTBD step size distribution towards more backward steps and shift the average forward step size to smaller values than the AAA ring. (c) A potential model for dynein stepping without accounting for flexible movement between AAA ring and MTBD. Left: Initial state in which both motor domains have the same angle between stalk and microtubule on-axis (see **Fig. 5.3**). Top: Potential steps that can be taken by the trailing motor domain - a short forward step during which the stepping motor domain does not pass the other motor domain or a larger forward step during which the stepping motor domain passes the other motor domain. Bottom: Potential steps that can be taken by the leading motor domain - a short backward step or a short forward step. (d) A potential model for dynein stepping taking the observed flexibility between AAA ring and MTBD into account. Left: Initial state in which both motor domains have a slightly different angle between stalk and microtubule on-axis (see **Fig. 5.3**). Top: Potential steps that can be taken by the trailing motor domain. Bottom: Potential steps that can be taken by the leading motor domain.

When we compared the stepping motions in which the relative movement between AAA ring and MTBD is not taken into account (c) or in which it is allowed (d), we found that the rigid model can not explain the experimentally observed conformational variety (**Fig. 5.3, Fig. 5.4**). In particular the stepping motions for the trailing as well as the leading motor domain shown on the most right are different than previously described. Here, the MTBD can for instance take a small backward step while the AAA ring does not seem to move along the on-axis. As shown in **Figure 5.2** and **Figure S5.9**, if the AAA ring does not move, it is most likely when the MTBD takes a small step or when the inter-MTBD on-axis distance is small (a).

Materials and Methods

Flow-cell preparation

The flow-cells were assembled as previously described[78]. Briefly, we cut custom three-cell flow chambers out of double-sided adhesive sheets (Soles2dance, 9474-08x12 - 3M 9474LE 300LSE) using a laser cutter. Moreover, we used glass slides (Thermo Fisher Scientific, 12-550-123) and 170 µm thick coverslips (Zeiss, 474030-9000-000) to assemble the flow cells. The coverslips were cleaned in a 5% v/v solution of Hellmanex III (Sigma, Z805939-1EA) at 50° C overnight and washed extensively with Milli-Q water afterwards.

Assembly of DNA FluoroCubes for dynein labeling

FluoroCubes were assembled as previously described[161]. For each of the three six dye FluoroCubes, we used four 32 bp long oligonucleotide strands of which three were modified with two dyes and one with a functional tag; either a HALO-ligand[103] for labeling of the HALO-tag or a CoA for labeling of the YBBR-tag. The organic dye modified oligonucleotides were purchased from IDT and the oligonucleotides with functional tags were synthesized by Biomers. For each of the three FluoroCubes, four oligos were mixed to a final concentration of 10 µM in folding buffer (5 mM Tris pH 8.5, 1 mM EDTA and 40 mM $MgCl_2$) and annealed by denaturation at 85° C for 5 min followed by cooling from 80° C to 65° C with a decrease of 1° C per 5 min. Afterwards the samples were further cooled from 65° C to 25° C with a decrease of 1° C per 20 min and then held at 4° C. Folding products were analyzed by 3.0% agarose gel electrophoresis in TBE (45 mM Tris-borate and 1 mM EDTA) with 12 mM $MgCl_2$ at 70 V for 2.5 hours on ice and purified by extraction and centrifugation in Freeze 'N Squeeze columns (BioRad Sciences, 732-6165). The gels were scanned using a Typhoon 9400 scanner (GE Healthcare).

Dynein expression, purification, and labeling

We used recombinant *S.cerevisiae* cytoplasmic dynein (Dyn1) truncated at the N-terminus (1219-4093 aa) as a monomeric version with the following genotype for all our dynein experiments: MATa his3-11,5 ura3-1 leu2-3,112 ade2-1 trp-1 PEP4::HIS5 pGAL-ZZ-TEV-SNAPf-3XHA-D6-DYN1(MTBDL5:YbbR)-gsDHA. Specifically, we used construct VY1067[78] which has a N-terminal SNAP-tag[104,160], a C-terminal Halo-tag[103] and a YBBR-tag[104] inserted into loop 5 of the MTBD. Dynein was expressed and purified as previously described[60,78] with the difference that before TEV-cleavage dynein was labeled with DNA FluoroCubes and single-stranded DNA. Therefore, we washed the beads with dynein bound with 200 ml of TEV buffer (50 mM Tris-HCl pH 8.0, 150 mM K-Acetate, 6 mM Mg-Acetate, 1 mM EGTA pH 8.0, 1 mM ATP, 10% Glycerol). Then, we split the beads into two equal amounts to label each fraction (fraction A and B)differently. Fraction A was labeled with 5 µM of HALO ligand, ATTO 488 FluoroCubes and 5 µM CoA ATTO 647N FluoroCubes. Fraction B was labeled with 5 µM of CoA Cy3N FluoroCubes. For both labeling reactions, we added Mg-Acetate to a final concentration of 6 mM and EGTA pH 8.0 to a final concentration of 1 mM to the purified FluoroCubes. Moreover, we added 2.5 µM of Sfp phosphopantetheinyl transferase to both reactions to enable YBBR-tag labeling[119]. Both reactions were incubated overnight. The next day, we washed both reactions with 200 ml of TEV buffer. Then, we labeled fraction A and B with 20 µM of reverse complementary oligonucleotides in TEV Buffer for 12 hours. For fraction A we used a benzylguanine (BG) modified oligo: BG - GGT AGA GTG GTA AGT AGT GAA. And for fraction B we used a benzylguanine (BG) modified oligo: TTC ACT ACT TAC CAC TCT ACC - BG. Both were ordered from Biomers. Afterwards, both fractions were washed with an additional 200 ml of TEV buffer. Next, we eluted both fractions by incubating with 2 µM TEV protease in TEV buffer overnight. The next day, both samples were eluted and mixed to allow for dimerization. Dynein with single organic dyes was prepared in the same way as FluoroCube labeled dynein, except that HALO Alexa 488 (Promega) was used instead of the HALO ATTO

488 FluoroCube, that CoA 647 (NEB) was used instead of the CoA ATTO 647N FluoroCube, and that CoA 547 (NEB) was used instead of the CoA Cy3N FluoroCube.

Microtubule preparation

Tubulin used in this study was purified and polymerized as previously described[20]. We used unlabeled tubulin and biotinylated tubulin which were mixed at an approximate ratio of 20:1 in BRB80 (80 mM Pipes (pH 6.8), 1 mM EGTA, and 1 mM $MgCl_2$). To start the polymerization reactions we added 1 mM GTP and incubated for 15 min in a 37°C water bath. Then, 20 μM of Taxol (Sigma, T1912) was added and the mixture was incubated for another 2 hours at 37°C. Every day before using microtubules in our experiments, microtubules were spun over a 25% sucrose cushion in BRB80 at ~160,000 g for 10 min.

Preparation of flow-cells with dynein

The flow chambers for the single-molecule assay were prepared as previously described[62]. Briefly, we added 10 μl of 5 mg/ml Biotin-BSA in BRB80 and incubated for 2 min. Then, we washed with 20 μl of DAB (50 mM K-Ac, 30 mM HEPES, pH 7.4, 6 mM $Mg(Ac)_2$, 1 mM EGTA) with 0.4 mg/ml κ-casein (Sigma, C0406). Next, we added 10 μl of 0.5 mg/ml Streptavidin in PBS and incubated for 2 min. Afterwards, we washed with 20 μl of DAB with 0.4 mg/ml κ-casein. Then, we added 10 μl of polymerized microtubules and incubated for 5 min. This was followed by a wash with 30 μl of DAB, 0.4 mg/ml κ-casein, and 10 μM Taxol. We then added dynein (either FluoroCube or single organic dye labeled) diluted in DAB with 0.4 mg/ml κ-casein and 10 μM Taxol and incubated for 3 min. Afterwards we washed with 10 μl of DAB, 0.4 mg/ml κ-casein, and 10 μM Taxol. For the experiments, which we used to extract dynein's steps, we then added 10 μl of DAB, 0.4 mg/ml κ-casein, 10 μM Taxol, 3 μM ATP, an ATP regeneration system (1 mM phosphoenolpyruvate (Sigma, 860077), ~0.01 U pyruvate kinase (Sigma, P0294), ~0.02 U lactate dehydrogenase (Sigma, P0294)), and the PCA/PCD/Trolox

oxygen scavenging system[76,136]. For the velocity and processivity comparison (**Fig. S5.4**), we added 10 µl of DAB, 0.4 mg/ml κ-casein, 10 µM Taxol, 1 mM ATP, and the PCA/PCD/Trolox oxygen scavenging system[76,136]. Lastly for the brightness and photostability comparison (**Fig S5.3**) we added 10 µl of DAB, 0.4 mg/ml κ-casein, 10 µM Taxol, and the PCA/PCD/Trolox oxygen scavenging system[76,136].

Fluorescent beads for image registration

To register the three channels, we used TetraSpeck™ beads (Thermo Fisher Scientific, T7279). We immobilized the beads for imaging by adding 10 µl of 1 mg/ml Poly-D-lysine (Sigma, P6407) in Milli-Q water to the flow-cell, followed by a 3 min incubation and a wash with 20 µl of BRB80 (80 mM Pipes (pH 6.8), 1 mM EGTA, and 1 mM $MgCl_2$). Afterwards, we added 10 µl of 1:1000 diluted TetraSpeck™ beads in BRB80 and incubated for 5 min. Finally, the flow-cell was washed with 40 µl of BRB80.

DNA-origami nanoruler

We designed and assembled DNA-origami nanorulers as previously described[101]. The three-color nanoruler design is based on the 12HB and is assembled with fluorescently labeled oligos with one dye of each ATTO 488, Cy3, and ATTO647N per ruler. Moreover, biotinylated oligos are incorporated into the structure on the opposite side of the fluorescent dyes to enable surface immobilization. The ATTO 488 and the ATTO 647N dye are separated by ~28 nm, the ATTO 488 and the Cy3 dye are separated by ~14 nm, and the Cy3 and the ATTO 647N dye are separated by ~14 nm. Flow-cells with nanorulers were prepared as follows: we first added 10 µl of 5 mg/ml Biotin-BSA in BRB80 and incubated for 2 min. Then, we washed with 20 µl of PBS (pH 7.4), added 10 µl of 0.5 mg/ml Streptavidin in PBS (pH 7.4) and incubated for another 2 min. Afterwards, we washed with 20 µl of PBS (pH 7.4) supplemented with 10 mM $MgCl_2$. Then, we added 10 µl of three-color nanoruler and incubated for 5 min. Finally, we washed with 30 µl

of PBS (pH 7.4) supplemented with 10 mM $MgCl_2$ and then added the PCA/PCD/Trolox oxygen scavenging system[76] in PBS (pH 7.4) supplemented with 10 mM $MgCl_2$.

Microscope setup

The data collections for all experiments were carried out at room temperature (~23° C). For imaging, we used a total internal reflection fluorescence (TIRF) inverted microscope (Nikon Eclipse Ti microscope) which is equipped with a 100× (1.45 NA) oil objective (Nikon, Plan Apo ƛ). Moreover, we used two Andor iXon 512x512 pixel EM cameras, DU-897E with a pixel size of 159 nm. The microscope is also equipped with two stepping motor actuators (Sigma Koki, SGSP-25ACTR-B0) mounted on a KS stage (KS, Model KS-N) and a custom-built cover to reduce noise from air and temperature fluctuations. A reflection based autofocus unit (FocusStat4) was custom adapted to our microscope (Focal Point Inc.). We used a 488 nm laser (Coherent Sapphire 488 LP, 150 mW), a 561 nm laser (Coherent Sapphire 561 LP, 150 mW), and a 640 nm laser (Coherent CUBE 640-100C, 100 mW) for data collection. In the upper turret of the microscope, we mounted a TIRF cube containing excitation filter (Chroma, zet405/491/561/638x), dichroic mirror (zt405/488/561/638rpc), and emission filter (Chroma, zet405/491/561/647m). The lower turret contained a filter cube (Chroma, TE/Ti2000_Mounted, 69000m, T660lpxr, ET700/75m) that directs ATTO 488 as well as Cy3 emission towards the back camera and the ATTO 647N emission towards the left camera. The acquisition software for all microsopy data was μManager[70] 2.0.

Single-molecule TIRF data collection

For the data collection of dynein stepping, we prepared one chamber with TetraSpeck™ beads and another chamber on the same microscopy slide with three-color dynein. We first collected a 20 by 20 grid of TetraSpeck™ beads. Therefore, we collected a micrograph with 100 msec exposure with the 488 nm laser, with the 561 nm laser, and with the 640 nm laser at any

position. After the collection at one position we moved the stage and waited 3 sec before collecting data at the new position to minimize drift effects.

Once the TetraSpeck™ beads data set was collected, we moved to the chamber with the three-color dynein and acquired six, 500-frame-long movies with 110 msec exposure times as follows: We collected images in all three channels in an alternating fashion, but skipped the 488 channel every other round in order to enable a fast acquisition with no dead time. Afterward collecting the dynein movies, we moved back to the TetraSpeck™ beads chamber to collect another 20 x 20 grid, which was used as a control to test whether any changes in image registration occurred during acquisition (**Fig. S5.1**). We only accepted datasets if σ_{reg} < 1nm.

For the velocity and processivity comparison (**Fig. S5.4**), we did not acquire any TetraSpeck™ beads but only acquired dynein movies with 100 frames total, with an exposure time of 110 msec and a 1.3 sec interval between acquisition sequences. For the brightness and photostability comparison (**Fig. S5.3**), we did not acquire any TetraSpeck™ beads but only acquired dynein movies with 200 frames total and with an exposure time of 110 msec.

For the data collection of the DNA-origami rulers, we followed the same protocol as for the three-color dynein except that we acquired 20 movies with an alternating exposure of 400 msec between all three channels.

All TetraSpeck™ bead, nanoruler, and dynein datasets were acquired with a '16 bit, conventional, 3 MHz' setting, a preamp gain of 5x and in conventional CCD mode (i.e., no EM gain). The intensity (irradiance) at the objective was 120 W/cm^2 (488 nm laser), 120 W/cm^2 (561 nm laser), and 160 W/cm^2 (640 nm laser).

Single-molecule TIRF data analysis of dynein stepping

All emitters of dynein and TetraSpeck™ beads were fitted and localized using the μManager[70] "Localization Microscopy' plug-in as previously described[78]. After localizing all probes, we registered the three channels as previously described[78] (**Fig. S5.1**). Then, tracks of

individual motors were extracted using the μManagers[70] "Localization Microscopy' plug-in. To this end, we set the minimum frame number to 125, the maximum number of missing frames to 350, the maximum distance between frames to 200 nm and the total minimum distances of the full track to 200 nm. Afterwards, we rotated tracks of individual motors using a principal component analysis (PCA) implemented in python. Next, we applied a custom Matlab (Matlab R2016b) script to identify individual steps using Chung-Kennedy edge-detecting algorithm as previously described[48] and further analyzed the data in a custom written python script. Only steps for which the step itself and the previous as well as the following step had a standard error of the mean of the 2D distance of less than 8 nm were considered for further analysis.

Image registration and distance measurements for DNA-origami nanoruler

The image registration and the distance measurements between the different dyes on the DNA-origami nanoruler (**Fig. S5.2**) were carried out as previously described[78]. Since this is a three-color dataset instead of a two-color dataset, we carried out the distance measurements for individual spot pairs (e.g. Cy3 and ATTO 488 or Cy3 and ATTO 647N or ATTO 488 and ATTO 647N). To extract spots which contained nanoruler with all three labels, we extracted them using the μManagers[70] "Localization Microscopy' plug-in. To this end, we set the minimum frame number to 18, the maximum number of missing frames to 2, the maximum distance between frames to 15 nm, the total minimum distances of the full track to 0 nm, and the maximum distances between each dye pair to 90 nm.

Monte Carlo simulation of dynein stepping

The set up of the Monte Carlo simulation is described in detail in **Figure S5.12**.

Figure and graph preparation

All figures were prepared by using ImageJ (light microscopy data), Affinity designer (version 1.6.1, Serif (Europe) Ltd), or Python (version 2.7, Python Software Foundation).

Statistics and error calculation

We discussed the inherent uncertainty due to random or systematic errors for each result and their validation in the relevant sections of the manuscript. Moreover, we included details about sample size, number of independent calculations, and the calculation of the error bars in the figures or in the respective figure captions.

Acknowledgements

We would like to thank Andrew Carter (MRC Laboratory of Molecular Biology) and Elizabeth Villa (University of California, San Diego) for supplying the Matlab script for step detection of dynein. The authors gratefully acknowledge funding from the National Institutes of Health: R01GM097312, 1R35GM118106 (R.D.V., S.N.), and the Howard Hughes Medical Institute (N.S., N.Z., and R.D.V.).

REFERENCES

1. Kiyomitsu, T. & Cheeseman, I. M. Cortical dynein and asymmetric membrane elongation coordinately position the spindle in anaphase. *Cell* **154**, 391–402 (2013).
2. Reck-Peterson, S. L., Redwine, W. B., Vale, R. D. & Carter, A. P. The cytoplasmic dynein transport machinery and its many cargoes. *Nature Reviews Molecular Cell Biology* vol. 19 382–398 (2018).
3. Viswanadha, R., Sale, W. S. & Porter, M. E. Ciliary Motility: Regulation of Axonemal Dynein Motors. *Cold Spring Harb. Perspect. Biol.* **9**, (2017).
4. Taschner, M. & Lorentzen, E. The Intraflagellar Transport Machinery. *Cold Spring Harbor Perspectives in Biology* vol. 8 a028092 (2016).
5. Roberts, A. J., Kon, T., Knight, P. J., Sutoh, K. & Burgess, S. A. Functions and mechanics of dynein motor proteins. *Nat. Rev. Mol. Cell Biol.* **14**, 713–726 (2013).
6. King, S. M. *Dyneins: Dynein Mechanics, Dysfunction, and Disease*. (Academic Press, 2017).
7. Gibbons, I. R. & Rowe, A. J. Dynein: A Protein with Adenosine Triphosphatase Activity from Cilia. *Science* **149**, 424–426 (1965).
8. Fletcher, D. A. & Mullins, R. D. Cell mechanics and the cytoskeleton. *Nature* **463**, 485–492 (2010).
9. Brouhard, G. J. & Rice, L. M. Microtubule dynamics: an interplay of biochemistry and mechanics. *Nat. Rev. Mol. Cell Biol.* **19**, 451–463 (2018).
10. Nogales, E. Structural Insights into Microtubule Function. *Annual Review of Biochemistry* vol. 69 277–302 (2000).
11. Can, S., Lacey, S., Gur, M., Carter, A. P. & Yildiz, A. Directionality of dynein is controlled by the angle and length of its stalk. *Nature* **566**, 407–410 (2019).
12. Hirokawa, N., Noda, Y., Tanaka, Y. & Niwa, S. Kinesin superfamily motor proteins and

intracellular transport. *Nature Reviews Molecular Cell Biology* vol. 10 682–696 (2009).

13. Derr, N. D. *et al.* Tug-of-War in Motor Protein Ensembles Revealed with a Programmable DNA Origami Scaffold. *Science* vol. 338 662–665 (2012).
14. Hancock, W. O. Bidirectional cargo transport: moving beyond tug of war. *Nature Reviews Molecular Cell Biology* vol. 15 615–628 (2014).
15. Tanaka, Y. & Hirokawa, N. Kinesin Superfamily Proteins (KIFs) as a Fundamental Component of Life: Intracellular Transport and Beyond. *Encyclopedia of Cell Biology* 608–619 (2016) doi:10.1016/b978-0-12-394447-4.20060-6.
16. Gennerich, A. & Vale, R. D. Walking the walk: how kinesin and dynein coordinate their steps. *Curr. Opin. Cell Biol.* **21**, 59–67 (2009).
17. Hartman, M. A. & Spudich, J. A. The myosin superfamily at a glance. *Journal of Cell Science* vol. 125 1627–1632 (2012).
18. Sweeney, H. L. & Houdusse, A. Structural and functional insights into the Myosin motor mechanism. *Annu. Rev. Biophys.* **39**, 539–557 (2010).
19. Gill, S. R. *et al.* Dynactin, a conserved, ubiquitously expressed component of an activator of vesicle motility mediated by cytoplasmic dynein. *J. Cell Biol.* **115**, 1639–1650 (1991).
20. McKenney, R. J., Huynh, W., Tanenbaum, M. E., Bhabha, G. & Vale, R. D. Activation of cytoplasmic dynein motility by dynactin-cargo adapter complexes. *Science* **345**, 337–341 (2014).
21. Schlager, M. A., Hoang, H. T., Urnavicius, L., Bullock, S. L. & Carter, A. P. In vitro reconstitution of a highly processive recombinant human dynein complex. *EMBO J.* **33**, 1855–1868 (2014).
22. Urnavicius, L. *et al.* Cryo-EM shows how dynactin recruits two dyneins for faster movement. *Nature* **554**, 202–206 (2018).
23. Grotjahn, D. A. *et al.* Author Correction: Cryo-electron tomography reveals that dynactin recruits a team of dyneins for processive motility. *Nat. Struct. Mol. Biol.* **25**, 355 (2018).

24. Marzo, M. G., Griswold, J. M. & Markus, S. M. Pac1/LIS1 stabilizes an uninhibited conformation of dynein to coordinate its localization and activity. *Nat. Cell Biol.* **22**, 559–569 (2020).
25. Htet, Z. M. *et al.* LIS1 promotes the formation of activated cytoplasmic dynein-1 complexes. *Nat. Cell Biol.* **22**, 518–525 (2020).
26. Elshenawy, M. M. *et al.* Lis1 activates dynein motility by modulating its pairing with dynactin. *Nature Cell Biology* vol. 22 570–578 (2020).
27. Burgess, S. A., Walker, M. L., Sakakibara, H., Knight, P. J. & Oiwa, K. Dynein structure and power stroke. *Nature* **421**, 715–718 (2003).
28. Carter, A. P., Cho, C., Jin, L. & Vale, R. D. Crystal structure of the dynein motor domain. *Science* **331**, 1159–1165 (2011).
29. Schmidt, H., Zalyte, R., Urnavicius, L. & Carter, A. P. Structure of human cytoplasmic dynein-2 primed for its power stroke. *Nature* **518**, 435–438 (2015).
30. Kon, T. *et al.* The 2.8 [thinsp] A crystal structure of the dynein motor domain. *Nature* **484**, 345–350 (2012).
31. Schmidt, H., Gleave, E. S. & Carter, A. P. Insights into dynein motor domain function from a 3.3-Å crystal structure. *Nat. Struct. Mol. Biol.* **19**, 492–7, S1 (2012).
32. Cho, C., Reck-Peterson, S. L. & Vale, R. D. Regulatory ATPase sites of cytoplasmic dynein affect processivity and force generation. *J. Biol. Chem.* **283**, 25839–25845 (2008).
33. Kon, T., Nishiura, M., Ohkura, R., Toyoshima, Y. Y. & Sutoh, K. Distinct functions of nucleotide-binding/hydrolysis sites in the four AAA modules of cytoplasmic dynein. *Biochemistry* **43**, 11266–11274 (2004).
34. Bhabha, G., Johnson, G. T., Schroeder, C. M. & Vale, R. D. How Dynein Moves Along Microtubules. *Trends Biochem. Sci.* **41**, 94–105 (2016).
35. Bhabha, G. *et al.* Allosteric communication in the dynein motor domain. *Cell* **159**, 857–868 (2014).

36. DeWitt, M. A., Cypranowska, C. A., Cleary, F. B., Belyy, V. & Yildiz, A. The AAA3 domain of cytoplasmic dynein acts as a switch to facilitate microtubule release. *Nat. Struct. Mol. Biol.* **22**, 73–80 (2015).

37. Cho, C., Reck-Peterson, S. L. & Vale, R. D. Regulatory ATPase Sites of Cytoplasmic Dynein Affect Processivity and Force Generation. *Journal of Biological Chemistry* vol. 283 25839–25845 (2008).

38. Kon, T., Nishiura, M., Ohkura, R., Toyoshima, Y. Y. & Sutoh, K. Distinct functions of nucleotide-binding/hydrolysis sites in the four AAA modules of cytoplasmic dynein. *Biochemistry* **43**, 11266–11274 (2004).

39. Roberts, A. J. *et al.* AAA+ Ring and linker swing mechanism in the dynein motor. *Cell* **136**, 485–495 (2009).

40. Kon, T. *et al.* Helix sliding in the stalk coiled coil of dynein couples ATPase and microtubule binding. *Nat. Struct. Mol. Biol.* **16**, 325–333 (2009).

41. Rao, L., Berger, F., Nicholas, M. P. & Gennerich, A. Molecular mechanism of cytoplasmic dynein tension sensing. *Nat. Commun.* **10**, 3332 (2019).

42. Gibbons, I. R. *et al.* The affinity of the dynein microtubule-binding domain is modulated by the conformation of its coiled-coil stalk. *J. Biol. Chem.* **280**, 23960–23965 (2005).

43. Oiwa, K. & Sakakibara, H. Recent progress in dynein structure and mechanism. *Curr. Opin. Cell Biol.* **17**, 98–103 (2005).

44. Shima, T., Kon, T., Imamula, K., Ohkura, R. & Sutoh, K. Two modes of microtubule sliding driven by cytoplasmic dynein. *Proc. Natl. Acad. Sci. U. S. A.* **103**, 17736–17740 (2006).

45. Gee, M. & Vallee, R. The role of the dynein stalk in cytoplasmic and flagellar motility. *Eur. Biophys. J.* **27**, 466–473 (1998).

46. Nishikawa, Y., Inatomi, M., Iwasaki, H. & Kurisu, G. Structural Change in the Dynein Stalk Region Associated with Two Different Affinities for the Microtubule. *J. Mol. Biol.* **428**, 1886–1896 (2016).

47. DeWitt, M. A., Chang, A. Y., Combs, P. A. & Yildiz, A. Cytoplasmic dynein moves through uncoordinated stepping of the AAA+ ring domains. *Science* **335**, 221–225 (2012).
48. Qiu, W. *et al.* Dynein achieves processive motion using both stochastic and coordinated stepping. *Nat. Struct. Mol. Biol.* **19**, 193–200 (2012).
49. Lippert, L. G. *et al.* Angular measurements of the dynein ring reveal a stepping mechanism dependent on a flexible stalk. *Proc. Natl. Acad. Sci. U. S. A.* **114**, E4564–E4573 (2017).
50. Imai, H. *et al.* Direct observation shows superposition and large scale flexibility within cytoplasmic dynein motors moving along microtubules. *Nat. Commun.* **6**, 8179 (2015).
51. Vale, R. D. The molecular motor toolbox for intracellular transport. *Cell* **112**, 467–480 (2003).
52. Vallee, R. B., Williams, J. C., Varma, D. & Barnhart, L. E. Dynein: An ancient motor protein involved in multiple modes of transport. *J. Neurobiol.* **58**, 189–200 (2004).
53. Vallee, R. B., McKenney, R. J. & Ori-McKenney, K. M. Multiple modes of cytoplasmic dynein regulation. *Nat. Cell Biol.* **14**, 224–230 (2012).
54. Kardon, J. R. & Vale, R. D. Regulators of the cytoplasmic dynein motor. *Nat. Rev. Mol. Cell Biol.* **10**, 854–865 (2009).
55. Pfister, K. K. *et al.* Genetic analysis of the cytoplasmic dynein subunit families. *PLoS Genet.* **2**, e1 (2006).
56. Vale, R. D. & Milligan, R. A. The way things move: looking under the hood of molecular motor proteins. *Science* **288**, 88–95 (2000).
57. Imamula, K., Kon, T., Ohkura, R. & Sutoh, K. The coordination of cyclic microtubule association/dissociation and tail swing of cytoplasmic dynein. *Proc. Natl. Acad. Sci. U. S. A.* **104**, 16134–16139 (2007).
58. Redwine, W. B. *et al.* Structural basis for microtubule binding and release by dynein. *Science* **337**, 1532–1536 (2012).
59. Carter, A. P. *et al.* Structure and functional role of dynein's microtubule-binding domain.

Science **322**, 1691–1695 (2008).

60. Reck-Peterson, S. L. *et al.* Single-molecule analysis of dynein processivity and stepping behavior. *Cell* **126**, 335–348 (2006).
61. DeWitt, M. A., Chang, A. Y., Combs, P. A. & Yildiz, A. Cytoplasmic dynein moves through uncoordinated stepping of the AAA+ ring domains. *Science* **335**, 221–225 (2012).
62. Yildiz, A. & Vale, R. D. Tracking Movements of the Microtubule Motors Kinesin and Dynein Using Total Internal Reflection Fluorescence Microscopy. *Cold Spring Harb. Protoc.* **2015**, db.prot086355 (2015).
63. Tomishige, M., Stuurman, N. & Vale, R. D. Single-molecule observations of neck linker conformational changes in the kinesin motor protein. *Nat. Struct. Mol. Biol.* **13**, 887–894 (2006).
64. Toropova, K. *et al.* Lis1 regulates dynein by sterically blocking its mechanochemical cycle. *Elife* **3**, (2014).
65. Kon, T., Oyama, T., Shimo-Kon, R., Suto, K. & Kurisu, G. X-ray structure of a functional full-length dynein motor domain. (2012) doi:10.2210/pdb3vkh/pdb.
66. Carter, A. P. Crystal clear insights into how the dynein motor moves. *J. Cell Sci.* **126**, 705–713 (2013).
67. Cleary, F. B. *et al.* Tension on the linker gates the ATP-dependent release of dynein from microtubules. *Nat. Commun.* **5**, 4587 (2014).
68. Livingstone, C. D. & Barton, G. J. Protein sequence alignments: a strategy for the hierarchical analysis of residue conservation. *Comput. Appl. Biosci.* **9**, 745–756 (1993).
69. Waterhouse, A. M., Procter, J. B., Martin, D. M. A., Clamp, M. & Barton, G. J. Jalview Version 2—a multiple sequence alignment editor and analysis workbench. *Bioinformatics* **25**, 1189–1191 (2009).
70. Edelstein, A., Amodaj, N., Hoover, K., Vale, R. & Stuurman, N. Computer control of microscopes using μManager. *Curr. Protoc. Mol. Biol.* **Chapter 14**, Unit14.20 (2010).

71. Pettersen, E. F. *et al.* UCSF Chimera—A visualization system for exploratory research and analysis. *J. Comput. Chem.* **25**, 1605–1612 (2004).
72. Katoh, K., Misawa, K., Kuma, K.-I. & Miyata, T. MAFFT: a novel method for rapid multiple sequence alignment based on fast Fourier transform. *Nucleic Acids Res.* **30**, 3059–3066 (2002).
73. Alva, V., Nam, S.-Z., Söding, J. & Lupas, A. N. The MPI bioinformatics Toolkit as an integrative platform for advanced protein sequence and structure analysis. *Nucleic Acids Res.* **44**, W410–5 (2016).
74. Mori, T., Vale, R. D. & Tomishige, M. How kinesin waits between steps. *Nature* **450**, 750–754 (2007).
75. Schneider, C. A., Rasband, W. S. & Eliceiri, K. W. NIH Image to ImageJ: 25 years of image analysis. *Nat. Methods* **9**, 671–675 (2012).
76. Aitken, C. E., Marshall, R. A. & Puglisi, J. D. An oxygen scavenging system for improvement of dye stability in single-molecule fluorescence experiments. *Biophys. J.* **94**, 1826–1835 (2008).
77. Mortensen, K. I., Churchman, L. S., Spudich, J. A. & Flyvbjerg, H. Optimized localization analysis for single-molecule tracking and super-resolution microscopy. *Nat. Methods* **7**, 377–381 (2010).
78. Niekamp, S. *et al.* Nanometer-accuracy distance measurements between fluorophores at the single-molecule level. *Proc. Natl. Acad. Sci. U. S. A.* (2019) doi:10.1073/pnas.1815826116.
79. Höök, P. *et al.* Long range allosteric control of cytoplasmic dynein ATPase activity by the stalk and C-terminal domains. *J. Biol. Chem.* **280**, 33045–33054 (2005).
80. Suloway, C. *et al.* Automated molecular microscopy: the new Leginon system. *J. Struct. Biol.* **151**, 41–60 (2005).
81. Mastronarde, D. N. Automated electron microscope tomography using robust prediction of

specimen movements. *J. Struct. Biol.* **152**, 36–51 (2005).

82. Voss, N. R., Yoshioka, C. K., Radermacher, M., Potter, C. S. & Carragher, B. DoG Picker and TiltPicker: software tools to facilitate particle selection in single particle electron microscopy. *J. Struct. Biol.* **166**, 205–213 (2009).
83. Lander, G. C. *et al.* Appion: an integrated, database-driven pipeline to facilitate EM image processing. *J. Struct. Biol.* **166**, 95–102 (2009).
84. Scheres, S. H. W. RELION: implementation of a Bayesian approach to cryo-EM structure determination. *J. Struct. Biol.* **180**, 519–530 (2012).
85. Punjani, A., Rubinstein, J. L., Fleet, D. J. & Brubaker, M. A. cryoSPARC: algorithms for rapid unsupervised cryo-EM structure determination. *Nat. Methods* **14**, 290–296 (2017).
86. Zheng, S. Q. *et al.* MotionCor2: anisotropic correction of beam-induced motion for improved cryo-electron microscopy. *Nat. Methods* **14**, 331–332 (2017).
87. Zhang, K. Gctf: Real-time CTF determination and correction. *J. Struct. Biol.* **193**, 1–12 (2016).
88. Adams, P. D. *et al.* PHENIX: a comprehensive Python-based system for macromolecular structure solution. *Acta Crystallogr. D Biol. Crystallogr.* **66**, 213–221 (2010).
89. Roy, R., Hohng, S. & Ha, T. A practical guide to single-molecule FRET. *Nat. Methods* **5**, 507–516 (2008).
90. Ha, T. Single-molecule methods leap ahead. *Nat. Methods* **11**, 1015–1018 (2014).
91. Churchman, L. S., Okten, Z., Rock, R. S., Dawson, J. F. & Spudich, J. A. Single molecule high-resolution colocalization of Cy3 and Cy5 attached to macromolecules measures intramolecular distances through time. *Proc. Natl. Acad. Sci. U. S. A.* **102**, 1419–1423 (2005).
92. Rust, M. J., Bates, M. & Zhuang, X. Sub-diffraction-limit imaging by stochastic optical reconstruction microscopy (STORM). *Nat. Methods* **3**, 793–795 (2006).
93. Betzig, E. *et al.* Imaging intracellular fluorescent proteins at nanometer resolution. *Science*

313, 1642–1645 (2006).

94. Churchman, L. S., Flyvbjerg, H. & Spudich, J. A. A non-Gaussian distribution quantifies distances measured with fluorescence localization techniques. *Biophys. J.* **90**, 668–671 (2006).
95. Pertsinidis, A., Zhang, Y. & Chu, S. Subnanometre single-molecule localization, registration and distance measurements. *Nature* **466**, 647–651 (2010).
96. Mortensen, K. I., Sung, J., Flyvbjerg, H. & Spudich, J. A. Optimized measurements of separations and angles between intra-molecular fluorescent markers. *Nat. Commun.* **6**, 8621 (2015).
97. Pitiot, A., Malandain, G., Bardinet, E. & Thompson, P. M. Piecewise affine registration of biological images. in *WBIR* 91–101 (Springer, 2003).
98. Goshtasby, A. Image registration by local approximation methods. *Image Vis. Comput.* **6**, 255–261 (1988).
99. Svoboda, K., Schmidt, C. F., Schnapp, B. J. & Block, S. M. Direct observation of kinesin stepping by optical trapping interferometry. *Nature* **365**, 721–727 (1993).
100. Schmied, J. J. *et al.* Fluorescence and super-resolution standards based on DNA origami. *Nat. Methods* **9**, 1133–1134 (2012).
101. Schmied, J. J. *et al.* DNA origami-based standards for quantitative fluorescence microscopy. *Nat. Protoc.* **9**, 1367–1391 (2014).
102. Höök, P., Yagi, T., Ghosh-Roy, A., Williams, J. C. & Vallee, R. B. The dynein stalk contains an antiparallel coiled coil with region-specific stability. *Biochemistry* **48**, 2710–2713 (2009).
103. Los, G. V. *et al.* HaloTag: a novel protein labeling technology for cell imaging and protein analysis. *ACS Chem. Biol.* **3**, 373–382 (2008).
104. Yin, J. *et al.* Genetically encoded short peptide tag for versatile protein labeling by Sfp phosphopantetheinyl transferase. *Proc. Natl. Acad. Sci. U. S. A.* **102**, 15815–15820 (2005).
105. Lew, M. D., Backlund, M. P. & Moerner, W. E. Rotational mobility of single molecules affects

localization accuracy in super-resolution fluorescence microscopy. *Nano Lett.* **13**, 3967–3972 (2013).

106. Sahl, S. J., Hell, S. W. & Jakobs, S. Fluorescence nanoscopy in cell biology. *Nat. Rev. Mol. Cell Biol.* **18**, 685–701 (2017).

107. Balzarotti, F. *et al.* Nanometer resolution imaging and tracking of fluorescent molecules with minimal photon fluxes. *Science* **355**, 606–612 (2017).

108. Yang, F., Moss, L. G. & Phillips, G. N., Jr. The molecular structure of green fluorescent protein. *Nat. Biotechnol.* **14**, 1246–1251 (1996).

109. Kim, Y. *et al.* Crystal structure of Thermus aquaticus DNA polymerase. *Nature* **376**, 612–616 (1995).

110. Gao, Y., Cao, E., Julius, D. & Cheng, Y. TRPV1 structures in nanodiscs reveal mechanisms of ligand and lipid action. *Nature* **534**, 347–351 (2016).

111. Luger, K., Mäder, A. W., Richmond, R. K., Sargent, D. F. & Richmond, T. J. Crystal structure of the nucleosome core particle at 2.8 A resolution. *Nature* **389**, 251–260 (1997).

112. Ali, M. M. U. *et al.* Crystal structure of an Hsp90-nucleotide-p23/Sba1 closed chaperone complex. *Nature* **440**, 1013–1017 (2006).

113. Klein, D. J., Schmeing, T. M., Moore, P. B. & Steitz, T. A. The kink-turn: a new RNA secondary structure motif. *EMBO J.* **20**, 4214–4221 (2001).

114. Xu, Z., Horwich, A. L. & Sigler, P. B. The crystal structure of the asymmetric GroEL–GroES–(ADP)7 chaperonin complex. *Nature* **388**, 741 (1997).

115. Cao, L. *et al.* The structure of apo-kinesin bound to tubulin links the nucleotide cycle to movement. *Nat. Commun.* **5**, 5364 (2014).

116. Fitzpatrick, J. M. & West, J. B. The distribution of target registration error in rigid-body point-based registration. *IEEE Trans. Med. Imaging* **20**, 917–927 (2001).

117. Thompson, R. E., Larson, D. R. & Webb, W. W. Precise nanometer localization analysis for individual fluorescent probes. *Biophys. J.* **82**, 2775–2783 (2002).

118. Ober, R. J., Ram, S. & Ward, E. S. Localization accuracy in single-molecule microscopy. *Biophys. J.* **86**, 1185–1200 (2004).

119. Yin, J., Lin, A. J., Golan, D. E. & Walsh, C. T. Site-specific protein labeling by Sfp phosphopantetheinyl transferase. *Nat. Protoc.* **1**, 280–285 (2006).

120. Franke, C., Sauer, M. & van de Linde, S. Photometry unlocks 3D information from 2D localization microscopy data. *Nat. Methods* **14**, 41–44 (2017).

121. Joo, C., Balci, H., Ishitsuka, Y., Buranachai, C. & Ha, T. Advances in single-molecule fluorescence methods for molecular biology. *Annu. Rev. Biochem.* **77**, 51–76 (2008).

122. Resch-Genger, U., Grabolle, M., Cavaliere-Jaricot, S., Nitschke, R. & Nann, T. Quantum dots versus organic dyes as fluorescent labels. *Nat. Methods* **5**, 763–775 (2008).

123. Zheng, Q. *et al.* Ultra-stable organic fluorophores for single-molecule research. *Chem. Soc. Rev.* **43**, 1044–1056 (2014).

124. Shaner, N. C., Steinbach, P. A. & Tsien, R. Y. A guide to choosing fluorescent proteins. *Nat. Methods* **2**, 905–909 (2005).

125. Wichner, S. M. *et al.* Covalent Protein Labeling and Improved Single-Molecule Optical Properties of Aqueous CdSe/CdS Quantum Dots. *ACS Nano* **11**, 6773–6781 (2017).

126. Wolfbeis, O. S. An overview of nanoparticles commonly used in fluorescent bioimaging. *Chem. Soc. Rev.* **44**, 4743–4768 (2015).

127. Schröder, T., Scheible, M. B., Steiner, F., Vogelsang, J. & Tinnefeld, P. Interchromophoric Interactions Determine the Maximum Brightness Density in DNA Origami Structures. *Nano Lett.* **19**, 1275–1281 (2019).

128. Woehrstein, J. B. *et al.* Sub–100-nm metafluorophores with digitally tunable optical properties self-assembled from DNA. *Science Advances* **3**, e1602128 (2017).

129. Rothemund, P. W. K. Folding DNA to create nanoscale shapes and patterns. *Nature* **440**, 297–302 (2006).

130. Douglas, S. M. *et al.* Rapid prototyping of 3D DNA-origami shapes with caDNAno. *Nucleic*

Acids Res. **37**, 5001–5006 (2009).

131. Ke, Y., Ong, L. L., Shih, W. M. & Yin, P. Three-dimensional structures self-assembled from DNA bricks. *Science* **338**, 1177–1183 (2012).

132. Wei, B., Dai, M. & Yin, P. Complex shapes self-assembled from single-stranded DNA tiles. *Nature* **485**, 623–626 (2012).

133. Scheible, M. B. *et al.* A Compact DNA Cube with Side Length 10 nm. *Small* **11**, 5200–5205 (2015).

134. Zheng, Q. *et al.* Electronic tuning of self-healing fluorophores for live-cell and single-molecule imaging. *Chem. Sci.* **8**, 755–762 (2017).

135. Grimm, J. B. *et al.* A general method to improve fluorophores for live-cell and single-molecule microscopy. *Nat. Methods* **12**, 244–50, 3 p following 250 (2015).

136. Rasnik, I., McKinney, S. A. & Ha, T. Nonblinking and long-lasting single-molecule fluorescence imaging. *Nat. Methods* **3**, 891–893 (2006).

137. Nicoli, F. *et al.* Proximity-Induced H-Aggregation of Cyanine Dyes on DNA-Duplexes. *J. Phys. Chem. A* **120**, 9941–9947 (2016).

138. Tomishige, M., Klopfenstein, D. R. & Vale, R. D. Conversion of Unc104/KIF1A kinesin into a processive motor after dimerization. *Science* **297**, 2263–2267 (2002).

139. Okada, Y., Higuchi, H. & Hirokawa, N. Processivity of the single-headed kinesin KIF1A through biased binding to tubulin. *Nature* **424**, 574–577 (2003).

140. Yildiz, A., Tomishige, M., Vale, R. D. & Selvin, P. R. Kinesin walks hand-over-hand. *Science* **303**, 676–678 (2004).

141. Stepp, W. L., Merck, G., Mueller-Planitz, F. & Ökten, Z. Kinesin-2 motors adapt their stepping behavior for processive transport on axonemes and microtubules. *EMBO Rep.* **18**, 1947–1956 (2017).

142. Reddy, B. J. N. *et al.* Heterogeneity in kinesin function. *Traffic* **18**, 658–671 (2017).

143. Ozhalici-Unal, H. & Armitage, B. A. Fluorescent DNA nanotags based on a self-assembled

DNA tetrahedron. *ACS Nano* **3**, 425–433 (2009).

144. Kretschy, N., Sack, M. & Somoza, M. M. Sequence-Dependent Fluorescence of Cy3- and Cy5-Labeled Double-Stranded DNA. *Bioconjug. Chem.* **27**, 840–848 (2016).

145. Femino, A. M., Fay, F. S., Fogarty, K. & Singer, R. H. Visualization of single RNA transcripts in situ. *Science* **280**, 585–590 (1998).

146. Chen, K. H., Boettiger, A. N., Moffitt, J. R., Wang, S. & Zhuang, X. RNA imaging. Spatially resolved, highly multiplexed RNA profiling in single cells. *Science* **348**, aaa6090 (2015).

147. Jungmann, R. *et al.* Multiplexed 3D cellular super-resolution imaging with DNA-PAINT and Exchange-PAINT. *Nat. Methods* **11**, 313–318 (2014).

148. Yang, S., Liu, W. & Wang, R. Control of the stepwise assembly–disassembly of DNA origami nanoclusters by pH stimuli-responsive DNA triplexes. *Nanoscale* **11**, 18026–18030 (2019).

149. Ke, Y. *et al.* Scaffolded DNA origami of a DNA tetrahedron molecular container. *Nano Lett.* **9**, 2445–2447 (2009).

150. Ohmann, A. *et al.* Controlling aggregation of cholesterol-modified DNA nanostructures. *Nucleic Acids Res.* **47**, 11441–11451 (2019).

151. Chen, Y., Deffenbaugh, N. C., Anderson, C. T. & Hancock, W. O. Molecular counting by photobleaching in protein complexes with many subunits: best practices and application to the cellulose synthesis complex. *Mol. Biol. Cell* **25**, 3630–3642 (2014).

152. Yildiz, A., Tomishige, M., Gennerich, A. & Vale, R. D. Intramolecular strain coordinates kinesin stepping behavior along microtubules. *Cell* **134**, 1030–1041 (2008).

153. Ray, S., Meyhöfer, E., Milligan, R. A. & Howard, J. Kinesin follows the microtubule's protofilament axis. *J. Cell Biol.* **121**, 1083–1093 (1993).

154. Niekamp, S., Stuurman, N. & Ronald, D. Folding of FluoroCubes v1 (protocols.io.8k2huye). doi:10.17504/protocols.io.8k2huye.

155. Tang, G. *et al.* EMAN2: an extensible image processing suite for electron microscopy. *J.*

Struct. Biol. **157**, 38–46 (2007).

156. Cianfrocco, M. A., DeSantis, M. E., Leschziner, A. E. & Reck-Peterson, S. L. Mechanism and regulation of cytoplasmic dynein. *Annu. Rev. Cell Dev. Biol.* **31**, 83–108 (2015).

157. Niekamp, S., Coudray, N., Zhang, N., Vale, R. D. & Bhabha, G. Coupling of ATPase activity, microtubule binding, and mechanics in the dynein motor domain. *EMBO J.* **38**, e101414 (2019).

158. Yildiz, A. *et al.* Myosin V walks hand-over-hand: single fluorophore imaging with 1.5-nm localization. *Science* **300**, 2061–2065 (2003).

159. Beater, S., Raab, M. & Tinnefeld, P. Toward quantitative fluorescence microscopy with DNA origami nanorulers. *Methods Cell Biol.* **123**, 449–466 (2014).

160. Keppler, A. *et al.* A general method for the covalent labeling of fusion proteins with small molecules in vivo. *Nat. Biotechnol.* **21**, 86–89 (2003).

161. Niekamp, S., Stuurman, N. & Vale, R. D. A 6-nm ultra-photostable DNA FluoroCube for fluorescence imaging. *Nat. Methods* **17**, 437–441 (2020).

162. Ferro, L. S., Can, S., Turner, M. A., ElShenawy, M. M. & Yildiz, A. Kinesin and dynein use distinct mechanisms to bypass obstacles. *Elife* **8**, (2019).

163. Gennerich, A., Carter, A. P., Reck-Peterson, S. L. & Vale, R. D. Force-induced bidirectional stepping of cytoplasmic dynein. *Cell* **131**, 952–965 (2007).

164. Nicholas, M. P. *et al.* Cytoplasmic dynein regulates its attachment to microtubules via nucleotide state-switched mechanosensing at multiple AAA domains. *Proc. Natl. Acad. Sci. U. S. A.* **112**, 6371–6376 (2015).

165. Belyy, V., Hendel, N. L., Chien, A. & Yildiz, A. Cytoplasmic dynein transports cargos via load-sharing between the heads. *Nat. Commun.* **5**, 5544 (2014).

166. Lin, J., Okada, K., Raytchev, M., Smith, M. C. & Nicastro, D. Structural mechanism of the dynein power stroke. *Nature Cell Biology* vol. 16 479–485 (2014).

167. Brenner, S., Berger, F., Rao, L., Nicholas, M. P. & Gennerich, A. Force production of human

cytoplasmic dynein is limited by its processivity. *Science Advances* vol. 6 eaaz4295 (2020).

168. Nicholas, M. P. *et al.* Control of cytoplasmic dynein force production and processivity by its C-terminal domain. *Nature Communications* vol. 6 (2015).

169. Belyy, V. *et al.* The mammalian dynein–dynactin complex is a strong opponent to kinesin in a tug-of-war competition. *Nature Cell Biology* vol. 18 1018–1024 (2016).

Publishing Agreement

It is the policy of the University to encourage open access and broad distribution of all theses, dissertations, and manuscripts. The Graduate Division will facilitate the distribution of UCSF theses, dissertations, and manuscripts to the UCSF Library for open access and distribution. UCSF will make such theses, dissertations, and manuscripts accessible to the public and will take reasonable steps to preserve these works in perpetuity.

I hereby grant the non-exclusive, perpetual right to The Regents of the University of California to reproduce, publicly display, distribute, preserve, and publish copies of my thesis, dissertation, or manuscript in any form or media, now existing or later derived, including access online for teaching, research, and public service purposes.

DocuSigned by:
Stefan Mekamp
14B6385D63CF442...
Author Signature

10/1/2020
Date